National Roadmap for Adaptation 2100

Portuguese Territorial Climate Change Vulnerability Assessment for XXI Century

REPORT

WP2 – CLIMATE PROJECTIONS, EXTREMES, AND INDICES

Mainland Portugal

Final Version

National Roadmap for Adaptation 2100

Portuguese Territorial Climate Change Vulnerability Assessment for XXI Century

---

Title: RNA2100 – Climate Projections, Extremes, and Indices – Mainland Portugal

Authors: Pedro Matos Soares (coord.), Daniela Lima, Rita Cardoso, Miguel Nogueira, Gil Lemos, Virgílio Bento, Ricardo Trigo.

February 2024

This report is a product of the National Roadmap for Adaptation 2100 project.

Through the Agreement on the European Economic Area (EEA), Iceland, Liechtenstein and Norway are partners in the internal market with the Member States of the European Union.

In order to promote a continuous and balanced strengthening of economic and trade relations, the parties to the EEA Agreement have established a and trade relations, the parties to the EEA Agreement established a multi-annual Financial Mechanism, known as the EEA. known as EEA Grants.

The EEA Grants aim to reduce social and economic disparities in Europe and to strengthen bilateral relations between these three countries and the beneficiary countries.

For the 2014-2021 period, a total contribution of 2.8 billion euros has been agreed for 15 beneficiary countries. for 15 beneficiary countries. Portugal will receive 102.7 million euros.

Funded by:

Promoter:

Partners:

Table of Contents

List of Figures

List of Tables

Summary

Warming and drying future conditions may significantly affect human and natural environment in Portugal. This report shows the importance of carrying out climate change assessments focusing on different greenhouse gas emission scenarios. The climate projections are found to be especially dramatic for the non-mitigated emission scenario (RCP8.5), while more manageable for the highly-mitigated scenario (RCP2.6). The results here revealed very distinct change magnitudes and patterns within the three RCPs, which will lead to substantially different socio-economic impacts and adaptation needs. Even under a strong mitigation scenario, substantial changes for sectoral climate indices are projected, which may strongly impact sectors like agriculture and water management. An in-depth analysis on the specific sectoral impacts on agriculture, forestry, coastal areas and cities will also be performed, assessing territorial-wide climate vulnerabilities, focusing on the hydrological balance, extreme events (*e.g.*, droughts and heatwaves), forest fires, sea level rise, storm surges and wave climate. The entire assessment is necessary to translate physical impacts into social and economic ones.

Continental Portugal (hereafter Portugal) is located in the western tip of the Mediterranean basin, in the transition zone between the arid to semiarid climates of subtropical regions and the humid climates typical of northern Europe. This region has been identified as a climate change "hotspot", with observed and projected rates of climate change exceeding global trends for most variables (Giorgi 2006; Lionello and Scarascia 2018; Cramer et al. 2018). Humid mild winters and dry warm/hot summers are common features that characterise both the Portuguese and Mediterranean climates. Indeed, observational records between 1860 and 2005 show a general trend for warmer and drier mean atmospheric conditions over these areas (Giorgi and Lionello 2008; Trenberth 2011; Turco et al. 2018). According to the Fifth and Sixth Assessment Reports of the Intergovernmental Panel on Climate Change (IPCC) (IPCC, 2013, 2021), the observed increase in mean temperature over the western Mediterranean basin during the last decades has been particularly pronounced in summer months, and the warming and drying trends across the Mediterranean will continue throughout the twenty-first century (Lionello and Scarascia 2018; Tuel and Eltahir 2020).

The projected warming and drying trends over Portugal were shown to be stronger for high anthropogenic emission scenarios, confirming the importance of the human component on the overall climate change projections when compared to the natural variability of the climate system, even at the regional scale (Barcikowska et al. 2018; Cramer et al. 2018). The goal of the Paris Agreement is to limit the global

temperature increase to 1.5 ºC relative to pre-industrial levels, while pursuing efforts to avoid the 2 ºC warming threshold. Nonetheless, even in a 2 ºC global warming scenario, a critical environmental situation will develop, related to the enhanced warming of land areas in summer and widespread reduction of precipitation, especially over the Mediterranean region. In this report, it is shown that, even under an optimistic scenario of strong mitigation (RCP2.6), Portugal is projected to experience an average warming between 1 ºC and 2 ºC, relative to the historical period. On the other hand, for the scenario without mitigation, *i.e.*, RCP8.5, a generalized warming exceeding 6 ºC is projected until the end of the 21st century. Temperature is projected to increase through all seasons and regions in Portugal during the 21st century, with a greater warming during summer (Cardoso et al. 2019), enhancing the land-sea thermal contrast. In fact, the projected intensification of the Azores anticyclone and its expansion to northeast due to the northward expansion of the Hadley Cell (Miyasaka and Nakamura 2005; Kang and Lu 2012), together with the strengthening of the Iberian thermal low, forces more intense and frequent summer winds parallel to the coast ("Nortada"), especially in the northwestern Iberian Peninsula, especially impacting the northern and central areas of Portugal (Cardoso et al. 2016; Soares et al. 2017b, c). In general, projections of maximum temperature were shown to have slightly larger magnitudes than those of minimum temperature, consistent with a slender amplification of the daily temperature range.

The frequency and intensity of extreme hot events was also shown to be projected to change considerably through most of the territory, evident even already during the first future climatological time-slice (2011-2040), especially in the southern regions. In fact, the 100-year return levels during historical climate are generally exceeded by the projected 10-year return levels from 2041-2070 onwards. Moreover, the intensity of extreme heat event is also projected to increase for future events. The expansion of the Azores high and its enhanced persistency in higher latitudes during winter is projected to lead to a reduction of the weather regimes that produce large-scale precipitation events (Bengtsson et al. 2009), and the strengthening of pressure and temperatures gradients may increase the advection of warmer continental air. On the other hand, the increase of pressure gradient along the coast may intensify the across-shore winds limiting the advection of moist air inland, which may explain the reduction of precipitation projected for intermediate and summer seasons. Although summer precipitation does not have a significant contribution for the annual total due to its lower values, projected decreases below -40% are expected during 2071-2100. Warming and drying conditions may cause a decline in the relative humidity, and consequently an increase in potential evapotranspiration.

Along with the warming, reflected in maximum temperatures, summer days, hot days, and very hot days are projected to become more frequent and intense. A northwestern-southeastern gradient is generally observed, with the south-eastern interior regions depicting a more pronounced increase than the north-

western coastal regions. Projected changes differ substantially among the emission scenarios, often duplicating in magnitude from RCP2.6 to RCP8.5. Under the worst-case scenario (RCP8.5), maximum temperatures above 25ºC are projected to be registered in more than half of the year (an increase of approximately 50% regarding the historical period), with up to 100 days above 35ºC. Conversely, for the strong mitigation scenario (RCP2.6), the projected increases for these variables are set at approximately 25%, and 50 days per year, respectively. The considerable projected increase in number of heat days may be detrimental to public health since it directly impacts the human thermoregulatory capacity (Kovats and Hajat 2008) which will be greatly aggravated if greenhouse gases are not considerably reduced (Kang and Lu 2012). Aligned with the projected increases in minimum temperature, tropical nights were shown to become more common, accompanied by an expected decrease in the number of cold and frost days. Since tropical nights are the main cause of thermal discomfort, such frequency increases may affect the thermal comfort conditions, and consequently human health (Karyono et al. 2020). Nocturnal thermal stress is projected to be further aggravated over cities by the urban heat island effect (Nogueira and Soares 2019; Nogueira et al. 2020), with significant implications to human health. Furthermore, in the north-eastern regions, a gradual shrinking of the area where the number of cold and frost days attain the maximum values during the historical period is projected to occur, throughout the 21st century. Aligned with the projections for cold days, results of the maximum number of consecutive cold days show a reduction throughout the 21st century (not shown). For all the emission scenarios and time periods, the frequency of cold waves is expected to decrease throughout the entire country. The steady decline in severity and frequency of cold waves over the last decades in the observations is a subject that has been recently discussed for high mid-latitudes of the northern hemisphere (Van Oldenborgh et al. 2019). In fact, the decline in cold and frost days may have a positive repercussion in the health system pressure during winter (Charlton-Perez et al. 2019).

Associated to the decrease in mean accumulated precipitation, the number of wet days is projected to decrease until the end of the 21st century, in line with Soares et al. (2017a). Consequently, the number of dry days is expected to increase, enhancing drying conditions. The magnitude of such projections is enhanced for the non-mitigated scenario when compared with the scenario with strong mitigation. After 2041, a decrease in the number of wet days is expected for RCP4.5 (RCP8.5), to less than 18 (24) days per year, worsened by the end of the 21st century, with a reduction of up 36 days under the RCP8.5. For the RCP2.6, the projected changes are negligible throughout the century, with a slight decrease up to 12 days over the northeastern region during the mid-21st century. In terms of moderate and heavy precipitation, clear projected reductions are visible, especially for the RCP4.5 and RCP8.5 scenarios, however, local increases are projected for the maximum 5-day accumulated values. These projections indicate that rainfall may become more concentrated into shorter time frames, implying an intensification of moderate/heavy

precipitation independently of the scenario. Such results may be linked to the expected increase in the average percentage of annual precipitation originating from days with moderate to heavy rainfall. Especially during autumn and winter, the westerly flux driven by the seasonal displacement of the Azores high-pressure system towards lower latitudes favours the influence of low-pressure systems, leading to especially rainy conditions over the northern and central coastal areas. The topography north of the Tagus River prevents most of the precipitable water from reaching the regions near the Spanish border, leading to lower accumulations there.

The projected climatological poleward displacement of the storm tracks over the North Atlantic due to the northward expansion of the Hadley Cell is a well-known consequence of climate change, leading to consistent reductions in wind speeds and accumulated precipitation in Portugal (Bengtsson et al. 2006; Ulbrich et al. 2008; Kang and Lu 2012; Harvey et al. 2014). In fact, the largest reductions of 10-m wind speeds are found in winter and autumn seasons over elevated terrain in northern and central-eastern regions, and over the southwestern coastal regions for the end of the 21st century. Precipitation changes depend on the season, region, and the emission scenario. The highly-(non-)mitigated emission scenario projections were shown to point to a moister (drier) winter. Although an overall decrease in the accumulated precipitation is expected, an intensification of heavy, short-term precipitation events is projected, especially over the northern region, which is in agreement with Soares et al. (2017a). In fact, although a reduction of stormy weather across Portugal is an expected reality, the intensity of individual storms may increase, originating not only concentrated precipitation events, but also increases in the maximum wind gusts in several areas of the country (Bengtsson et al. 2009).

Throughout most of mainland Portugal, projections of 10-m wind speeds showed a general decrease, especially for intensities above 5.5 m/s, even on mountainous areas in northern and central Portugal. Implications from these results are especially evident for the renewable energy sector. In the first three months of 2022, 36.9% of the country's clean energy was generated through the wind, being the largest source at national scale (APREN 2022). Furthermore, 11 of the 16 wind energy production parks in Portugal are located in the northern and central regions, where the projected decreases in wind intensities tend to be greater. Adaptation of the renewable energy sector to climate change may require a revaluation of the geographical distribution of wind energy generation turbines. The sole location where a consistent projected increase in frequency of occurrence of 10-m wind speeds above 5.5 m/s was shown to be the Lisbon district, associated to the intensification of northerly winds ("Nortada"). Notice that these results are in agreement with (Nogueira et al. 2019), which reported the largest projected reduction on wind energy production to occur during winter and autumn over northern Portugal, with a small increase during summer over Lisbon metropolitan area and Alentejo. In fact, it is important to point out that despite the small magnitude of the

average 10-m wind speed projected changes, the impact on wind turbine energy production is substantial due to the logarithm wind profile combined with the cubic dependence of wind energy production on wind speed, and the high and low cut-off thresholds of wind turbines for energy production (Soares et al. 2017b, 2019; Lima et al. 2021).

Scientific Deliverables:

Lima DCA, Gil Lemos; Virgílio A. Bento; Miguel Nogueira; Pedro M.M. Soares (2023) **A multi-variable constrained ensemble of regional climate projections under multi-scenarios for Portugal – Part I: an overview of impacts on means and extremes**. Climate Services, 30 (100351). https://doi.org/10.1016/j.cliser.2023.100351

Lima DCA, Virgílio A. Bento; Gil Lemos; Miguel Nogueira; Pedro M.M. Soares (2023) **A multi-variable constrained ensemble of regional climate projections under multi-scenarios for Portugal – Part II: sectoral climate indices**. Climate Services, 30 (100377). https://doi.org/10.1016/j.cliser.2023.100377

Soares PMM and Daniela C.A. Lima (2022) **Water scarcity down to earth surface in a Mediterranean climate: the extreme future of soil moisture in Portugal**. Journal of Hydrology, 615 B (128731). https://doi.org/10.1016/j.jhydrol.2022.128731

Cardoso RM, Daniela C.A. Lima; Pedro M.M. Soares (2023) **How persistent and hazardous will extreme temperature events become in a warming Portugal**. Weather and Climate Extremes, 41 (100600). https://doi.org/10.1016/j.wace.2023.100600

1. Introduction

The Intergovernmental Panel on Climate Change Fifth Assessment Report (IPCC 2013) established the existence of unequivocal evidence of the anthropogenic influence on the Earth's climate since the beginning of the industrial revolution. This influence comprises a warming trend of the atmosphere and oceans, the reduction of sea-ice coverage and the rise of sea-level. Developing successful mitigation and adaptation strategies, to minimize the human impact on future climate and restrict the unavoidable climate change-driven impacts to societies and the environment, requires accurate quantitative science-based climate information. Numerical models of the Earth's climate system grounded in sound physical principles are the best available tools to provide this detailed climate information for the past and the future.

State-of-the-art Global Climate Models (GCMs) can simulate the Earth's climate over the past century and project its future evolution under different scenarios of human development. However, climate projections obtained from global models are affected by three types of uncertainties: future scenario uncertainty, natural variability, and model uncertainty (Hawkins and Sutton 2009; Deser et al. 2012). One way to tackle these uncertainties is to use an ensemble, consisting of a set of climate simulations generated by different models (usually produced by different research centres), spanning different scenarios of future greenhouse gas emissions, and initialized with different initial conditions. Refined climate projections are then quantified, along with the associated uncertainty, by combining the information from multiple model outputs (ensemble members) for each scenario. The Coupled Model Intercomparison Project (CMIP) (Meehl et al. 2000) provides the best example of an international concentrated effort to produce such ensembles, providing the basis for the IPCC assessment reports.

A major shortcoming of GCMs is their coarse horizontal grid resolutions, on the order of 100 km or less, due to computational constraints. This issue has been shown to represent a major error source, largely due to the need of introducing simplified representations of many unresolved important processes occurring at scales smaller than the grid spacing (Flato et al. 2013; Palmer and Stevens 2019; Bock et al. 2020). Additionally, this coarse resolution poses a significant limitation for regional and local climate change impact assessments, since much of the complex spatial heterogeneities that determine local climate, and its evolution are not represented. This includes relevant details of topographic features, coastlines, vegetation cover, urban areas, which have been widely demonstrated to have a significant modulating impact on the local weather and climate patterns, as it has been previously demonstrated for Portugal (Soares et al. 2017a; Cardoso et al. 2019; Nogueira et al. 2019).

The need for accurate and detailed high-resolution climate information led to coordinated efforts to dynamically downscale ensembles of global model simulations, using Regional Climate Models (RCMs)

nested into the GCMs output. This technique allows for a considerably higher spatial resolution over the domain of interest, hence, a more realistic representation of important surface heterogeneities (such as topography, coast lines, and land surface characteristics) and of mesoscale atmospheric processes. The increased resolution comes at the cost of the model domain spanning over a limited area. Recent examples of RCM ensembles are the Ensemble-Based Predictions of Climate Changes and Their Impacts (ENSEMBLES, (Hewitt and Griggs 2004)), the North American Regional Climate Change Assessment Program (NARCCAP, (Mearns et al. 2009)), and the Coordinated Regional Climate Downscaling Experiment (CORDEX (Giorgi et al. 2009)). The present work leverages on the latest European branch of CORDEX (EURO-CORDEX, (Jacob et al. 2014, 2020)) which provides regional climate projections for Europe at a horizontal grid resolution of about 12 km, obtained by dynamically downscaling the CMIP5 ensemble using a set of RCMs.

One of the shortcomings that must be addressed while constructing optimized regional climate projections based on the EURO-CORDEX is the fact that this is an ensemble of opportunity. This means that while some aspects are coherent amongst the ensemble members (*e.g.*, the spatial domains), others are very heterogeneous. While the main source of heterogeneity is related to the IPCC emission scenarios covered by each model, an additional issue with ensembles of opportunity is the lack of independence among certain models (Bishop and Abramowitz 2013; Abramowitz and Bishop 2015; Sanderson et al. 2015). A further source of complexity arises when the ensemble is built considering the individual performances of its members, since it depends on the chosen error metrics, variables and analysed region (Kotlarski et al. 2015; Prein et al. 2016; Casanueva et al. 2016; Knist et al. 2017; Frei and Isotta 2019; Jacob et al. 2020). The latter issue has been found to be particularly relevant at the sub-national level for Portugal (Soares et al. 2017b, a; Cardoso et al. 2019; Nogueira et al. 2019). Overall, these problems require a careful analysis prior to the selection of the models and criteria used to build the ensemble climate projections. Furthermore, they imply that giving equal weight to all models (the "democratic" approach) is suboptimal (Eyring et al. 2019). In fact, weighting individual models based on their performance over the specific domain, variables and metrics of interest has been shown to improve the quality of the climate projections derived from ensembles (Christensen et al. 2010; Wenzel et al. 2016; Knutti et al. 2017; Sanderson et al. 2017; Eyring et al. 2019; Nogueira et al. 2019).

Here, a detailed analysis of the available simulations in the EURO-CORDEX dataset for the different relevant climate variables and over the different periods is carried, along with comprehensive evaluation of precipitation, and daily maximum and minimum temperatures over Portugal. The recently released Iberia01 gridded observation dataset (Herrera et al. 2019) was considered as reference. Subsequently, an optimized multi-model ensemble is constructed based on performance-dependent weights for the different available

models. Finally, the optimized ensemble is used to obtain high resolution climate projections for the main climate variables and a large number of climate indices relevant for stakeholders and policymakers. Three different future Representative Concentration Pathways are considered: the business-as-usual RCP8.5 scenario, the moderate emission RCP4.5 scenario, and the strong mitigation RCP2.6 scenario (see (van Vuuren et al. 2011) for a detailed description of the RCPs). The main climate change signals over Portugal are presented here along with a quantification of the respective uncertainties. The manuscript is organized as follows: the datasets and analysis methodologies employed are described in Section 2 as the climate indices computed to characterize the Portuguese climate and its future evolution; the main results of the comprehensive EURO-CORDEX RCM error assessment are presented in Section 3; a brief description of the large-scale drivers of climate change over Portugal and the Mediterranean region are presented in Section4; the results on the future climate change signals in Portugal are described in Section 5 and the results on the future climate change of climate extremes and indices in Portugal are presented in Section 6.

2. Data and Methods

2.1. EURO-CORDEX Simulations

The CORDEX experiment (Giorgi et al. 2009) aggregated many RCM simulations to ensure large continental scale climate ensembles. The EURO-CORDEX simulations were developed under the CORDEX effort (Jacob et al. 2014, 2020), providing regional climate projections over a shared European domain with a horizontal grid resolution of 0.11º (Figure 2.1), obtained by dynamically downscaling CMIP5 GCMs.

Four EURO-CORDEX experiments are considered here, namely one for the historical period (1971-2000), and three for the future periods (2011–2100) considering a different emission scenario: RCP2.6, RCP4.5, and RCP8.5. Three future 30-year timeframes were assessed: 2011-2040, 2041-2070 and 2071-2100. All EURO-CORDEX ensemble members available through the Earth System Grid Federation (ESFG) data portal in September/2020 were considered here. It is worth noticing that the number of ensemble members varies depending on the experiment, ranging between 20 and 45 (Table 2.1). Of these, only 13 RCMs concurrently cover all experiments. These differences are taken into account when building the ensemble climate projections for Portugal, as explained in Section 2.4. The variables retrieved and used in this study were daily total precipitation, 2-m maximum and minimum daily temperatures, daily mean wind speed at 10 m height, maximum of daily maximum wind gusts.

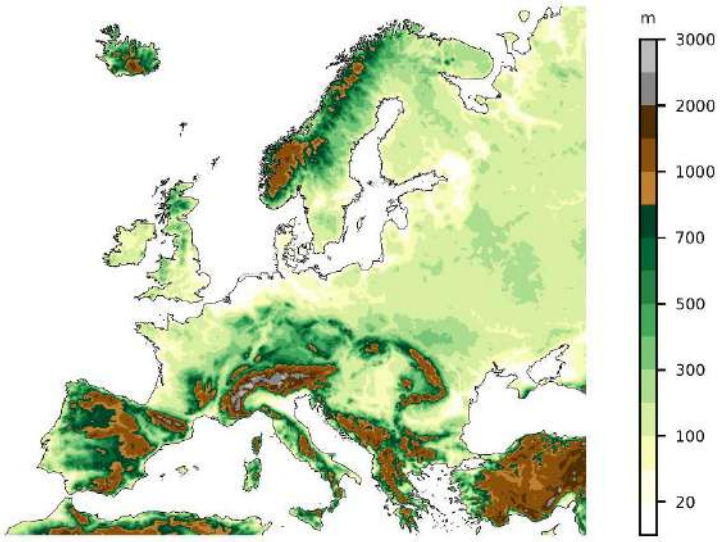

Figure 2.1 The EURO-CORDEX model domain at 0.11° resolution. The colours represent the topographic height (in meters).

Table 2.1 EURO-CODEX RCMs used in this study, along with the forcing GCMs, the responsible institute, and the available RCP scenarios. In grey are highlighted GCM-RCM combinations available for all experiments.

RCM	Institute	GCM	RCP2.6	RCP4.5	RCP8.5	Acronym
CCLM4-8-17	CLM	CNRM-CM5		X	X	CLM1
		EC-Earth	X	X	X	CLM2
		HadGEM2-ES		X	X	CLM3
		MPI-ESM-LR		X	X	CLM4
COSMO-crCLIM-v1-1	CLM	EC-Earth			X	CLM-E1
		HadGEM2-ES			X	CLM-E2
		MPI-ESM-LR			X	CLM-E3
		NorESM1-M			X	CLM-E4
ALADIN63	CNRM	CNRM-CM5	X	X	X	CNRM1
		HadGEM2-ES			X	CNRM2
		MPI-ESM-LR			X	CNRM3
HIRHAM5	DMI	CNRM-CM5			X	DMI1
		EC-Earth	X	X	X	DMI2
		HadGEM2-ES	X	X	X	DMI3
		MPI-ESM-LR			X	DMI4
		NorESM1-M		X	X	DMI5
REMO2015	GERICS	CNRM-CM5	X		X	GERICS1
		IPSL-CM5A-LR	X			GERICS2
		MPI-ESM-LR			X	GERICS3
		NorESM1-M	X	X	X	GERICS4
		GFDL-ESM2G	X			GERICS5
RegCM4-6	ICTP	EC-Earth			X	ICTP1
		HadGEM2-ES	X		X	ICTP2
		MPI-ESM-LR	X		X	ICTP3
WRF381P	IPSL	CNRM-CM5			X	IPSL1
		EC-Earth			X	IPSL2
		IPSL-CM5A-MR		X	X	IPSL3
		HadGEM2-ES			X	IPSL4
		NorESM1-M			X	IPSL5
RACMO22E	KNMI	CNRM-CM5	X	X	X	KNMI1
		EC-Earth	X	X	X	KNMI2
		IPSL-CM5A-MR			X	KNMI3
		HadGEM2-ES	X	X	X	KNMI4
		MPI-ESM-LR	X		X	KNMI5
		NorESM1-M	X		X	KNMI6

HadREM3-GA7-05	MOHC	EC-Earth	X		X	MOHC1
		HadGEM2-ES	X		X	MOHC2
		MPI-ESM-LR			X	MOHC3
REMO2009	MPI	MPI-ESM-LR	X	X	X	MPI
RCA4	SMHI	CNRM-CM5		X	X	SMHI1
		EC-Earth	X	X	X	SMHI2
		IPSL-CM5A-MR		X	X	SMHI3
		HadGEM2-ES	X	X	X	SMHI4
		MPI-ESM-LR	X	X	X	SMHI5
		NorESM1-M	X	X	X	SMHI6

2.2. Iberia01 Observations

The Iberia01 observational gridded dataset was considered as reference to evaluate the performance of the historical EURO-CORDEX simulations. Iberia01 covers the 1971-2015 period, with a horizontal resolution of 0.1º, providing daily values for precipitation, and maximum and minimum temperatures based on a dense network of weather stations over the Iberian Peninsula, including 3486 and 275 stations for precipitation and temperature, respectively (Herrera et al. 2019). For comparison with the EURO-CORDEX historical simulations, the 1971-2000 time-slice was considered, being the common period between observations and the historical runs. Over Portugal and for the considered period, the number of stations for precipitation was around 500, whilst for temperature was around 50.

Herrera et al. (2019) showed that Iberia01 reproduces well the spatial pattern of precipitation and temperature in what concerns both mean and extremes. Concerning temperature, there is a lack of stations in almost all country, with special emphasis in the northeast region and along some coastal areas. Regarding precipitation, the available observational networks cover all the country, with highest the temporal missing data in northwest regions and along coastal regions north of Lisbon (Herrera et al. 2019). These issues increase the observational uncertainty in the mentioned regions.

2.3. Model evaluation metrics

The ability of the EURO-CORDEX simulations to reproduce the main properties of the observed climate within mainland Portugal was assessed at each grid-point, considering Iberia01 (IB-01) as observational reference. The IB-01 does not have an observational gridded dataset for the 10-m wind speed. Hence, only precipitation, maximum and minimum temperatures were evaluated. Nevertheless, EURO-CORDEX 10-m wind speeds have been previously evaluated revealing good performances over Portugal, corresponding

to mean and extreme (95th percentile) biases generally lower than 1 m/s and 3 m/s, respectively (Moemken et al. 2018; Nogueira et al. 2019; Vautard et al. 2021).

Since the EURO-CORDEX RCMs and the regular gridded observational dataset have different resolutions, the high-resolution daily precipitation and temperature results (observational grid IB-01) are interpolated conservatively (Suklitsch et al. 2008) to the EURO-CORDEX grid at 0.11°. To account for differences in surface height between the grid points in IB-01 and target grid points in the RCM grid, the temperatures are corrected with an adiabatic adjustment (6.5 K/km) to mean sea level beforehand and after the interpolation, they are adiabatically adjusted to the RCM grid topography.

The historical climate simulations use GCM outputs as lateral boundary conditions, which means that they have a daily non-synchronised climate compared with the observations. Consequently, only a statistical comparison can be performed between the EURO-CORDEX RCMs and the Iberia01. Therefore, a Julian year with 366 daily means was computed for each RCM and observational dataset. Thus, the use of this daily climatology makes possible the comparison between the observations and EURO-CORDEX simulations temporal mean values, from monthly to yearly scales, allowing the scrutiny of the non-synchronised present climate.

The historical simulations' evaluation was carried over the 1971-2000 period, considering eight different error metrics, namely the mean bias, mean absolute error, root mean squared error, normalized standard deviation, spatial correlation, Willmott-D Score, Perkins skill score, and Yule-Kendall skewness. The selection of this set of error metrics provides different ways to quantify the performance of each model, giving a more robust assessment of the quality of simulations.

The mean bias or mean percentual bias, used for temperature and precipitation, respectively, measures the models' systematic errors, and are defined as:

$$Bias = \frac{1}{N}\sum_{k=1}^{N}(p_k - o_k) \quad or \quad Bias\% = \frac{\sum_{k=1}^{N}(p_k - o_k)}{\sum_{k=1}^{N} o_k} \tag{1}$$

where o_k and p_k are respectively the observed and simulated 366 daily means at grid-point k, and N is the total number of grid-points.

The mean absolute error (MAE) for temperature or mean absolute percentual error (MAPE) for precipitation follow a similar formulation as bias and mean percentual bias but for absolute errors:

$$MAE = \frac{1}{N}\sum_{k=1}^{N}|p_k - o_k| \quad or \quad MAPE = \frac{\sum_{k=1}^{N}|p_k - o_k|}{\sum_{k=1}^{N} o_k} \tag{2}$$

The root-mean squared error (RMSE) is defined as:

$$RMSE = \sqrt{\frac{1}{N}\sum_{k=1}^{N}(p_k - o_k)^2} \tag{3}$$

The normalized standard deviation measure is the ratio between the standard deviation of the modelled and observed time-series, and is expressed as:

$$\sigma_n = \frac{\sigma_p}{\sigma_o} = \frac{\sqrt{\frac{1}{N}\sum_{k=1}^{N}(p_k - \bar{p})^2}}{\sqrt{\frac{1}{N}\sum_{k=1}^{N}(o_k - \bar{o})^2}} \tag{4}$$

where σ_o and σ_p are respectively standard deviations of the observed and simulated time-series, respectively, while $\bar{o}$ and $\bar{p}$ represent the respective mean values. The closer the σ_n values are to unit, the better the model is representing the observed variability. The spatial correlation (Wilks 2006) was also computed, given by:

$$r = \frac{\sum_{k=1}^{N}(o_k - \bar{o})\,(p_k - \bar{p})}{\sqrt{\sum_{k=1}^{N}(o_k - \bar{o})^2 \sum_{k=1}^{N}(p_k - \bar{p})^2}} \tag{5}$$

The Willmott-D Score (Willmott et al. 2012) is a combined measure of the differences in mean and standard deviation between model and observations, with $D = 1$ for a perfect skill and $D = -1$ for no skill:

$$D = \begin{cases} 1 - \dfrac{\sum_{k=1}^{N}|p_k - o_k|\,|p_k - o_k|}{2\sum_{k=1}^{N}|o_k - \bar{o}|}, & if \sum_{k=1}^{N}|p_k - o_k| \le 2\sum_{k=1}^{N}|o_k - \bar{o}| \\ \dfrac{2\sum_{k=1}^{N}|o_k - \bar{o}|}{\sum_{k=1}^{N}|p_k - o_k|} - 1, & if\ 2\sum_{k=1}^{N}|o_k - \bar{o}| < \sum_{k=1}^{N}|p_k - o_k| \end{cases} \tag{6}$$

The models' ability to reproduce the observed probability distribution functions (PDFs) was quantified by the Perkins skill score (Perkins et al. 2007), henceforth denoted S:

$$S = 100 \times \sum_{i=1}^{B} min\,[E_{p,i}, E_{o,i}] \tag{7}$$

where E_p and E_o are, respectively, the simulated and observed empirical PDFs, min[x,y] represents the minimum two values, and B is the total number of bins used to compute the empirical PDF. This score

provides a measure of similarity between the simulated and observed empirical PDFs, with $S = 100\%$ if the model reproduces the observed empirical PDF perfectly and decreasing towards zero as the similarity between the PDFs decreases. Here the S score was computed in two different ways: for the full PDF (S), and for the average of two sections following (Boberg et al. 2009). For precipitation and maximum temperature, the first section encompasses the data from the minimum value (P_0) to the 90th percentile (P_{90}) and another from P_{90} to the maximum value (P_{100}), hereafter $S90$; for minimum temperature the two sections are from P_0 to the 10th percentile (P_{10}) and from P_{10} to P_{100}, hereafter $S10$.

Finally, the Yule-Kendall skewness measure (Ferro et al. 2005) quantifies the matching between the skewness of the simulated and observed PDFs:

$$YK = \left[\frac{(P_{95}-P_{50})-(P_{50}-P_5)}{(P_{95}-P_5)}\right]_{model} - \left[\frac{(P_{95}-P_{50})-(P_{50}-P_5)}{(P_{95}-P_5)}\right]_{obs} \quad (8)$$

where P_j represents the jth percentiles computed from the simulated and observed daily time-series datasets. The closer the YK is to zero, the better the model represents the observed skewness.

2.4. Multi-model ensemble building

Previous works have evidenced that different members of large multi-model ensembles are characterized by different performances in simulating given variables (Knutti et al. 2017; Sanderson et al. 2017; Nogueira et al. 2019). Additionally, these studies have shown that model accuracy also depends on the region, variable, season, amongst other factors. Furthermore, it is common for several models within large multi-model ensembles to share components (sometimes being different versions of the same model), thus being not truly independent (Bishop and Abramowitz 2013; Abramowitz and Bishop 2015; Sanderson et al. 2015, 2017). These issues raise doubts on the often assumed 'model democracy' (one model one vote), where each model contributes equally to the ensemble average, which has been argued to be suboptimal (Eyring et al. 2019).

Here, a ranked average model weighting ensemble construction was considered following (Christensen et al. 2010). Our recent works show the added value of this methodology when compared to 'model democracy' for precipitation, temperature, and wind ensemble projections over Portugal (Soares et al. 2017b, a; Cardoso et al. 2019; Nogueira et al. 2019). In this way, the multi-model ensemble for a given variable *p* was obtained by computing a weighted average over the *M* ensemble members:

$$p_{ENS} = \frac{\sum_{m=1}^{M} w_m p_m}{\sum_{m=1}^{M} w_m} \quad (9)$$

Similarly, the ensemble averaged PDFs were obtained by computing a weighted average over all individual model PDFs:

$$Z_{ENS} = \sum_{m=1}^{M} w_m Z_m \quad (10)$$

The weights w_m were obtained considering the individual performance of each model (ensemble member) in reproducing the Iberia01 observations over the historical reference period (1971-2000), measured by the eight different error metrics presented in Section 2.2. First, for each error metric, the individual models were ranked in descending order from the best performing (ranked 1) to the worst performing (largest error, ranked M which is equal to the number of ensemble members). Prior to the ranking, the inverse of the absolute error value was computed for the bias, MAE and RMSE. This was done for these error metrics since the best performing model corresponded to the lower values in their original formulation. Additionally, since the best performance of normalized standard deviation corresponds to a value of 1, this metric was transformed prior to ranking as:

$$\vartheta_n = \begin{cases} \sigma_n \ \ if\ \sigma_n < 1 \\ \dfrac{1}{\sigma_n} \ \ if\ \sigma_n > 1 \end{cases} \quad (11)$$

Following the same reasoning, the Yule-Kendall was also transformed prior to ranking as:

$$YK_{new} = \begin{cases} YK + 1 \ \ if\ YK < 0 \\ \dfrac{1}{YK + 1} \ \ if\ YK > 0 \end{cases} \quad (12)$$

Subsequently, an overall individual model rank was obtained by multiplying the ranks for all error metrics. Finally, the individual model weight was obtained by normalizing the overall individual model rank by the sum of all overall individual model ranks (from all ensemble members), such that the sum of the weights is equal to 1.

Besides the evaluation of the precipitation, maximum and minimum temperatures, which are provided by all the individual EURO-CORDEX RCMs, four different multi-model ensembles to represent these parameters were also analysed (see below). This allows the assessment of the ability of each ensemble to simulate historical and future projected conditions, as well as the quantification of their uncertainty. Additionally, five different groups of EURO-CORDEX RCMs were considered to compute the different multi-model ensembles: all the 45 RCMs; 13 RCMs that have in common all the experiments; the 22 RCMs from RCP2.6; the 20 RCMs from RCP4.5; and the 43 RCMs from RCP8.5 (Table 2.1 shows all this information).

Hence, for the precipitation, maximum and minimum temperatures (V) four multi-model ensembles were constructed as follows:

[1] For each variable, the ensemble is built assuming the respective model weight, *i.e.*, the weighted sum of the 13 models using the weights for that variable, hereafter called ENS1:

$$ENS1 = \sum_{m=1}^{M} V_m w_{V_m} \tag{13}$$

[2] For each variable, the ensemble is built assuming the average of the weights of the three variables, *i.e.*, a new weight is computed as the average of the three weights and the ensemble of each variable is computed with that weight, hereafter called ENS2:

$$ENS2 = \sum_{m=1}^{M} V_m \left(\frac{w_{p_m} + w_{tx_m} + w_{tn_m}}{3} \right) \tag{14}$$

[3] ENS3 is computed as ENS2 but the precipitation weight corresponds to 50%, and the maximum and minimum temperature contributes with 25% each one:

$$ENS3 = \sum_{m=1}^{M} V_m \left(0.5 w_{p_m} + 0.25 w_{tx_m} + 0.25 w_{tn_m} \right) \tag{15}$$

[4] The last ensemble is built following the so-called "democratic approach", where the 13 models are equally weighted, and each ensemble variable consists of the simple average between the models:

$$ENS4 = \frac{\sum_{m=1}^{M} V_m}{M} \tag{16}$$

Finally, to analyse the future projections of climate variables over Portugal, only one of these 4 ensembles is selected. Multi-weighted ensembles, considering multi-variable performances, such as ENS2 and ENS3, may be advantageous when compared to democratic multi-model ensembles (Eyring et al. 2019; Cos et al. 2022). Therefore, ENS1 and ENS4 are estimated with the aim of having a comparable benchmark for the evaluation of the multi-weighted ensembles (ENS2 and ENS3).

2.5. Definition of Climate Extremes and Climate Indices

A detailed description of the Portuguese climate and its projected changes throughout the twenty-first century was constructed based on a set of climate indices (CIs) following the World Meteorology Organisation's definition (Frich et al. 2002), the CCl/CLIVAR/JCOMM Expert Team on Climate Change

Detection and Indices (ETCCDI) and the European Climate Assessment & Dataset (ECA&D, (ECA&D 2013)). These indices were computed from daily EURO-CORDEX data considering four different periods - historical (1971-2000), early-21st-century (2011-2040), mid-21st-century (2041-2070) and end-of-21st-century (2071-2100). Additionally, three different emission scenarios were considered for each future period: RCP2.6, RCP4.5 and RCP8.5. Each CI was computed for each model at monthly, seasonal, and yearly granularities:

$$\langle CI \rangle_g = \frac{1}{30} \sum_{y=y0}^{y0+30} \left[(1/Ng) \sum_{d=d_{0,g}}^{d0+Ng} CI \right] \quad (17)$$

where $<>_g$ denotes the climatological average at a chosen granularity, g (monthly, seasonal, or yearly), y0 denotes the starting year of the chosen 30-year climatological period, $d_{0,g}$ denotes the starting day of the considered granularity period (*i.e.*, first day of the chosen month, first day of the chosen season, or first day of the year), and N_g denotes the total number of days in the considered granularity period.

The CIs were computed over Portugal at 0.11º resolution (Figure 2.2a). Subsequently, relative administrative spatial aggregations were performed, corresponding to three different levels of the Nomenclature of Territorial Units for Statics: NUTS I (corresponding to the national level), NUTS II (corresponding to the regional level), and NUTS III (corresponding to the sub-regional level). The Portuguese NUTS aggregations considered in the present work are summarized in Table 2.2. Notice that the Azores and Madeira islands were not included in this analysis, since they are not covered by the EURO-CORDEX domain.

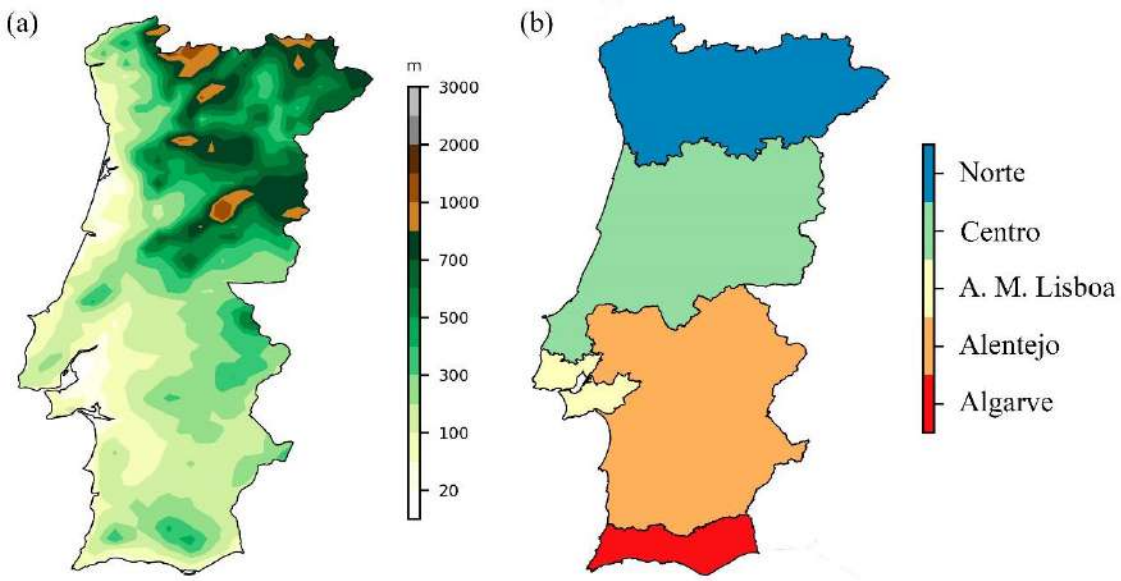

Figure 2.2 (a) The Portuguese domain, where the colours represent the topographic height (in meters). (b) The five sub-regional domains, identified as the Nomenclature of Territorial Units for Statistics (NUTS) regions: Norte (northern Portugal), Centro (central Portugal), A. M. Lisboa (the metropolitan region of Lisbon), Alentejo and Algarve regions.

Table 2.2 Portuguese NUTS (Nomenclature of Territorial Units for Statics) aggregations considered in the present work: NUTS I corresponds to the national level, NUTS II corresponds to the regional level, and NUTS III corresponds to the sub-regional level.

NUTS I	NUTS II	NUTS III
Continente	Norte	Alto Minho
		Cávado
		Ave
		Alto Tâmega
		Tâmega e Sousa
		Terras de Trás-os-Montes
		Douro
		Área Metropolitana do Porto
	Centro	Região de Aveiro
		Viseu Dão Lafões
		Região de Coimbra
		Beiras e Serra da Estrela
		Beira Baixa
		Região de Leiria
		Médio Tejo

	Oeste
Área Metropolitana de Lisboa	Área Metropolitana de Lisboa
Alentejo	Lezíria do Tejo
	Alto Alentejo
	Alentejo Central
	Alentejo Litoral
	Baixo Alentejo
Algarve	Algarve

2.5.1. Temperature extremes

For each model, the climatological mean of daily maximum 2-meter air temperature, Tx, and daily minimum 2-meter air temperature, Tn, were computed from Equation (17). The climatological mean daily mean 2-meter air temperature, Tm, was obtained by computing the average between Tx and Tn for each day, and then employing Equation (17). The climatological mean diurnal 2-meter air temperature range, DTR was obtained by taking the difference Tx-Tn for each day and then employing Equation (17).

The number of extreme hot days, TxG35, hot days, TxG30, and summer days, TxG25, corresponding to the number of days where Tx exceeded 35 ºC, 30 ºC and 25 ºC respectively, were also computed. These were obtained by counting the number of days exceeding the respective temperature threshold for each year. Their values are provided as the average number of days per year exceeding the respective threshold over the considered period. Similarly, the number of tropical nights, TnG20, and the number of frost days, TnL0, correspond respectively to the average number of days per year where Tn exceeded 20 ºC and the number of days where Tn was below 0 ºC. The maximum number of consecutive extreme hot days, CDTxG35, corresponds to the yearly average of the largest number of consecutive days where Tx exceeds 35 ºC. Similarly, the maximum number of consecutive cold days, CDTnL7, corresponds to the yearly average of the largest number of consecutive days where Tn was below 7 ºC.

The number of days in heatwave, HWD, is defined as a period of five or more consecutive days with Tx above the 90^{th} percentile following (Frich et al. 2002). Conversely, the number of days in coldwave, CWD, is defined as a period of five or more consecutive days with Tn below the 10^{th} percentile. The reference percentiles for HWD and CWD were computed following (Zhang et al. 2005) procedure, which avoids artificial discontinuities at the beginning and the end of the base period percentiles time series (historical). This procedure is (from (Zhang et al. 2005), section 4):

1) The 30-yr base period is divided into one 'out of base' year, the year for which exceedance is to be estimated, and a 'base period' consisting of the remaining 29 years from which the thresholds would be estimated.
2) A 30-yr block of data is constructed by using the 29-yr base period dataset and adding an additional year of data from the base period (replicating one year in the base period). This constructed 30-yr block is used to estimate thresholds.
3) The out-of-base year is then compared with these thresholds, and the exceedance rate for the out-of-base year is obtained.
4) Steps 2 and 3 are repeated an additional 28 times, by repeating each of the remaining 28 in-base years in turn to construct the 30-yr block.
5) The final index for the out-of-base year is obtained by averaging the 29 estimates obtained from steps 2, 3 and 4.

The reference percentiles for HWD and CWD were obtained for each day of the year using a 31-day moving window, following the methodology described in (Russo et al. 2015). The percentile-based heatwave and coldwave definitions minimize the impact of biases on the results since each threshold is set for each grid point and model. This is a common approach in several studies using results from multiple models to investigate the projected changes in the PDF tails (Meehl and Tebaldi 2004; Fischer and Schär 2010; Schoetter et al. 2015). On the other hand, the use of fixed reference values (*e.g.*, CDTxG35 and CDTnL7) has a direct correspondence to relevant thresholds, to evaluate impacts.

To analyse the impact of these heatwaves, we assess the average number per year, duration, the areal extension, and severity. The latter follows Russo et al. (2015) and is the sum of the daily adimentionalised maximum temperature during the event:

$$M_d(T_d) = \begin{cases} \dfrac{T_d - P_{25}}{P_{75} - P_{25}} \; if \; T_d > P_{25} \\ 0 \qquad\quad if \; T_d \leq P_{25} \end{cases} \tag{18}$$

Where $M_d(T_d)$ is the daily maximum temperature magnitude of the consecutive days composing the heatwave, T_d is the daily maximum temperature above the daily percentile threshold (P_{90} or P_{95}), P_{25} and P_{75} are 25th and 75th annual percentiles, respectively, of the historical maximum temperature daily time series as in Cardoso et al. (2019). The daily percentile threshold is obtained for each day of the year using a 31-day window centred on the day (Russo et al. 2015). Using the entire time series allows the detection of early spring and late autumn heatwaves due to the lower 25th percentile. The daily severity is measured as a fraction of the interquartile difference, thus whenever $M_d(T_d)$ [Equation 18] is above one, the maximum temperature is not only above the daily 90th or 95th percentile but also in the highest 25% of the

entire time series (P_{75}). If $M_d(T_d) = 2$ then the temperature anomaly to the historical 25th percentile is twice the heatwave magnitude unit, *i.e.*, the historical interquartile range. The maximum severity is given by the sum of $M_d(T_d)$ during each heatwave. This approach is intrinsically linked to the length of the event and, short heatwaves with high daily severities can be overshadowed by long mild heatwaves. Since the impact of the first can be stronger than the latter, here we will also analyse the mean severity (S_M), *i.e.*, the mean of the daily severities during each heatwave. In this work, whenever a heatwave's S_M is above the historical' s mean severity 90th percentile, then it is considered an extreme event. Four degrees of severity will be contemplated: *low severity* when S_M <1, *severe* when $1 < S_M < P_{75}$, *high severity* when $P_{75} < S_M < P_{90}$ and *extreme* $S_M > P_{90}$.

Additional, to analyse the extreme maximum temperature, the return levels for the 10-, 30-, 50-, and 100-year return periods were computed by fitting the annual maximum values from each grid-point to a GEV distribution, for each period and climate scenario. To perform an extreme event analysis, the duration of the climate records is a relevant parameter. Since each of the considered periods spans for 30 years, the process of fitting these data to a GEV distribution generates extrapolated values when the return periods are longer than 30 years, and therefore, the 50- and 100-year return levels should be considered within the scope of this limitation. The temperature indices computed in this report are summarised in Table 2.3.

Table 2.3 Summary of temperature indices and extremes used in this study.

Acronym	Description
Tm	Daily mean 2-meter air temperature [ºC]
DTR	Daily thermal range at 2-meters [ºC]
Tx	Daily maximum 2-meter air temperature [ºC]
TxG35	Number of very hot days [days]
TxG30	Number of hot days [days]
TxG25	Number of summer days [days]
CDTxG35	Maximum number of consecutive very hot days [days]
HW	Heatwave: number, average and maximum duration
Tx YY	YY-year return levels of daily maximum 2-meter air temperature [ºC]
Tn	Daily minimum 2-meter air temperature [ºC]
TnG20	Number of tropical nights [days]
TnL0	Number of frost days [days]
TnL7	Number of cold days [days]
CDTnL7	Maximum number of consecutive cold days [days]
CW	Coldwave: number, average and maximum duration

2.5.2. Precipitation extremes

For each model, the climatological mean daily average precipitation, Pm was computed from Equation (17). The climatological mean cumulative precipitation, P_{ac}, was computed as:

$$P_{ac} = \frac{1}{30} \sum_{y=y0}^{y0+30} \left[\sum_{d=d0,g}^{d0+Ng} Pr_d \right] \quad (19)$$

where Pr_d is the total precipitation accumulated during day d. This CI measures climatological average total accumulated precipitation over a given granularity period.

The average number of days with precipitation greater than 1 mm, 10 mm, 20 mm, and 50 mm (respectively PacG1, PacG10, PacG20, and PacG50) were obtained by counting the number of days where the respective daily precipitation threshold was exceeded for each year. The value was divided by 30 to obtain averaged values per year. The percentage of total annual precipitation resulting from days with more than 10 mm/day and 50 mm/day accumulations was computed. These CIs are denoted PacG10% and PacG50% respectively. They provide quantitative estimates of the amount of precipitation resulting from moderate-to-heavy (10 mm/day) and heavy (50 mm/day) precipitation days only.

The maximum precipitation accumulated over a 5-day period, MaxPac5d, was computed for each year over the entire considered 30-year period. The maximum number of consecutive days with precipitation, CDPG1, and without precipitation, CDPL1, were respectively computed as the largest number of consecutive days where Pr_d > 1 mm/day and Pr_d < 1 mm/day per year for30-year climatological period. The average duration of precipitation periods, AvCDPG1, was obtained by identifying all wet periods, as the consecutive number of days where the condition Pr_d > 1 mm/day holds and averaging over the duration of all wet periods for each grid-point and climatological period. Similarly, the maximum duration of precipitation periods, MaxCDPG1, was obtained by identifying all wet periods where Pr_d>1 mm/day, determining their duration by counting the respective number of consecutive days where the condition holds, and determining the maximum over the duration of all wet periods for each grid-point per year and climatological period. The maximum duration of dry periods, MaxCDPL1, was obtained by identifying all wet periods where Pr_d<1 mm/day, determining their duration by counting the respective number of consecutive days where the condition holds, and determining the maximum over the duration of all dry periods for each grid-point per year and climatological period. A summary of the precipitation indices is addressed in Table 2.4.

To analyse the extreme precipitation, the return levels for the 10-, 30-, 50-, and 100-year return periods were computed by fitting the annual maximum values from each grid point to a GEV distribution, for each period and climate scenario. To perform an extreme event analysis, the duration of the climate records is important. Since each of the considered periods spans for 30 years, it should be noted that the process of fitting these data to a GEV distribution generates extrapolated values when the return periods are longer

than those 30 years, and therefore, the 50- and 100-year return levels should be considered within the scope of this limitation.

Table 2.4 Summary of precipitation indices and extremes used in this study.

Acronym	Description
Pm	Daily average precipitation [mm/day]
Pac	Mean cumulative precipitation per period [mm]
MaxPac5d	Maximum of 5-day accumulated precipitation [mm]
Pac YY	YY-year return levels of the daily total precipitation [mm]
PacG1	Number of days with precipitation exceeding 1 mm [days]
PacG10	Number of days with precipitation exceeding 10 mm [days]
PacG20	Number of days with precipitation exceeding 20 mm [days]
PacG50	Number of days with precipitation exceeding 50 mm [days]
PacG10%	The percentage of total annual precipitation from days with more than 10 mm/day accumulation
PacG50%	The percentage of total annual precipitation from days with more than 50 mm/day accumulation
AvCDPG1	Average duration of periods where precipitation exceeds 1 mm/day [days]
MaxCDPG1	Maximum consecutive rainy days where precipitation exceeds 1 mm/day [days]
MaxCDPL1	Maximum consecutive dry days where precipitation is below 1 mm/day [days]

2.5.3. Wind extremes

The climatological mean of daily average 10-meter height wind speed of each model, Vh10, was computed from Equation (17). The maximum of daily average 10-meter height wind speed, MaxVh10, was computed as the absolute maximum within the entire 30-year climatological period for each granularity. The maximum of daily maximum wind gust, MaxVgust, was computed as the absolute maximum value within the entire 30-year climatological period for each granularity.

The number of days with daily mean 10-meter height wind speed exceeding 5.5 m/s and 10.8 m/s, (respectively Vh10G5.5 and Vh10G10.5) were obtained by counting the number of days exceeding the respective threshold at each granularity and over each climatological period. Their values are provided as the average number of days per year exceeding the respective threshold over the considered period. Similarly, the number of days with 10-meter wind speed below 2.0 m/s, Vh10L2.0, was also computed.

The climatological mean of daily average 30- and 60-meter heights wind speeds, respectively Vh30 and Vh60, were also computed. However, the EURO-CORDEX database does not provide wind speed estimates at these levels. This limitation was circumvented by employing an empirical power-law extrapolation following (Peterson and Hennessey Jr. 1978) and (Nogueira et al. 2019):

$$Vhz = Vh10 \left(\frac{z}{10}\right)^{1/7} \tag{20}$$

where Vhz is wind speed at the target height z (here 30 m and 60 m). This extrapolation is recognized as a reasonable approximation of the wind vertical profile in the surface layer characterized by neutral conditions and smooth areas. Although more complex formulas have been proposed, no consensus has been reached on their performance, and Equation (15) remains the most common formula applied to all locations and conditions (see, *e.g.*, (Pryor and Barthelmie 2011; Tobin et al. 2015; Soares et al. 2020) for sensitivity analysis and discussions on this subject).

To analyse the extreme maximum wind gust, the return levels for the 10-, 30-, 50-, and 100-year return periods were computed by fitting the annual maximum values from each grid-point to a GEV distribution, for each period and climate scenario. To perform an extreme event analysis, the duration of the climate records is a relevant parameter. Since each of the considered periods spans for 30 years, the process of fitting these data to a GEV distribution generates extrapolated values when the return periods are longer than 30 years, and therefore, the 50- and 100-year return levels should be considered within the scope of this limitation. A summary of the wind speed indices is addressed in Table 2.5.

Table 2.5 Summary of the RNA2100 variables and indices related with 10-m wind speed.

Acronym	Description
Vh10	Daily mean wind speed at 10-meters [m/s]
MaxVh10	Maximum daily mean wind speed at 10-meters [m/s]
MaxVgust	Maximum of daily maximum wind gust [m/s]
MaxVgust YY	YY-year return levels of the daily maximum wind gust
Vh10L2.0	Number of days with 10-meter wind speed below 2.0 m/s [days]
Vh10G5.5	Number of days with 10-meter wind speed greater than 5.5 m/s [days]
Vh10G10.5	Number of days with 10-meter wind speed greater than 10.5 m/s [days]
Vh30	Daily mean wind speed at 30-meters [m/s]
MaxVh30	Maximum daily mean wind speed at 30-meters [m/s]
Vh60	Daily mean wind speed at 60-meters [m/s]
MaxVh60	Maximum daily mean wind speed at 60-meters [m/s]

2.5.4. Climate Indices and other variables

Humidity and Potential Evapotranspiration

Near-surface air relative humidity, RH, was computed from EURO-CORDEX 2-meter air temperature, 2-meter specific humidity, q, and surface pressure, p_s, using the following approximation:

$$RH = \max\left[\min(mr/mr_{sat}, 1), 0\right] x100 \quad (21)$$

Where mr and mr_{sat} are the mixing ratio and saturation mixing ratio computed as described in Hardy (1998). The climatological mean daily average RH, RHm, was then obtained by employing Equation (17).

The potential evapotranspiration for the reference culture, PET, was estimated from the Food and Agriculture Organization (FAO) Penman-Monteith equation (Allen et al. 1989):

$$PET = [0.408\,\Delta\,(R_n - G) + \gamma[900/(T_m + 373)]\,V_{h2}\,(e_s - e_a)] / (\Delta + \gamma(1 + 0.34V_{h2}) \quad (22)$$

where R_n is the net radiation at the surface, G is the soil heat flux density, Tm is the daily mean 2-meter air temperature, V_{h2} is the daily mean 2-meter wind speed (obtained using the power-law approximation in Equation (19)), e_s is the saturation vapor pressure, e_a is the actual vapor pressure, γ is the psychrometric constant, and Δ is the slope of the vapor pressure curve. The climatological mean potential evapotranspiration, PET_g, was then computed from Equation (17).

Soil moisture and Evaporation

In what concerns the total soil moisture, the land surface models within the EURO-CORDEX RCMS have different soil characteristics, especially the number and depths of soil layers and the saturation levels (Knist et al. 2017). Consequently, a direct comparison of the total soil moisture content is not meaningful, however it is expected that the RCMs can reproduce the typical intra-annual and interannual variabilities, as well as consistent future changes within the model system. For each model, the climatological mean total soil moisture, $<sm>_g$, was computed from the daily average EURO-CORDEX integrated soil moisture content, and then Equation (17) was employed. In addition, the standardised soil moisture anomaly was computed with respect to the daily means of the historical period and standardised by the daily standard deviations of the historical period (Orlowsky and Seneviratne 2013).

The 30-year climatological mean evapotranspiration rate, $<ET>_g$, was determined from the daily EURO-CORDEX upward latent heat flux at the surface, *hfls*, using the following equation:

$$ET = \frac{hfls}{\lambda} \quad (23)$$

where λ is the latent heat of vaporization ($\lambda = [2.501 - 0.00237 \times T] \times 10^6\, Jkg^{-1}$) where T is the 2-meter air temperature. $<ET>_g$, was then computed from Equation (17).

Radiation

The climatological mean global solar radiation, $<GSR>_g$, was computed from the daily average EURO-CORDEX downward solar radiative fluxes at the surface, which were converted from W/m^2 to MJ/m2 (by multiplying by 3600x24) and then Equation (17) was employed.

Thermal comfort indices

The Universal Thermal Climate Index (UTCI) was computed following the operational procedure presented by (Bröde et al. 2012). This index aims to assess outdoor thermal conditions in terms of one-dimensional quantity summarising the interaction of environmental temperature, wind speed, humidity, and long- and short-wave radiative fluxes. The assessment is based on the physiological response of the human body walking at a speed of 4 km/h. To this end, a thermo-physiological model coupled to a clothing model is employed (Bröde et al. 2012; Fiala et al. 2012). The behavioural adaptation of clothing insulation, the distribution of clothing over different body parts, and the reduction of thermal and evaporative clothing resistances caused by wind and movement of the wearer is considered. The index is a function of the environmental air temperature, mean radiant temperature, T_{mrt} (the equivalent black-body temperature that exchanges the same net radiative energy with a human subject as the environment), wind speed and vapor pressure:

$$UTCI = f(T_{air}; T_{mrt}; WS; pv) = T_{air} + offset(T_{air}; T_{mrt}; WS; pv) \quad (24)$$

The UTCI was employed to obtain a heat stress characterization using the classes presented in Table 2.6. A summary of the UTCI indices is addressed in Table 2.7.

Table 2.6 UTCI based event classification.

UTCI value	Classification
≥ 46	Extremely hot
$[38, 46[$	Very hot
$[32, 38[$	Hot
$[26, 32[$	Moderately hot
$]9, 26[$	No heat stress
$]0, 9]$	Slightly cold
$]-13, 0]$	Moderately cold
$]-27, -13]$	Cold
$]-40, -27]$	Very cold
≤ 40	Extremely cold

Table 2.7 Summary of the RNA2100 indices related with UTCI.

Acronym	Description
UTCI	Universal Thermal Climate Index [ºC]

Drought Indices

Computation of the Standard Precipitation Index (SPI) was performed by fitting a two-parameter gamma probability distribution to the long-term simulated monthly precipitation for each grid-point. The resultant cumulative distribution function (CDF) is then transformed into a normal distribution so that the mean SPI for the location and desired period is zero (see (Mckee et al. 1993) and (Edwards and McKee 1997) for details on SPI computation). This calculation can be repeated for multiple timescales. Here the 12-month (SPI-12) timescale is considered. Positive SPI values indicate greater than median precipitation, while negative values indicate less than median precipitation. We followed the criteria proposed by (Mckee et al. 1993) and recommended by the World Meteorological Organization (WMO 2012) to classify wet and drought periods based on SPI (Table 2.8).

Table 2.8 SPI based event classification.

SPI value	Classification
≥ 2.0	Extremely wet
[1.5 , 2.0[	Very wet
[1.0 , 1.5[	Moderately wet
]-1.0 , 1.0[	Near normal
]-1.5 , -1.0]	Moderately dry
]-2.0 , -1.5]	Severely dry
≤ -2.0	Extremely dry

The Standardized Precipitation Evapotranspiration Index (SPEI) is analogous to the SPI but uses the difference between monthly rainfall and monthly potential evapotranspiration, thus accounting for the temperature factor and considering the influence of surface evaporation changes, which is more sensitive to the drought reaction caused by global temperature rise. Therefore, SPEI has been described to be more suitable under increasing temperatures (Vicente-Serrano et al. 2010, 2014, 2020), and to better represent hydrological drought in the Iberian Peninsula, when compared to SPI (Vicente-Serrano et al. 2014, 2020). Here the SPEI is calculated using monthly data. The SPEI is very easy to calculate, and it is based on the original SPI calculation procedure. The first step is the calculation of the PET (precipitation minus evapotranspiration). Then, the difference between the monthly average precipitation and PET is normalized as log-logistic probability distribution as described in (Vicente-Serrano et al. 2010). A summary of the SPI and SPEI indices is addressed in Table 2.9.

Table 2.9 Summary of the RNA2100 indices related with drought.

Acronym	Description
SPI-12	Standardized precipitation index with 12-month accumulation period
SPEI-12	Standardized precipitation-evapotranspiration index with 12-month accumulation period

Köppen-Geiger classification system

The Köppen-Geiger system classifies climate into five main classes and 30 sub-types (Köppen 1936). The classification is based on seasonality and threshold values of monthly averaged air temperature and precipitation. The Köppen-Geiger climate classification is a highly suitable means to aggregate complex climate gradients into a simple but ecologically meaningful classification scheme, and where different regions with similar classification share common vegetation characteristics. The wide use of the Köppen-Geiger classification reflects the fact that climate has since long been recognized as the major driver of global vegetation distribution. There have been many modifications proposed to the Köppen system since the pioneering work of Wladimir Köppen in 1900. Here we follow the Köppen-Geiger climate classification as described in (Peel et al. 2007), which was also used more recently by (Beck et al. 2018). This classification is identical to that presented by (Köppen 1936) with three differences. First, the temperate (C) and cold (D) climates are distinguished using a 0 °C threshold instead of a 3 °C threshold. Second, the arid (B) sub-climates W (desert) and S (steppe) were identified depending on whether 70% of precipitation occurred in summer or winter. Third, the sub-climates s (dry summer) and w (dry winter) within the C and D climates were made mutually exclusive by assigning s when more precipitation falls in winter than in summer and assigning w otherwise. Note that the tropical (A), temperate (C), cold (D), and polar (E) climates are mutually exclusive but may intersect with the arid (B) class. To account for this, climate type B was given precedence over the other classes. The Köppen-Geiger climate classification system used here follows the description presented in Table 2.10, along with the defining criteria.

Table 2.10 Description of Köppen-Geiger system classification and defining criteria. Adapted from (Peel et al. 2007). Variable definitions: MAT = mean annual air temperature ($°C$); T_{cold} = air temperature of the coldest month ($°C$); T_{hot} = air temperature of the warmest month ($°C$); T_{mon10} = the number of months with air temperature $> 10°C$ (unitless); MAP = mean annual precipitation (mm y^{-1}); P_{dry} = precipitation in the driest month (mm $month^{-1}$); P_{sdry} = precipitation in the driest month in summer (mm $month^{-1}$); P_{wdry} = precipitation in the driest month in winter (mm $month^{-1}$); P_{swet} = precipitation in the wettest month in summer (mm $month^{-1}$); P_{wwet} = precipitation in the wettest month in winter (mm $month^{-1}$); $P_{threshold} = 2 \times MAT$ if $> 70\%$ of precipitation falls in winter, $P_{threshold} = 2 \times MAT + 28$ if $> 70\%$ of precipitation falls

in summer, otherwise $P_{threshold} = 2 \times MAT + 14$. Summer (winter) is the six-month period that is warmer (colder) between April-September and October-March.

1st	2nd	3rd	Description	Criterion
A			Tropical	Not (B) & $T_{cold} \geq 18$
	f		- Rainforest	$P_{dry} \geq 60$
	m		- Monsoon	Not (Af) & $P_{dry} \geq 100 - MAP/25$
	w		- Savannah	Not (Af) & $P_{dry} < 100 - MAP/25$
B			Arid	$MAP < 10 \times P_{threshold}$
	W		- Desert	$MAP < 5 \times P_{threshold}$
	S		- Steppe	$MAP \geq 5 \times P_{threshold}$
		h	- Hot	$MAT \geq 18$
		k	- Cold	$MAT < 18$
C			Temperate	Not (B) & $T_{hot} > 10$ & $0 < T_{cold} < 18$
	s		- Dry summer	$P_{sdry} < 40$ & $P_{sdry} < P_{wwet}/3$
	w		- Dry winter	$P_{wdry} < P_{swet}/10$
	f		- Without dry season	Not (Cs) or (Cw)
		a	- Hot summer	$T_{hot} \geq 22$
		b	- Warm summer	Not (a) & $T_{mon10} \geq 4$
		c	- Cold summer	Not (a or b) & $1 \leq T_{mon10} < 4$
D			Cold	Not (B) & $T_{hot} > 10$ & $T_{cold} \leq 0$
	s		- Dry summer	$P_{sdry} < 40$ & $P_{sdry} < P_{wwet}/3$
	w		- Dry winter	$P_{wdry} < P_{swet}/10$
	f		- Without dry season	Not (Ds) or (Dw)
		a	- Hot summer	$T_{hot} \geq 22$
		b	- Warm summer	Not (a) & $T_{mon10} \geq 4$
		c	- Cold summer	Not (a, b, or d)
		d	- Very cold winter	Not (a or b) & $T_{cold} < -38$
E			Polar	Not (B) & $T_{hot} \leq 10$
	T		- Tundra	$T_{hot} > 0$
	F		- Frost	$T_{hot} \leq 0$

Agriculture Indices

Climatic indices have been successfully used to support agriculture management practices across the world. Thermal growing season (GSL) describes the length of time in a calendar year when temperatures are consistently warm enough for agricultural activity, *i.e.*, the part of the year when soil temperatures at 50 cm

below the soil surface are higher than biologic zero (5 °C). As this quantitative determination requires in-ground instrumentation, which is not usually available, growing season can be estimated by approximating the number of frost-free days. It is defined as the 30-year climatological average of the yearly number of days between the first five-day period with average temperatures above 5 °C to the first five-day period with temperatures below 5 °C. An index which reflects the amount of water available in the soil, is the Aridity index defined as the ratio between the annual precipitation (p) and the annual potential evapotranspiration (PET) (Equation 25). It is a critical environmental factor affecting the evolution of natural vegetation and therefore rain erosivity by considering rainfall and air temperature. The Aridity index climate classification system used here follows the description presented in Table 2.11.

$$AI = \frac{P}{PET} \tag{25}$$

Table 2.11 Aridity Index Classification.

AI value	Classification
≥ 0.65	Humid
[0.5 , 0.65[	Dry Subhumid
[0.2 , 0.5[	Semi-arid
[0.05 , 0.2[	Arid
< 0.05	Hyper-arid

Additionally, to the climate indices from the previous sections relevant for agriculture (*e.g.*, all temperature and precipitation thresholds, drought, PET, soil moisture, etc…), here a set of bioclimatic indices relevant for viticulture is presented as an example of the possible bioclimatic indicators that can be calculated. Further indices will be included in WP7 when adaptation storylines will be developed.

The timings and duration of the grapevine phenological stages are strongly tied to the prevailing atmospheric conditions, and these are even responsible for the variability in grapevine yield, wine production and quality. These climatic conditions limit the geographic distribution of this crop and are key factors in determining the varietal suitability and wine types of a given region. Two temperature thresholds are relevant in the grapevine phenological cycle: −17°C is commonly considered the lethal lower temperature limit for Vitis vinifera, 10°C is the base temperature needed for the onset of its yearly vegetative cycle. However, high temperatures during the ripening season can lead to reduced yields and poor fruit quality (Kliewer 1977; Collins et al. 2006). Grapevines have the capacity to tolerate temperatures as low as -15 to -20 °C during the early stages of growth and for short time periods during winter (Hidalgo 2002). However, its production is especially vulnerable to frost during spring, which could irreversibly damage

the vineyard (Spellman 1999). Furthermore, annual precipitation and its seasonal distribution are also critical. High soil moisture is needed during budburst and shoot and inflorescence development, followed by dry conditions from flowering to berry ripening. Complex bioclimatic indices which include the influence of temperature and precipitation are commonly used in viticulture zoning studies. Since grapevines need a specific heat accumulation to complete their phenological stages, the Growing Season Suitability (GSS) provides a useful tool to evaluate the suitability of a particular region for wine production (Santos et al. 2012). It is the 30-year climatological average of the mean number of days between April and September when the mean temperature is above 10 °C. Another mean temperature index, the Growing Degree Day (GDD) or Winkler index (Winkler et al. 1974), gives the general ripening capability and wine style for different regions. It represents the 30-year climatological average of the sum of mean temperatures above 10 °C between April and October. However, GDD index does not adjust for increasing daylight duration with higher latitudes. Conversely, the Huglin index (HI) is also a thermal index that considers daily mean and maximum temperatures from April to September. With respect to the GDD, HI weights daily maximum temperature more and improves the fitting of potential sugar content of the grape (Huglin 1978). Moreover, it also has the advantage of considering the increasing length of the daylight towards higher latitudes. The production of high-quality wines not only needs high daily temperatures but also cool nights during ripening. The Cool Night index (CI) provides a relative measure of ripening potential, being equal to the 30-year climatological average of the minimum temperature during the month before harvest (Tonietto and Carbonneau 2004). Precipitation during the growing season is one of the most discriminating climatic variables (Blanco-Ward et al. 2007). The Growing Season Precipitation (GSP) gives the 30-year climatological average of the accumulated precipitation between April and September. A measure of hydric regime, *i.e.* effectiveness of precipitation in the growing season (Magalhães 2008), is given by the Selianinov Index (SI). In this index, the 30-year climatological average of the sum of the quotient of precipitation by the mean temperature above 10 °C between April to September. Additionally, the Hydrothermic Index of Branas, Bernon and Levadoux (HyI; (Branas et al. 1946)) considers both precipitation and temperature regimes for estimating the risk of downy mildew disease. It considers the 30-year climatological average of the sum of the product of the mean temperature and precipitation between April to September. A summary of climate indices presented in this report is presented in Table 2.12.

Table 2.12 Climate Indices for wine production. Definition and usefulness.

Index	Definition	Utility
Growing season suitability (GSS)	$GSS = \frac{\sum_{Apr}^{Sep} d_{Tmean>10\,^{\circ}C}}{\sum_{Apr}^{Sep} d}$	Useful as a zoning tool (Santos et al. 2012)

Growing Degree Day (GDD) or Winkler index	$GDD = \sum_{Apr}^{Oct} max[(T_{mean} > 10\ °C) - 10,0]$	GDD < 1111 Too cold. 1111 < GDD < 1389 Only early ripening varieties achieve high quality 1389 < GDD < 1667 Early and mid-season table wine varieties (TWV) produce good quality wines 1667 < GDD < 1944 Favourable for high production of standard to good quality table wines 1944 < GDD < 2222 Favourable for high production, but acceptable table wine quality at best 2222 < GDD < 2500 Typically only suitable for extremely high production, fair quality table wines, or TWV destined for early season consumption are grown 2500 < GDD < 2778 Only suitable for extremely high production. GDD > 2778 Too warm.
Huglin Heliothermal Index (HI)	$HI = \sum_{Apr}^{Sep} \frac{(T_{mean} - 10) + (T_{max} - 10)}{2} d$ Lat ≤ 40 N d=1 40º 1' N < Lat ≤ 42 N d=1.02 42º 1' N < Lat ≤ 44 N d=1.03 44º 1' N < Lat ≤ 46 N d=1.04 46º 1' N < Lat ≤ 48 N d=1.05 48º 1' N < Lat ≤ 50 N d=1.06 50º 1' N < Lat ≤ 52 N d=1.07 52º 1' N < Lat ≤ 54 N d=1.08 Lat > 54 N d=1.09	HI ≤ 1500 very cool. Only the very early/early varieties can reach maturity 1500 <HI ≤ 1800 cool. Allow a very large range of grape varieties to ripen (white or red) 1800 <HI ≤ 2100 temperate. Later varieties ripening varieties can reach maturity 2100 <HI ≤ 2400 temperate warm 2400 <HI ≤ 3000 warm. Potential which exceeds the heliothermal needs to ripen the varieties HI > 3000 very warm
Cool night index (CI)	$CI = \sum_{Sep} \frac{T_{min}}{30}$	very cool nights (CI ≤ 12 °C), cool nights (12 < CI ≤ 14 °C) temperate nights (14 < CI ≤ 18 °C) warm nights (CI > 18 °C)
Growing season precipitation (GSP)	$GSP = \sum_{Apr}^{Sep} P$	GSP > 600 mm: excessively wet GSP <200 mm: extremely dry
Selianinov Index (SI)	$SI = \sum_{Apr}^{Sep} \frac{P}{(T_{mean} - 10)}$ $SI = 0\ if\ (T_{mean} - 10) \leq 0$	SI<1 - insufficient 1< SI < 3 - normal SI >3 - excessive
Hydrothermal Index (HyI)	$Hyl = \sum_{Apr}^{Sep} T_{mean} \times P$	HyI < 2500 °Cmm - low HyI > 5100 °Cmm - high

3. EURO-CORDEX error assessment

Evaluating the ability of the RCMs historical simulations to represent the present climate is fundamental for climate change assessment studies. Therefore, an extensive evaluation of the precipitation and maximum and minimum temperature was performed for the EURO-CORDEX RCMs, comparing their results against the observational dataset Iberia01.

3.1. Precipitation Evaluation

Two standard statistical errors (the normalized bias, and the normalized mean average error, MAPE) are displayed in Figure 3.1a and b, focused on the RCMs ability to represent the mean structure of precipitation at different temporal scales, from monthly, seasonally to yearly. The normalized biases in Figure 3.1a show that most of the EURO-CORDEX models are able to reasonably describe the mean precipitation patterns during the historical period. The results from 12 out of the 45 models show normalized biases of less than 10%, while 21 of them present values below 20%. Overall, the simulations tend to overestimate precipitation, with only 10 out of 45 showing an underestimation. The MAPEs in Figure 3.1b also indicate a good performance, since most of the simulations present values between 10 and 40% for all the time scales analysed. Considering simultaneously the normalized bias and MAPE, the overall performance KNMI2, 3 and 4, the IPSL4 and MOHC2 stands out. The RCMs daily normalized precipitation PDF skill scores (S and S90) are shown in Figure 3.1c. The high S and the S90 scores, above 85%, mean that over 85% of the modelled PDFs match the one derived from observations. IPSL and ICTP are exceptions since most of them have scores below 85%. All the CLM-E, CNRM, MPI and SMHI simulations show S and S90 skill scores in the range of 90% to 98%.

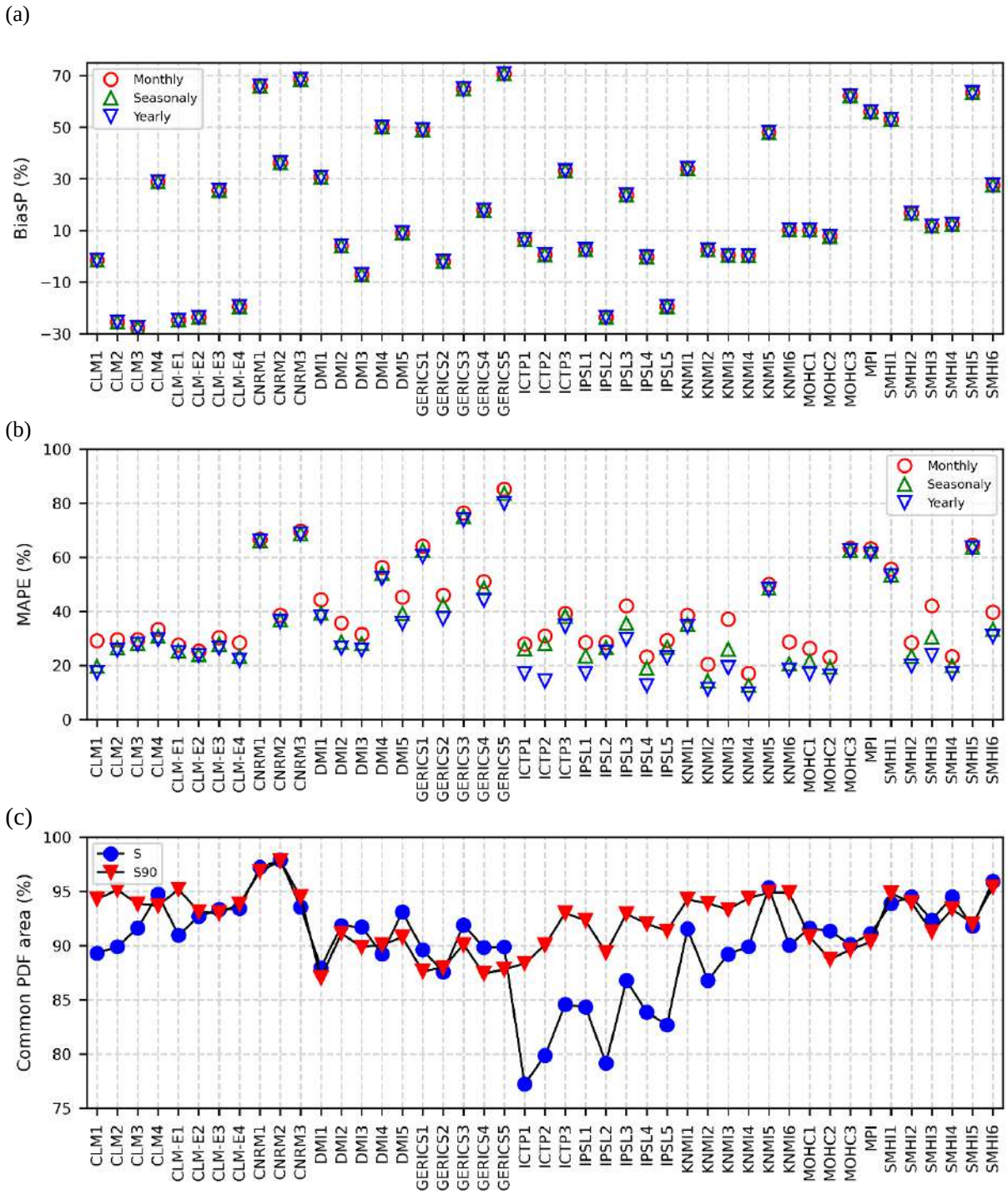

Figure 3.1 Climatological error measures of EURO-CORDEX RCMs precipitation for the Portuguese mainland (1971-2000). The normalized bias is represented in (a), and the MAPE is represented in (b), given in percentage. The errors are computed for different accumulation periods of precipitation (monthly in red, seasonally in green and yearly in blue) pooling all data together. (c) PDF matching skill scores S (blue) and S90 (red) for daily precipitation PDFs simulated by the historical EURO-CORDEX RCMs over Portuguese mainland during the 1971–2000 period.

3.2. Maximum Temperature Evaluation

Figure 3.2a and b display two standard statistical errors (bias and MAE) of the maximum temperature at different temporal scales, from monthly, seasonally to yearly. Overall, there is an underestimation of the maximum temperature, only 3 out of the 45 models have positive biases. 20 out of 45 models show negative biases of lower than 1.5ºC. Regarding the MAEs, the magnitudes of most values are similar to the bias. Such similarities could indicate a systematic temperature underestimation, which could be due to a cold bias in the forcing GCMs. This issue is, nevertheless, expected, since the mean bias found for the multi-GCM CMIP5 historical experiments is of around -1 ºC, and MAE lays between 0.5 and 1.5 (according to chapter 9 of WG1AR5, IPCC 2014). The similarity between the simulated and reference temperature distributions is summarised by the S and S90 scores in Figure 3.2c. The distributions show an overlap with the observations above 75% for most of simulations.

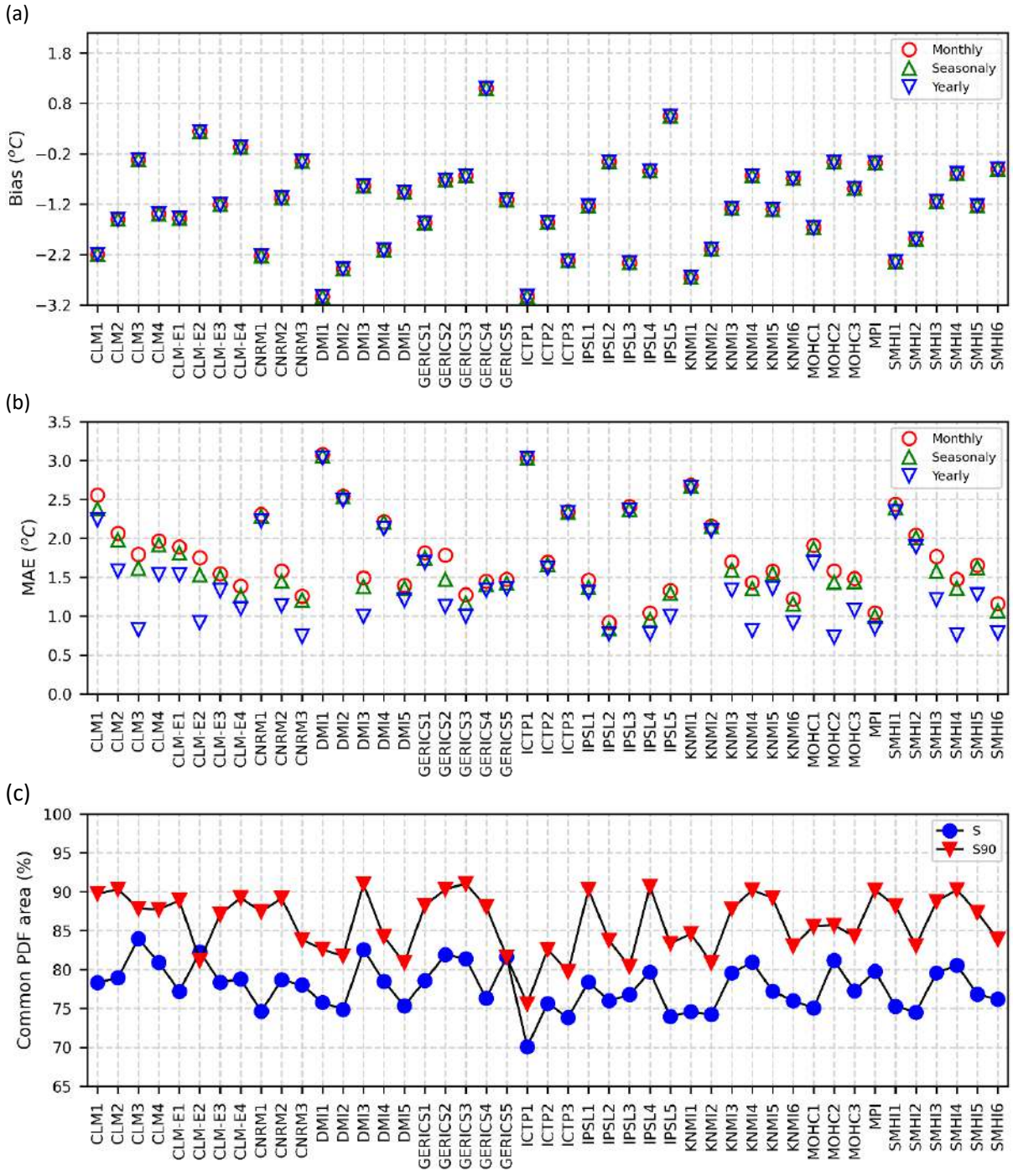

Figure 3.2 Climatological error measures of EURO-CORDEX RCMs maximum temperature for the Portuguese mainland (1971-2000). The bias is represented in (a), and MAE is represented in (b). The errors are computed for different time periods of maximum temperature (monthly in red, seasonally in green and yearly in blue) pooling all data together. (c) PDF matching skill scores S (blue) and S90 (red) for daily maximum temperature PDFs simulated by the historical EURO-CORDEX RCMs over Portuguese mainland during the 1971–2000 period.

3.3. Minimum Temperature Evaluation

Contrary to the maximum temperature, the minimum temperature biases are no longer consistently negative, and around one-third of the models' simulations show positive biases (Figure 3.3a and b). Nevertheless, as for the maximum temperature, the KNMI and SMHI simulations show a systematic negative bias, inherited from the respective GCMs. The biases and MAEs are smaller for the minimum temperature than for the maximum temperature. The similarity between the simulated and observed distributions is also generally greater for the minimum temperature (Figure 3.3c), which might be related to the colder bias of the maximum temperature. The overlap between the distributions is greater than 75% in most cases.

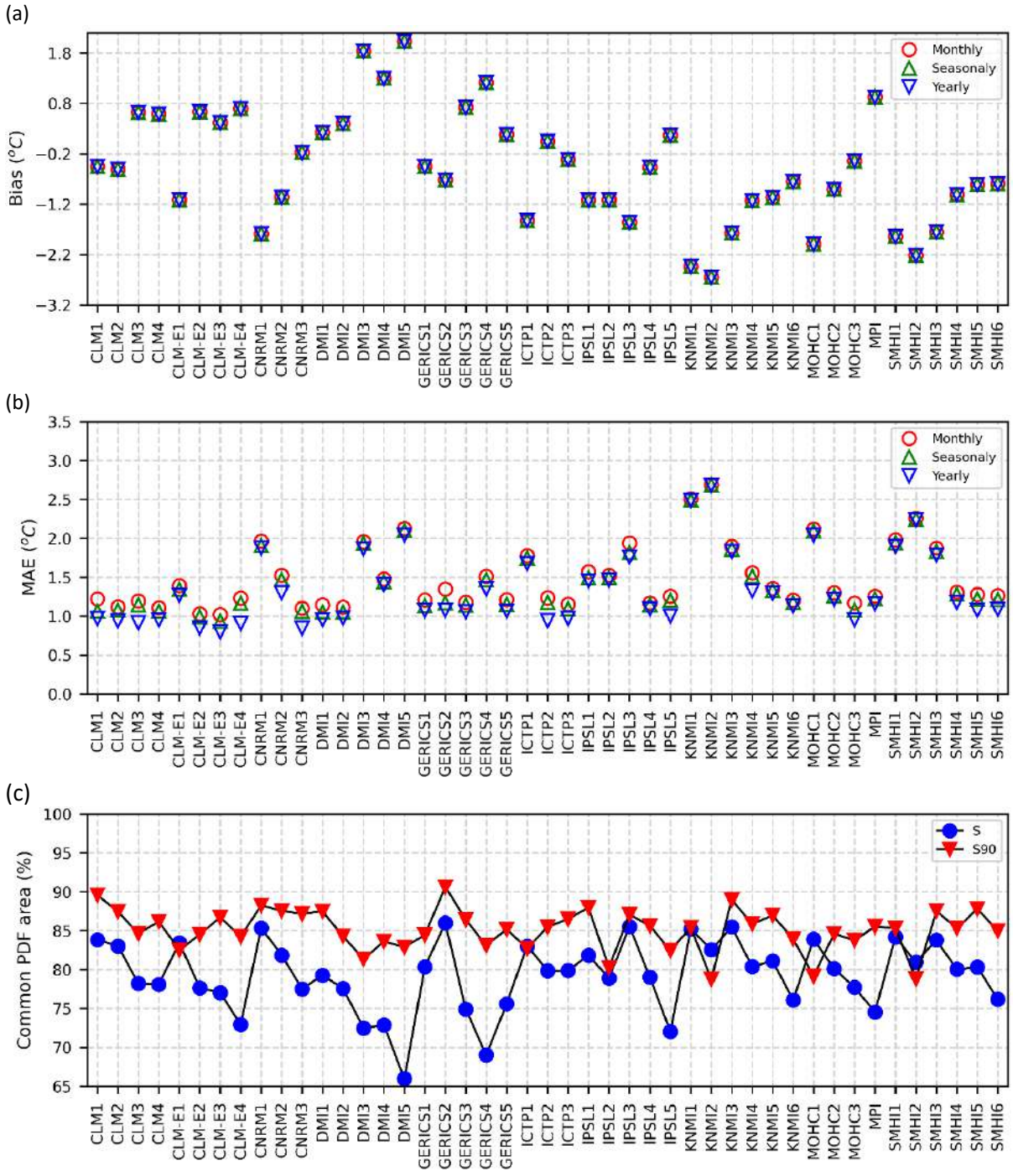

Figure 3.3 Climatological error measures of EURO-CORDEX RCMs minimum temperature for the Portuguese mainland (1971-2000). The bias is represented in (a), and MAE is represented in (b). The errors are computed for different time periods of minimum temperature (monthly in red, seasonally in green and yearly in blue) pooling all data together. (c) PDF matching skill scores S (blue) and S90 (red) for daily minimum temperature PDFs simulated by the historical EURO-CORDEX RCMs over Portuguese mainland during the 1971–2000 period.

3.4. Multi-Model Ensemble Evaluation

Based on the analysis of the multi-model ensembles groups built with different numbers of RCMs (not shown), only the results of the multi-model ensemble that includes the 13 RCMs, that have all the RCPs, are presented in this report. The four multi-model ensembles were evaluated in the same manner as individual RCMs by computing the same error statistics. Figure 3.4a and b display two standard statistical errors (normalized bias and MAPE, in %, for precipitation; bias and MAE for maximum and minimum temperatures) focused on the four multi-model ensembles' ability to represent the accumulated precipitation, maximum and minimum temperatures at different temporal scales, from monthly, seasonally to yearly. The ENS1 performs better than the other ENSs in each variable, which is expected since it only considers the performance of each individual variable, but at the cost of compromising the physical consistency of multi-variables analysis, indices, and impacts. Looking at the other three ensembles, the ENS3 is the best performing ensemble for precipitation and maximum temperature, whilst for the minimum temperature this is the ENS2 although bias and MAE for both ensembles are close to each one. In the observed the S and S90 scores (Figure 3.4c), the differences between the ensembles are rather small.

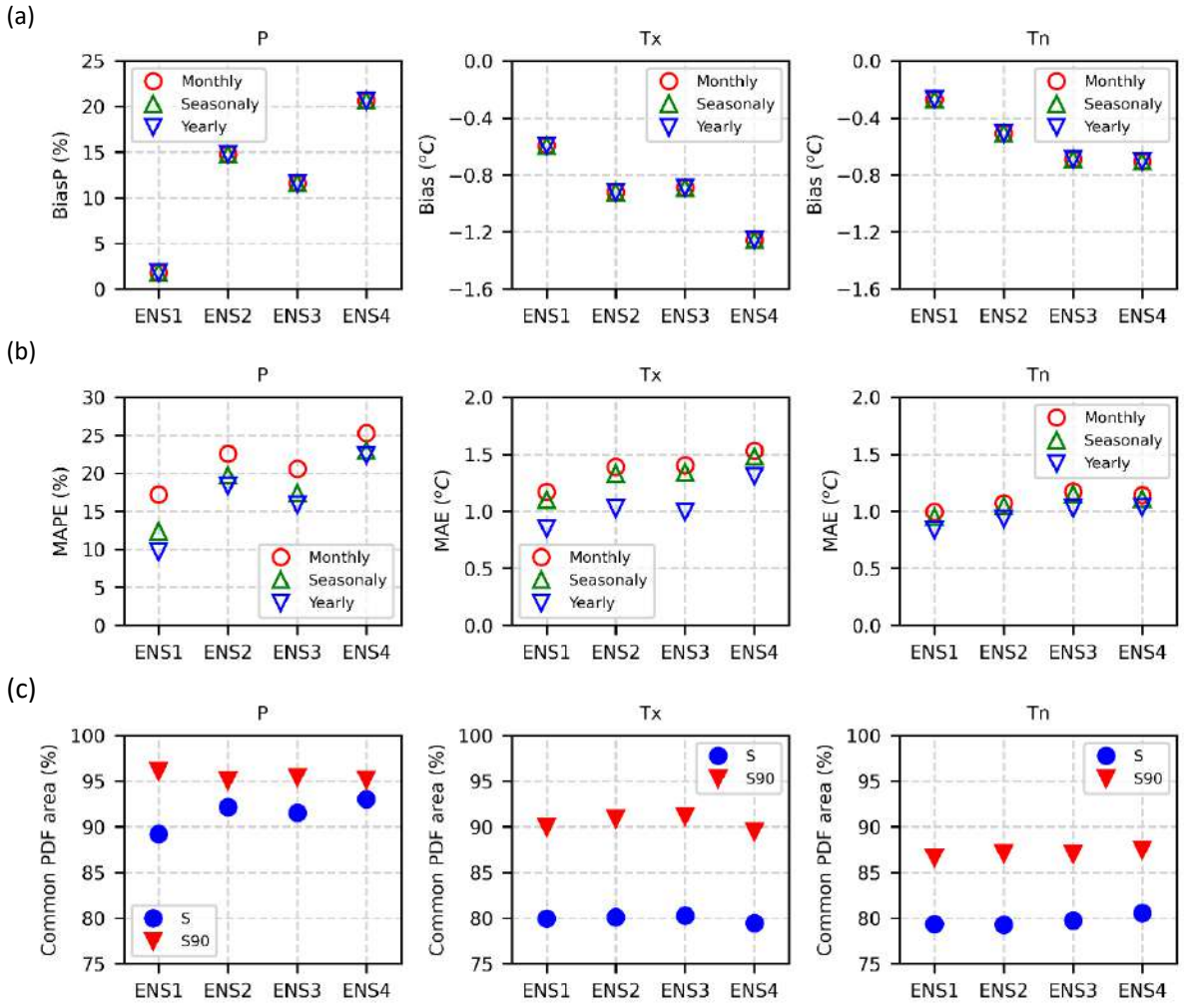

Figure 3.4 Climatological error measures of EURO-CORDEX multi-model ensemble common precipitation (left), maximum (middle) and minimum (right) temperature for the Portuguese mainland (1971-2000). The bias is represented in (a), and MAE is represented in (b). For precipitation, both metrics were normalized by the mean, and the values are given in percentage (normalized bias and MAPE, respectively). The errors are computed for different time periods (monthly in red, seasonally in green and yearly in blue) pooling all data together. (c) PDF matching skill scores S (blue) and S90 (red) for daily precipitation (left), maximum (middle) and minimum (right) temperature, respectively, PDFs simulated by the historical EURO-CORDEX RCMs over Portuguese mainland during the 1971–2000 period.

Differences of yearly and seasonal accumulated precipitation, maximum and minimum temperatures between EURO-CORDEX multi-model ensembles (Common – 13RCMs) and the gridded observational dataset for mainland Portugal are presented in Figure 3.5. Overall, the ensembles overestimate the precipitation with the mean value of the differences closer to 100 mm, except the ENS1 where the mean value is closer to 0 mm but the differences range from, approximately, -150 to 200 mm. Looking at the maximum and minimum temperatures, an underestimation is observed in all ensembles, except during the summer due to a negative bias found in the northern region and a positive bias in the southern region of Portugal (not shown).

Despite the better generalized performance of ENS1, it should be noted that assigning different weights to different variables might lead to inconsistencies in the climate change assessment, especially when addressing minimum and maximum temperatures, both obtained from the same "mother"-variable: temperature. For this reason, ENS3 (Equation 15), which shows the second-best performance (after ENS1), as well as the lowest spreads in comparison with ENS2 and ENS4, was chosen as the 13-member EURO-CORDEX RCM multi-model ensemble to be considered in the characterization of Portugal's future climate, and associated uncertainties. The multi-model ensemble of the climate extremes and indices defined in Section 2.4 were computed following the formulation of the ENS3 (Equation 15), which considers the weights of each of the 13RCMs.

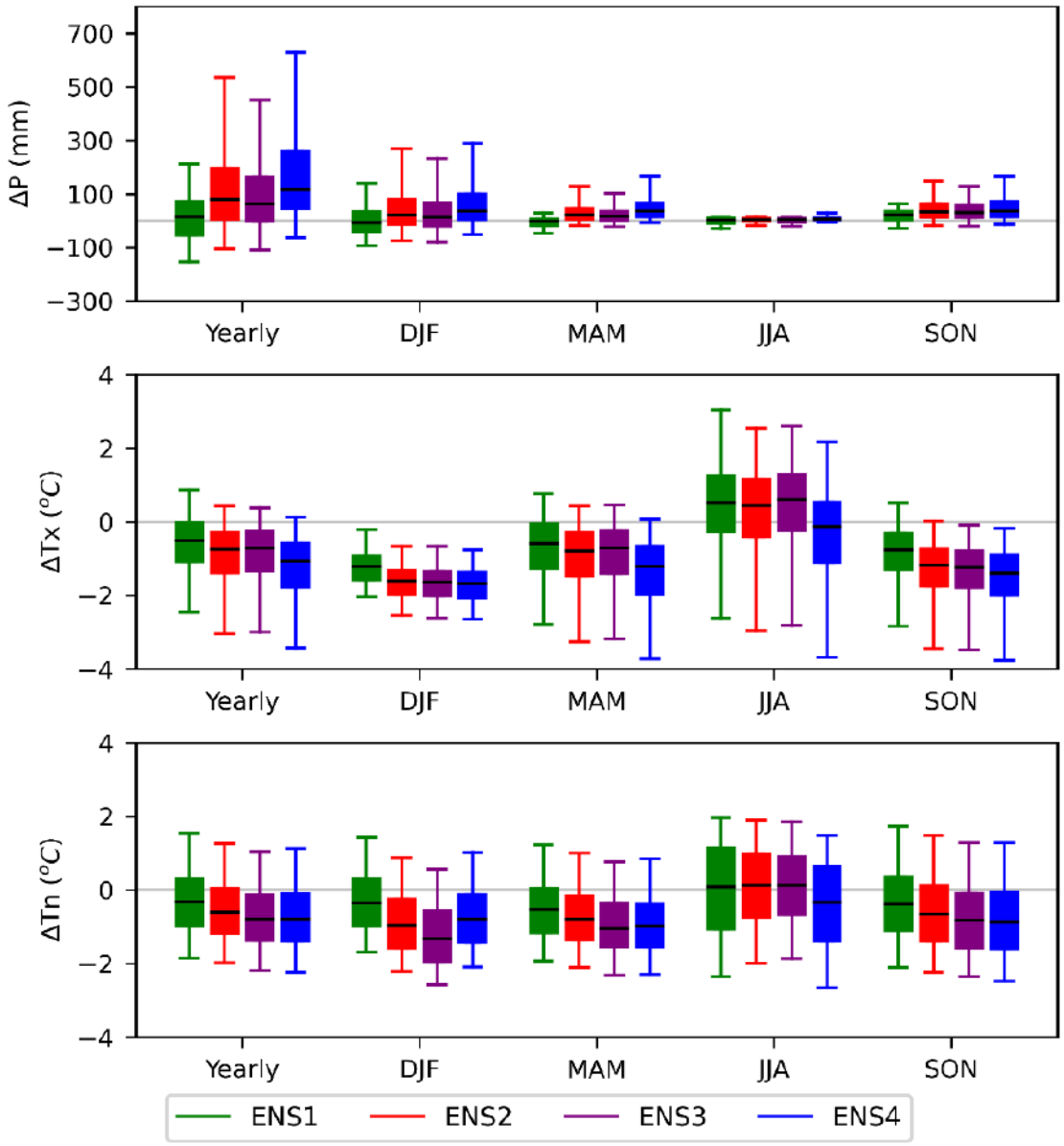

Figure 3.5 Differences of yearly and seasonal mean precipitation (top), maximum temperature (middle) and minimum temperature (bottom) between EURO-CORDEX multi-model ensembles (Common – 13RCMs) and the gridded observations in the same regular grid.

4. Large-scale drivers of climate change over Portugal and Mediterranean region

The Mediterranean basin is in the transition zone between the arid to semiarid subtropical, and the humid climates of northern Europe, being very sensitive to changes in global climate. Indeed, it has been identified as a climate change "hotspot", with observed and projected rates of climate change exceeding global trends for most variables (Giorgi 2006; Lionello and Scarascia 2018; Cramer et al. 2018).

Between 1860 and 2005, the observational records show a general trend for warmer and drier mean atmospheric conditions over the Mediterranean (Giorgi and Lionello 2008; Trenberth 2011; Turco et al. 2018). According to the Fifth Assessment Report of the Intergovernmental Panel on Climate Change (IPCC 2013) the observed increase in mean temperature over the western Mediterranean during the last decades, has been particularly pronounced during the summer months, in contrast with the high-latitudes, in northern Europe, where warming has been strongest in winter. An even sharper contrast between northern Europe and the Mediterranean emerges for mean precipitation trends: several studies reported a drying trend for Mediterranean in contrast with a wetting tendency in northern Europe. This contrast is consistent with the thermodynamic "wet-get-wetter and dry-get-dryer" conceptual picture of Held and Soden (2006). Such conceptual model emerges from changes in general circulation manifested by the intensification of the meridional circulation cells, expansion of the Hadley Cell, and a north-eastward shift of storm tracks in response to global warming.

Projections from Global Climate Models (GCMs) and Earth System Models (ESMs) indicate that the warming and drying trends across the Mediterranean basin will continue throughout the twenty-first century. Lionello and Scarascia (2018) analysed the output from the phase 5 Coupled Model Intercomparison Project (CMIP5) simulations and found a projected warming trend for the Mediterranean region around 20% stronger than the global average throughout the twenty-first century. This is accompanied by a decrease in average precipitation over this region at a rate approximately -20 mm/K (corresponding to -4%/K). Moreover, their results showed that the Mediterranean warming is stronger during summer than during winter (exceeding the summer global warming average in about 50%), as well as during daytime in comparison to night-time, leading to an increase of the amplitude of both daily and annual temperature ranges. Finally, their analysis showed that the precipitation reduction over the Mediterranean affects all seasons. This drying effect was found to be particularly pronounced over large portions of the Iberian, Balkan, and Anatolian Peninsulas. The only exception to the overall future projected reduction of precipitation occurs in the northern areas of the Mediterranean regions, during winter. Nonetheless, the overall, basin average, winter precipitation reduction over the entire Mediterranean

emerges as a robust signal in climate models and observations, with local reductions up to 40%, posing a massive challenge for water resources management and agriculture (Tuel and Eltahir 2020).

The average temperature increases and rainfall reduction over the Mediterranean are accompanied by an increase in atmospheric evaporative demand, which is projected to result in longer and more frequent droughts, and an overall increase in aridity (Kim et al. 2014; Vicente-Serrano et al. 2014, 2020; Schleussner et al. 2016). Additionally, high temperature extremes (including heatwaves) are projected to occur more frequently, while low temperature extremes are projected to become less frequent (IPCC 2013). Notice that despite a decrease in mean precipitation, heavy rainfall indices show significant increases across most of the Mediterranean (Sillmann et al. 2013; Barcikowska et al. 2018; Cramer et al. 2018). Finally, according to the IPCC (2013), there is low confidence on the declining mean wind trends over Europe in recent decades due to problematic anemometer data and natural climate variability. The future trends for mean and extreme winds over the Mediterranean region also show a high degree of uncertainty, both in magnitude and signal.

The projected warming and drying trends for the Mediterranean are stronger for high anthropogenic emission scenarios, reaffirming the weight of the human component on the overall climate change projections, compared to natural variability of the climate system (Barcikowska et al. 2018; Cramer et al. 2018). Nonetheless, even in a +2 K global warming scenario, a critical environmental situation will develop, related to warming of land areas in summer and widespread reduction of precipitation, particularly serious for the southern Mediterranean region, namely the Iberian, Balkan, and Anatolian peninsulas (Cramer et al. 2018). This projected summer drying effect results from increased the land-sea temperature contrast between the Mediterranean Sea and surrounding land areas, along with an intensification of the Azores anticyclone in response to global warming. In turn, this results in a reduction of weather regimes producing precipitation events in the northern part of the Mediterranean basin and an increased sea level pressure gradient across the central and eastern Mediterranean, which is consistent with increased advection of warm dry continental air masses towards the central and eastern Mediterranean (Lionello and Scarascia 2018). During winter, a projected sea level pressure increase in the central Mediterranean is associated to a reduction of the eastward circulation component and advection of moist air from the Atlantic, which could help explaining the projected precipitation reduction trends (Lionello and Scarascia 2018). Barcikowska et al. (2018) also suggested that the strong drying projected trends in the southwestern Mediterranean may be related to both divergence of moisture and enhancement of the temperature contrast between slowly warming SSTs along the Canary Current and rapidly warming land.

A complete theory explaining the observed and projected warming and drying responses by climate models for the Mediterranean regions remains to be presented. The evolution of spatially averaged precipitation

over the Mediterranean has been associated with changes in the regional circulation patterns, with large-scale upper-tropospheric flow changes and the reduction in regional land-sea temperature contrast being identified has the two main drivers (Tuel and Eltahir 2020). However, much of these changes emerge from internal climate variability which induces strong interdecadal variability in observations and model simulations. Indeed, Giorgi and Bi (2009) found that internal variability will dominate the precipitation signal in the Mediterranean until 2040. Looking back at the twentieth century, Mariotti (2010) highlighted the importance of decadal variability in determining observed climate anomalies in the Mediterranean region. Only after the 1980s do the indicators show higher trends of warming over this region when compared to global ones.

On the one hand, the effect North Atlantic Oscillation (NAO), the jet-stream, the mid-latitude storm-track variability, and blocking frequencies play a central role in controlling precipitation and temperature variability over northern Europe (Sousa et al., 2017, 2018). On the other hand, the drying of the southern Mediterranean regions was associated with the expanding Hadley Cell and the corresponding anomalous subsidence and divergence on its poleward flank, which is also intricately linked to the NAO and the mid-latitude storm-track variability. Previous studies have also highlighted the importance of the low-frequency ocean dynamics (specifically the Atlantic Multi-decadal Oscillation, AMO), volcanic eruptions, and other atmospheric variability models, such as the El Niño Southern Oscillation (ENSO) and the Easter Pacific (EP) pattern, in modulating the impact of the NAO and North-Atlantic storm-tracks on European and North African climate variability, contributing to the complexity of the Mediterranean climate response problem.

The intricate links between internal climate variability and Mediterranean climate response implies that climate models need to accurately simulate these interactions. However, the CMIP3 and CMIP5 multi-model future projections produce large spread in simulated trend of winter NAO and the resulting circulation response. Moreover, many climate models are unable to accurately reproduce troposphere-stratosphere couplings, resulting in important biases in the North Atlantic tropospheric jet variability. Overall, these previous studies highlight the necessity for having realistically resolved climate and weather at regional scales to obtain accurate projections of Mediterranean climate response, and its implications for climate change adaptation strategies.

In the last decade two types of extreme atmospheric circulation phenomena have gained much attention over the north-western sector of the north-Atlantic Ocean and also over continental Western Europe, namely Atmospheric Rivers (ARs) and Tropical Cyclones (TCs). Therefore, taking into account their apparent growing frequency and the extreme risk to coastal societies that these phenomena might entail we will provide now a short overview of both:

1) Tropical Cyclones (TCs)

In recent years a growing attention has been paid to the increasing role played by TCs around the world including the entire North Atlantic, with a 6% increase per decade at the global scale (Kossin et al., 2020). These authors showed that between 1979 and 2017 the proportion of major hurricanes to all hurricanes is increasing in most ocean basins and in the north Atlantic the proportion of major hurricanes was found to be increasing by 49% per decade in the period of 1979-2017 (Kossin et al., 2020).

Located at mid-latitudes, Western Europe is usually considered to be unaffected by TCs, however there is growing evidence of being increasingly prone to nearby post-tropical transitions, and therefore a higher number of Post-Tropical Cyclones (PTCs) reaching land (Sainsbury et al., 2020). Thus, it is important to take into consideration the potential change that both TC and PTC will suffer in a warming climate.

The increment in the frequency of strong TCs in western Atlantic (Kossin et al., 2020) has now been confirmed also over the eastern half of the North Atlantic Ocean (Lima et al., 2021). Three recent TCs in the north-eastern part of the north Atlantic basin have underpinned the importance of considering the destructive potential of TCs (Lima et al., 2021). All three events had significant impacts in continental Portugal (Ophelia in 2017 and Leslie in 2018), and in the archipelago of Azores (Lorenzo in 2019), after briefly reaching category 5 a few days before, a primer for the North-eastern Atlantic region.

2) Atmospheric Rivers (ARs)

Atmospheric Rivers are relatively narrow and elongated filaments of high-water vapor transport, and their occurrence is generally interpreted as large atmospheric water vapor transport events in the extra-tropics. The water vapor in ARs is supplied by tropical and/or extratropical moisture sources and these systems frequently lead to heavy precipitation where they are forced upward – for example, by mountains or by ascent in the warm conveyor belt. There is a growing interest in understanding the contribution of ARs in the Atlantic Ocean to extreme precipitation and floods in western Europe (Ramos et al 2015, Pereira et al 2018). However, AR impacts are not always hazardous, as they can also be responsible for providing beneficial water supply (*e.g.*, Dettinger, 2013).

Ramos et al. (2016) evaluated changes of ARs reaching Europe in simulations from six Coupled Model Intercomparison Project Phase 5 (CMIP5) global climate models (GCMs). Results confirmed a strong tendency for increased vertically integrated horizontal water transport at the end of the 21st century under the two scenarios considered (RCP4.5 and RCP8.5) compared to the historical period (1980–2005), while the number of ARs is projected to double on average for the same period. These changes are robust between models and are associated with higher air temperatures and thus enhanced atmospheric moisture content, together with higher precipitation associated with extratropical cyclones. This suggests an increased risk of

intense precipitation and floods along the Atlantic European Coasts from the Iberian Peninsula to Scandinavia.

5. Annual and Seasonal Mean Changes

The results presented from this chapter onwards are based on the EURO-CORDEX multi-model ensemble, computed following the formulation of the ENS3 (Equation 15), which considers a multi-variable weighting approach for each of the 13 RCMs.

5.1. Temperature

Mean Temperature

The EURO-CORDEX ensemble projected an increase of annual averaged daily mean temperature throughout mainland Portugal between 0.0 ºC and +2.0 ºC for the 2011-2040 period compared to the 1971-2000 reference period, regardless of the considered emission scenario (Figure 5.1). The differences in projected daily mean temperature among emission scenarios grow significantly throughout the twenty-first century (Figure 5.1). For the mid-century period (2041-2070), the projected anomalies for annual averaged daily mean temperature for the RCP2.6 scenario remain below +2.0 ºC. For RCP4.5, the 2041-2070 daily average temperature anomalies ranged between +1.0 ºC and +2.0 ºC over western Portugal and +2.0 ºC and +3.0 ºC over eastern Portugal. For RCP8.5 the mid-century anomalies range between +2.0 ºC and +3.0 ºC over continental Portugal. Finally, the end-of-century period showed larger differences in annual averaged daily mean temperature anomalies over the region between the three scenarios (Figure 5.1). While no change is expected for the RCP2.6 scenario, the anomalies remain between +1.0 ºC and +2.0 ºC, for the RCP4.5 scenario, the anomalies range between +2.0 ºC and +3.0 ºC for the entire country, and for the RCP8.5 scenario, the anomalies range between +3.0 ºC and +4.0 ºC over western Portugal, and between +4.0 ºC and +5.0 ºC over the remaining land.

The daily mean temperature anomalies show relevant seasonality, with strongest increases during JJA and lower increases during DJF (Figure 5.1). The growing impact of the different high emission scenarios is particularly notorious during boreal summer, where the RCP8.5 scenario for the end-century period showed the strongest daily mean temperature anomalies, ranging between +6.0 ºC and +7.0 ºC over north-eastern Portugal. This reflects a different of about 5 ºC between RCP2.6 and RCP8.5. During boreal winter, the differences between RCP2.6 and RCP8.5 scenarios was minor for the 2011-2040 period, and around 2 ºC for the 2071-2100 period. The maximum daily mean temperature anomalies for the end-of-century period in DJF ranged between +3.0 ºC and +4.0 ºC with widespread occurrence throughout Portugal.

The uncertainties associated with the EURO-CORDEX multi-model ensemble daily mean temperature projections are relatively small (Figure 5.2), mostly below 0.8 ºC for all periods and emissions scenarios,

except during SON for mid- and end-of-century projections under RCP8.5 scenario over north-eastern Portugal and most of the country, respectively, where the inter-model standard-deviation ranged between 0.8 ºC and 1.4 ºC, coinciding with strong anomalies of more than +4.0 ºC and +5.0 ºC. The signal of the change was coherent amongst more than 66% of the models in all locations, periods, and emission scenarios.

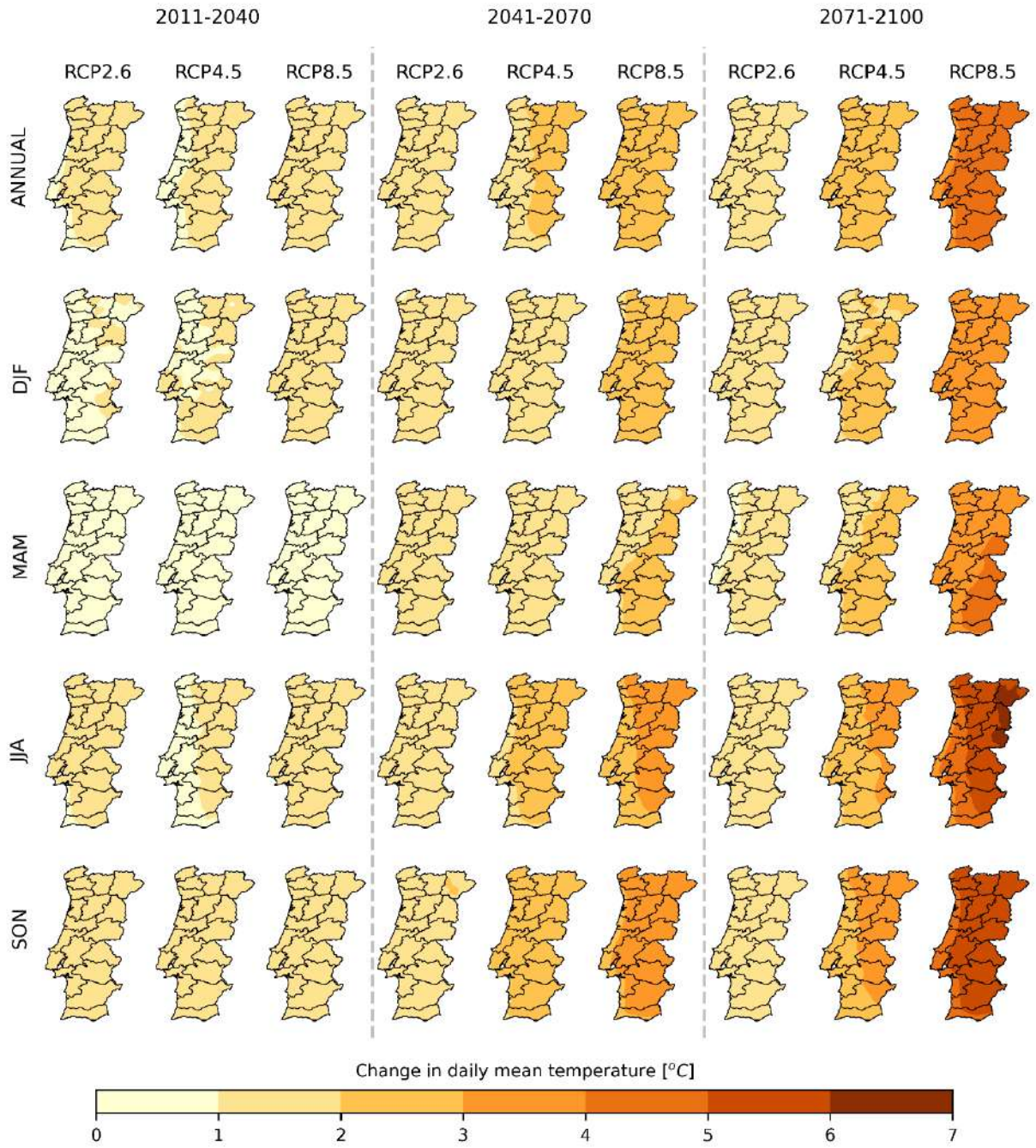

Figure 5.1 Future projected changes in daily mean temperature over mainland Portugal, considering the 1971-2000 period as reference. The different rows from top to bottom represent averaged taken over all months,

DJF, MAM, JJA and SON respectively. The different columns represent the future periods considering different GHG emission scenarios.

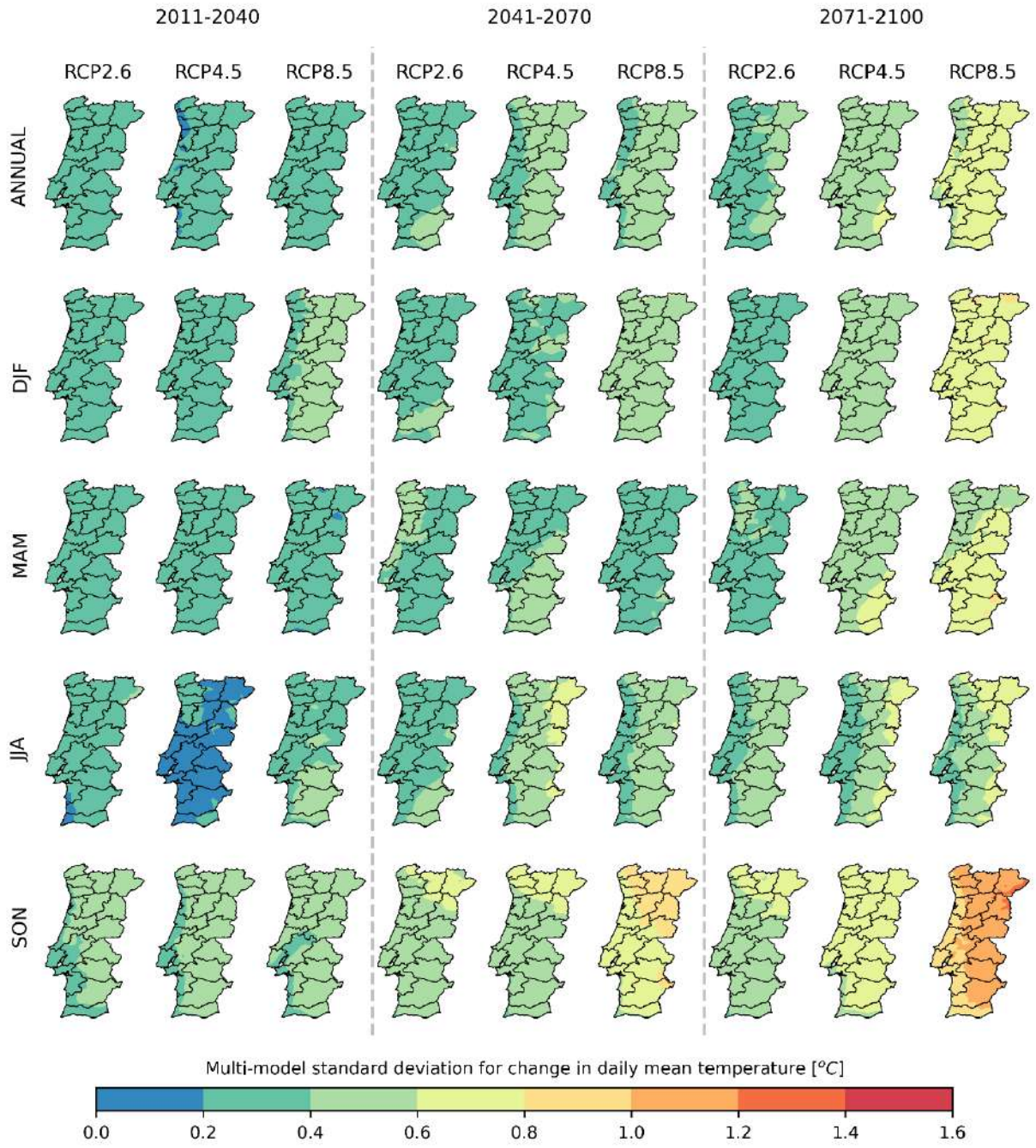

Figure 5.2 Multi-model spread in future projected changes in daily mean temperature over mainland Portugal, considering the 1971-2000 period as reference. The spread is quantified by the standard deviation of the anomalies between different models. The different rows from top to bottom represent averaged taken over all months, DJF, MAM, JJA and SON respectively. The different columns represent the future periods considering different GHG emission scenarios. Grid-points where the temperature change signal does not agree in at least 66% of the models is identified by dotted hatching (no occurrences for Tm).

Changes in daily mean temperature averaged over the entire year for NUTS II showed a similar behaviour over the different regions (Figure 5.3). For the 2011-2040 period, temperature anomalies associated with RCP2.6 and RCP4.5 displayed an entangled behaviour, while those related with RCP8.5 already started to move towards larger positive anomalies in all regions. Anomalies derived assuming RCP4.5 start to increase in the mid-century period, while those related to RCP2.6 maintain their relatively small values. During this period the anomalies related to RCP8.5 increased considerably, surpassing the +2.0 ºC over all regions, with A.M. Lisboa showing the lighter increases (circa +2.0 ºC). Finally, at the end-of-century, the temperature anomalies remain somehow similar with RCP2.6, slightly increased with RCP4.5 surpassing the +2.0 ºC in all regions, and once again increased considerably with RCP8.5, reaching values from 3 ºC to 5 ºC. During all periods it was notorious that the region of A.M. Lisboa was the one with lighter increases, whereas region Norte and Alentejo showed the larger increases in daily mean temperature. The absolute values of daily mean temperature for the different NUTS and hydrological basins for all time periods and scenarios can be found in Supplementary Material as Figures A1-4. It is also worth noticing that although the ensemble mean (displayed as a black dot) was typically similar to the multi-model median mean temperature in the historical period, from mid-century onwards its climate sensitivity, represented by the temperature anomalies, is above the multi-model median, and in most cases above the multi-model 75th percentile.

These results are shown in more detail when dividing mainland Portugal in NUTS III regions (Figure 5.4). Results for the 2011-2040 period are very similar to those presented for NUTS II. Indeed, the same behaviour is found, with temperature anomalies associated to RCP2.6 and RCP4.5 being rather indifferentiable when regions are sub-divided, and those associated to RCP8.5 start to show a slight increase. For the mid- and end-century, more prominent differences may be found. An example is the obvious east-west gradient that defines the regions, *i.e.*, for regions in the Norte, Centro, and Alentejo, NUTS III sub-regions that are closer to the ocean always present lower temperature anomalies (Alto Minho, Cávado, A.M. Porto, Região de Aveiro, Região de Leiria, Oeste, and Alentejo Litoral), which is a feature also found in the simultaneously NUTS II and NUTS III region of A.M. Lisboa. A similar behaviour is found when dividing Portugal in its hydrographic basins (Figure 5.5), with small differences between temperature anomalies in the beginning of the century for RCP2.6 and RCP4.5, and a relatively small increase in anomalies when RCP8.5 is considered. For mid- and end- of the century, larger anomalies are presented when considering RCP4.5 and RCP8.5, with special emphasis to the 2071-2100 period with RCP8.5. Once again larger anomalies of daily temperature may be found in basins that cover the interior of the country, such as Douro, Tejo, or Guadiana, and lower anomalies in basins mainly focused on coastal Portugal, such as Ancora e RC, Ribeiras do Oeste, and Ribeiras do Alentejo.

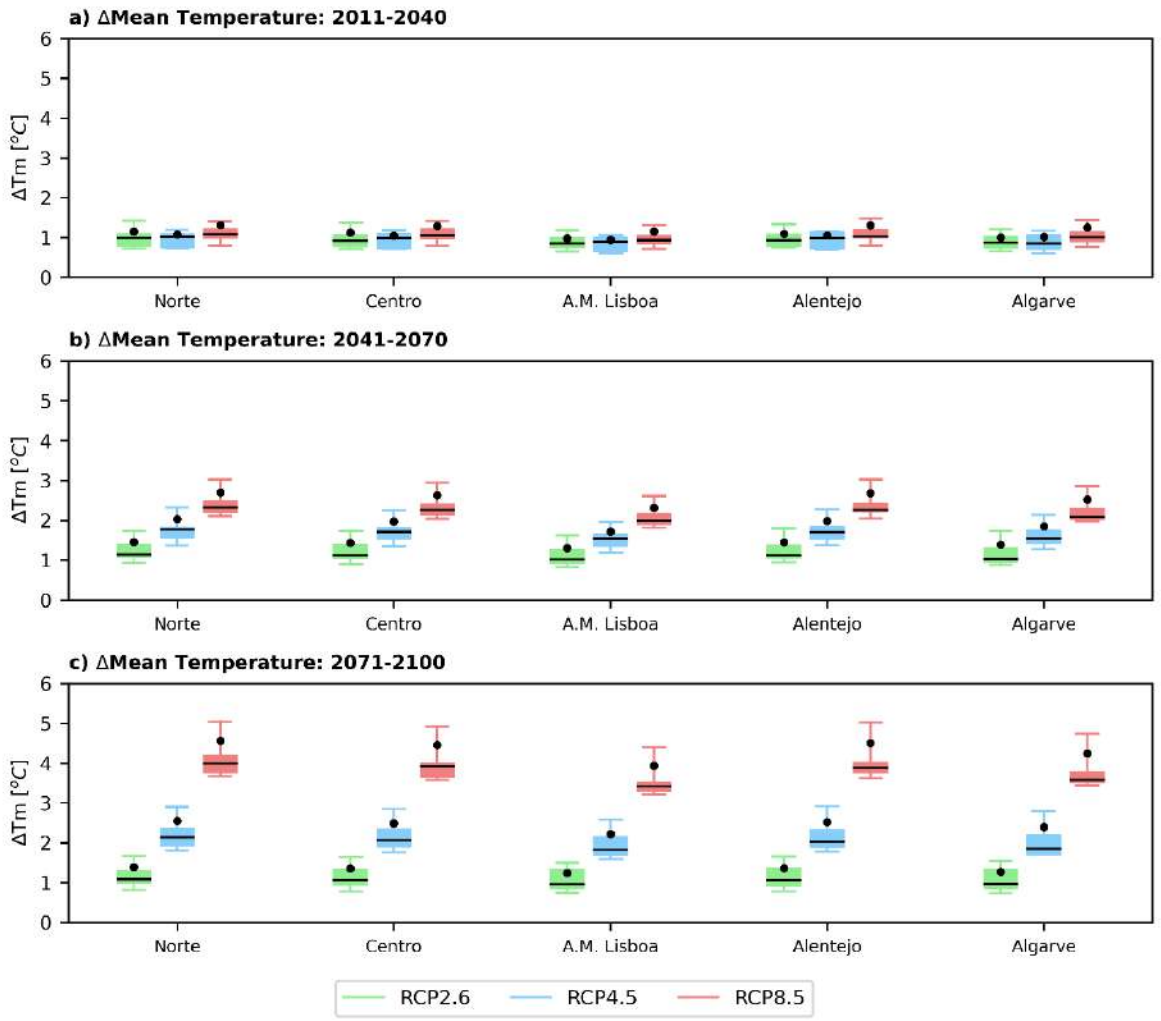

Figure 5.3 Future projected changes in daily mean temperature averaged over the full year for the NUTS II regions. Three future periods are shown: a) 2011-2040, b) 2041-2070, and c) 2071-2100, under all emission scenarios – RCP2.6 (green), RCP4.5 (blue) and RCP8.5 (red). The black point represents the multi-model ensemble mean. The 1971-2000 period is used as reference.

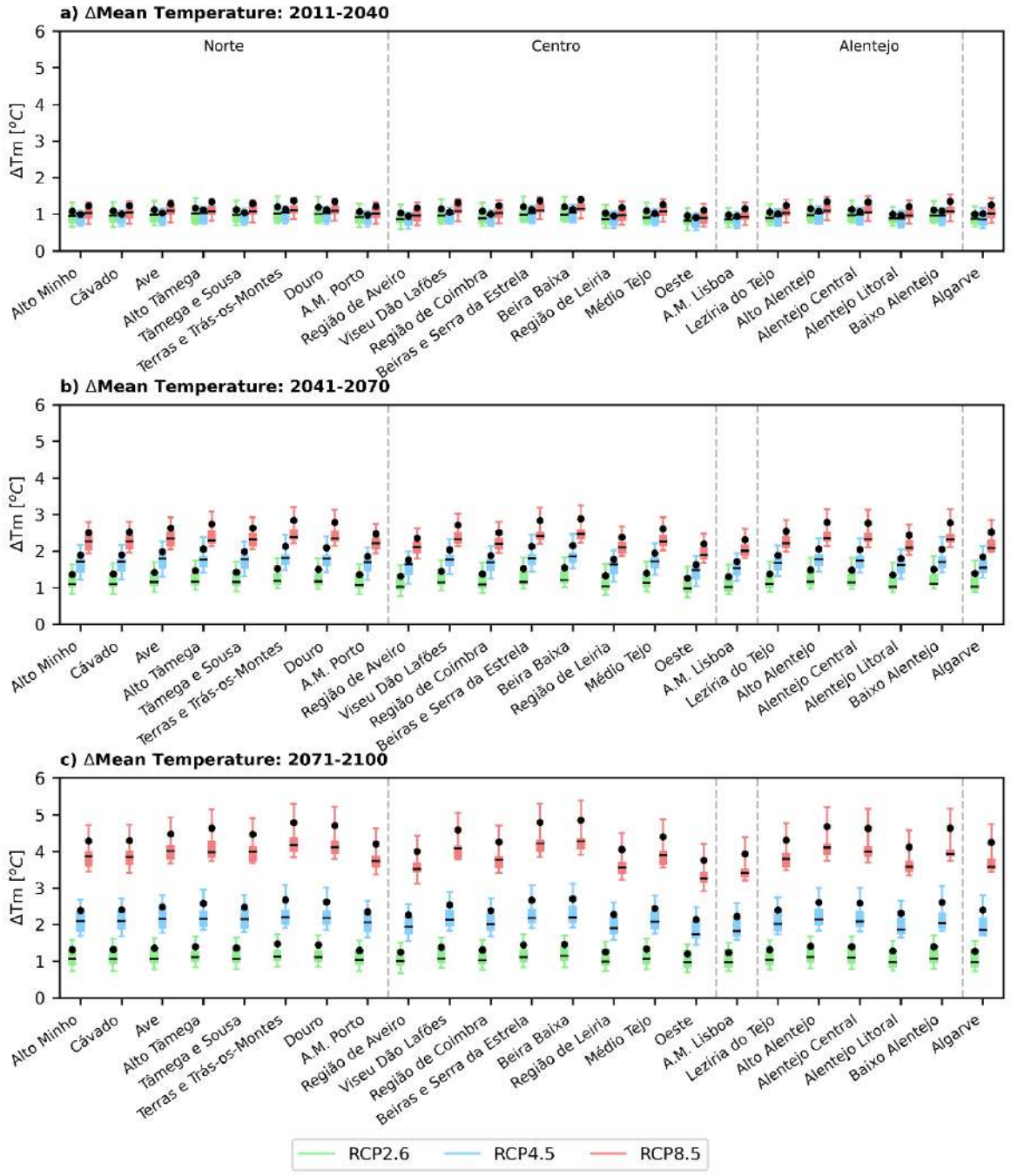

Figure 5.4 Future projected changes in daily mean temperature averaged over the full year for the NUTS III regions. Three future periods are shown: a) 2011-2040, b) 2041-2070, and c) 2071-2100, under all emission scenarios – RCP2.6 (green), RCP4.5 (blue) and RCP8.5 (red). The 1971-2000 period as reference. The black point represents the multi-model ensemble mean. The 1971-2000 period is used as reference.

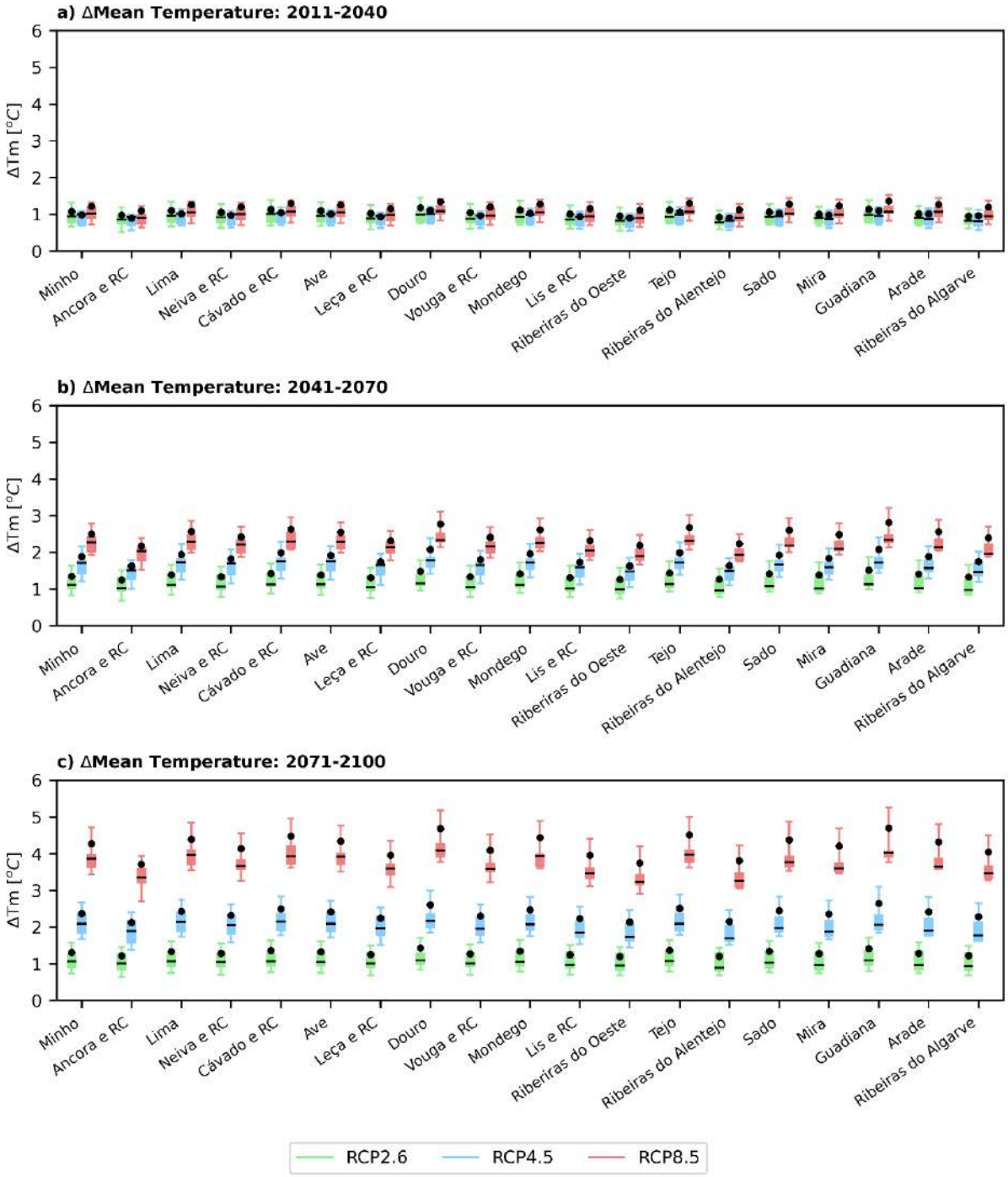

Figure 5.5 Future projected changes in daily mean temperature averaged over the full year for the different basins. Three future periods are shown: a) 2011-2040, b) 2041-2070, and c) 2071-2100, under all emission scenarios – RCP2.6 (green), RCP4.5 (blue) and RCP8.5 (red). The 1971-2000 period as reference. The black point represents the multi-model ensemble mean. The 1971-2000 period is used as reference.

Maximum Temperature

The projected changes for annual averaged daily maximum temperature (Figure 5.6) show similar patterns to the ones found for daily mean temperature. This includes the west-to-east increasing anomaly gradients, the relatively homogeneous magnitude changes over the 2011-2040 period for all emission scenarios, ranging between +1.0 ºC and +2.0 ºC over most of Portugal, except for slightly lower values (between +0.0 ºC and +1.0 ºC) over coastal regions for RCP4.5 and RCP2.6, the increasing anomalies among scenarios throughout the twenty-first century, with some exceeding +5.0 ºC by 2071-2100 for RCP8.5 over north-eastern Portugal, but remaining mostly below +2.0 ºC for RCP2.6.

The seasonality of the daily maximum temperature (Figure 5.6) anomalies also display maximum values during JJA and minimum values during DJF. For both cases, the strongest JJA daily maximum temperature anomalies under RCP8.5 scenario for the end-of-century period occurred over north-eastern Portugal reaching magnitudes larger than +6.0 ºC. During winter, the daily maximum temperature anomalies under RCP8.5 scenario for the end-of-century ranged between +3.0 ºC and +4.0 ºC over most of continental Portugal.

The results showed small uncertainties associated with the projected daily maximum anomalies (Figure 5.7). Indeed, the sign of the anomalies agreed amongst more than 2/3 of the models in all cases, while the magnitude of the inter-model standard-deviation was mostly below 0.8 ºC, with the exception of the anomalies for MAM and SON at end-of-century period under scenario RCP8.5 where the standard deviation reached values up to around 1.4 ºC in SON; and the anomalies for SON in RCP8.5 during the mid-century, reaching standard-deviations of circa 1.0 ºC.

Looking at the future projected changes in daily maximum temperature for the different NUTS II (Figure 5.8), NUTS III regions (Figure 5.9), and hydrographic basins (Figure 5.10), positive anomalies were projected over all regions under all emission scenarios – RCP2.6, RCP4.5 and RCP8.5, being stronger for higher emission scenarios, and amplifying throughout the twenty-first century, except for RCP2.6 where it stabilizes. As in mean temperature anomalies, the warming signal is generally weaker for coastal regions. For the end-century period, the 10^{th} to 90^{th} percentile inter-model spread represented by the boxplot whiskers is smaller than inter-scenario differences, providing confidence on the large impact of global GHG emissions to regional warming over Portugal. The absolute values of daily maximum temperature for the different NUTS and hydrological basins for all time periods and scenarios can be found in Supplementary Material as Figures A5-8.

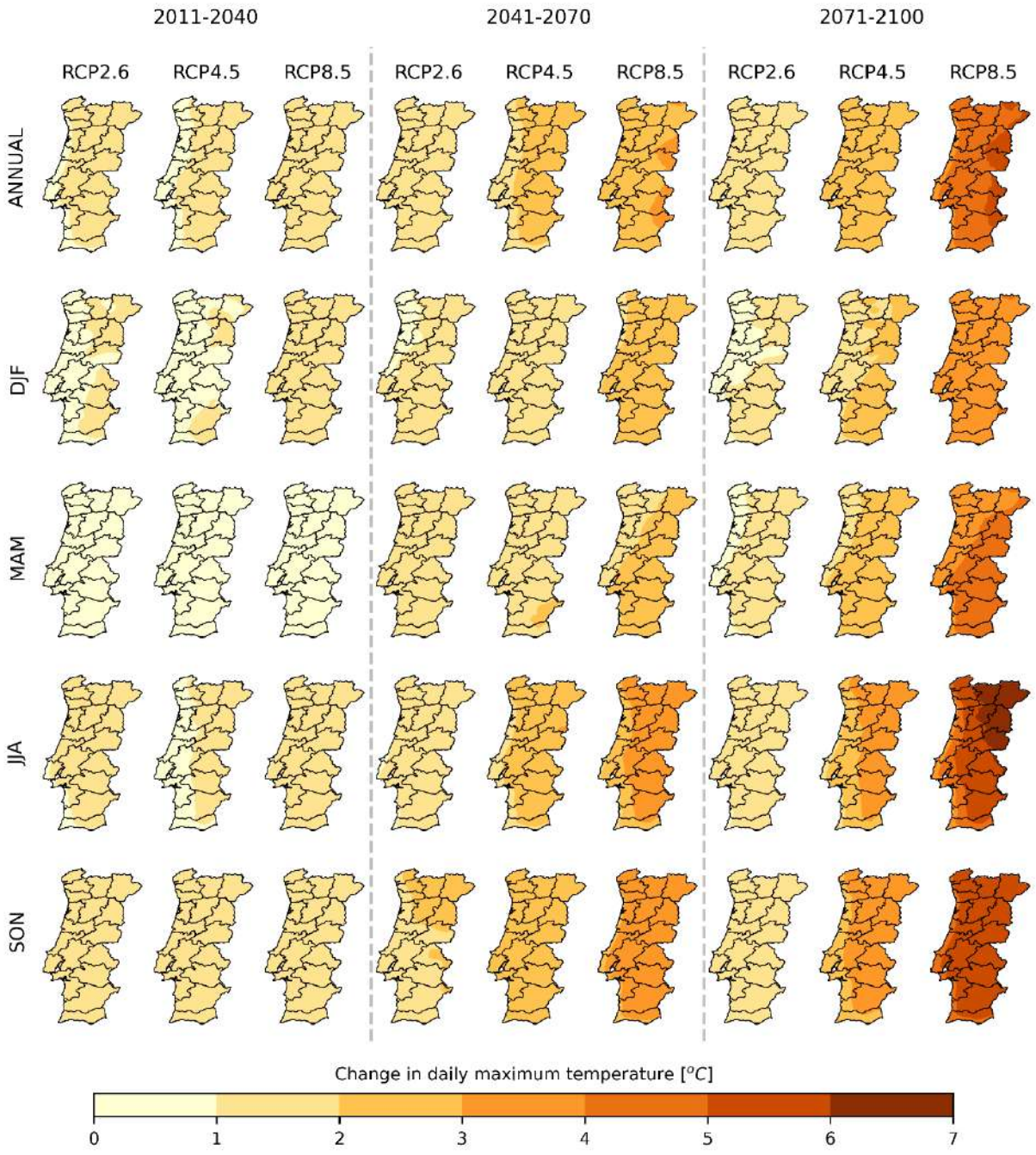

Figure 5.6 Future projected changes in daily maximum temperature over mainland Portugal, considering the 1971-2000 period as reference. The different rows from top to bottom represent averaged taken over all months, DJF, MAM, JJA and SON respectively. The different columns represent the future periods considering different GHG emission scenarios.

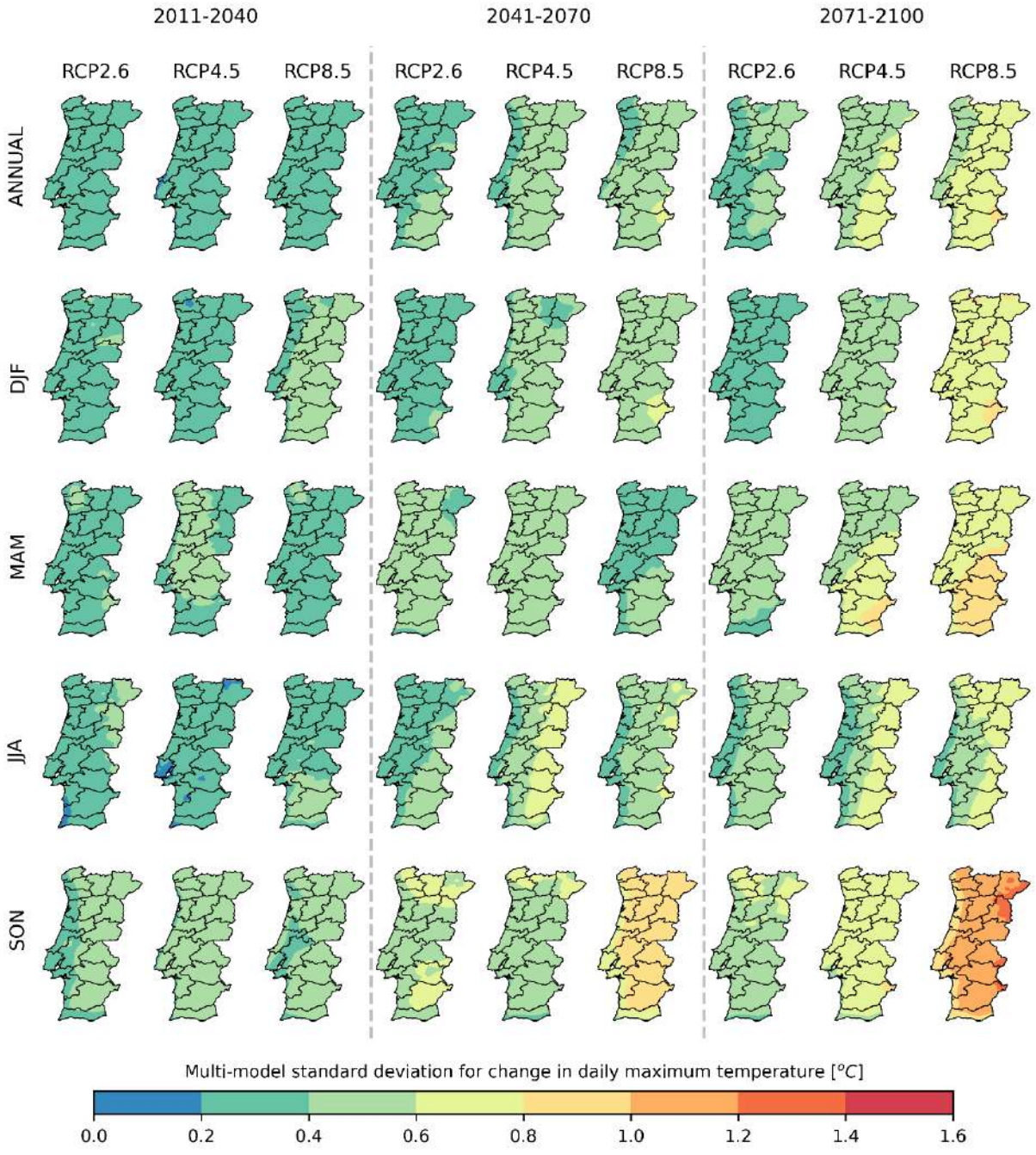

Figure 5.7 Multi-model spread in future projected changes in daily maximum temperature over mainland Portugal, considering the 1971-2000 period as reference. The spread is quantified by the standard deviation of the anomalies between different models. The different rows from top to bottom represent averaged taken over all months, DJF, MAM, JJA and SON respectively. The different columns represent the future periods considering different GHG emission scenarios. Grid-points where the temperature change signal does not agree in at least 66% of the models is identified by dotted hatching (no occurrences for Tx).

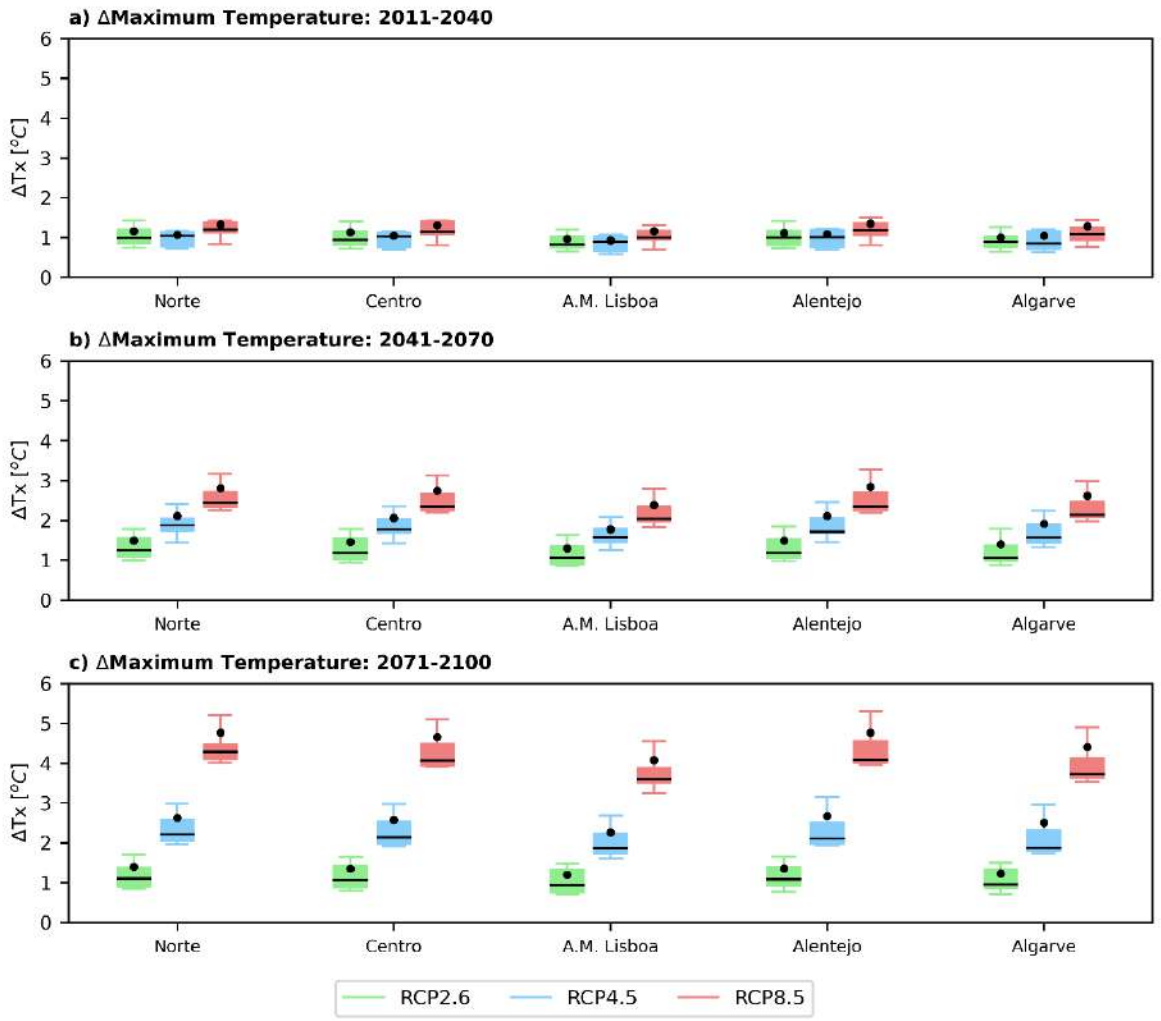

Figure 5.8 Future projected changes in daily maximum temperature averaged over the full year for the NUTS II regions. Three future periods are shown: a) 2011-2040, b) 2041-2070, and c) 2071-2100, under all emission scenarios – RCP2.6 (green), RCP4.5 (blue) and RCP8.5 (red). The black point represents the multi-model ensemble mean. The 1971-2000 period is used as reference.

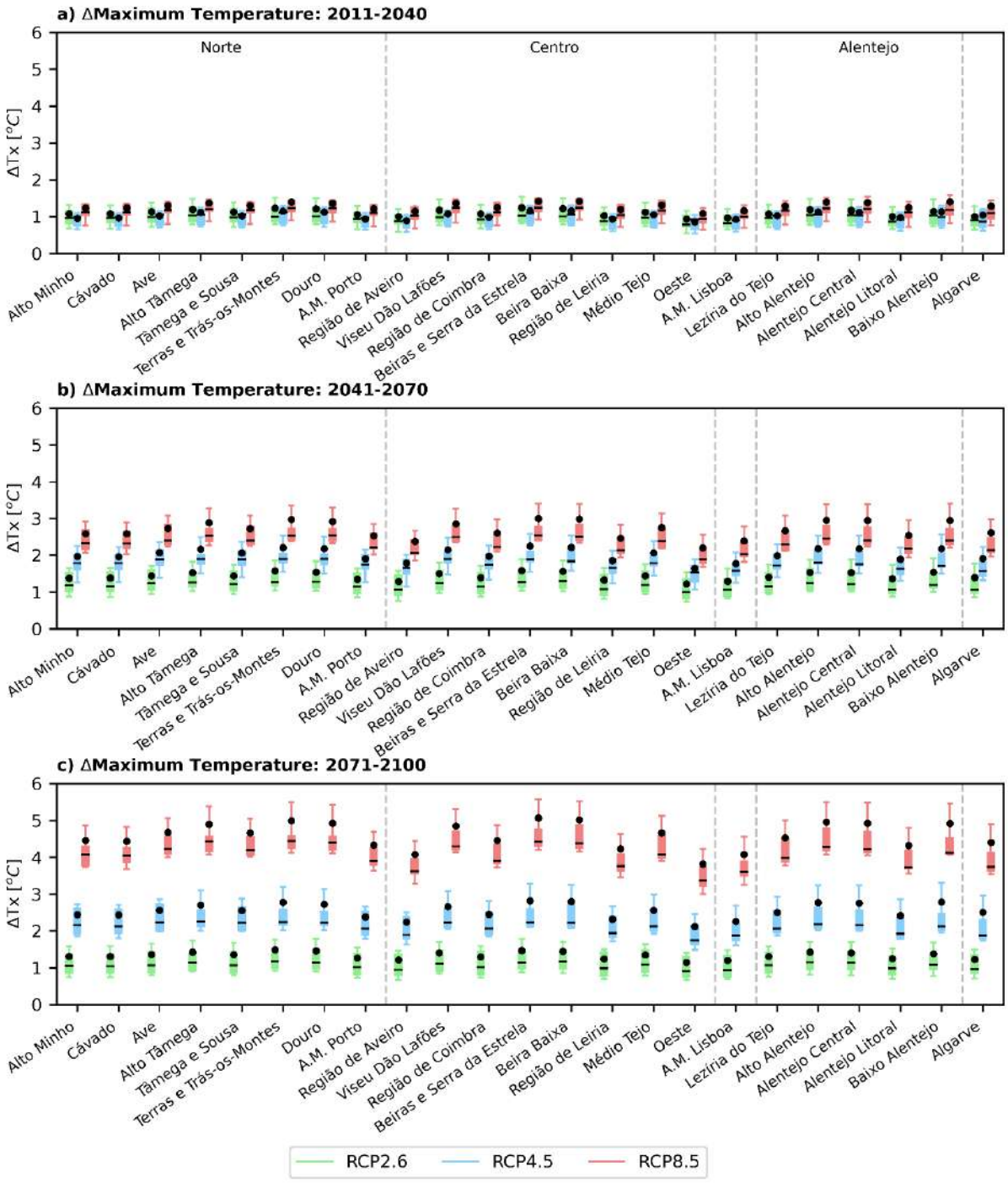

Figure 5.9 Future projected changes in daily maximum temperature averaged over the full year for the different NUTS III regions. Three future periods are shown: a) 2011-2040, b) 2041-2070, and c) 2071-2100, under all emission scenarios – RCP2.6 (green), RCP4.5 (blue) and RCP8.5 (red). The black point represents the multi-model ensemble mean. The 1971-2000 period is used as reference.

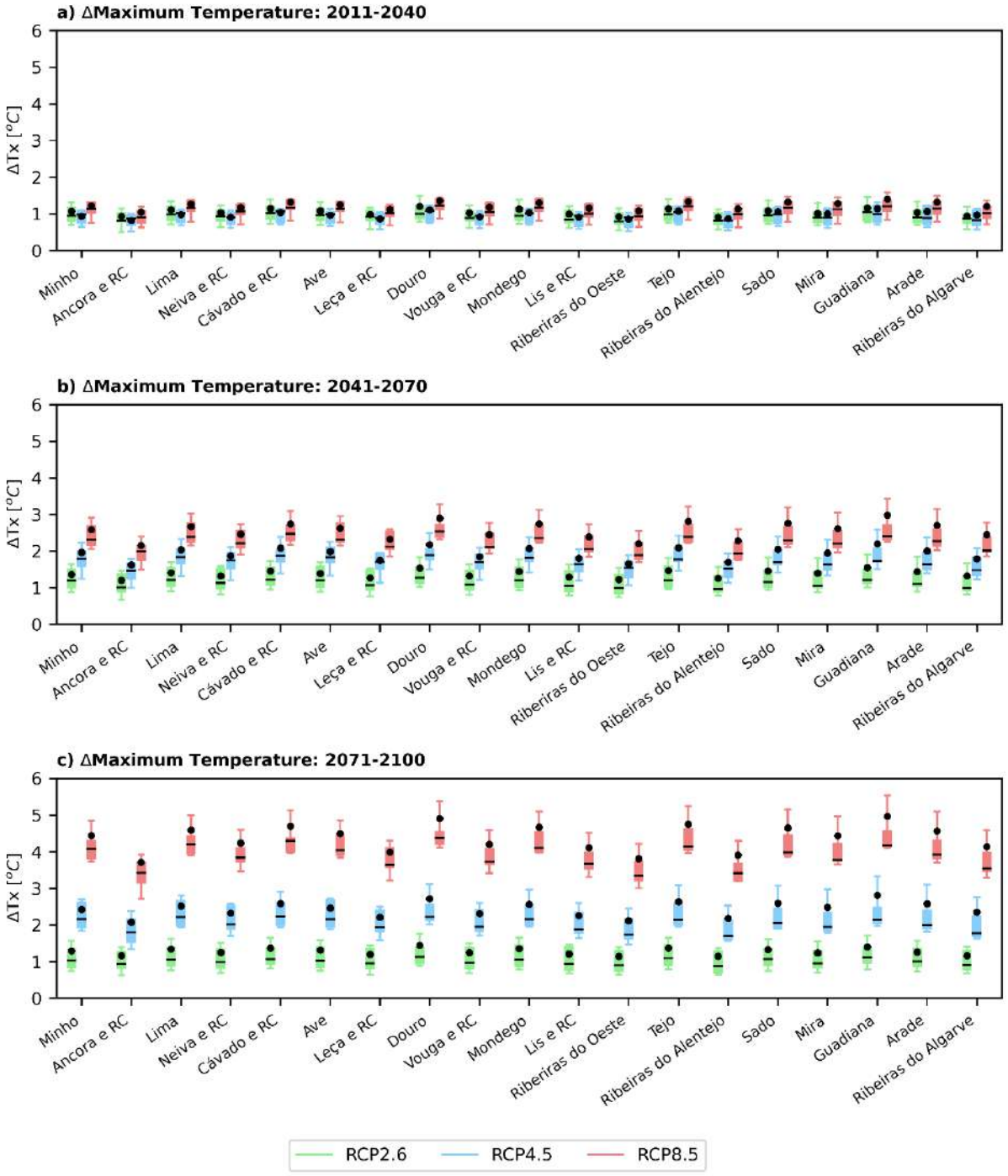

Figure 5.10 Future projected changes in daily maximum temperature averaged over the full year for the different basins. Three future periods are shown: a) 2011-2040, b) 2041-2070, and c) 2071-2100, under all emission scenarios – RCP2.6 (green), RCP4.5 (blue) and RCP8.5 (red). The black point represents the multi-model ensemble mean. The 1971-2000 period is used as reference.

Minimum Temperature

The projected changes for annual averaged daily minimum temperature (Figure 5.11) show similar patterns to the ones found for daily mean and maximum temperatures. This includes the west-to-east increasing anomaly gradients, the relatively homogeneous magnitude changes over the 2011-2040 period for all emission scenarios, ranging between +1.0 ºC and +2.0 ºC over most of Portugal, the increasing differences between scenarios throughout the twenty-first century, with the anomalies exceeding +4.0 ºC by 2071-2100 for RCP8.5 over most of continental Portugal, but remaining mostly below +2.0 ºC for RCP2.6. The maximum anomalies in minimum temperature are however circa 1 ºC lower than in maximum and mean temperatures.

As before, the seasonality of the daily minimum temperature (Figure 5.11) anomalies display maximum values during JJA and SON and minimum values during DJF and MAM. For both cases, the strongest JJA and SON daily minimum temperature anomalies under RCP8.5 scenario for the end-of-century period occur over north-eastern Portugal reaching magnitudes larger than +5.0 ºC. During winter and spring, the daily minimum temperature anomalies under RCP8.5 scenario for the end-of-century ranged between +3.0 ºC and +4.0 ºC over continental Portugal.

The results show small uncertainties associated with the projected daily minimum temperature (Figure 5.12) anomalies. Indeed, the sign of the anomalies agreed amongst more than 2/3 of the models in all cases, while the magnitude of the inter-model standard-deviation is mostly below 0.8ºC, with the exception of the anomalies for SON at mid- and end-of-century periods under scenario RCP8.5 where the standard deviation reached values up to around 1.0 ºC and 1.4 ºC, respectively.

Looking at the future projected changes in daily minimum temperature for the different NUTS II (Figure 5.13), NUTS III regions (Figure 5.14), and hydrographic basins (Figure 5.15), positive anomalies are projected over all regions under all emission scenarios – RCP2.6, RCP4.5 and RCP8.5, being stronger for higher emission scenarios, and amplifying throughout the twenty-first century, except for RCP2.6 where it stabilizes. As in mean and maximum temperature anomalies, the warming signal is generally weaker for coastal regions. For the end-century period, the 10^{th} to 90^{th} percentile inter-model spread represented by the boxplot whiskers is smaller than inter-scenario differences, providing confidence on the large impact of global GHG emissions to regional warming over Portugal. The absolute values of daily minimum temperature for the different NUTS and hydrological basins for all time periods and scenarios can be found in Supplementary Material as Figures A9-12.

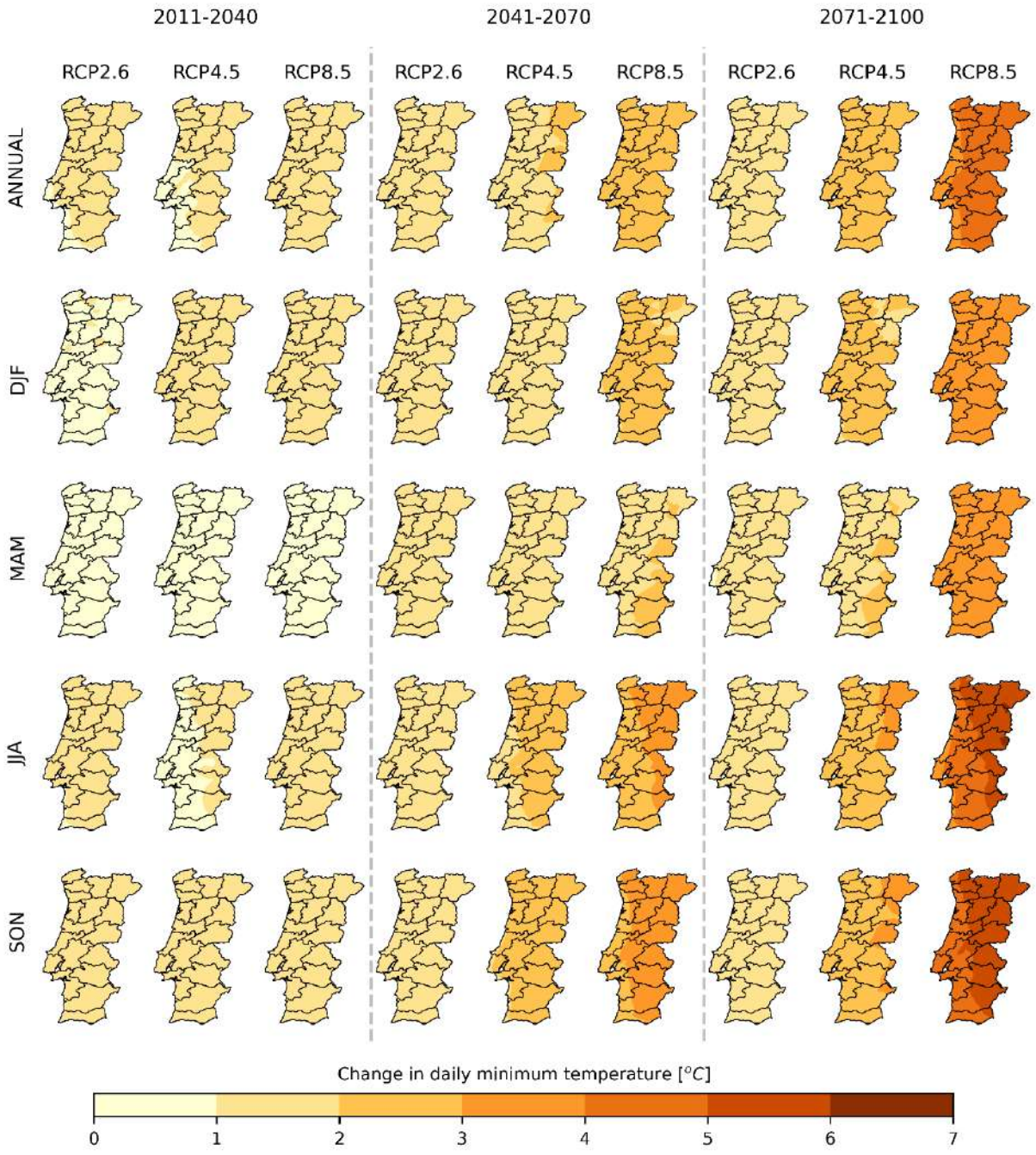

Figure 5.11 Future projected changes in daily minimum temperature over mainland Portugal, considering the 1971-2000 period as reference. The different rows from top to bottom represent averaged taken over all months, DJF, MAM, JJA and SON respectively. The different columns represent the future periods considering different GHG emission scenarios.

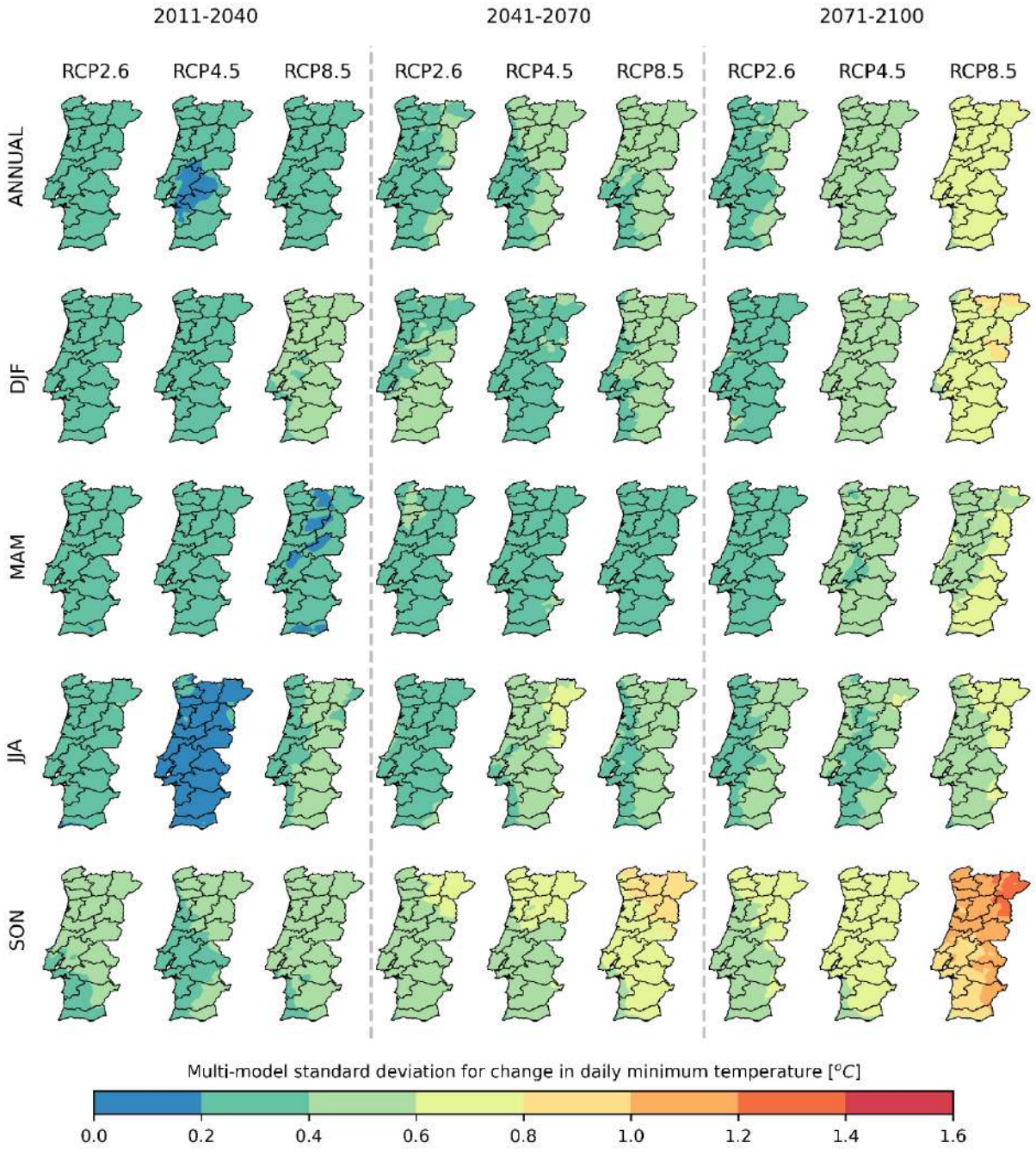

Figure 5.12 Multi-model spread in future projected changes in daily minimum temperature over mainland Portugal, considering the 1971-2000 period as reference. The spread is quantified by the standard deviation of the anomalies between different models. The different rows from top to bottom represent averaged taken over all months, DJF, MAM, JJA and SON respectively. The different columns represent the future periods considering different GHG emission scenarios. Grid-points where the temperature change signal does not agree in at least 66% of the models is identified by dotted hatching (no occurrences for Tn).

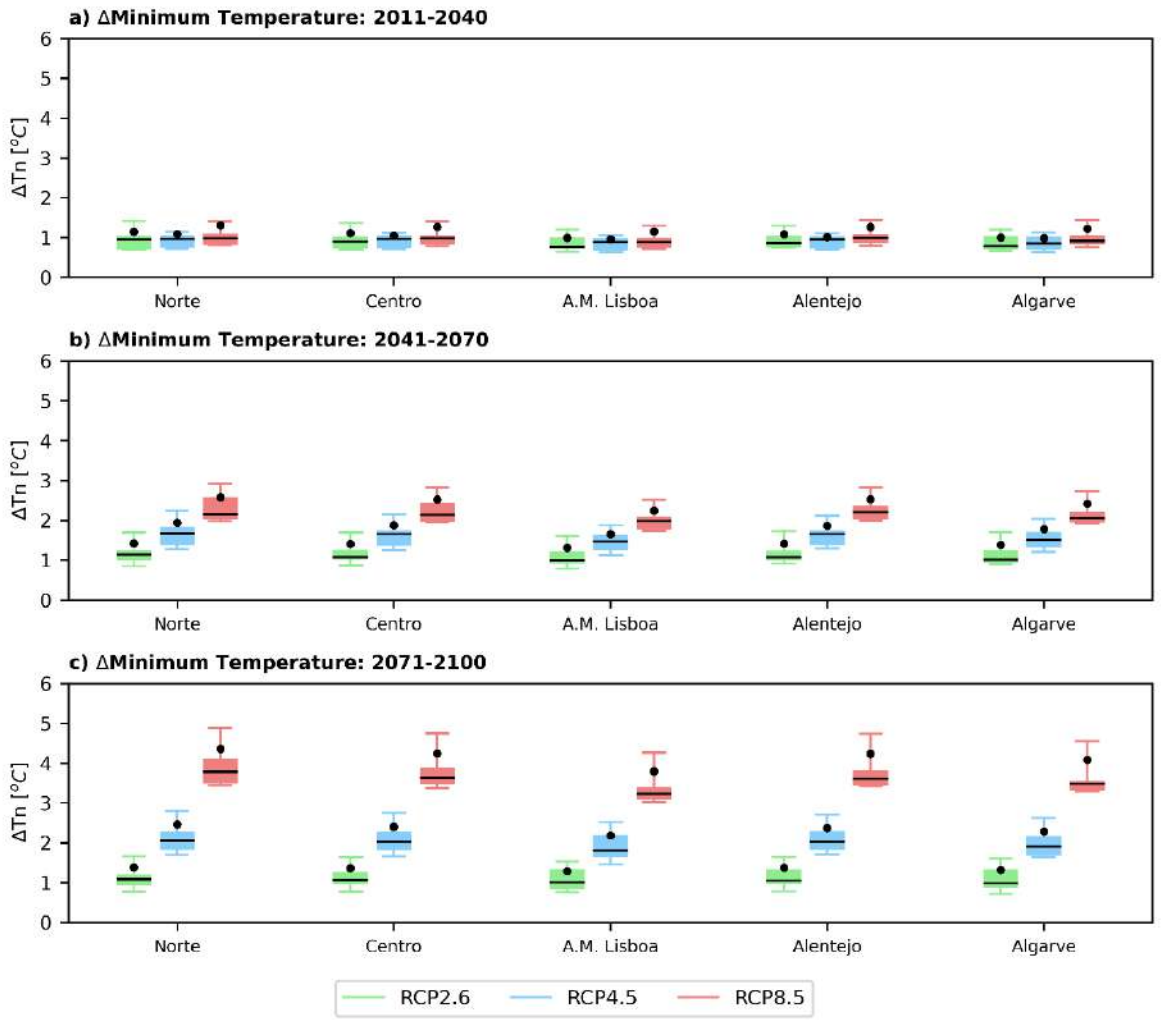

Figure 5.13 Future projected changes in daily minimum temperature averaged over the full year for the NUTS II region. Three future periods are shown: a) 2011-2040, b) 2041-2070, and c) 2071-2100, under all emission scenarios – RCP2.6 (green), RCP4.5 (blue) and RCP8.5 (red). The black point represents the multi-model ensemble mean. The 1971-2000 period is used as reference.

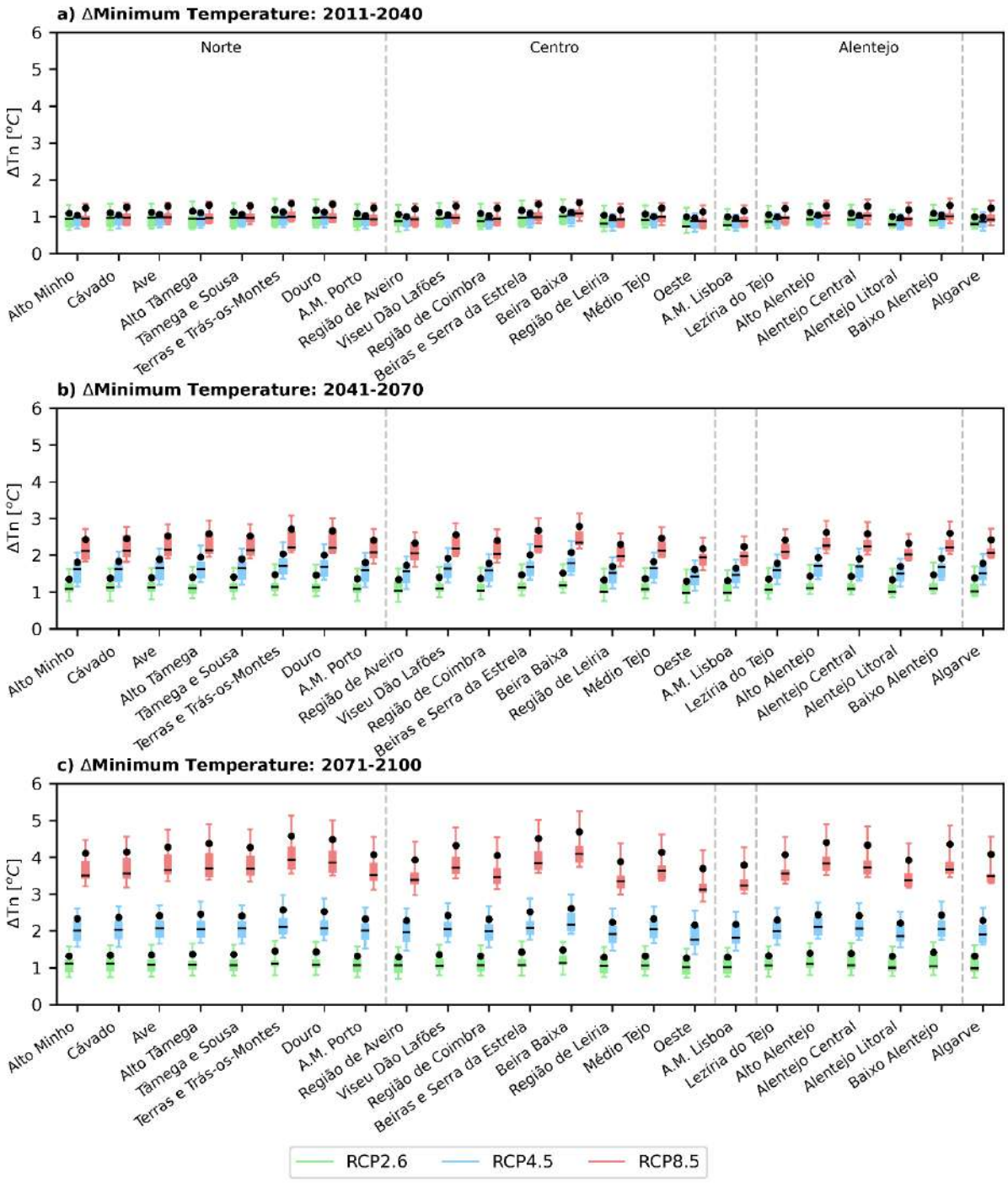

Figure 5.14 Future projected changes in daily minimum temperature averaged over the full year for the different NUTS III regions. Three future periods are shown: a) 2011-2040, b) 2041-2070, and c) 2071-2100, under all emission scenarios – RCP2.6 (green), RCP4.5 (blue) and RCP8.5 (red). The black point represents the multi-model ensemble mean. The 1971-2000 period is used as reference.

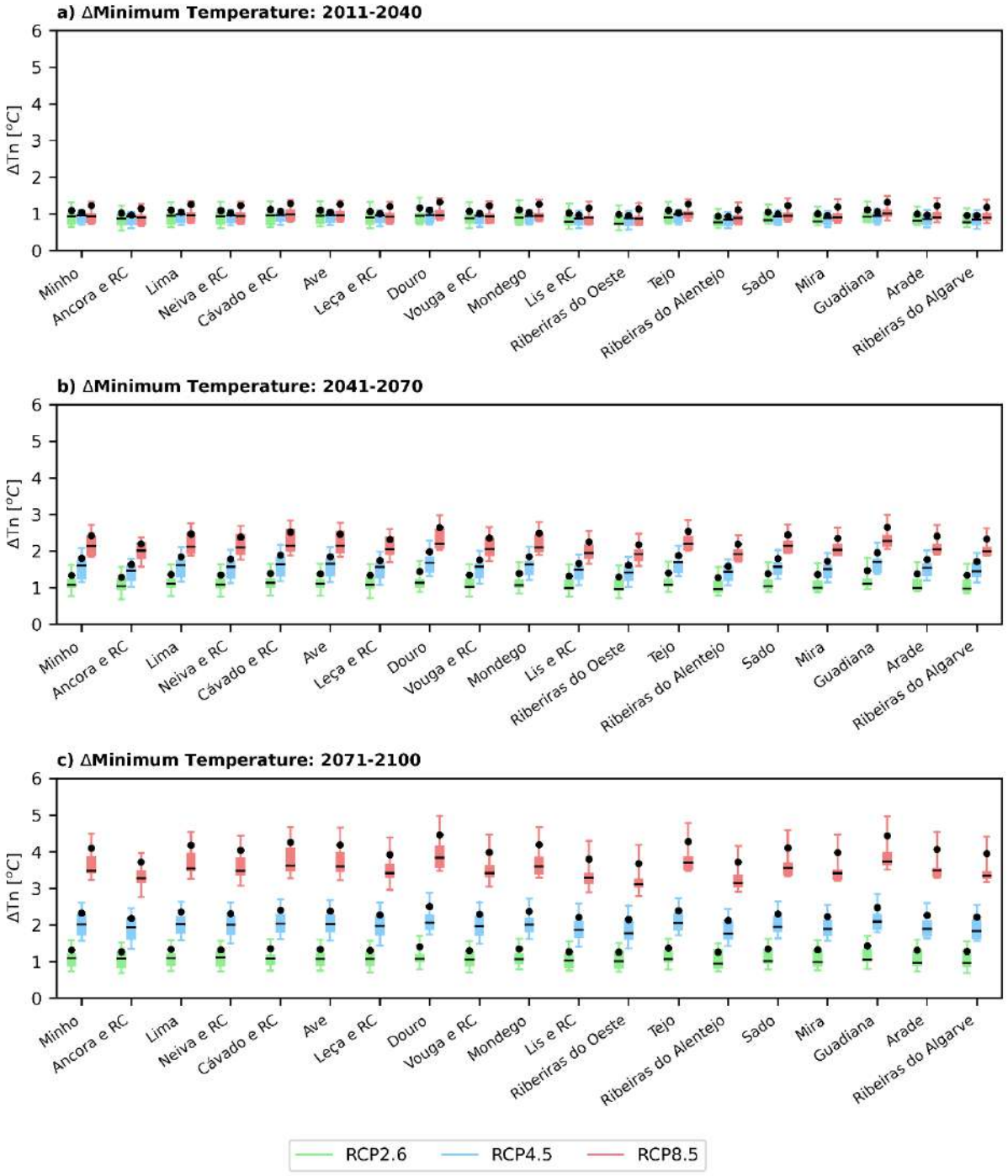

Figure 5.15 Future projected changes in daily minimum temperature averaged over the full year for the different basins. Three future periods are shown: a) 2011-2040, b) 2041-2070, and c) 2071-2100, under all emission scenarios – RCP2.6 (green), RCP4.5 (blue) and RCP8.5 (red). The black point represents the multi-model ensemble mean. The 1971-2000 period is used as reference.

Diurnal Temperature Range

The strong similarities in the climate change signal for both minimum and maximum temperatures envisage a weak change in the diurnal temperature range (DTR). In fact, DTR anomalies are considerably lower than the daily mean temperature (Figure 5.16). Indeed, the annual average DTR anomalies are below 0.25 ºC for the 2011-2040 and below 0.50 ºC for the 2041-2070 periods under all scenarios. Moreover, the coastal regions displayed a relatively small reduction (up to -0.5º) of the annual average DTR for all periods under RCP2.6 scenario, with increasing area of incidence for the end-of-century period. DTR reductions were also found for RCP4.5 and RCP8.5 coastal regions, particularly for the 2011-2040 period. The maximum annual average DTR anomalies were in the +0.50 ºC to +0.75 ºC, occurring over central Portugal for end-of-century under RCP8.5 scenario. The later indicate that as the century progresses, the maximum temperature increases at a faster rate than the minimum for both RCPs (4.5 and 8.5). Furthermore, it is worth noticing that the models mostly agree on the sign of the annual averaged DTR changes under all scenario over continental Portugal (Figure 5.17).

While DTR is weak from DJF to JJA in the first period for all RCPs, in SON anomalies from 0.25 ºC to 0.50 ºC are already projected (Figure 5.16). In mid-century, the anomalies in MAM, JJA and SON are similar. The maximum DTR anomaly between +1.0ºC and +1.25ºC emerges during MAM for end-of-century under RCP8.5 scenario over southern Alentejo. However, anomalies found during the four seasons were mostly of the same order as the multi-model standard-deviation (Figure 5.17), *i.e.*, circa 0.50 ºC. Furthermore, DTR change signal does not agree in at least 66% of the models over the entire mainland Portugal in DJF and MAM for RCP2.6 at the beginning of the century, and in MAM for RCP4.5 on the same period, which is surpassed when moving to mid- and end- of century, where the models agree for all grid-points.

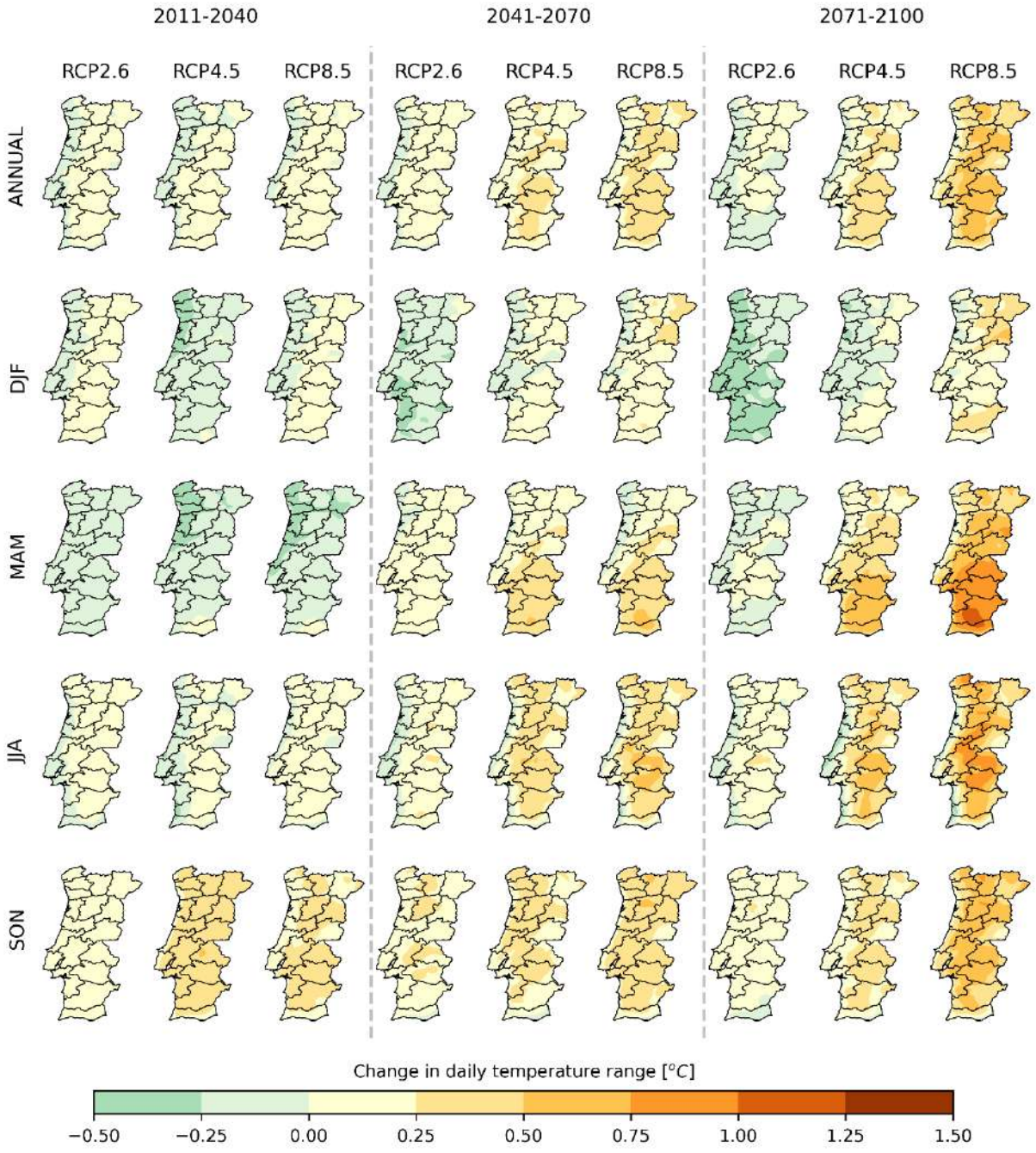

Figure 5.16 Future projected changes in daily temperature range over mainland Portugal, considering the 1971-2000 period as reference. The different rows from top to bottom represent averaged taken over all months, DJF, MAM, JJA and SON respectively. The different columns represent the future periods considering different GHG emission scenarios.

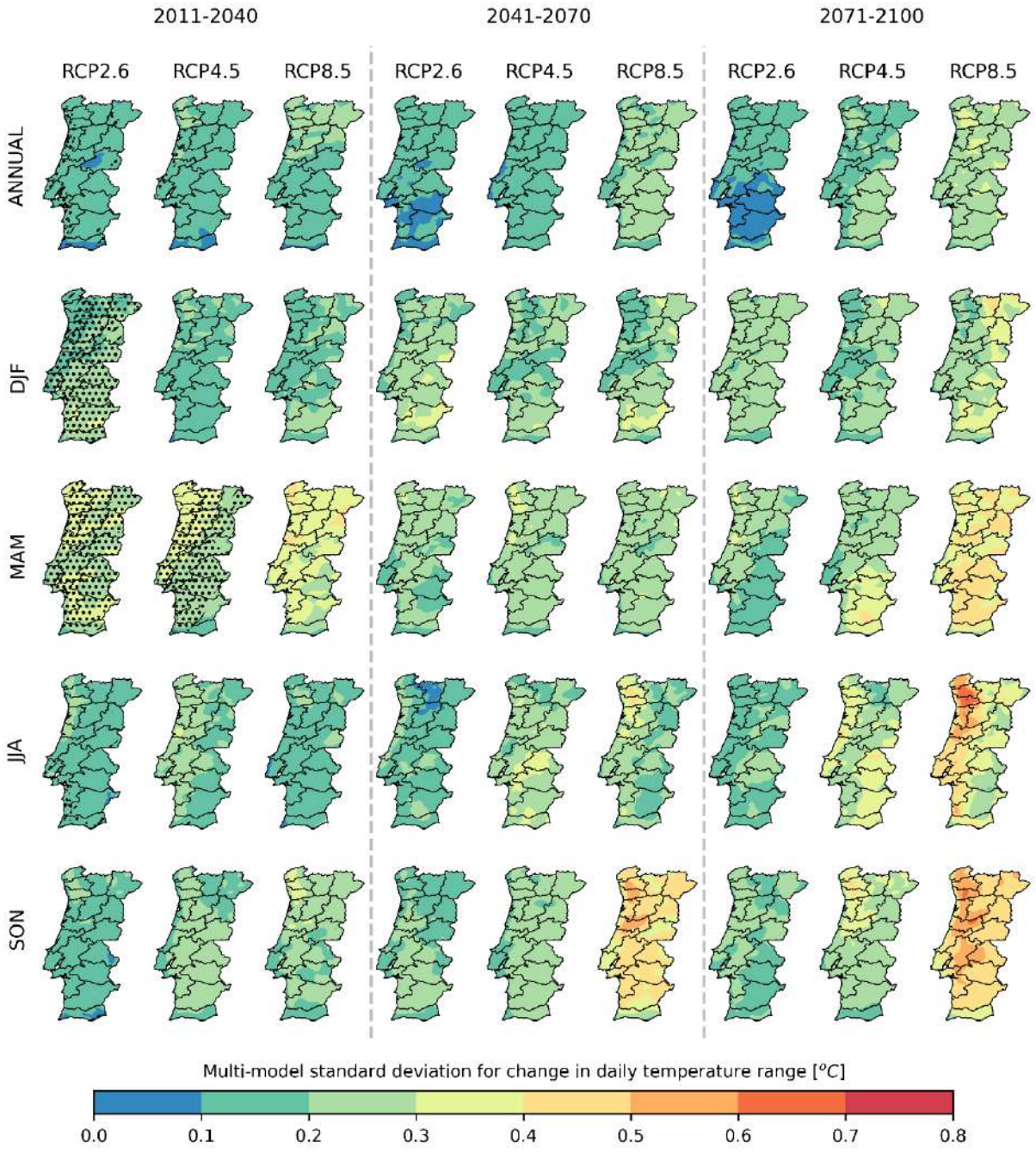

Figure 5.17 Multi-model spread in future projected changes in daily temperature range over mainland Portugal, considering the 1971-2000 period as reference. The spread is quantified by the standard deviation of the anomalies between different models. The different rows from top to bottom represent averaged taken over all months, DJF, MAM, JJA and SON respectively. The different columns represent the future periods considering different GHG emission scenarios. Grid-points where the daily temperature range change signal does not agree in at least 66% of the models is identified by dotted hatching.

5.2. Precipitation

The future projected changes (in %) associated to the mean total accumulated precipitation over mainland Portugal, both at annual and seasonal scales, are presented in Figure 5.18. Overall, the annual projections indicate a decrease in precipitation throughout the 21st century. Considering the 2011-2040 period, the projected changes are comparable between the three scenarios, ranging from -10% to +5%. For the mid-21st century (2041-2070), the projections indicate an amplification of the drying conditions, especially for the RCP4.5 and RCP8.5 scenarios, with negative changes for the entire country, down to -20% and -30%, respectively. While the projected decreases for RCP4.5 tend to stabilize towards the end of the 21st century (2071-2100), between -20% and -5%, the ones for RCP8.5 show a further aggravation, culminating in values down to -40% in southwestern Portugal. Figure A18 in the Supplementary Material shows that, for the 2071-2100 period under RCP8.5, the absolute projected changes for total annual precipitation in mainland Portugal, range between -150 mm and -250 mm, considering all the members from the EURO-CORDEX ensemble.

The seasonal projections for the mean total accumulated precipitation, in Figure 5.19, show distinct features throughout the year. In fact, wetted winters (DJF) are projected in most of mainland Portugal, considering RCP2.6 after 2041 (up to +30%), and for RCP4.5 before 2040 (but also visible for northern Portugal towards 2100; below +20%). During spring (MAM), the three scenarios agree on a projected increase in precipitation in northern Portugal during 2011-2040 (the RCP8.5 extends this projection to the central regions as well), followed by a widespread decrease towards the end of the 21st century for RCP4.5 and RCP8.5, peaking below -30% and -40%, respectively. Summer (JJA) and autumn (SON) seasons are marked by consistent projected decreases for all periods and scenarios, peaking below -50% for the RCP8.5 during summer.

The spread of the future projected changes, considering all the EURO-CORDEX ensemble members, is shown in Figure 5.19, as the multi-model standard deviation of the projected changes (in %). At the annual scale, the spreads are generally low (below 20%), except for the 2071-2100 period under the RCP8.5 scenario (between 15% and 35%). Seasonally, the spreads are higher during summer, possibly due to the lower total precipitation values, peaking for the RCP8.5, between 50% and 55%. Similarly, to the temperature (in Figure 5.2 and Figure 5.17), most ensemble members agree on the signal of the projected changes throughout all time periods, seasons, and scenarios. Exceptions are visible for the RCP2.6 scenario during 2011-2040, especially for the winter (DJF) and spring (MAM) seasons. Note that, for these instances, the expected changes in the mean total precipitation (in Figure 5.18) are mostly between -5% and +5%.

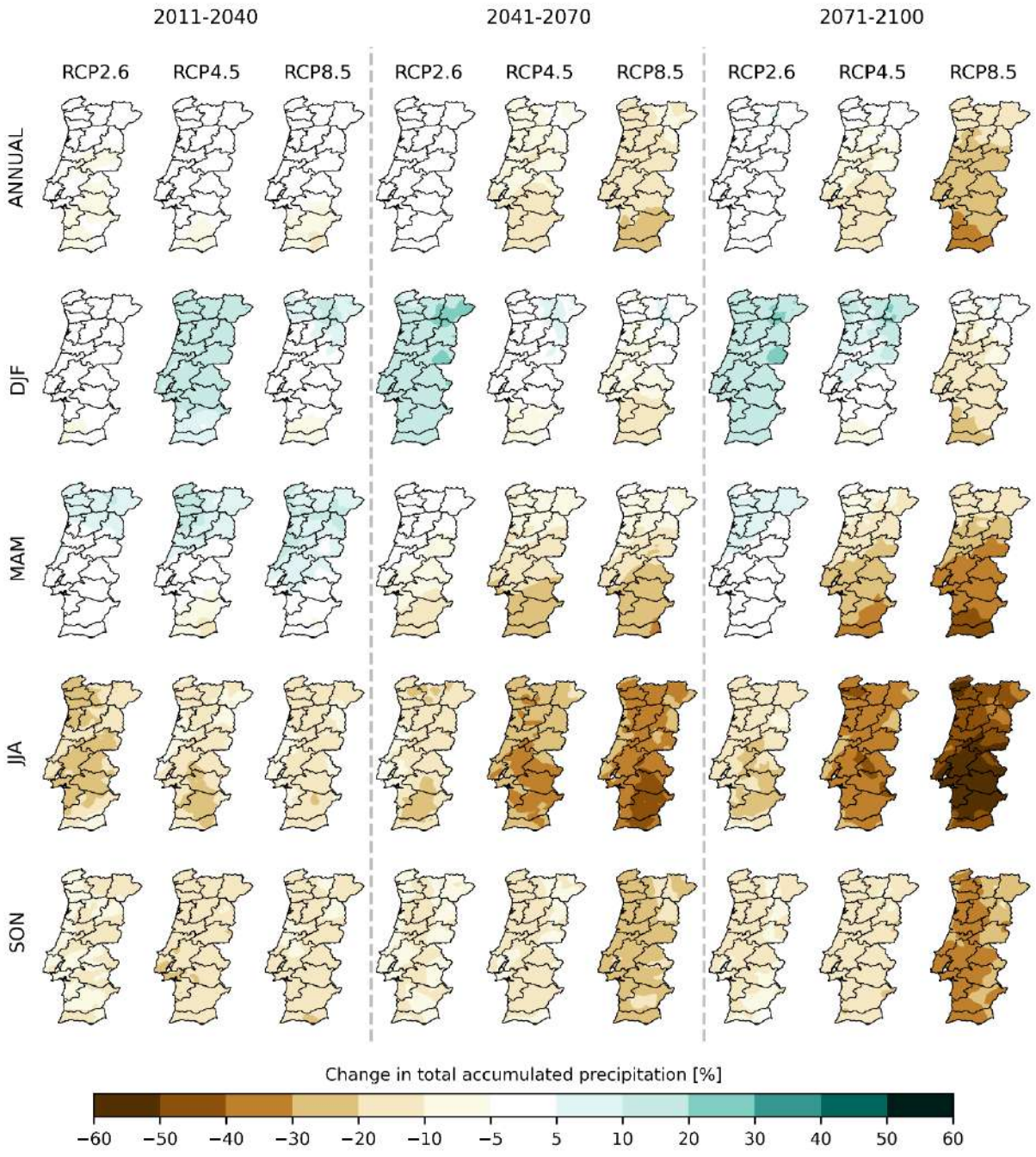

Figure 5.18 Future projected changes in total accumulated precipitation over mainland Portugal, given as percentual change considering the 1971-2000 period as reference. The different rows from top to bottom represent averaged taken over all months, DJF, MAM, JJA and SON respectively. The different columns represent the future periods considering different GHG emission scenarios.

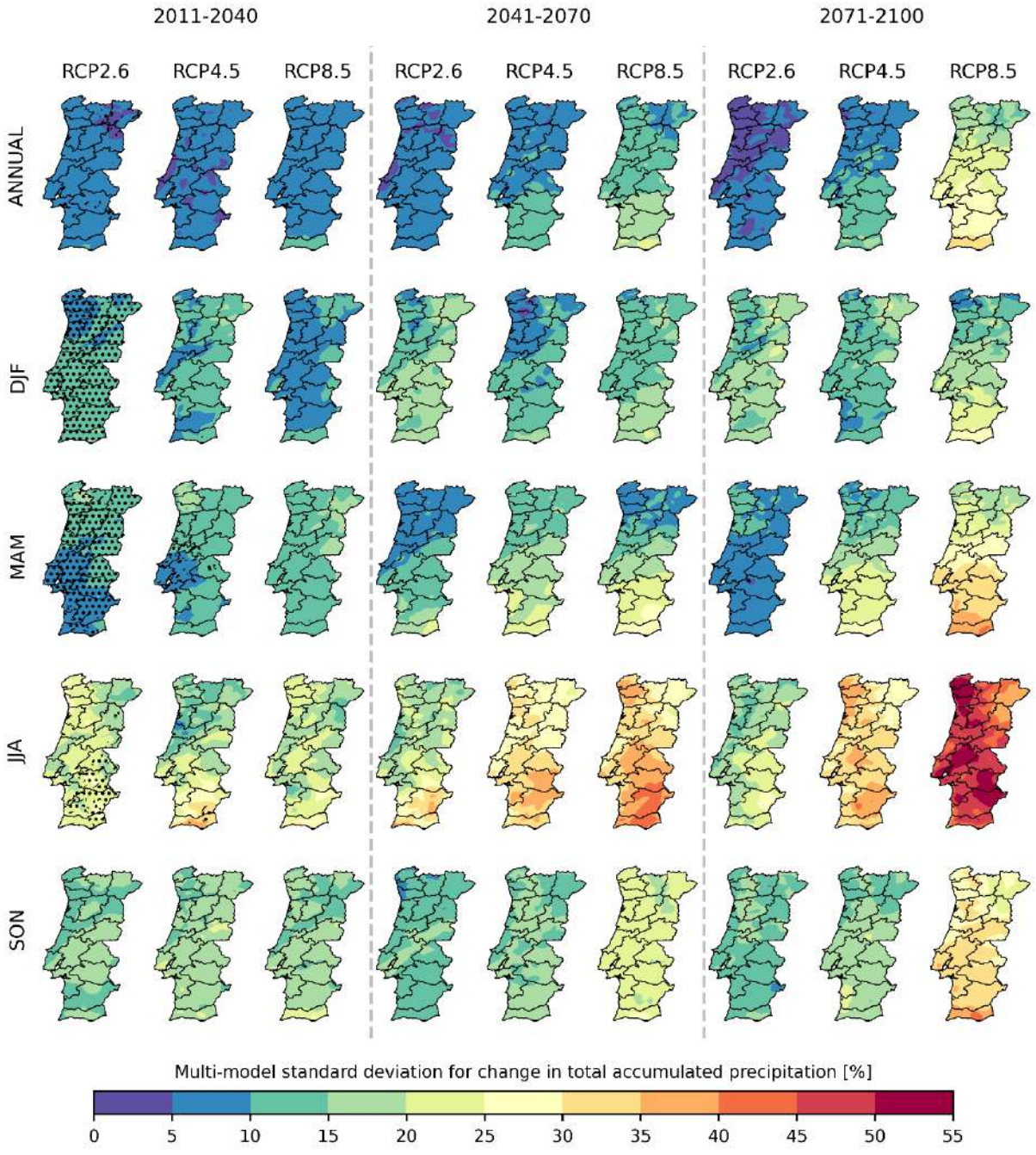

Figure 5.19 Multi-model spread in future projected changes total accumulated precipitation over mainland Portugal, given as percentual change considering the 1971-2000 period as reference. The spread is quantified by the standard deviation of the anomalies between different models. The different rows from top to bottom represent averaged taken over all months, DJF, MAM, JJA and SON respectively. The different columns represent the future periods considering different GHG emission scenarios. Grid-points where the precipitation change signal does not agree in at least 66% of the models are identified by dotted hatching.

The projected changes in the annual mean total accumulated precipitation (in %), considering the NUTS2 regions of mainland Portugal, are shown in Figure 5.20, for the three periods and scenarios analysed. The associated total accumulated values and the absolute projected changes (in mm) for each instance are presented in Figures A14 and A15 of the Supplementary Material. Overall, while the projections associated to the RCP2.6 scenario show a slight decrease in precipitation during 2011-2040, this pattern is reversed towards the end of the 21st century, with all the regions showing slight projected increases during 2071-2100 (below +5%). Note that these results are in agreement with Figure 5.18, falling within the range of the white-colour threshold. The RCP2.6 is an optimistic scenario which considers a reversal in the growing emissions trend between 2020 and 2040, being the net balance close to zero between 2080 and 2100. This is the only scenario considering projected increases in annual precipitation (on average, from all the EURO-CORDEX members) after 2040, which would result in an extra +20 mm to +50 mm per year from the Algarve to the Norte NUTS2 regions (Figure A15 in Supplementary Material).

Considering the RCP4.5, the projections indicate a decrease in precipitation for all regions after 2040 (the Norte and Centro regions are expected to experience a slight increase during 2011-2040, however below +5%; Figure 5.20). For the 2041-2070 period, the ensemble mean projected decreases range between -15% (Algarve and Alentejo regions) and -5% (Norte region). While such values are also, on average, representative of the 2071-2100 period, some members of the EURO-CORDEX ensemble show slightly worse drying conditions by the end of the 21st century, down to -20% (-15%) in the Algarve (Alentejo).

For the RCP8.5, the annual mean total accumulated precipitation is projected to decrease across the five NUTS2 regions, for the three future time-slices (except in the Norte region during 2011-2040; Figure 5.20). The projections associated to this scenario are more aggressive than the ones for the RCP4.5 (as previously shown in Figure 5.18), especially in southern Portugal. In fact, during 2041-2070, decreases of at least -10% are to be expected, and by 2071-2100, this value doubles to at least -20%. The Algarve is projected to be greatly affected under RCP8.5, for which the mean precipitation values are expected to be reduced in 25% (35%) during the 2041-2070 (2071-2100) period. Between the EURO-CORDEX ensemble members, projections of -35% (-40%) are observable. The Alentejo and A. M. Lisboa regions are also projected to be extensively affected under RCP8.5, showing however slightly lower percentual projected decreases, followed by the Centro and Norte regions. Note that if the absolute values are taken into consideration, the pattern is the opposite. Since the mean total accumulated precipitation is lower (higher) in the southern (northern) regions of mainland Portugal (Figure A14 in Supplementary Material), the absolute values of projected change are, in this case, also lower (higher) in the same regions. Figure A15 in Supplementary Material shows absolute projected decreases of approximately 300 mm in the Norte and Centro regions,

and between 150 mm and 200 mm in the A. M. Lisboa, Alentejo and Algarve regions, for the RCP8.5 scenario.

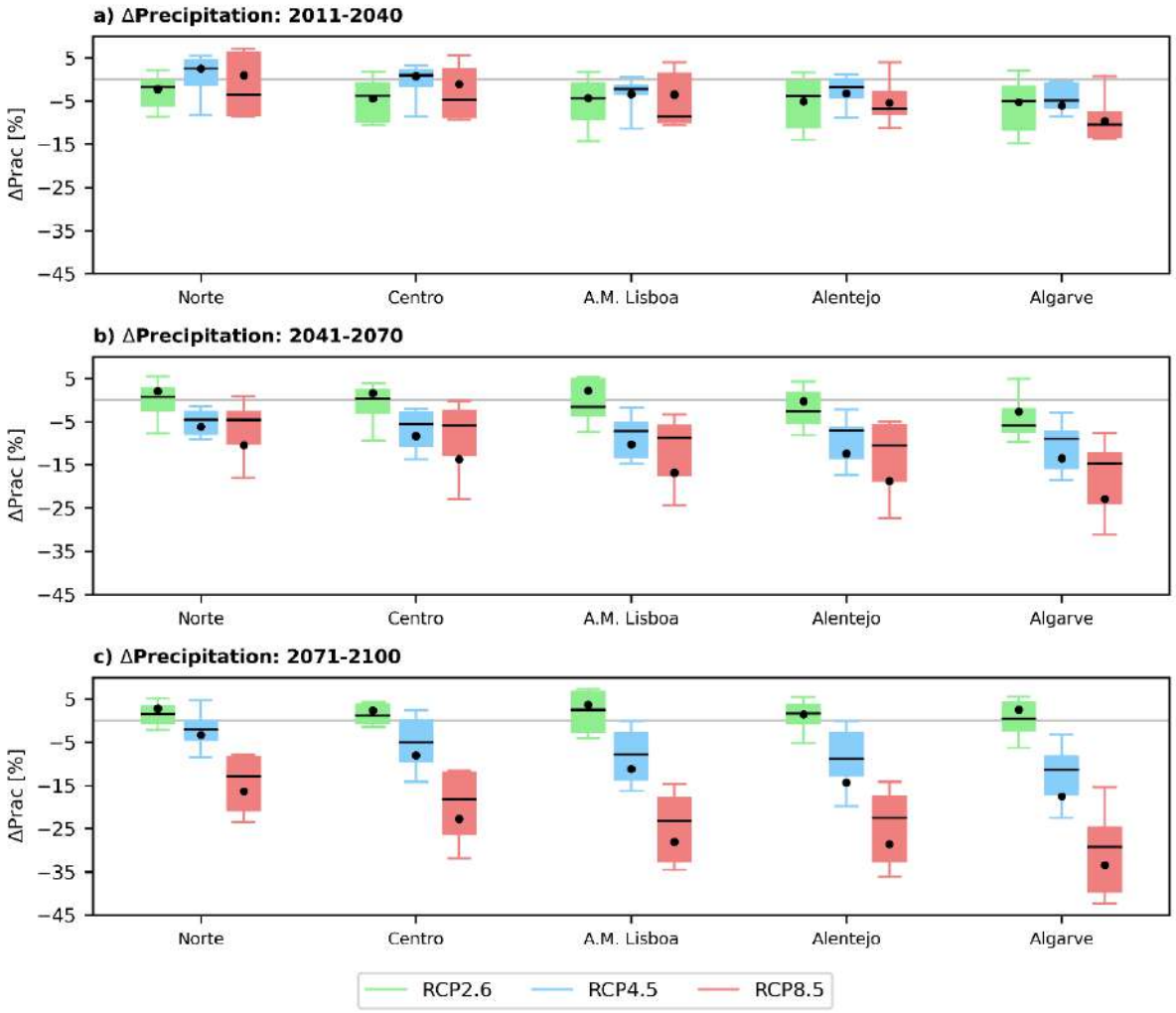

Figure 5.20 Future projected changes in yearly accumulated precipitation (in percentage) for the different NUTS II regions. Three future periods are shown: a) 2011-2040, b) 2041-2070, and c) 2071-2100, under all emission scenarios – RCP2.6 (green), RCP4.5 (blue) and RCP8.5 (red). The black point represents the multi-model ensemble mean. The 1971-2000 period is used as reference.

The projected changes in the annual mean total accumulated precipitation (in %), considering the NUTS3 regions of mainland Portugal, are shown in Figure 5.21, similar to Figure 5.20. The associated total accumulated values and the absolute projected changes (in mm) for each instance are presented in Figures A16 and A17 of the Supplementary Material. Generally, the patterns are similar to the ones regarding the major associated NUTS2 regions, with precipitation projected to become scarcer, especially after 2040, and considering the RCP8.5 scenario.

Inside the Norte NUTS2 region there are 8 sub-regions (NUTS3), from which the A. M. Porto and Tâmega e Sousa can be highlighted, due to the more aggressive drying (in %), projected to occur during 2071-2100 under RCP8.5, peaking, on average, slightly below -20%. The three northwesternmost sub-regions Alto Minho, Cávado and Ave, although projected to become relatively less dry than the aforementioned ones (between -15% and -20%), comprehend the greatest absolute expected changes in annual mean total precipitation (due to the higher mean accumulated values, surpassing 2000 mm per year; Figure A16 in Supplementary Material), of approximately -400 mm, with members of the EURO-CORDEX ensemble projecting changes as extreme as -700 mm (Figure A17 in Supplementary Material). The projections for the annual mean total accumulated precipitation in the main drainage basins of these sub-regions, in Figure 5.22 and Figures A18 and A19 in Supplementary Material are in agreement with the results from Figure 5.21 and Figures A16 and A17 in Supplementary Material, being the major projected losses in precipitation observed for the Lima River basin, of approximately -20% (-450 mm) in Figure 5.22 (Figure A19 in Supplementary Material).

Moving south, the overall annual mean total accumulated precipitation along the 8 NUTS3 sub-regions of the NUTS2 Centro region tends to decrease, however, the impact of climate change on its values tends to increase, especially considering the RCP4.5 and RCP8.5 scenarios. The Região de Coimbra, Beira Baixa, Região de Leiria, Médio Tejo and Oeste sub-regions show projected decreases of approximately -10% (-25%) for the RCP4.5 (RCP8.5) during 2071-2100 (Figure 5.21), corresponding to absolute changes of between -100 mm and -150 mm (-200 mm and -300 mm; Figure A17 in Supplementary Material). Across the drainage basins associated to these sub-regions, the ones projected to become more affected by the drying conditions are the Lis e RC, Ribeiras do Oeste and Tejo ones, for which the projections are similar to the aforementioned ones (Figure 5.22 and Figure A19 in Supplementary Material).

Inside the Alentejo NUTS2 region there are 5 NUTS3 sub-regions showing similar projected changes in the annual mean total accumulated precipitation, in comparison with the main region, in Figure 5.21. Between the sub-regions, the Alentejo Litoral and Baixo Alentejo show, on average, the greatest projected decreases in precipitation, which are visible for all scenarios and time-slices, but peaking at approximately -30% during 2071-2100, under RCP8.5. Note that these sub-regions' annual mean total precipitation ranges, historically, between 500 mm and 600 mm (Figure A16 in Supplementary Material), and therefore, the associated absolute expected differences range between -150 mm and -200 mm.

In the Algarve region (the same for NUTS2 and NUTS3), three drainage basins are found: Guadiana, Arade and Ribeiras do Algarve (Figure 5.22 and Figures A18 and A19 in Supplementary Material). While in the Guadiana basin the projected change in the annual mean total precipitation for the 2071-2100 period under RCP4.5 (RCP8.5) is just slightly below -15% (-25%), for the remaining, values down to -20% (-35%) are

projected. When analyzing the EURO-CORDEX ensemble, for the Arade and Ribeiras do Algarve basins, precipitation reductions of over 20% (40%) are found for some members Figure 5.22), corresponding to the most drastic projections for all the drainage basins over mainland Portugal.

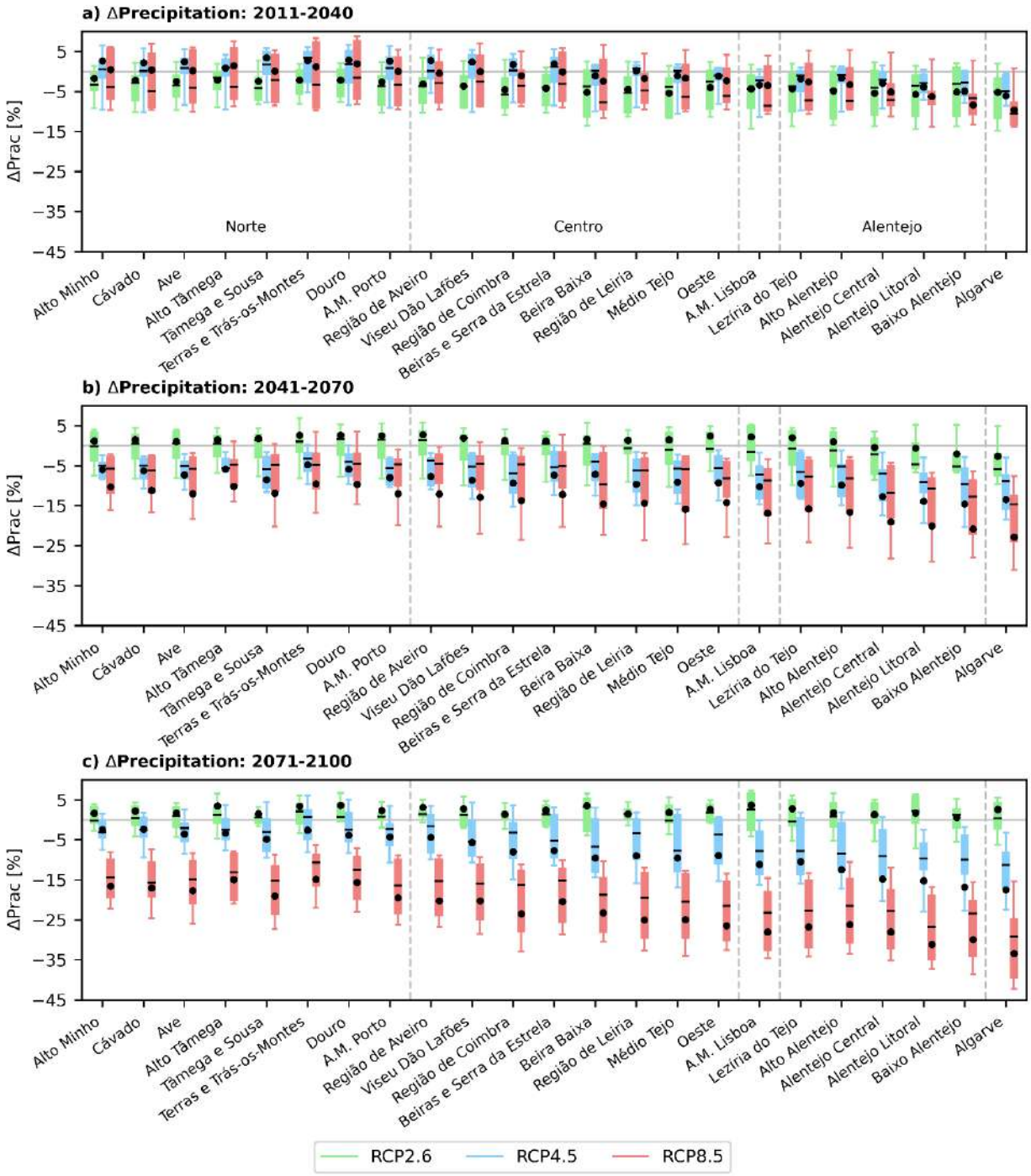

Figure 5.21 Future projected changes in yearly accumulated precipitation (in percentage) for the different NUTS III regions. Three future periods are shown: a) 2011-2040, b) 2041-2070, and c) 2071-2100, under all

emission scenarios – RCP2.6 (green), RCP4.5 (blue) and RCP8.5 (red). The black point represents the multi-model ensemble mean. The 1971-2000 period is used as reference.

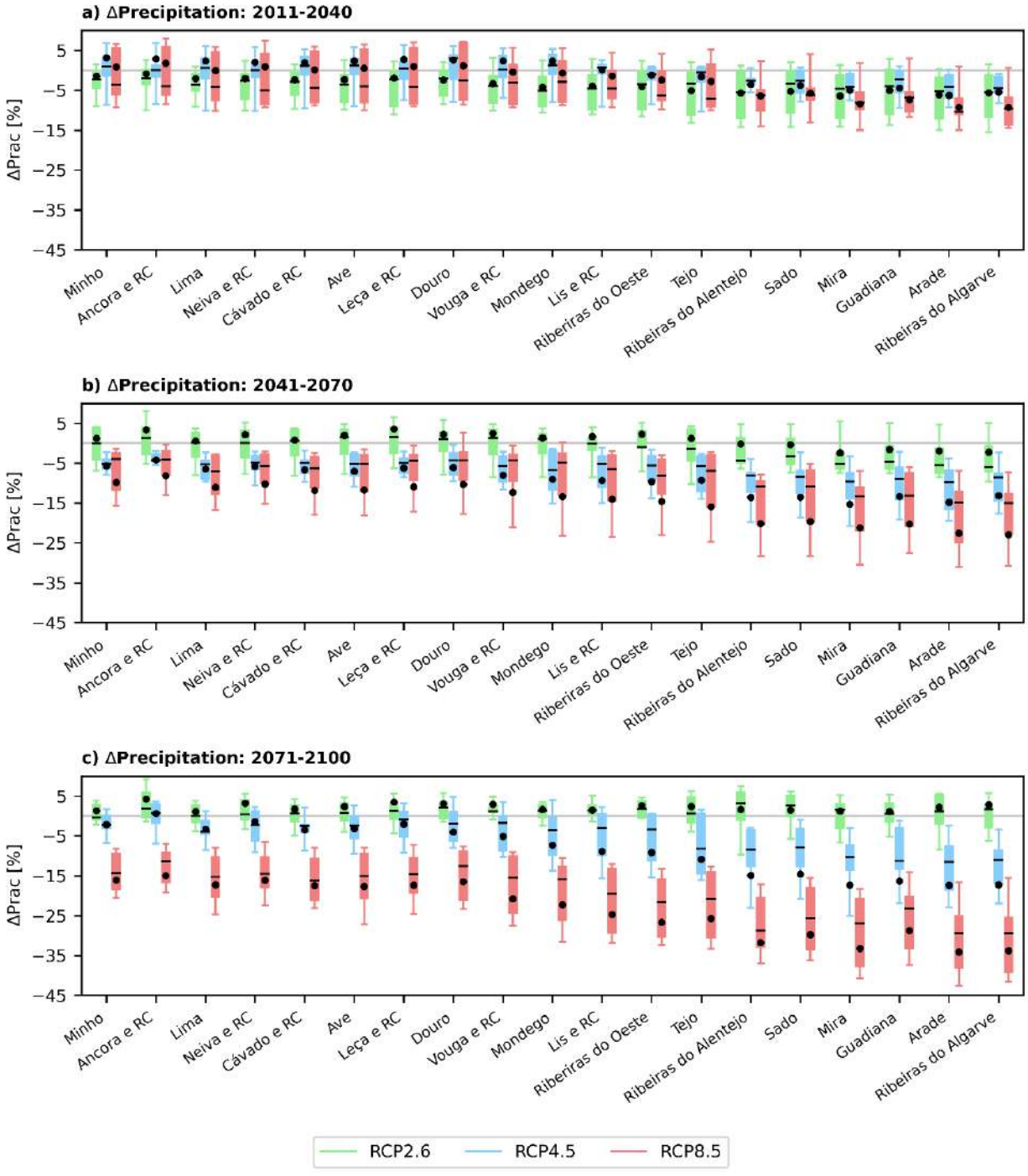

Figure 5.22 Future projected changes in yearly accumulated precipitation (in percentage) for the different basins. Three future periods are shown: a) 2011-2040, b) 2041-2070, and c) 2071-2100, under all emission scenarios – RCP2.6 (green), RCP4.5 (blue) and RCP8.5 (red). The black point represents the multi-model ensemble mean. The 1971-2000 period is used as reference.

5.3. Wind

The EURO-CORDEX multi-model ensemble future projections for mean wind speed at 10 m shows very small changes throughout all seasons (Figure 5.23). It can be observed that the largest changes are found during winter and autumn for end-of-century under RCP8.5 scenario with a decrease in wind speed that reaches -0.6 m/s. During summer, an increase in 10-m wind speed is found over the A.M. Lisboa for the begin-of-century, increase in intensity for end-of-century under both RCP4.5 and RCP8.5 scenarios, reaching +0.4 m/s. Also, over Alentejo region an increase in 10-m wind speed is also observed under RCP8.5 for mid and end-of-century, and under RCP4.5 for end-of-century. Under RCP2.6, most of future projections of wind speed at 10 m are closer to zero, except for the autumn season where a small decrease is found over Portugal for the mid- and end-of-century (-0.2 m/s). The inter-model spread for these results is small in all cases, and lack of agreement in the signal of the anomalies for begin-of-century period under RCP2.6 is merely a reflection of the near-zero magnitude changes (Figure 5.24).

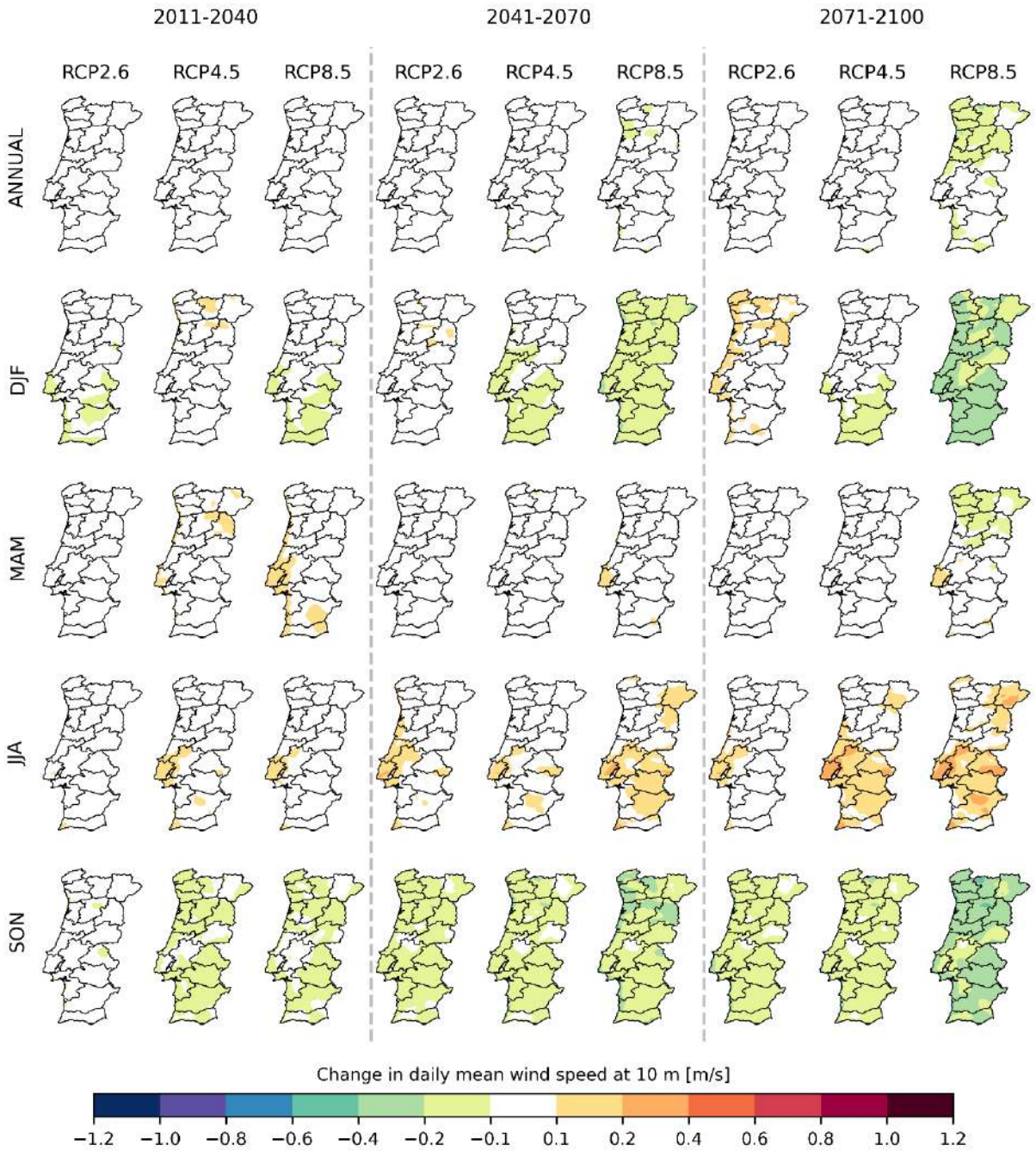

Figure 5.23 Future projected changes in daily mean wind speed at 10m over mainland Portugal, considering the 1971-2000 period as reference. The different rows from top to bottom represent averaged taken over all months, DJF, MAM, JJA and SON respectively. The different columns represent the future periods considering different GHG emission scenarios.

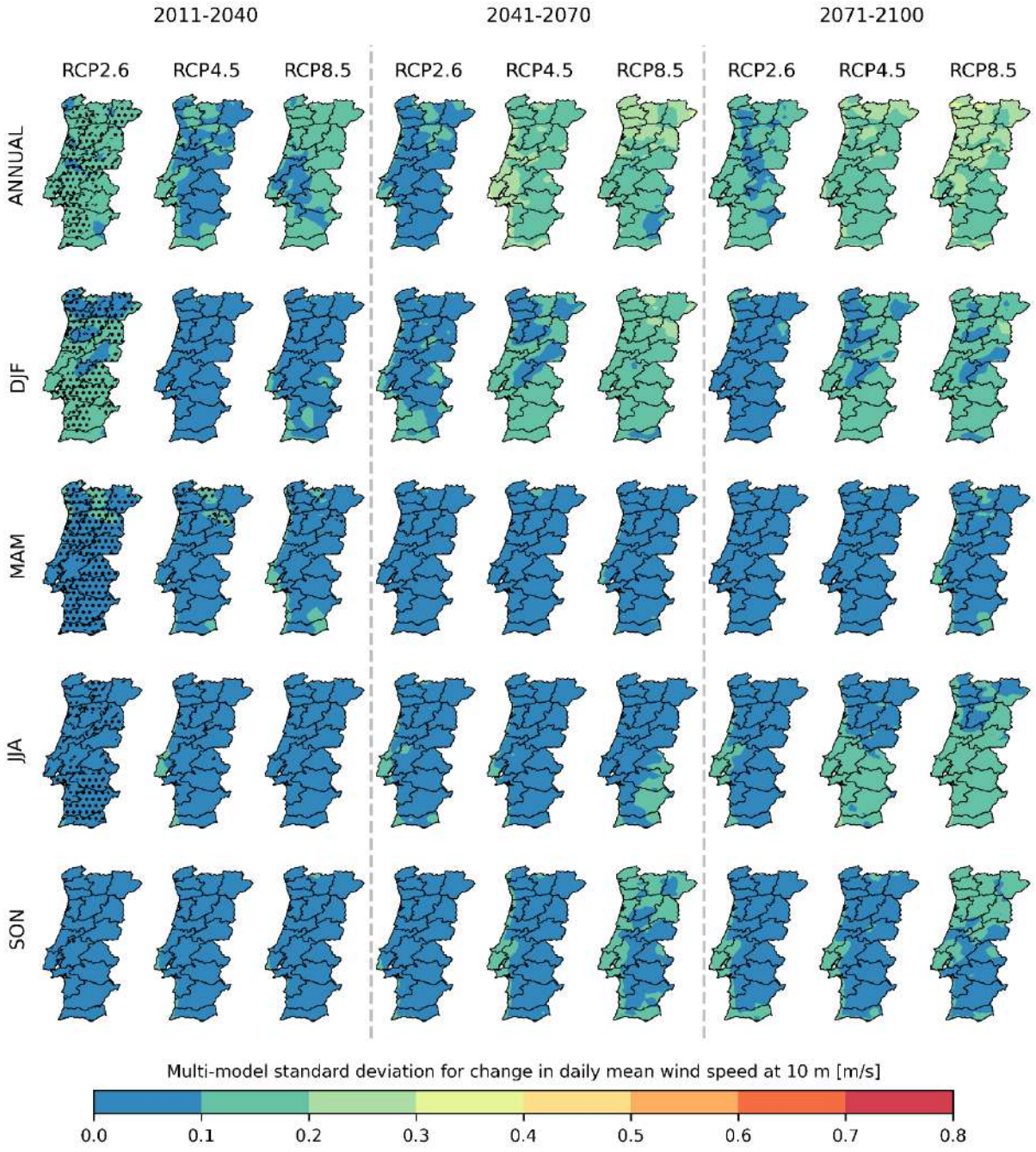

Figure 5.24 Multi-model spread in future projected changes in daily mean wind speed at 10 m over mainland Portugal, considering the 1971-2000 period as reference. The spread is quantified by the standard deviation of the anomalies between different models. The different rows from top to bottom represent averaged taken over all months, DJF, MAM, JJA and SON respectively. The different columns represent the future periods considering different GHG emission scenarios. Grid-points where the wind speed change signal does not agree in at least 66% of the models is identified by dotted hatching.

6. Climate Extremes

In the following three subsections several indices regarding temperature extremes (heat and cold), precipitation extremes, and wind speed are described. To ease readability the figures are organized in similar fashion, where each one is divided in three panels identified with the letters (a) – (c). The first panel, denoted (a), describes the annual climatological average of a given index over continental Portugal, where maps for the historical, and the three future periods and emissions are displayed. The middle panel, denoted (b), presents the climatological anomaly of that index, *i.e.*, the difference of the different future periods and scenarios against the historical. Finally, in the last panel, (c), the multi-model standard deviation for the change in the index is shown. Following previous sections, grid-points where the change signal does not agree in at least 66% of the models is identified by dotted hatching.

6.1. Temperature Extremes

Heat Extremes

Summer days (number of days per year where daily maximum temperature exceeds 25 ºC) are displayed in Figure 6.1. The historical period shows a north-south increasing gradient of summer days in continental Portugal, ranging between about 40 – 100 days per year in the first region, and 100 – 140 in the latter (Figure 6.1a). For future scenarios, the patterns remain somehow similar. However, it is worth noticing that for the end of the century assuming the worst-case scenario, the entire country shows more than 100 summer days, with regions in the south presenting numbers close to 200 (more than 6.5 months). The anomalies of the future scenarios against the historical period further stress this point (Figure 6.1b). However, these also bring forward the larger increase of summer days in the coastal regions. Indeed, starting in the mid-century (RCP4.5 and RCP8.5), and stretching to the end of the century (all RCPs), stronger anomalies are noticeable in the western coastal land regions. However, it is also worth noticing that these regions also present the largest standard deviations (Figure 6.1c). The larger uncertainty in the coastal areas notwithstanding, at least 66 % of the models agree in the change signal for all grid-points, periods, and scenarios.

Hot days (number of days per year where daily maximum temperature exceeds 30ºC), in Figure 6.2, show similar patterns to those from summer days, showing a north-south increasing gradient of hot days, here ranging in the historical period between 0 – 40 days per year in northern regions, and 60 – 100 days in the southern to south-eastern regions (Figure 6.2a). For the end of the century assuming the worst-case scenario, the entire country shows more than 60 hot days per year, with regions in the south-eastern presenting numbers close to 160. Contrariwise to summer days, there are no conspicuous anomalies in the coastal regions of Portugal (Figure 6.2b). In this case, anomalies tend to be higher towards interior regions of the country, varying between 10 – 20 days in the 2011 – 2040 period; 20 – 30 and 30 – 40 days for mid-century

RCP2.6/RCP4.5 and RCP8.5, respectively; and 10 – 20, 30 – 40, 60 – 70 days for RCP2.6, RCP4.5, and RCP8.5, respectively, at the end of the century. In this case, the largest standard deviations are mainly found in the northern regions. Indeed, the largest standard deviations (close to 20 days) in RCP8.5 at the end of the century are not in the regions with larger anomalies (Figure 6.2c). Nonetheless, at least 66 % of the models agree in the change signal for all grid-points, periods, and scenarios.

Very hot days (number of days per year where daily maximum temperature exceeds 35ºC) are presented in Figure 6.3. Here, the historical period shows a south-eastern cluster of very hot days in continental Portugal, ranging between about 10 – 40 days, whereas the remaining territory is mainly defined by 0 – 10 very hot days per year (Figure 6.3a). For future scenarios, there is a gradual extension of this cluster to north and to the coast. For the end of the century assuming the worst-case scenario, the southeaster cluster presents near to 100 very hot days, and the remaining country will experience more than 30 days, except for the coastal regions, which remain within 0 – 20 days. The anomalies referent to the historical period (Figure 6.3b) clearly shows this stretch of the southeaster cluster to the rest of the country, with anomalies of 10 – 20 days in that region in the beginning of the century (all RCPs), and for mid-century with RCP2.6. In this period, RCP4.5 and RCP8.5 start to show the stretch of the anomalies to north and coastal regions, reaching anomalies of circa 40 days in the worst emission case. Finally, at the end of the century anomalies strongly vary depending on the RCP: 0 – 20 days for RCP2.6, 0 – 40 days for RCP4.5, and 20 – 70 days for RCP8.5 (with coastal regions showing lighter anomalies of 10 – 20 days). As with hot days, the largest standard deviations (close to 20 days) are in the northeaster region of Portugal, not coinciding with the larger anomalies (Figure 6.3c). At least 66 % of the models agree in the change signal for all grid-points, periods, and scenarios.

Consecutive very hot days (maximum number of consecutive days per year where daily maximum temperature exceeds 35ºC) is shown in Figure 6.4. Results presented for this index are very similar to those concerning very hot days. The main differences being a slight decrease in the number of days (Figure 6.4a), a lower extension of the anomalies to coastal regions (Figure 6.4b), and in this case higher standard deviations in regions where the anomalies are greater (Figure 6.4c). At least 66 % of the models agree in the change signal for all grid-points, periods, and scenarios.

Heatwaves, characterized by the number of occurrences per year with a minimum of 5 consecutive days in heatwave, the average duration, and the maximum duration of the events are shown in Figure 6.5, Figure 6.6 and Figure 6.7, respectively, considering the entire year. In the historical period, the number of heatwaves per year vary between 1 and 2 over mainland Portugal (Figure 6.5). The average duration of these events varies between 6 and 7 days over the entire country (Figure 6.6), whilst the maximum duration of a heatwave in the historical period can reach 20 days (Figure 6.7). For all the scenarios and future periods,

the rise in the number of heatwaves is larger near the Spanish border than near the coast (Figure 6.5). For the beginning of the century, all RCPs project 3 to 5 events near the coast and 4 to 6 in the remaining regions. For the middle of century, the west-east gradient in the average number of heatwaves increases for 4 to 6 in RCP2.6, 5 to 8 in RCP4.5, and 6 to 10 in RCP8.5. For the end of the century and assuming the worst-case scenario, the average number of heatwaves can reach 15 events per year. The average duration of heatwaves increases considerably near the Spanish border, reaching an average of 12 days per event in RCP8.5 for the end-of-century. The areas near the coast have smaller rises with a projection of average duration of 9 days per heatwave. For RCP2.6 and RCP4.5, there is not a marked west-east gradient but still increases of 1 to 2 days in average duration of heatwaves can be expected. Looking into the future projections of the maximum duration of a heatwave, a significant increase is expected. For the end-of-century and assuming the worst-case scenario, the maximum duration of a heatwave can reach two months. Although in the other two RCPs the increase is smaller, the projections show a maximum duration that can reach one months. At least 66% of the models agree in the change signal for all grid-points, periods, and scenarios, showing high consistency between the ensemble members. Figure 6.8, Figure 6.9 and Figure 6.10 display the same as shown in Figure 6.5, Figure 6.6 and Figure 6.7 but considering only the distribution between March and November, removing the winter season.

Looking to the results, the increase in the frequency of occurrence of heatwaves occurs not only during the warmest months but also during winter season due to the increase of maximum temperature projected. In the historical period, the average number of heatwaves per year fluctuates between 1 and 2 over continental Portugal (Figure 6.8). For all the scenarios and future periods, the rise in the number of heatwaves is larger in the interior than near the coast. For all heatwaves and at the beginning of the century, all RCPs project 2 to 3 events near the coast and 3 to 4 in the remaining regions. Additionally, in some localised regions near the border, 4 to 5 heatwaves are projected in RCP8.5. The west-east gradient increases for the middle of the century, and as expected, the escalation in GHGs corresponds to a steeper gradient. For the end of the century, the GHG reduction from 2020 onwards in RCP2.6 leads to a scenario like the beginning of the century. In RCP4.5, 5 to 6 heatwaves are projected for the middle of the century near the Spanish border. At the end of the century, the tapering of emissions from mid-century onwards still implies an increase of one heatwave relative to mid-century. In the worst-case scenario (RCP8.5), the average number of heatwaves is projected to become between 9 and 11 for most of the country, reaching 12 events per year in a small area in the south. The average length of heatwaves is 6 to 7 days within the historical period and increases considerably near the Spanish border, reaching an average of 13 days per event in RCP8.5 for the end-of-century. As before, a west-east gradient is observable, whereby the areas near the coast have smaller rises with an average duration of 8 to 10 days per heatwave (Figure 6.9). For RCP2.6 and RCP4.5, there is not such a marked west-east gradient but still increases of 1 to 2 days in the average duration of heatwaves

can be expected. Looking at the future projections of the maximum duration of a heatwave, a significant increase is expected for RCP8.5 where the maximum duration of a heatwave can reach more than two months in the northeast (Figure 6.10). Although in the other two RCPs the increase is smaller, the projections show a maximum duration that can surpass one month. The multi-model spread in future projected heatwaves, considering the 1971-2000 period as a reference, is quantified by the standard deviation of the anomalies between different models. The standard deviation is always lower than the change signal and at least 66 % of the models agree with the change signal for all grid-points, periods, and scenarios, which shows high consistency between the ensemble members and low uncertainty in the projections.

The cumulative distribution of the length of the events for the entire country (Figure 6.11a) shows that, for both percentile thresholds (90 and 95th), 60% of heatwaves in the historical period last between 5 to 6 days, with 90% of heatwaves persisting for less than 7 days and with a maximum length of less than 20 days. In RCP2.6 the median length is circa 6 days for the three time slots (2011-2040, 2041-2070, 2071-2100), but even the small increase in GHGs leads to an expansion of the maximum temperature probability distribution function's tail and now 90% of the events have less than 11 days (an increase in the duration of 5 days). For the very extreme events, where the maximum temperatures are above the 95th percentile, there is no change in the median, but 90% of these events last less than 9 days at the beginning and end of the century and 10 days at mid-century. In RCP4.5, for the mid and late 21st century, 50% of heatwaves last one more day than in the historical period and 90% are also five days longer (12 days). At the end of the century, for RCP8.5, the number of the shortest heatwaves (5 and 6 days) are half of the historical and the median length is now close to 8 days. Now 40% of heatwaves (from the median to P_{90}) endure between 9 and 17 days, with the very extreme events where temperatures are consecutively above the 95th percentile, persevering between 8 and 15 days. The median of the mean severity (average of the daily severity during each heatwave) is 1.15, with 29% of events with low severity ($S_m < 1$) (Figure 6.11b). Since heatwaves during the periods between May and September (MJJAS – enlarged summer) have mean severities above 1 (not shown), these lower severity events occur in early spring and late autumn. 90% of heatwaves have average severities lower than 2, i.e, in extreme events $S_m \geq 2$. High severity events take place when $S_m \geq 1.8$. The average severity of the heatwaves does not change significantly with the length of the heatwave (not shown), *i.e.*, when analysed for events with lengths of 5, 6, 7, 8, 9, 10, 15 and 20 days, it oscillates between 1.1 and 1.4 for the median number of events and 1.2 and 1.8 for 75% of events (higher values correspond to the smallest heatwaves, indicating the occurrence of extreme temperatures within the event which drive an increase in the average, as well as the presence of short events above P_{95}). Although the mean severity increases by 0.2 in all percentiles by mid-century, in RCP2.6; at the end of the 21st century the severity distribution is similar to the historical. In RCP4.5, the median of the events has an average severity of 1.2,

with only 26% with low severity by the end of the century (a reduction of 3% relative to the historical period). In this scenario and by the end of the century, there is an increase in events in the early spring and late autumn with average severities larger than 1 (there is a 5% and 4% increase of high severity events for temperatures above P_{90} and P_{95} respectively). The stabilisation of the GHGs by mid-century has the potential to reduce the severity of the extreme heatwaves at the end of the century to values similar to the early 21st century. For RCP8.5, less than a quarter of heatwaves are projected to have low severities and the median of the events has mean severity of circa 1.3, indicating that the maximum temperature becomes more skewed to larger values. 50% have mean severities above 1.5. This is even more significant in the occurrence of the very extreme events, whereby an increase of 10% of the extreme events and the maximum mean severity is 3.8 (a value not registered in the historical time series). The land percentage covered by the heatwave events is shown in Figure 6.11c. In the historical period, 50% of the events occupy less than 8% of continental Portugal, 75% cover only 35% of land and only 5% envelop more than 83%. As the GHGs increase, an areal expansion occurs. While in RCP2.6 and at the end of the century, 50% of heatwaves cover less than 11%, and 10% of the heatwaves expand beyond 80% of the territory; in RCP8.5, 50 % of the events will envelop up to 45% of land and more than 90% of territory will be in heatwave in 20% of the events. In this most severe scenario, 50% of the extreme heatwaves ($T_{max} > P_{95}$) will overlay less than 27% of land and only 10% will fill more than 91%.

Return levels associated with 10-, 30-, 50-, and 100-years events for daily maximum temperature are displayed in Figure 6.12 for the five regions of NUTS II. For the historical period, the return levels of maximum temperature are spatially less discrepant between the return periods, with differences of 2–3 ºC between them, and with lower uncertainty among models. The A.M. Lisboa and Alentejo are the regions with higher return levels, between 42 ºC and 45 ºC in a day. For the beginning of the century, there is a slight increase in the return values in all regions. However, the differences are low between the RCPs. From the mid- to end-of-century, there is an increase in the return levels, strongest for the emission scenario without mitigation. Assuming the RCP8.5 during 2071-2100, it is expected that every 10 years an extreme value of maximum temperature of 49 ºC (48 ºC) occurs in the Alentejo (A.M. Lisboa) area, increasing to 51 ºC (50.5 ºC) every 100 years. For the remaining regions, it is projected that the return levels increase throughout the 21st century, 30-year return levels close (remaining regions) or higher (Alentejo) than 50 ºC.

Tropical nights (number of days per year where daily minimum temperature exceeds 20ºC), displayed in Figure 6.13, in the historical period vary between 0 – 10 nights over a substantial part of continental Portugal, with the exception of the southern coastal region and south and central interior regions, whereas 10 – 30 tropical nights may occur (Figure 6.13a). For the beginning of the century, all RCPs show an increase in tropical nights in central and southern Portugal. A substantial increase in tropical nights occurs

from mid- to end- century over RCP4.5 and RCP8.5. For the end of the century assuming the worst-case scenario, the southeaster cluster, the southern coast, and other regions near the coast of Lisbon and in the central interior of the country presents near to 100 tropical nights, and the remaining country will experience more than 30 nights. The anomalies of the future scenarios against the historical period further stress this point (Figure 6.13b), with an increase of tropical nights present in all periods and scenarios in the southern coast, southeaster, and central interior regions, which go from an increase of 10 – 20 nights in the beginning of the century and mid-century RCP2.6, to an increase that surpasses 80 nights in the end-century RCP8.5. The largest standard deviations occur in the west coastal region (35 to 50 nights), nevertheless being relatively small where the largest anomalies are found (Figure 6.13c). At least 66 % of the models agree in the change signal for all grid-points, periods, and scenarios.

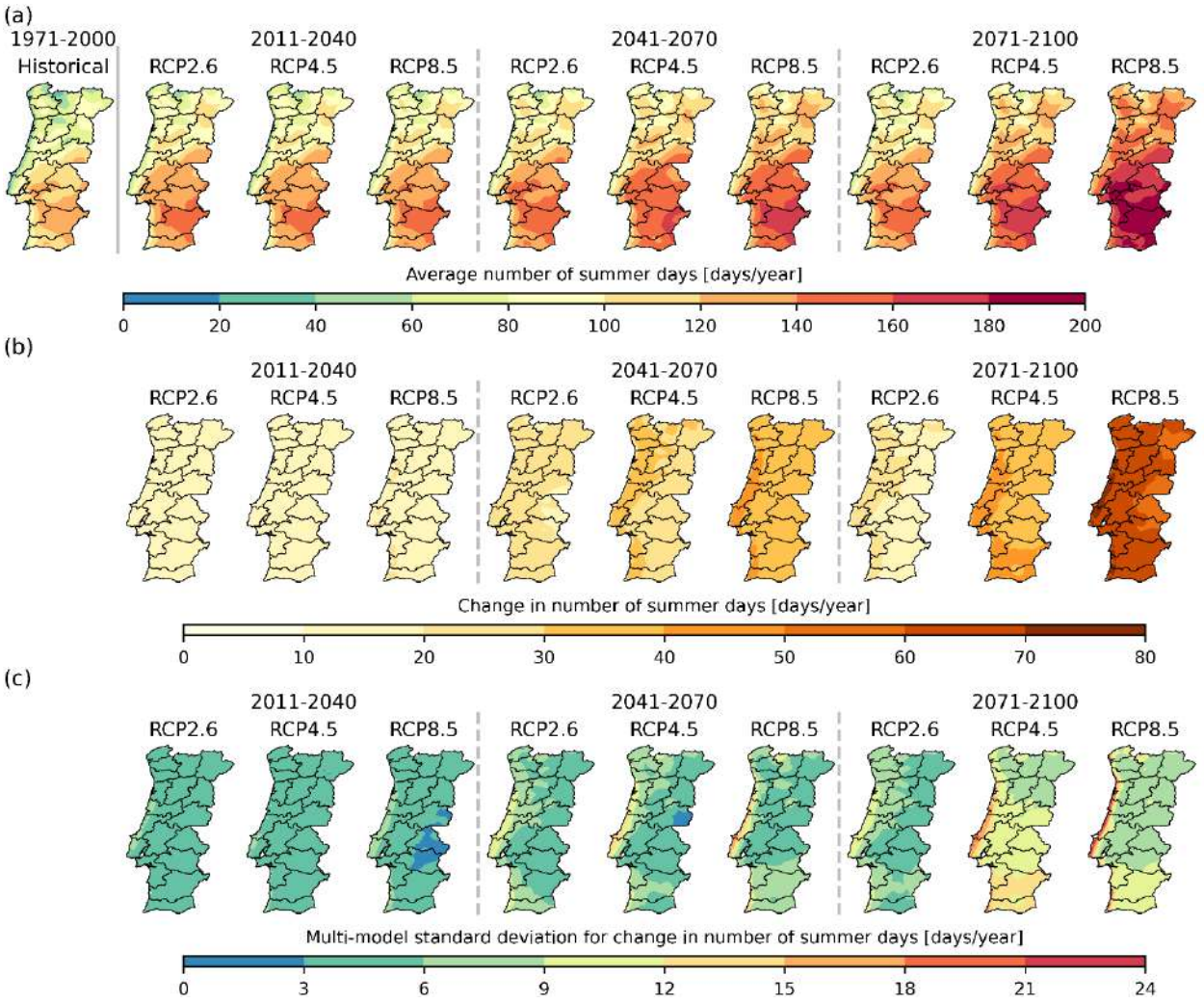

Figure 6.1 (a) Annual average number of days per year where daily maximum temperature exceeds 25ºC (summer days) over mainland Portugal, for historical period (1971-2000) and for the future periods considering different GHG emission scenarios. (b) Future projected changes in the average number of summer days, considering the 1971-2000 period as reference. (c) Multi-model spread in future projected changes in average number of summer days, considering the 1971-2000 period as reference. The spread is quantified by the

standard deviation of the anomalies between different models. Grid-points where the change signal does not agree in at least 66% of the models is identified by dotted hatching (no occurrences for TxG25).

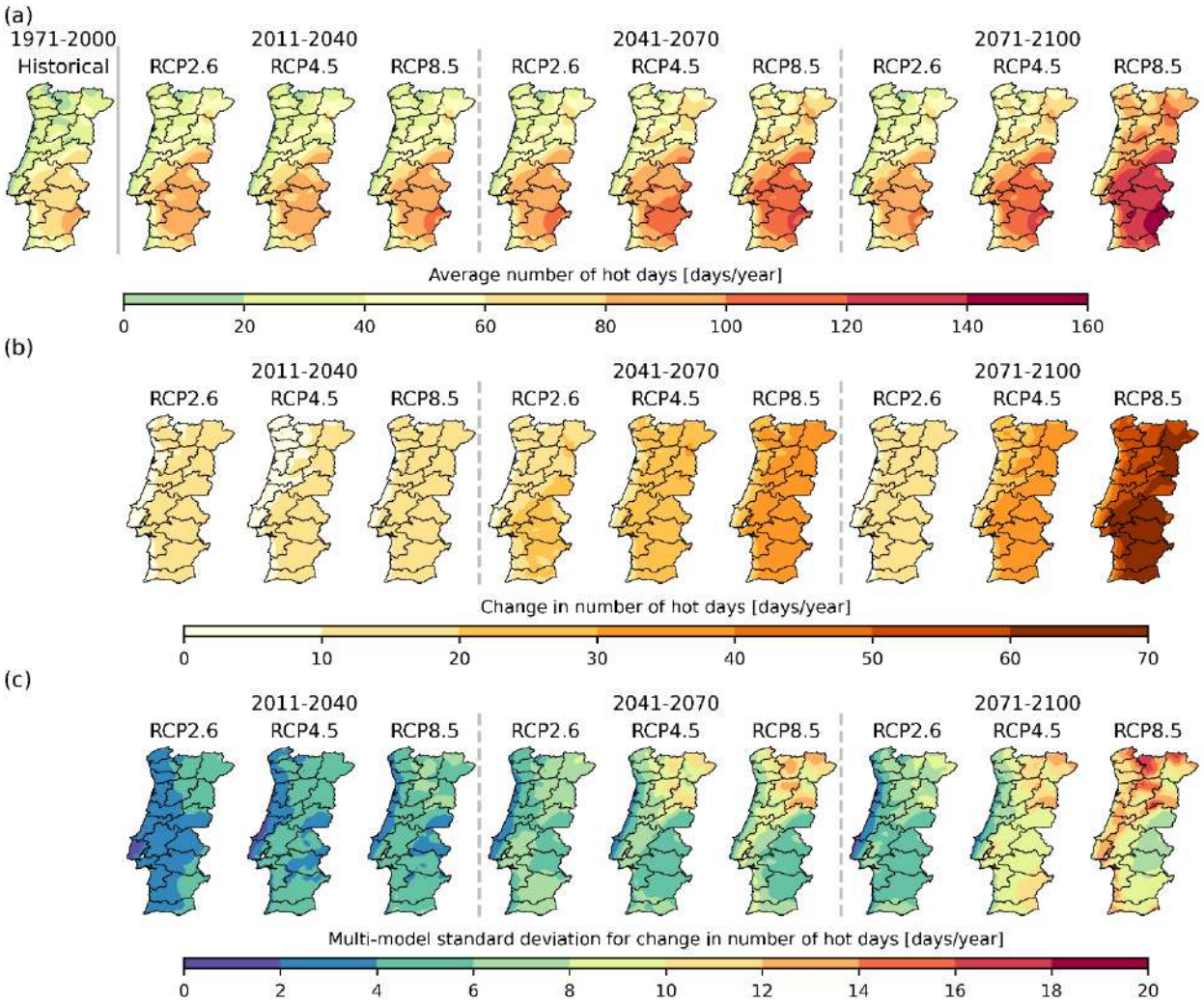

Figure 6.2 (a) Annual average number of days per year where daily maximum temperature exceeds 30°C (hot days) over mainland Portugal, for historical period (1971-2000) and for the future periods considering different GHG emission scenarios. (b) Future projected changes in the average number of hot days, considering the 1971-2000 period as reference. (c) Multi-model spread in future projected changes in average number of hot days, considering the 1971-2000 period as reference. The spread is quantified by the standard deviation of the anomalies between different models. Grid-points where the change signal does not agree in at least 66% of the models is identified by dotted hatching (no occurrences for TxG30).

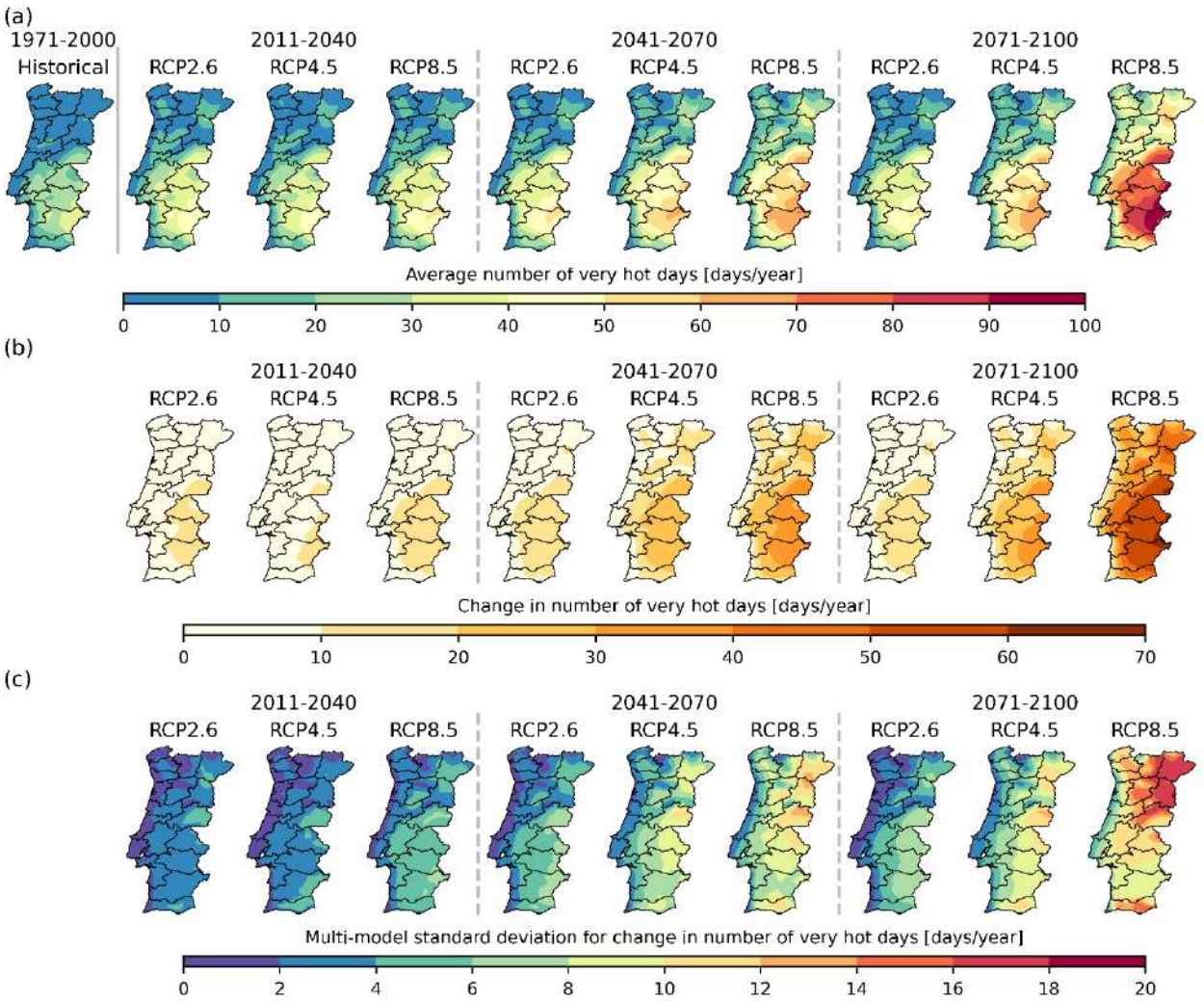

Figure 6.3 (a) Annual average number of days per year where daily maximum temperature exceeds 35ºC (very hot days) over mainland Portugal, for historical period (1971-2000) and for the future periods considering different GHG emission scenarios. (b) Future projected changes in the average number of very hot days, considering the 1971-2000 period as reference. (c) Multi-model spread in future projected changes in average number of very hot days, considering the 1971-2000 period as reference. The spread is quantified by the standard deviation of the anomalies between different models. Grid-points where the change signal does not agree in at least 66% of the models is identified by dotted hatching (no occurrences for TxG35).

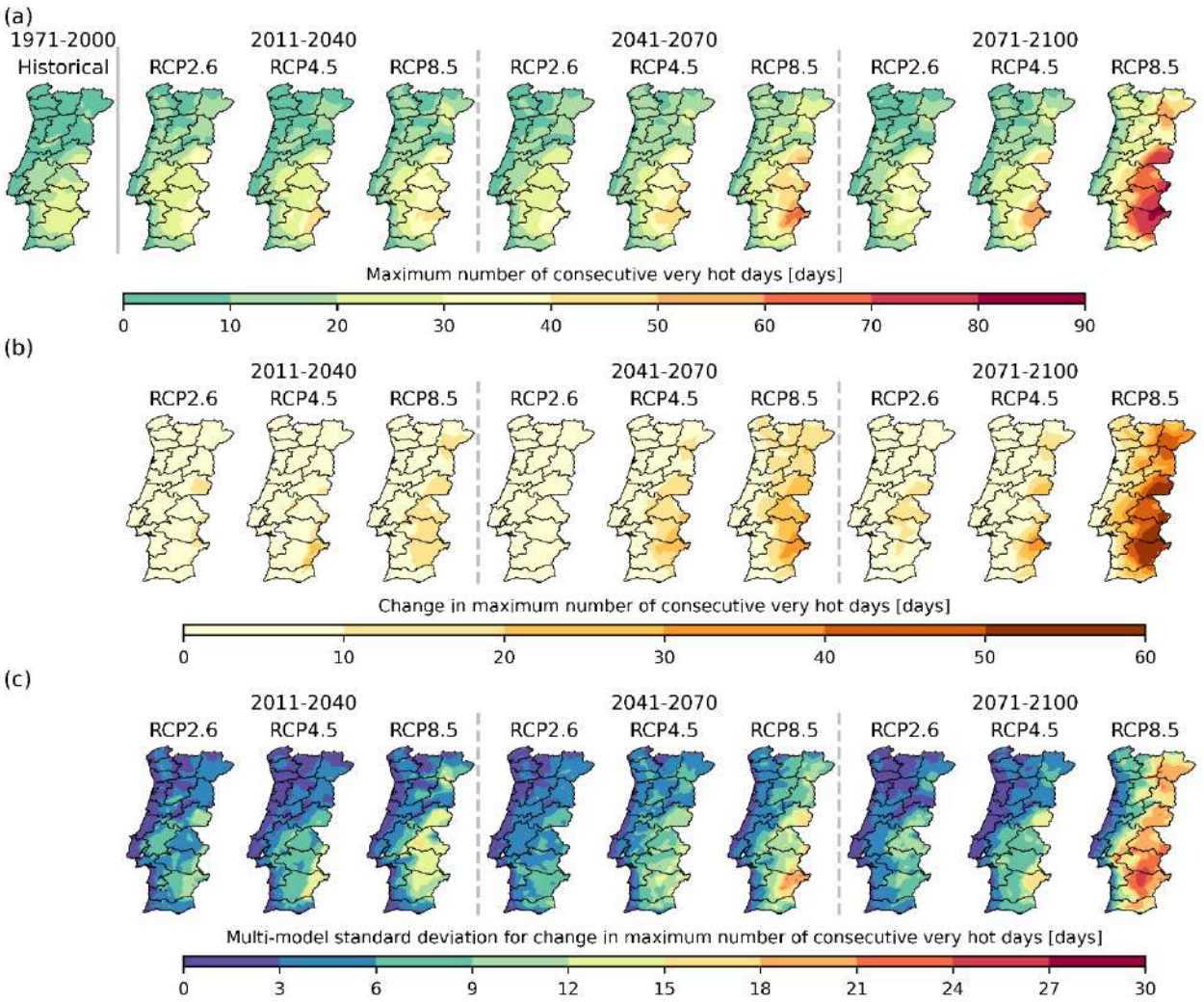

Figure 6.4 (a) Annual average of maximum number of consecutive days per year where daily maximum temperature exceeds 35ºC (very hot days) over mainland Portugal, for historical period (1971-2000) and for the future periods considering different GHG emission scenarios. (b) Future projected changes in the average of maximum number of consecutive very hot days, considering the 1971-2000 period as reference. (c) Multi-model spread in future projected changes in average of maximum number of consecutive very hot days, considering the 1971-2000 period as reference. The spread is quantified by the standard deviation of the anomalies between different models. Grid-points where the change signal does not agree in at least 66% of the models is identified by dotted hatching (no occurrences for CDTxG35).

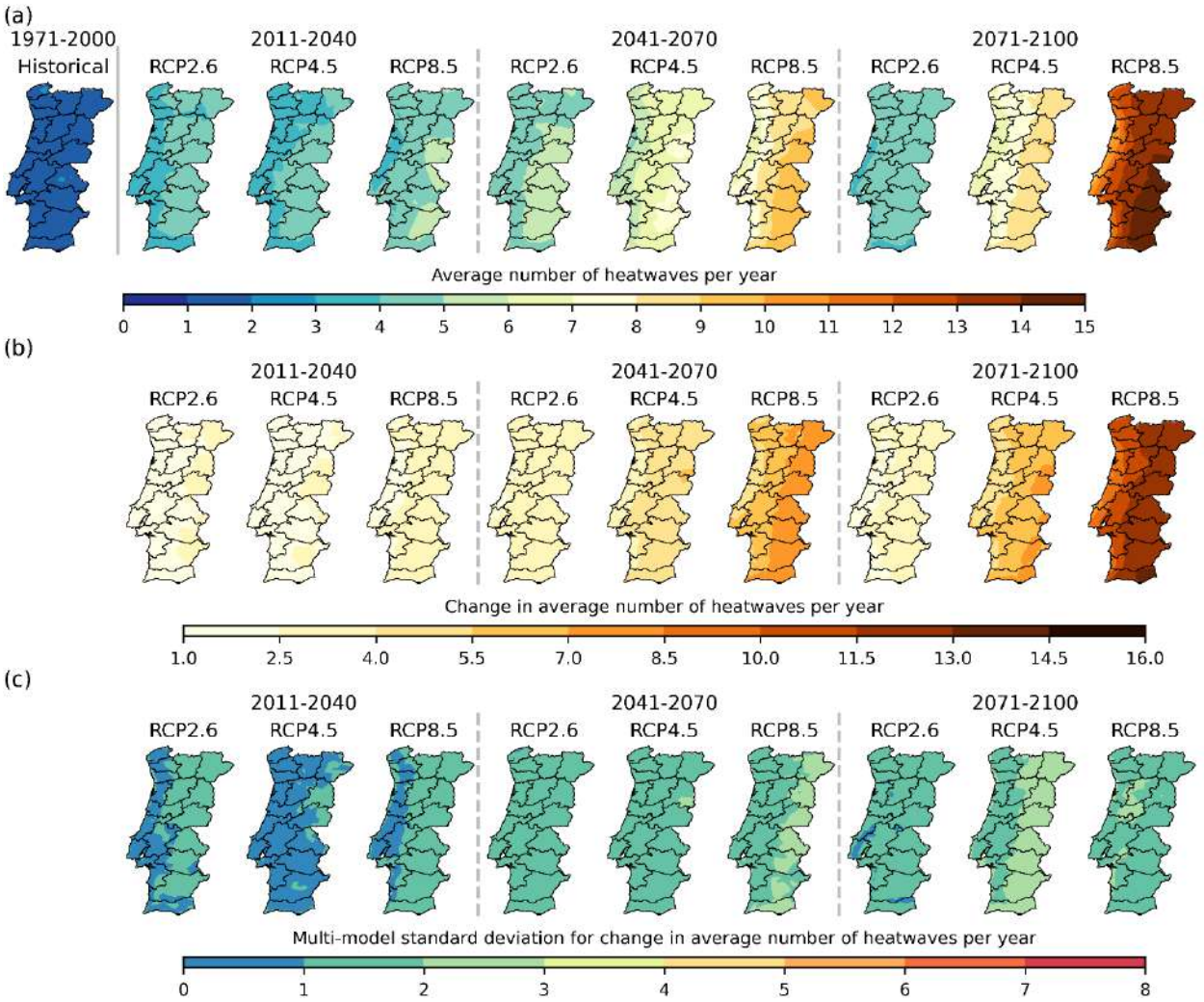

Figure 6.5 (a) <u>Full annual</u> average number of heatwaves per year over mainland Portugal, for historical period (1971-2000) and for the future periods considering different GHG emission scenarios. (b) Future projected changes in the average number of heatwaves per year, considering the 1971-2000 period as reference. (c) Multi-model spread in future projected changes in average number of heatwaves per year, considering the 1971-2000 period as reference. The spread is quantified by the standard deviation of the anomalies between different models. Grid-points where the change signal does not agree in at least 66% of the models is identified by dotted hatching (no occurrences for HW).

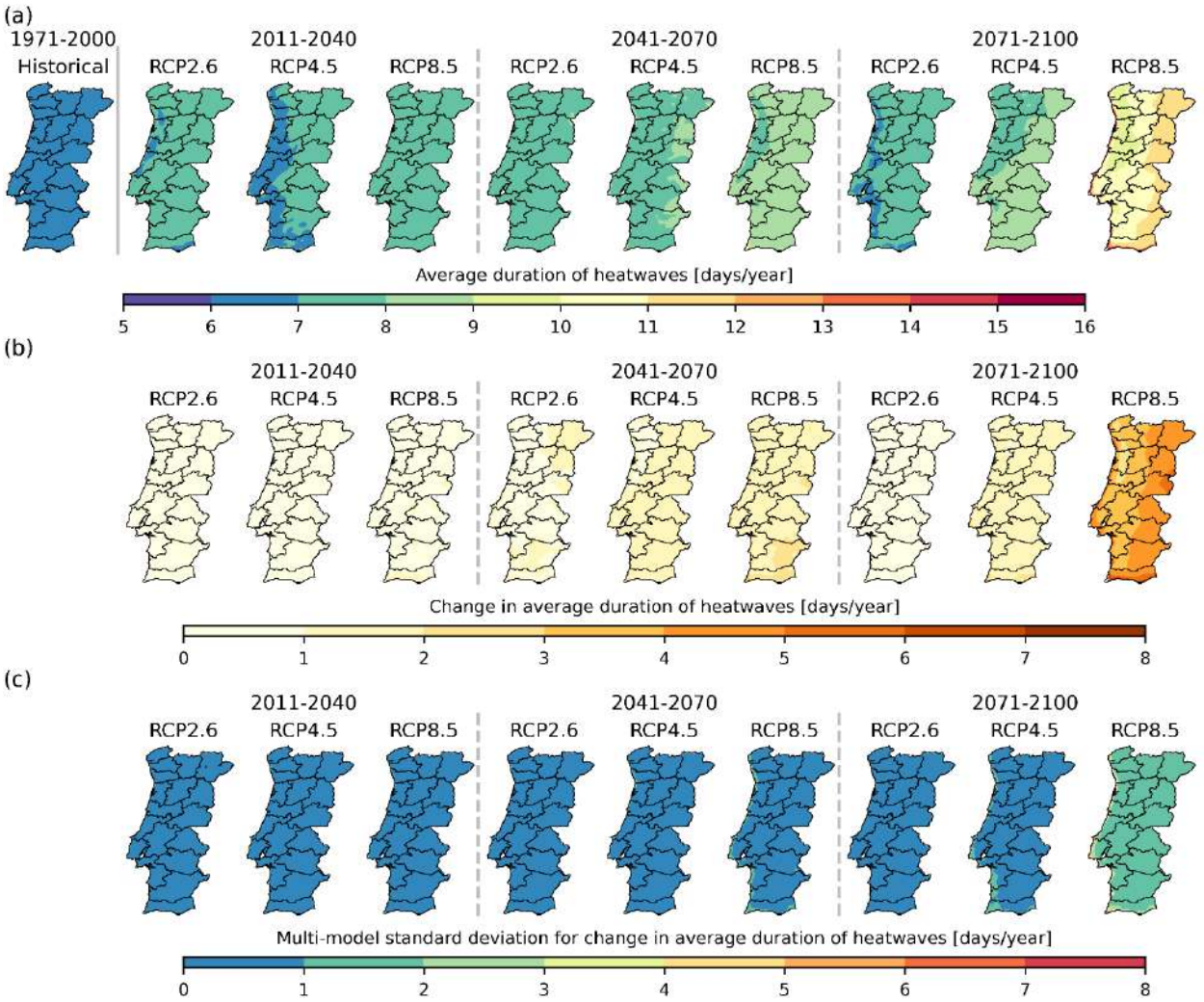

Figure 6.6 (a) <u>Full annual</u> average duration of heatwaves per year over mainland Portugal, for historical period (1971-2000) and for the future periods considering different GHG emission scenarios. (b) Future projected changes in the average duration of heatwaves per year, considering the 1971-2000 period as reference. (c) Multi-model spread in future projected changes in average duration of heatwaves per year, considering the 1971-2000 period as reference. The spread is quantified by the standard deviation of the anomalies between different models. Grid-points where the change signal does not agree in at least 66% of the models is identified by dotted hatching (no occurrences for HW).

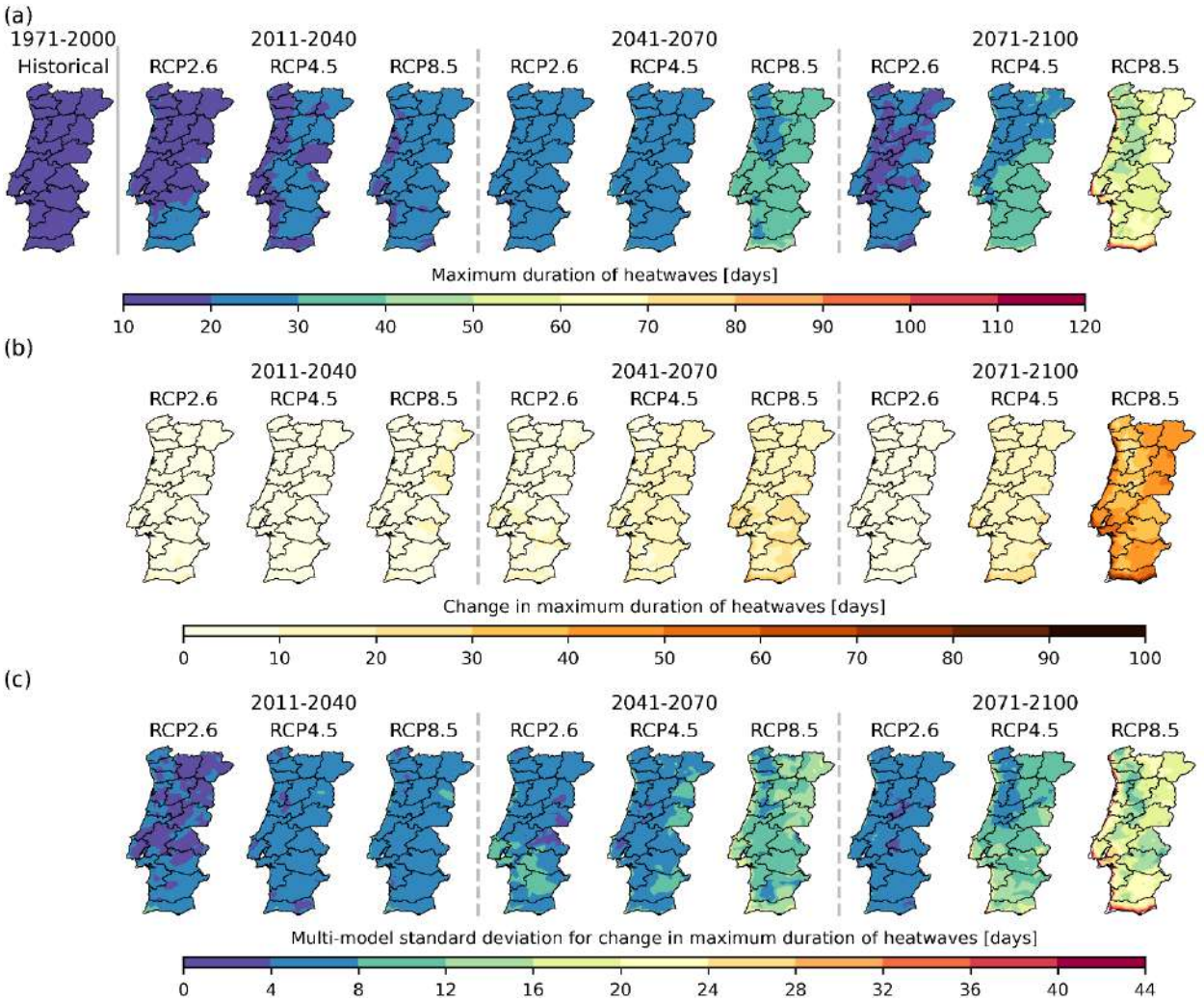

Figure 6.7 (a) <u>Full Annual</u> maximum duration of heatwaves over mainland Portugal, for historical period (1971-2000) and for the future periods considering different GHG emission scenarios. (b) Future projected changes in the maximum duration of heatwaves, considering the 1971-2000 period as reference. (c) Multi-model spread in future projected changes in maximum duration of heatwaves, considering the 1971-2000 period as reference. The spread is quantified by the standard deviation of the anomalies between different models. Grid-points where the change signal does not agree in at least 66% of the models is identified by dotted hatching.

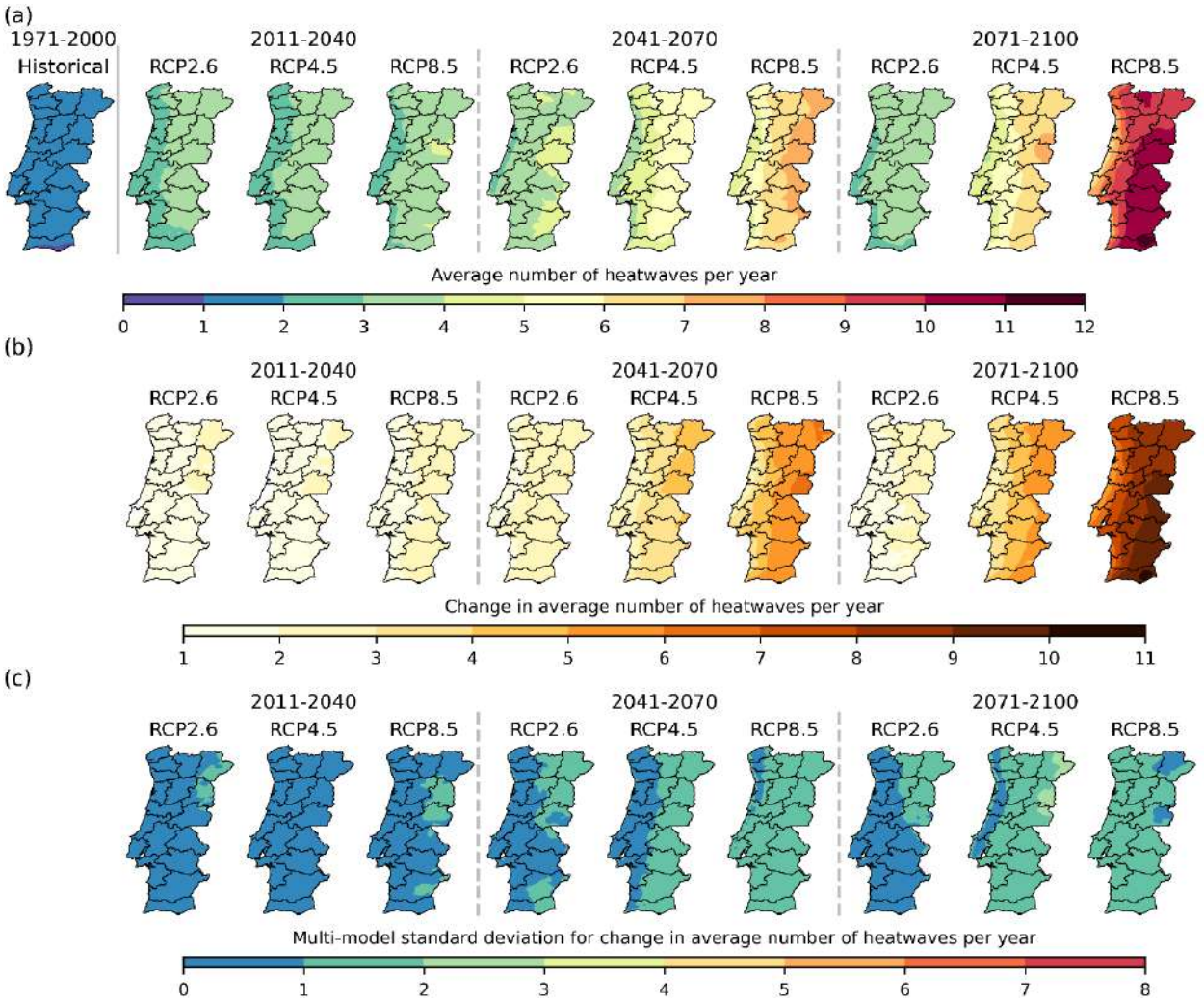

Figure 6.8 (a) March-November average number of heatwaves per year over mainland Portugal, for historical period (1971-2000) and for the future periods considering different GHG emission scenarios. (b) Future projected changes in the average number of heatwaves per year, considering the 1971-2000 period as reference. (c) Multi-model spread in future projected changes in average number of heatwaves per year, considering the 1971-2000 period as reference. The spread is quantified by the standard deviation of the anomalies between different models. Grid-points where the change signal does not agree in at least 66% of the models is identified by dotted hatching (no occurrences for HW).

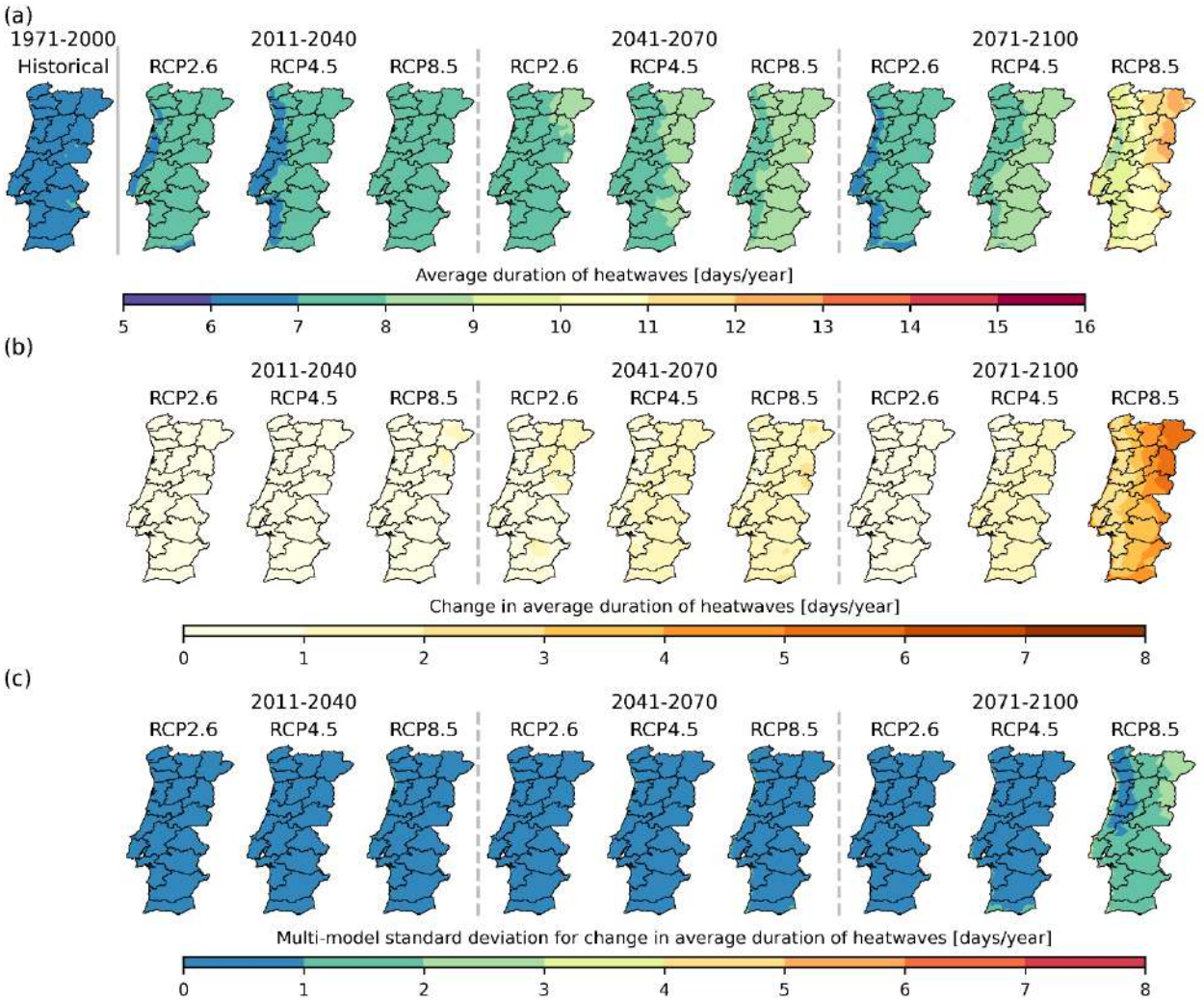

Figure 6.9 (a) March-November average duration of heatwaves per year over mainland Portugal, for historical period (1971-2000) and for the future periods considering different GHG emission scenarios. (b) Future projected changes in the average duration of heatwaves per year, considering the 1971-2000 period as reference. (c) Multi-model spread in future projected changes in average duration of heatwaves per year, considering the 1971-2000 period as reference. The spread is quantified by the standard deviation of the anomalies between different models. Grid-points where the change signal does not agree in at least 66% of the models is identified by dotted hatching (no occurrences for HW).

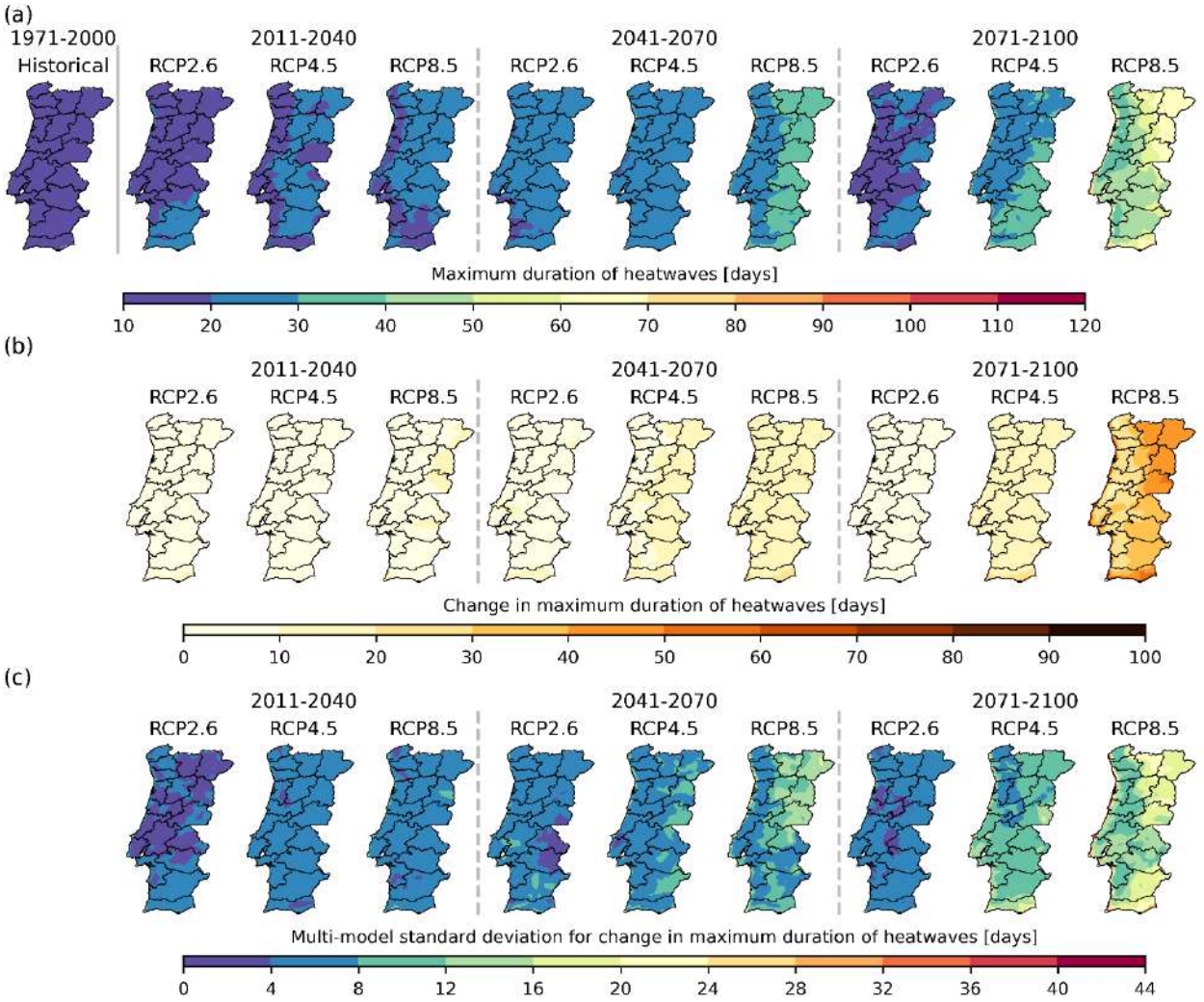

Figure 6.10 (a) March-November maximum duration of heatwaves over mainland Portugal, for historical period (1971-2000) and for the future periods considering different GHG emission scenarios. (b) Future projected changes in the maximum duration of heatwaves, considering the 1971-2000 period as reference. (c) Multi-model spread in future projected changes in maximum duration of heatwaves, considering the 1971-2000 period as reference. The spread is quantified by the standard deviation of the anomalies between different models. Grid-points where the change signal does not agree in at least 66% of the models is identified by dotted hatching.

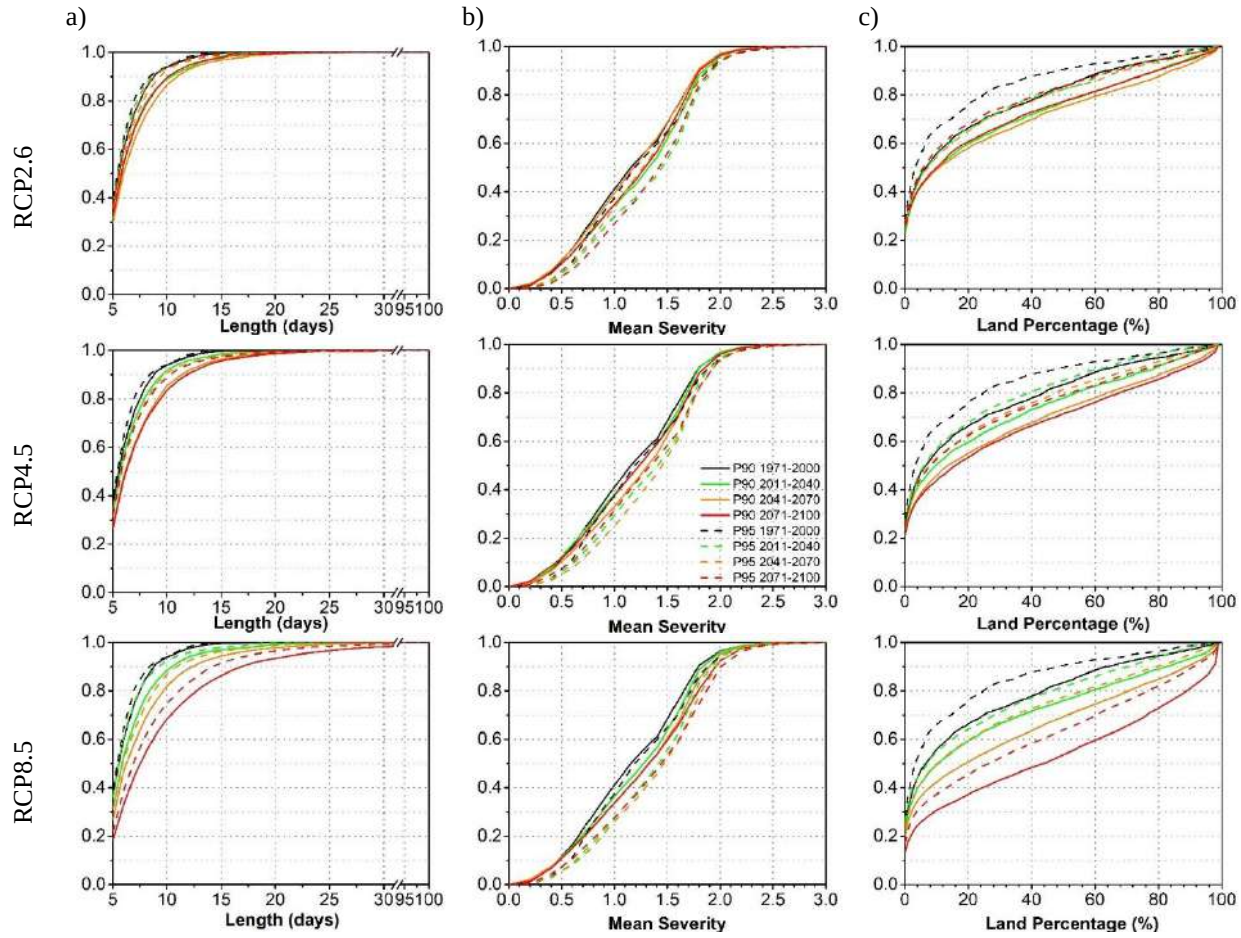

Figure 6.11 Multi-model ensemble empirical cumulative distribution functions of heatwave a) length (days), b) severity and c) areal extension (%) for the historical period (1971-2000) and for the future periods considering different GHG emission scenarios.

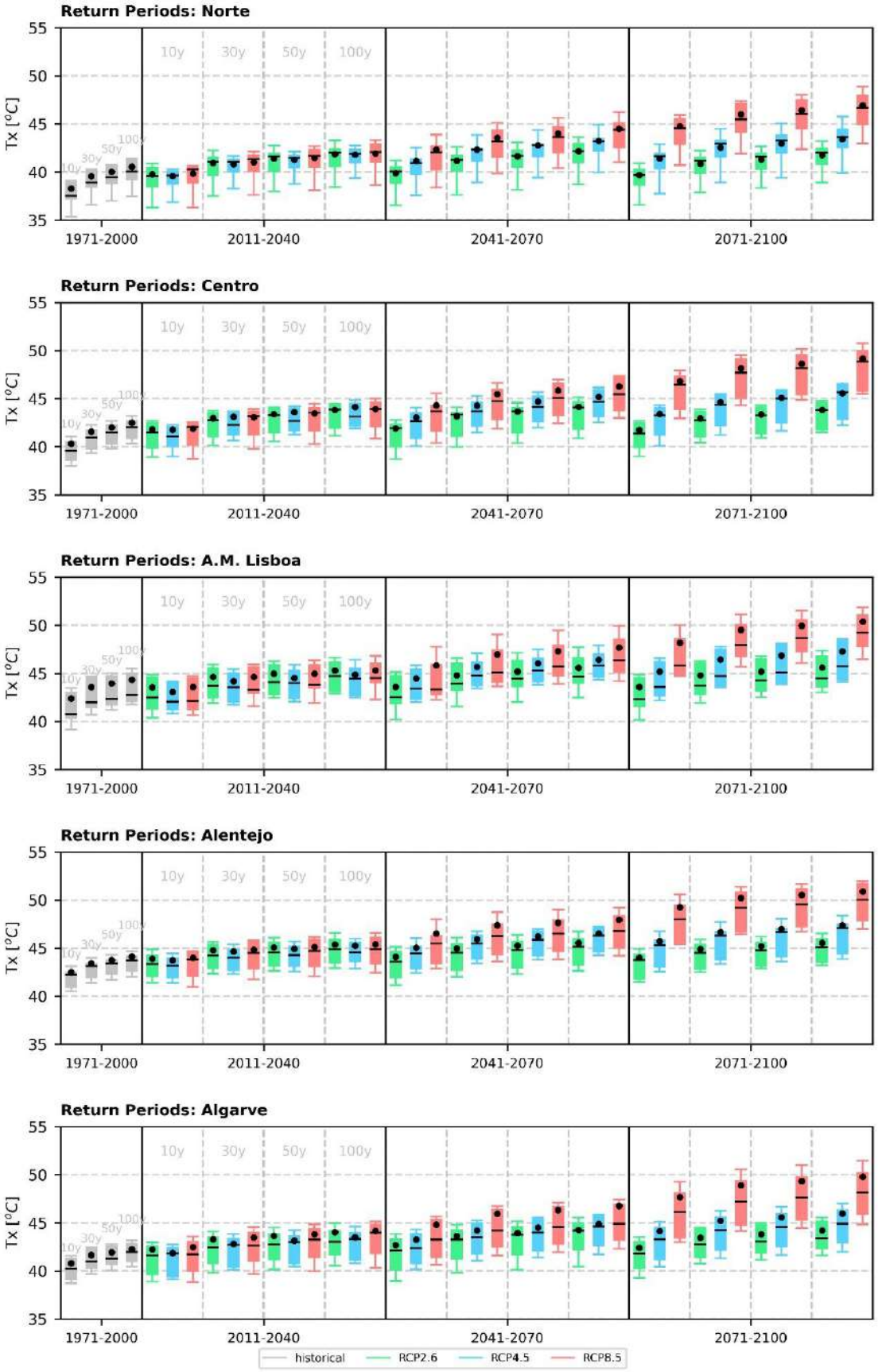
Return Periods: Norte
Return Periods: Centro
Return Periods: A.M. Lisboa
Return Periods: Alentejo
Return Periods: Algarve
Tx [°C]
55
50
45
40
35
10y
30y
50y
100y
1971-2000
2011-2040
2041-2070
2071-2100
historical
RCP2.6
RCP4.5
RCP8.5

Figure 6.12 Return levels associated with 10-, 30-, 50-, and 100-years events for daily 2-m maximum temperature for NUTS II regions: Norte, Centro, A.M. Lisboa, Alentejo and Algarve, from top to bottom. Three future periods are shown: 2011-2040, 2041-2070, and 2071-2100, under all emission scenarios – RCP2.6 (green), RCP4.5 (blue) and RCP8.5 (red), with historical period (grey) for 1971-2000 period. The black point represents the multi-model ensemble mean. Individual boxes span from the 25th to the 75th percentile, with the median represented by a straight line, and the whiskers span from 10th to the 90th percentile.

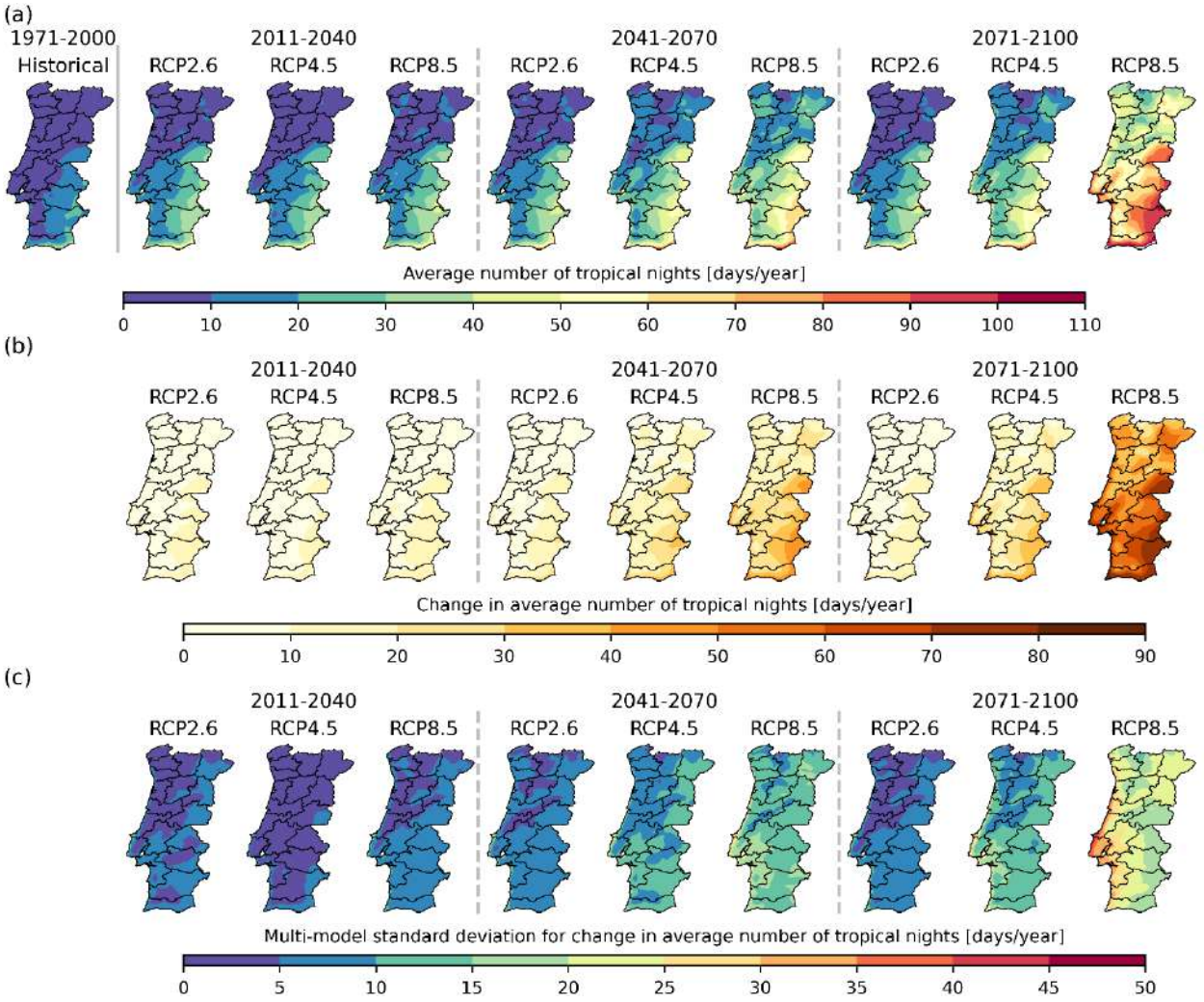

Figure 6.13 (a) Annual average number of days per year where daily minimum temperature exceeds 20°C (tropical nights) over mainland Portugal, for historical period (1971-2000) and for the future periods considering different GHG emission scenarios. (b) Future projected changes in the average number of tropical nights, considering the 1971-2000 period as reference. (c) Multi-model spread in future projected changes in average number of tropical nights, considering the 1971-2000 period as reference. The spread is quantified by the standard deviation of the anomalies between different models. Grid-points where the change signal does not agree in at least 66% of the models is identified by dotted hatching (no occurrences for TnG20).

Cold Extremes

Frost days (number of days per year where daily minimum temperature is below 0ºC) are presented in Figure 6.14. Here, the historical period shows a northeaster cluster of frost days in continental Portugal, ranging between about 50 – 80 days, a band of 0 - 10 days in the vicinity of the coast, and the remaining territory is mainly characterised by 10 – 30 frost days per year (Figure 6.14a). For future scenarios, there is a gradual shrinking of the coldest cluster, with less frost days observed. For the end of the century assuming the worst-case scenario, the north-eastern cluster presents 10 – 20 frost days, and the remaining country less than 10 days are projected. The anomalies referent to the historical period (Figure 6.14b) clearly show the decrease in frost days in the north-eastern region, with negative anomalies of less 10 – 20 days in that region in the beginning of the century (all RCPs), and for mid-century with RCP2.6. In this period, RCP4.5 and RCP8.5 start to show larger anomalies, reaching a loss of 40 days in the worst emission case. Finally, at the end of the century negative anomalies strongly vary depending on the RCP: losses of 10 – 20 days for RCP2.6, 20 – 30 days for RCP4.5, and 40 – 60 days for RCP8.5. The largest standard deviations (close to 21 days) are in the north-eastern region of Portugal, coinciding with the larger anomalies (Figure 6.14c). At least 66 % of the models agree in the change signal for all grid-points, periods, and scenarios.

Cold days (number of days per year where daily minimum temperature is below 7ºC) is shown in Figure 6.15. As with frost days, the historical period shows a north-eastern cluster of cold days in continental Portugal, ranging between about 180 – 240 days, whereas the remaining territory is mainly defined by 100 – 180 cold days per year, except in the coastal region of central and southern Portugal, where less than 100 cold days are found (Figure 6.15a). For future scenarios, there is a gradual decrease of cold days over the entire country. For the end of the century assuming the worst-case scenario, the north-eastern cluster presents 100 – 140 cold days, and most of the remaining country identifies less than 80 days. The anomalies referent to the historical period (Figure 6.15b) clearly shows the decrease in cold days over the entire region, with negative anomalies between 0 – 20 days in the beginning of the century (all RCPs), and for mid-century with RCP2.6 (reaching 20 – 30 days in small regions in this case). In this period, RCP4.5 and RCP8.5 start to show larger anomalies, reaching losses between 40 – 50 days in the worst emission case. Finally, at the end of the century negative anomalies strongly vary depending on the RCP: losses of 10 – 20 days for RCP2.6, 40 – 50 days for RCP4.5, and 50 – 90 days for RCP8.5. The largest standard deviations (15 to 21 days) are in the southern coastal region of Portugal, not coinciding with the larger anomalies (Figure 6.15c). At least 66 % of the models agree in the change signal for all grid-points, periods, and scenarios.

Consecutive cold days (maximum number of consecutive days per year where daily minimum temperature is below 7ºC) is displayed in Figure 6.16. Results presented for this index are very similar to those

concerning frost days. The main differences being a substantial increase in the magnitude of the number of days (Figure 6.16a), and consequently larger anomalies focused mainly in the north-eastern region (Figure 6.16b), and higher standard deviations in regions where the anomalies are greater (Figure 6.16c). At least 66 % of the models agree in the change signal for most grid-points, periods, and scenarios (except few points in the 2011 – 2040 period for RCP2.6 in the southern region of Portugal).

Coldwaves, characterized by the number of occurrences per year with a minimum of 5 consecutive days in coldwave, the average duration, and the maximum duration of the events are shown in Figure 6.17, Figure 6.18 and Figure 6.19, respectively. In the historical period, the number of coldwaves per year is around 1 (Figure 6.17). The average duration of these events varies between 6 – 7 days over the entire country (Figure 6.18), whilst the maximum duration of a coldwave in the historical period can reach 13 days near the coastal regions and 19 days in the interior regions (Figure 6.19). For all the scenarios and future periods, the reduction in the number of coldwaves is expected over all country (Figure 6.17), following the projections of an increase in minimum temperature. For the beginning to the end of the century, the projections show a maximum of 1 event every 2 years. The average duration of coldwaves decreases slightly, reaching an average of 5-7 days throughout the century. Assuming the worst-case scenario for the end-of-century, it is expected a coldwave event at each 4 years. Looking to the future projections of the maximum duration of a coldwave phenomenon, a significant reduction is expected. For the end-of-century and assuming the worst-case scenario, the maximum duration of a coldwave is less than 7 days. Although in the other two RCPs the decrease is smaller, the projections show a maximum duration that can reach 9 days. At least 66 % of the models agree in the change signal for all grid-points, periods, and scenarios. In the beginning of the century, in RCP2.6, some grid-points do not agree in the climate change signal for average duration of coldwaves and the maximum duration of this event.

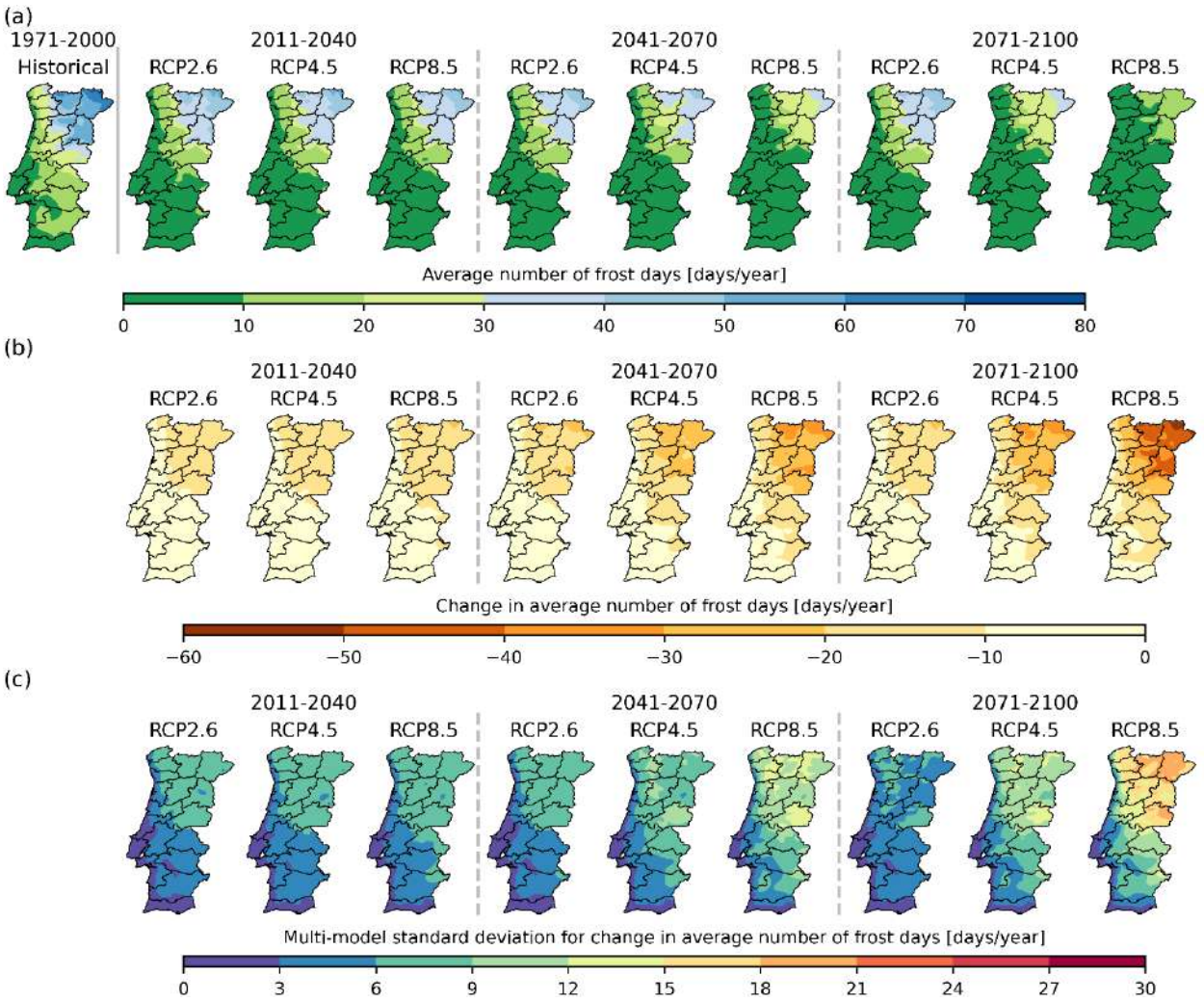

Figure 6.14 (a) Annual average number of days per year where daily minimum temperature is below 0ºC (frost days) over mainland Portugal, for historical period (1971-2000) and for the future periods considering different GHG emission scenarios. (b) Future projected changes in the average number of frost days, considering the 1971-2000 period as reference. (c) Multi-model spread in future projected changes in average number of frost days, considering the 1971-2000 period as reference. The spread is quantified by the standard deviation of the anomalies between different models. Grid-points where the change signal does not agree in at least 66% of the models is identified by dotted hatching (no occurrences for TnL0).

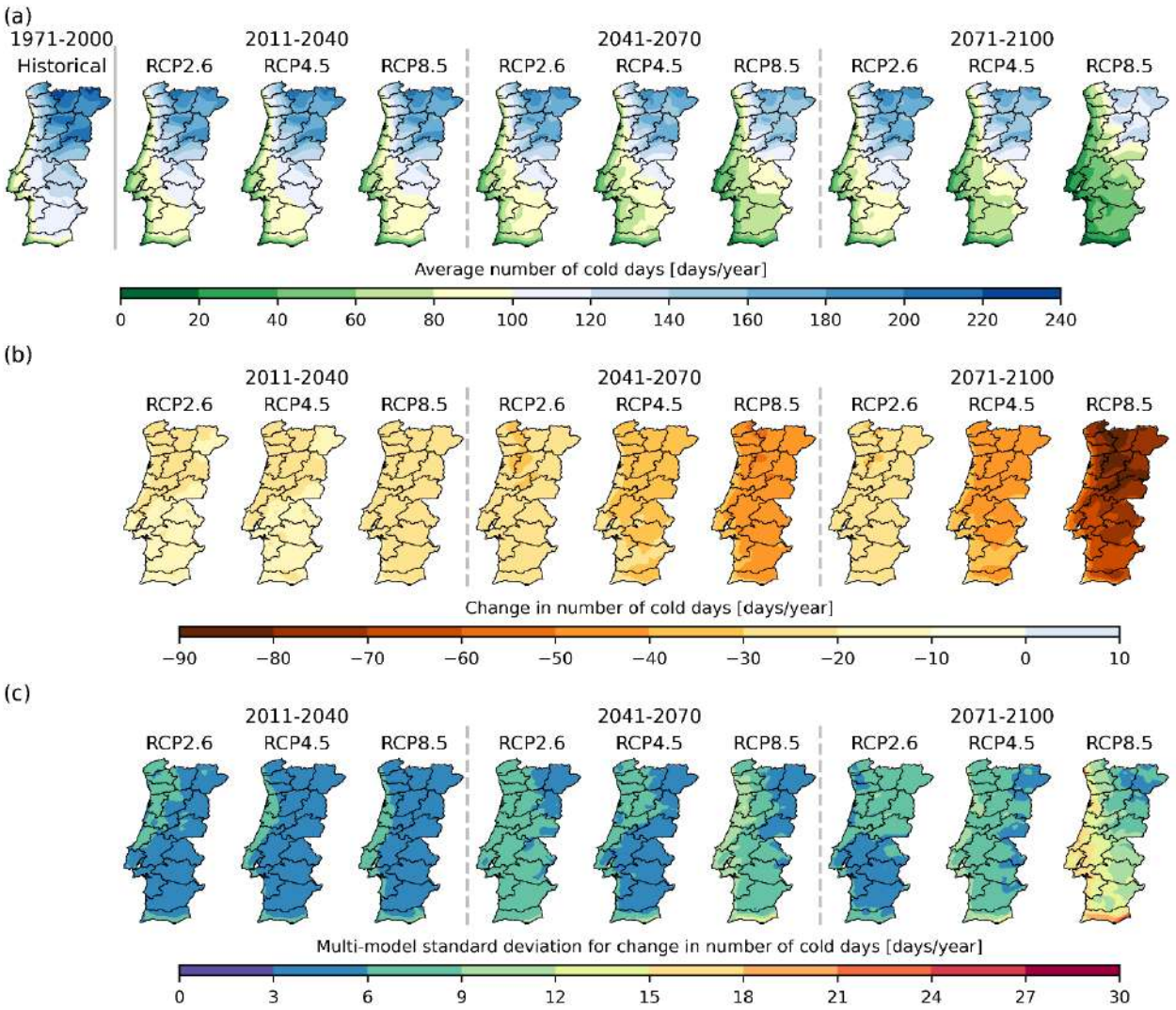

Figure 6.15 (a) Annual average number of days per year where daily minimum temperature is below 7ºC (cold days) over mainland Portugal, for historical period (1971-2000) and for the future periods considering different GHG emission scenarios. (b) Future projected changes in the average number of cold days, considering the 1971-2000 period as reference. (c) Multi-model spread in future projected changes in average number of cold days, considering the 1971-2000 period as reference. The spread is quantified by the standard deviation of the anomalies between different models. Grid-points where the change signal does not agree in at least 66% of the models is identified by dotted hatching (no occurrences for TnL0).

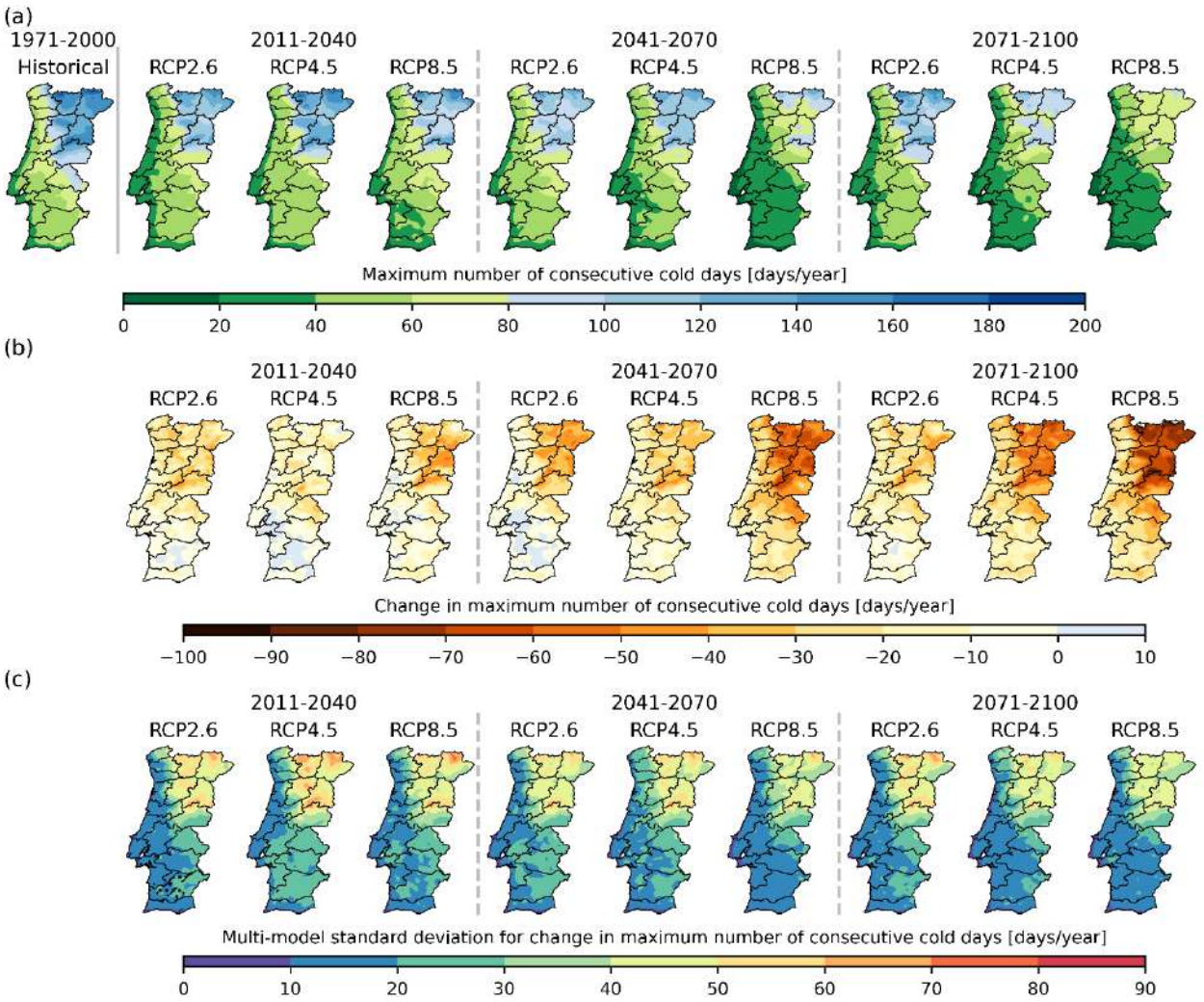

Figure 6.16 (a) Annual average of maximum number of consecutive days per year where daily minimum temperature is below 7ºC (cold days) over mainland Portugal, for historical period (1971-2000) and for the future periods considering different GHG emission scenarios. (b) Future projected changes in the average of maximum number of consecutive cold days, considering the 1971-2000 period as reference. (c) Multi-model spread in future projected changes in average of maximum number of consecutive cold days, considering the 1971-2000 period as reference. The spread is quantified by the standard deviation of the anomalies between different models. Grid-points where the change signal does not agree in at least 66% of the models is identified by dotted hatching (no occurrences for CDTnL7).

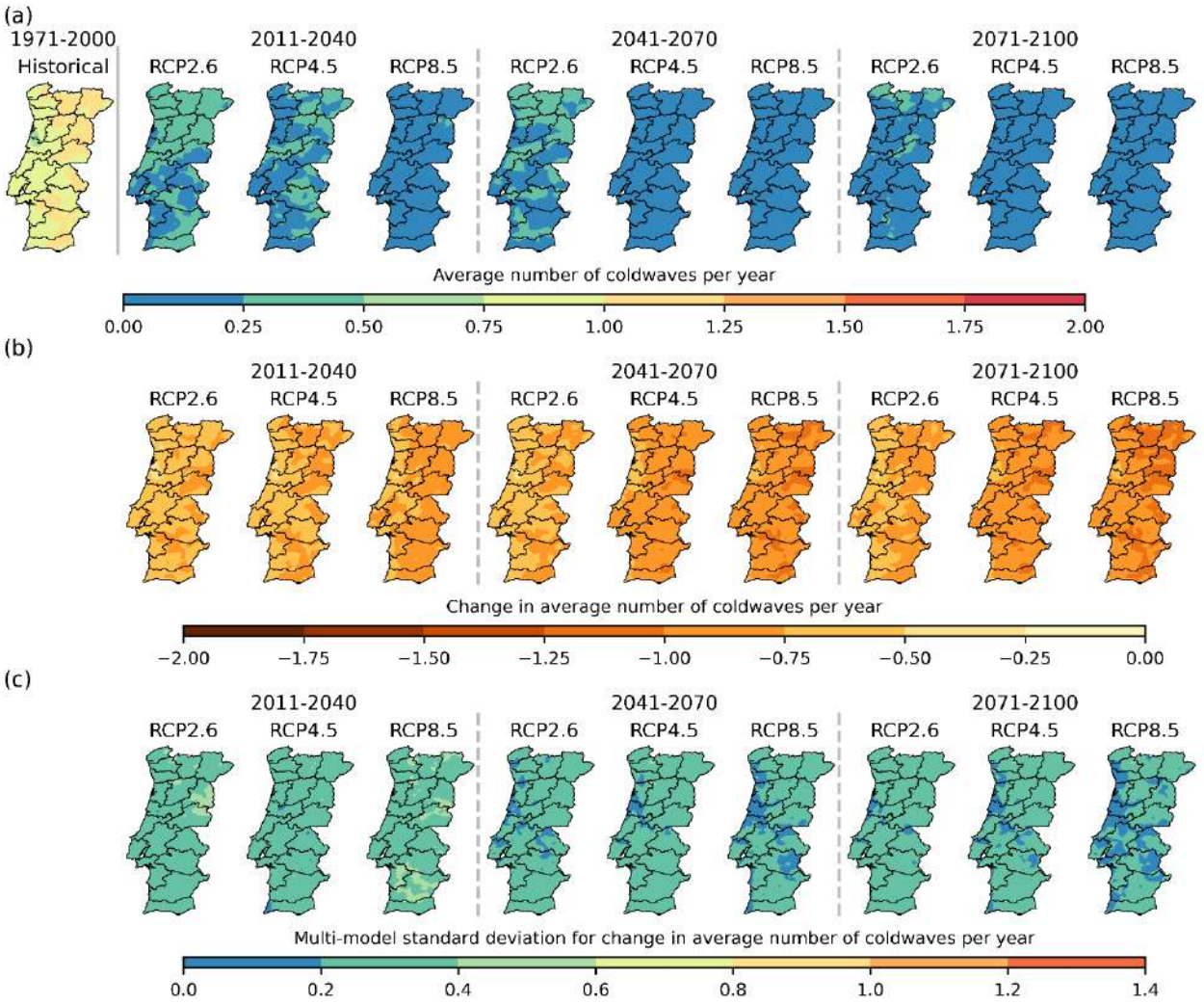

Figure 6.17 (a) Annual average number of coldwaves per year over mainland Portugal, for historical period (1971-2000) and for the future periods considering different GHG emission scenarios. (b) Future projected changes in the average number of coldwaves per year, considering the 1971-2000 period as reference. (c) Multi-model spread in future projected changes in average number of coldwaves per year, considering the 1971-2000 period as reference. The spread is quantified by the standard deviation of the anomalies between different models. Grid-points where the change signal does not agree in at least 66% of the models is identified by dotted hatching (no occurrences for CW).

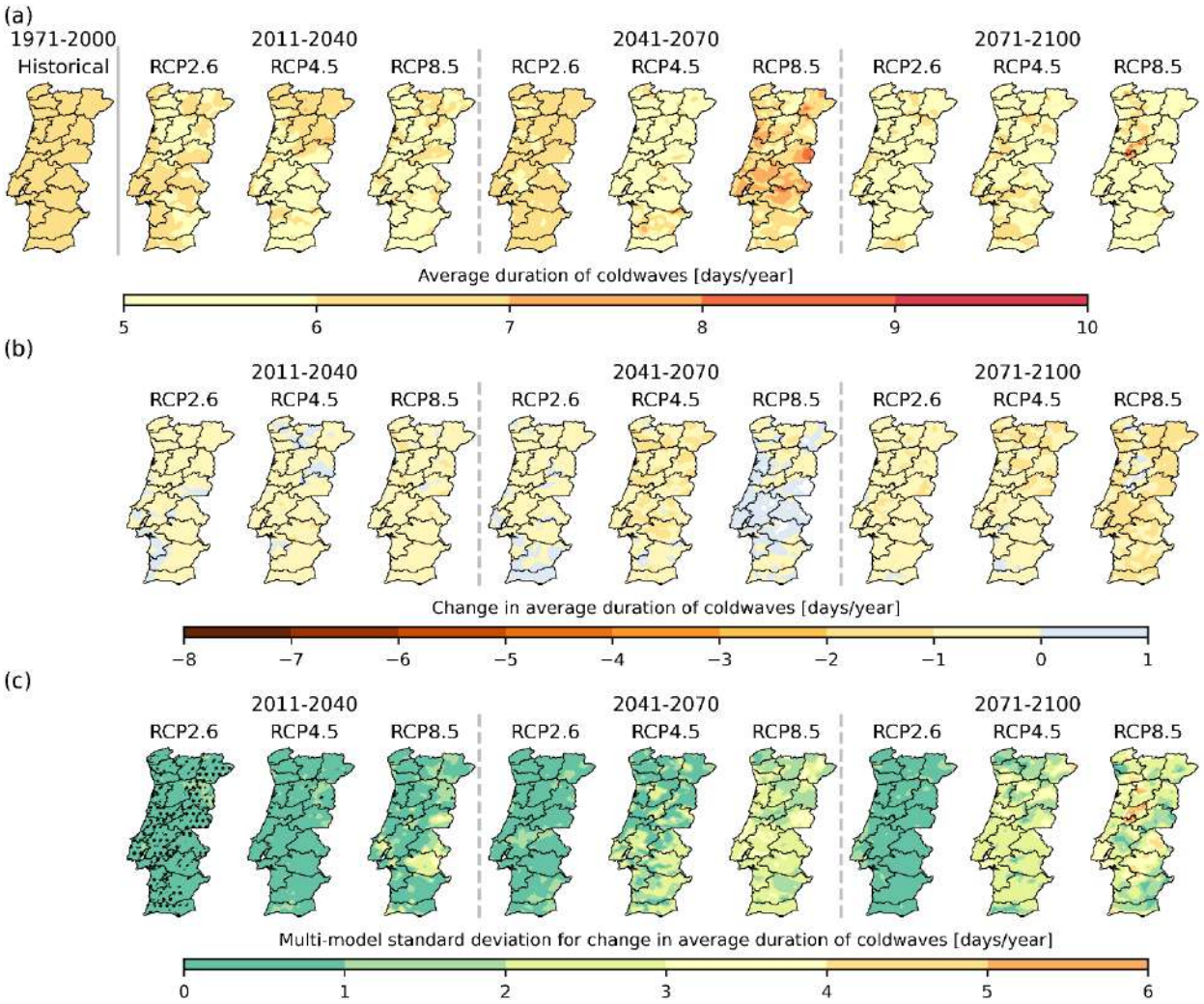

Figure 6.18 (a) Annual average duration of coldwaves per year over mainland Portugal, for historical period (1971-2000) and for the future periods considering different GHG emission scenarios. (b) Future projected changes in the average duration of coldwaves per year, considering the 1971-2000 period as reference. (c) Multi-model spread in future projected changes in average duration of coldwaves per year, considering the 1971-2000 period as reference. The spread is quantified by the standard deviation of the anomalies between different models. Grid-points where the change signal does not agree in at least 66% of the models is identified by dotted hatching.

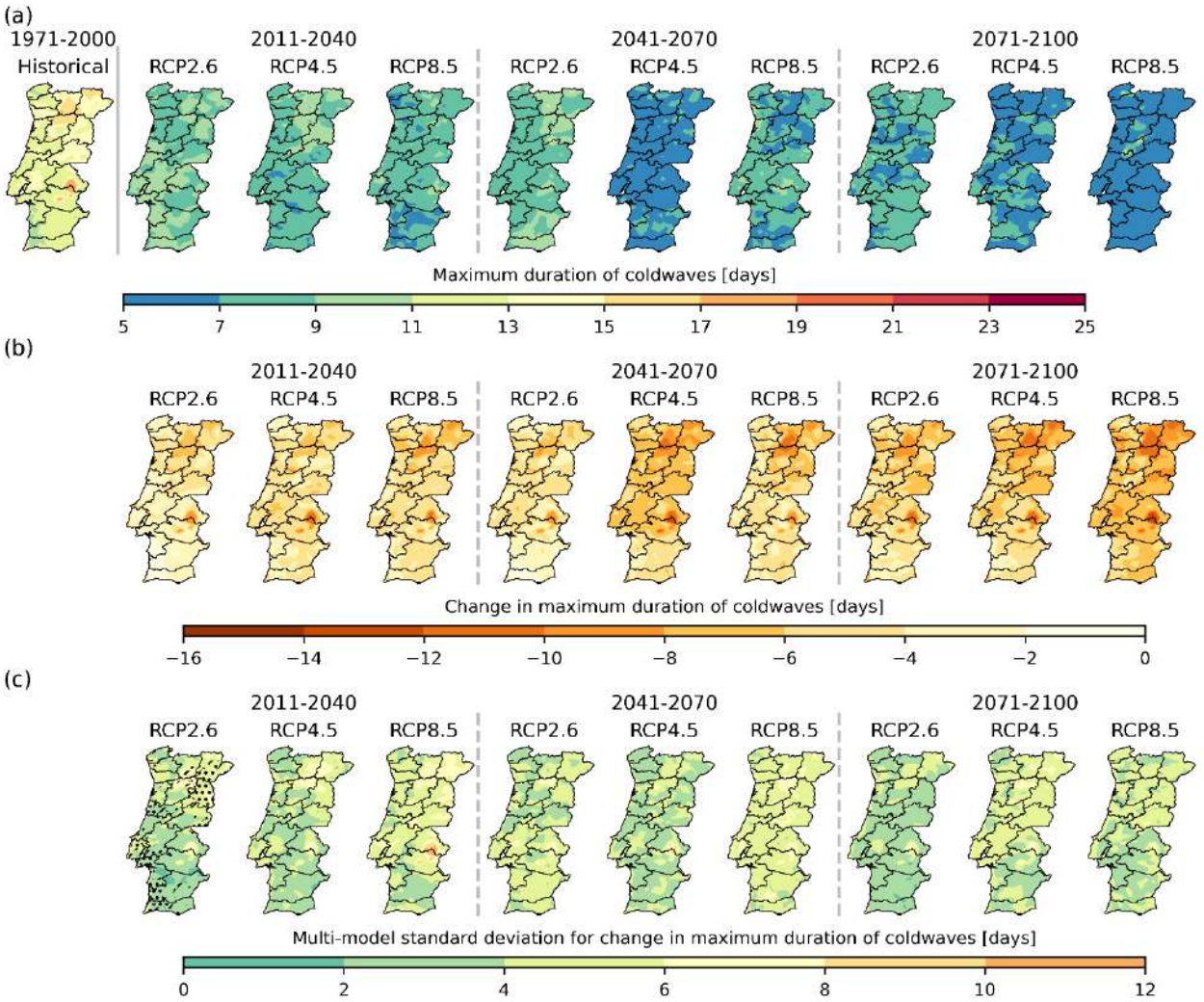

Figure 6.19 (a) Maximum duration of coldwaves over mainland Portugal, for historical period (1971-2000) and for the future periods considering different GHG emission scenarios. (b) Future projected changes in the maximum duration of coldwaves, considering the 1971-2000 period as reference. (c) Multi-model spread in future projected changes in maximum duration of coldwaves, considering the 1971-2000 period as reference. The spread is quantified by the standard deviation of the anomalies between different models. Grid-points where the change signal does not agree in at least 66% of the models is identified by dotted hatching (no occurrences for HWD).

6.2. Precipitation Extremes

Maximum of 5-day accumulated precipitation is displayed in Figure 6.20. Overall, during 1971-2000, the values are shown to be higher in the northwestern portion of mainland Portugal, generally between 300 mm and 500 mm, but locally surpassing 600 mm in the region of Peneda-Gerês National Park (Figure 6.20a). While the geographic pattern of the maximum 5-day accumulated precipitation is projected to remain similar in the future, the associated values are expected to increase throughout most of the territory. For the 2011-2040, 2041-2070 and 2071-2100 periods, projected increases up to 80 mm (all scenarios), 120

mm (RCP4.5) and 200 mm (RCP8.5) are visible in Figure 6.20b, respectively. Such results indicate that, in the future, rainfall is projected to become more concentrated into shorter time frames. The consistency and spreads of the ensemble projections, in Figure 6.20c, show that while the members tend to agree on the signal of the projected changes (except for the RCP2.6 scenario during 2011-2040), their uncertainty is, most of the times, comparable to the overall projections.

Number of days with precipitation exceeding 1 mm is shown in Figure 6.21. Figure 6.21a shows that precipitation values above 1 mm per day are most common in the northwestern portion of the mainland Portugal, as in Figure 6.20a, exceeding 140 days per year. In the opposite end is south-eastern Portugal, showing values between 60 to 80 days per year. While the changes in the projections for the 2011-2040 period are negligible, a projected reduction in the number of rainy days (above 1 mm) is clearly noticeable from 2041 onwards, especially considering the RCP4.5 and RCP8.5 scenarios (Figure 6.21b). In fact, for the 2041-2070 period, this reduction is set at -6 to -12 days (-12 to -18 days) for RCP4.5 (RCP8.5), peaking during 2071-2100 for RCP8.5, where areas ranging from -30 to -36 days (-18 to -24 days) are visible in the North (South and Interior) of the country. On a national scale, such projections correspond, roughly, to a 1/3 decrease in the number of days with more than 1 mm of precipitation. Figure 6.21c shows high consistency between the ensemble members on the sign of the projected changes, along with low uncertainties (spread) in comparison to their overall magnitude.

Number of days with precipitation exceeding 20 mm is presented in Figure 6.22. Figures A20 and A21, in the Supplementary Material, show similar indices, however, considering a threshold of 10 mm and 50 mm, respectively. Again, the region of the country showing the more frequent threshold exceedances is the northwestern, roughly between Aveiro and Viana do Castelo, for which rainy days above 10 mm, 20 mm and 50 mm occur between 40 and 80 days, 20 and 50 days and 4 and 18 days per year, respectively, during the 1971-2000 reference period. Considering the 2011-2040 period, in Figure 6.22b (as well as Figure A20b and Figure A21b, in the Supplementary Material), projections show negligible changes for all scenarios (similarly to Figure 6.21b). For the 2041-2070 period, a reduction in the number of moderate to heavy rainy days is detectable, for the 10 mm (-4 to -12 days) and 20 mm (-2 to -8 days) thresholds. These are still negligible for the RCP2.6 scenario, and more dominant for RCP8.5. By the end of the 21st century (2071-2100), while the projections stabilize for the RCP4.5, a worsening of the drying conditions is expected under RCP8.5. For the 10 mm and 20 mm thresholds, the number of rainy days is expected to decrease by 12 to 20, and 4 to 12, respectively, along the western half of Portugal mainland. Note that, for the 50 mm threshold, the frequency of exceedance is not projected to change considerably (Figure A21b in the Supplementary Material), except under RCP8.5 after 2041, in the northwesternmost part of the country (Peneda-Gerês National Park), where a reduction down to -2 days is visible. The uncertainty associated to

this projection is, however, greater than its magnitude. For the remaining thresholds (in Figure 6.22c and Figure A20c in the Supplementary Material), the ensemble members tend to agree on their climate change signal, and the uncertainties are relatively low.

Duration of periods with consecutive rainy days (accumulation greater than 1 mm/day) is shown in Figure 6.23. Along mainland Portugal, during 1971-2000, values range from 1.5 up to 4 days. As before, lower (greater) values are visible for the south-eastern (north-western) portions of the country. In this instance, the projections only tend to assume non-negligible changes for the RCP8.5 scenario, for which the average duration of precipitation is projected to reduce by 0.2 to 0.6 days, especially during 2071-2100. The robustness of such projection is asserted by the associated spread, below 0.2 days.

Maximum number of consecutive rainy days (more than 1 mm/day) is presented in Figure 6.24. During 1971-2000 (Figure 6.24a), accumulated precipitation values above 1 mm can happen, consecutively, for 10-15 days (30-40 days) in the southeast (northwest) of mainland Portugal. Such durations are consistent with the dry (wet) climate of the South (North) of the country, as previously shown. The projections for this index, in Figure 6.24b, show quite different patterns for each of the future periods and scenarios. During 2011-2040, the number of consecutive rainy days is projected to reduce in the central region of the country, especially under RCP2.6 and RCP8.5, down to -8 days per year. In the South (RCP2.6) and North (RCP8.5), however, the maximum duration of rainy periods is projected to increase, up to 10 and 14 days, respectively. For the 2041-2070 period, the projected patterns are different, with an expected increase through most of the country for RCP2.6 (up to 12 days), and a widespread decrease of slightly lower magnitude for RCP8.5 (down to -8 days). By the end of the 21st century, the extensive projected reduction in the maximum consecutive rainy days under RCP8.5, for the entire country should be highlighted. For this scenario, the decline in the central and southwestern regions, has a maximum of -14 days per year. While high consistency between ensemble members regarding the projected change signal is visible in Figure 6.24c, the uncertainty is comparable to the magnitude of the projections in all instances, except for the 2071-2100 RCP8.5 period, for which precipitation was shown to be projected to become more concentrated into shorter time frames.

Percentage of total precipitation originating from days with accumulated values exceeding 10 mm is shown in Figure 6.25. During 1971-2000, values between 60% and 90% are visible for the entire coastal stretch of mainland Portugal, with highest values along the northern portion. Values between 30% and 60% are observable in the interior regions. Especially during autumn and winter, the mostly westerly flux driven by the displacement of the Azores high-pressure system towards lower latitudes favours the transit of convective systems over the northern and central coastal areas. The topography north of the Tagus river

preclude that moisture from reaching the regions near the Spanish border, leading to lower accumulations (Figure 6.25a). The projected changes, nevertheless, show that it is the interior of the country that may expect a bigger portion of its total accumulated values to originate from days with more than 10 mm of precipitation, in the future. From +2% to +8% for both the 2011-2040 and 2041-2070 periods, up to +10% and +12% for the 2071-2100 period, under RCP4.5 and RCP8.5, respectively. Such projections are consistent with increased accumulated values in shorter time frames (as supported by Figure 6.20, Figure 6.23 and Figure 6.24), possibly resulting from greater atmospheric instability and enhanced convective activity (mesoscale precipitation phenomena) in these regions. Figure 6.25c shows that most of the ensemble members agree on the signal of the referred projections. The uncertainty, while comparable to the magnitude of the projected changes along the coastal areas, tends to be proportionally lower in the interior regions, allowing robust projections.

Percentage of total precipitation originating from days with accumulated values exceeding 50 mm is presented in Figure 6.26. In Figure 6.26a, it is visible that for most of the country, less than 5% of the total annual mean precipitation originates from days with accumulated values above 50 mm. The exception is the northwesternmost part of mainland Portugal, revealing percentages up to 40%. The projections associated to this index, in Figure 6.26b, show overall increases in the average percentages, generally within +2% to +4% assuming greater values for the 2071-2100 period and RCP8.5 scenario (up to +10% along the northern coastlines). Such results indicate that while moderate precipitation days (~ 10 mm/day) are expected to play a bigger role in the interior regions in the future, heavy rainy days and extreme events (above 50 mm/day) are projected to increase throughout most of mainland Portugal. Similarly, to Figure 6.25c, in Figure 6.26c, while high consistency is visible between ensemble members, the overall uncertainty is also relatively high.

Maximum number of consecutive dry days (less than 1 mm/day) is shown in Figure 6.27. During 1971-2100 (Figure 6.27a), consecutive drying conditions can occur for 40-60 days (120-140 days) in the northwest (southeast) of mainland Portugal, compatible with the longer and dryer summer seasons along the Alentejo and Algarve regions. For the 2011-2040 period, the projections indicate slightly longer periods without considerable precipitation (or less than 1 mm/day), for all scenarios, mostly ranging between +5 and +30 days (RCP2.6 and RCP4.5) but peaking at +45 days along the central littoral regions, for RCP8.5 (Figure 6.27b). During 2041-2070, an aggravation of the drying conditions is expected, mostly for the RCP4.5 and RCP8.5, for which most of the country shows an increase between 15 and 30, in the consecutive dry days. By the end of the 21st century, the RCP8.5 shows further exacerbation, with projected changes between +30 and +60 days throughout most of Portugal mainland, peaking close to +75 days in the northeast (Guarda district; from 80 to 100 days during the reference period to an expected 140 to 160 days). Figure

6.27c shows, similarly to the previous ones, a good degree of agreement between ensemble members on the signal of the projected changes, even for RCP2.6 during 2011-2040 (which usually shows the most disparity). The uncertainty, while generally lower than the climate change signal, can attain similar magnitude especially in the interior regions (*e.g.*, Figure 6.27c, for 2071-2100 under RCP8.5). This may be due to the projected increase in moderate to heavy rainy days there (Figure 6.25c and Figure 6.26c), associated to mesoscale meteorological phenomena, leading to greater uncertainty in the overall maximum duration of consecutive dry days.

Return levels associated with 10-, 30-, 50-, and 100-years events for daily precipitation are displayed in Figure 6.28 for the five regions of NUTS II. Looking to Figure 6.28, the return levels increase when considering a higher return period, and there is a sub-regional variability in return levels. The Norte is the region with the higher return levels when compared with the other, but also with the higher variability between the models. Considering the historical period, a return level of 100 mm in a day is expected to occur every 10 years, increasing to around 220 mm in every 100 years in the Norte region. For the A.M. Lisboa, the return levels are quite similar for each return period, around 100 mm in a day. There is a rising in return levels throughout the 21st century strongest in the non-mitigation scenario. For the end-of-century and assuming the worst-case scenario, it is expected that every 10 years an extreme precipitation of about 150 mm occurs during a day, increasing to 260 mm every 100 years. For the remaining regions an increase is also expected but below 200 mm in a day. The results of 50- and 100-years events need to carefully analyse since the return levels were computed with a 30-y distribution, which may increase the uncertainty in both results.

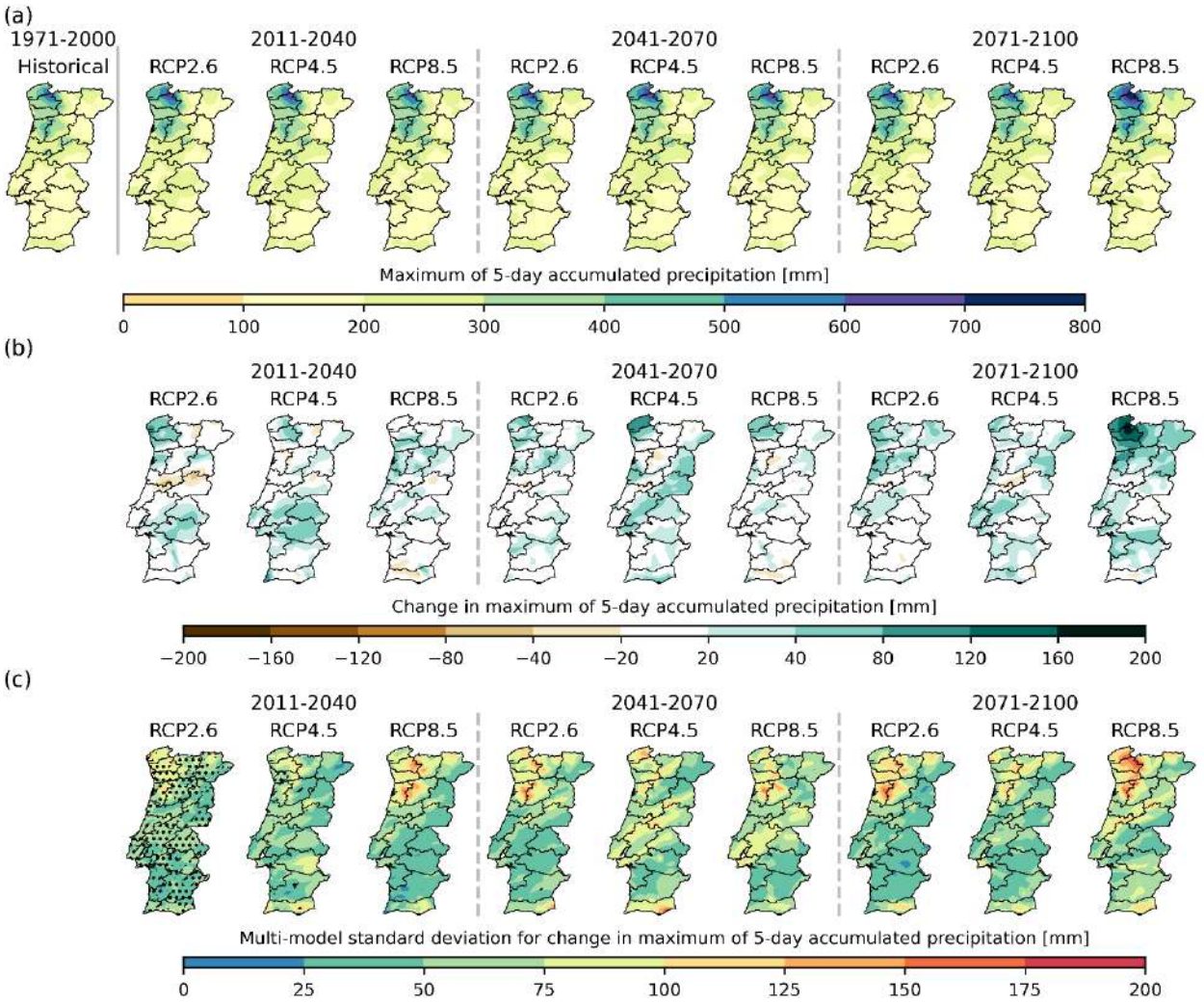

Figure 6.20 (a) Annual climatology of maximum of 5-day accumulated precipitation for historical period (1971-2000) and for the future periods considering different GHG emission scenarios. (b) Future projected changes in maximum cumulative precipitation over 5 days period over mainland Portugal, considering the 1971-2000 period as reference. (c) Multi-model spread in future projected changes in maximum cumulative precipitation over 5 days period over mainland Portugal, considering the 1971-2000 period as reference. The spread is quantified by the standard deviation of the anomalies between different models. Grid-points where the change signal does not agree in at least 66% of the models is identified by dotted hatching.

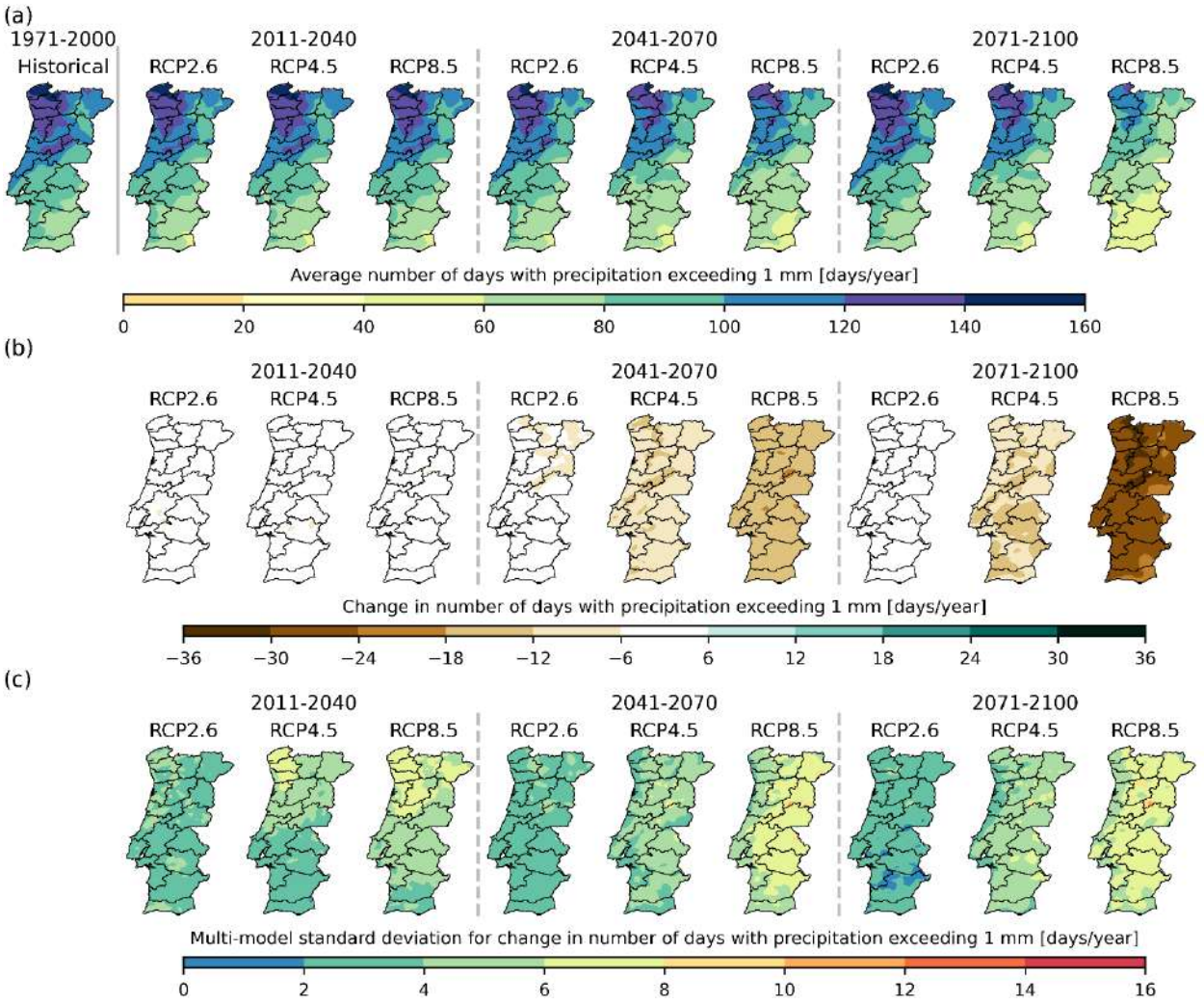

Figure 6.21 (a) Annual average number of days with precipitation exceeding 1 mm for historical period (1971-2000) and for the future periods considering different GHG emission scenarios. (b) Future projected changes in average number of days with precipitation exceeding 1 mm over mainland Portugal, considering the 1971-2000 period as reference. (c) Multi-model spread in future projected changes in average number of days with precipitation exceeding 1 mm over mainland Portugal, considering the 1971-2000 period as reference. The spread is quantified by the standard deviation of the anomalies between different models. Grid-points where the change signal does not agree in at least 66% of the models is identified by dotted hatching.

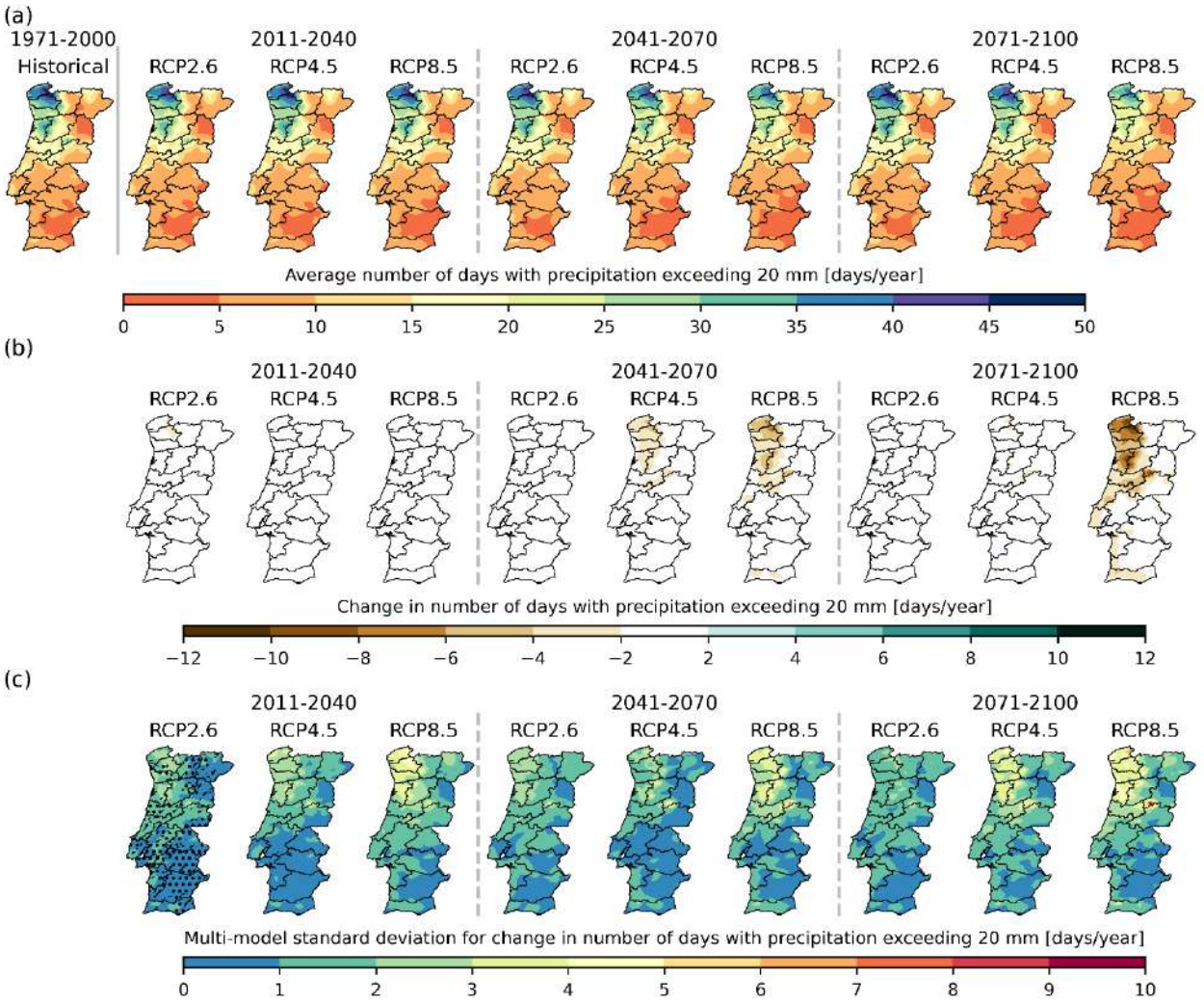

Figure 6.22 (a) Annual average number of days with precipitation exceeding 20 mm for historical period (1971-2000) and for the future periods considering different GHG emission scenarios. (b) Future projected changes in average number of days with precipitation exceeding 20 mm over mainland Portugal, considering the 1971-2000 period as reference. (c) Multi-model spread in future projected changes in average number of days with precipitation exceeding 20 mm over mainland Portugal, considering the 1971-2000 period as reference. The spread is quantified by the standard deviation of the anomalies between different models. Grid-points where the change signal does not agree in at least 66% of the models is identified by dotted hatching.

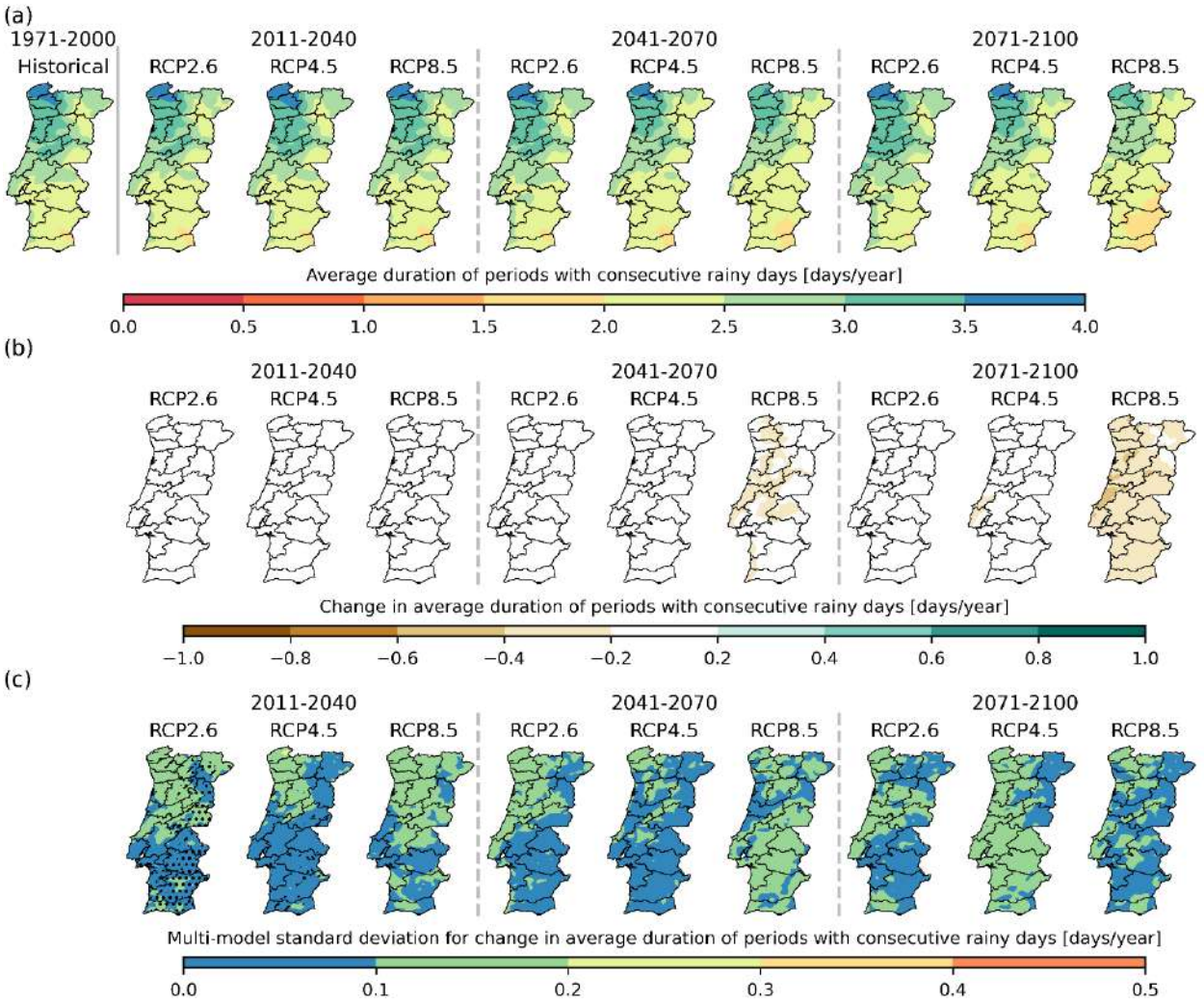

Figure 6.23 (a) Annual average duration of periods with consecutive rainy days (precipitation exceeding 1 mm/day) for historical period (1971-2000) and for the future periods considering different GHG emission scenarios. (b) Future projected changes in average duration of periods with consecutive rainy days over mainland Portugal, considering the 1971-2000 period as reference. (c) Multi-model spread in future projected changes in average duration of periods with consecutive rainy days over mainland Portugal, considering the 1971-2000 period as reference. The spread is quantified by the standard deviation of the anomalies between different models. Grid-points where the change signal does not agree in at least 66% of the models is identified by dotted hatching.

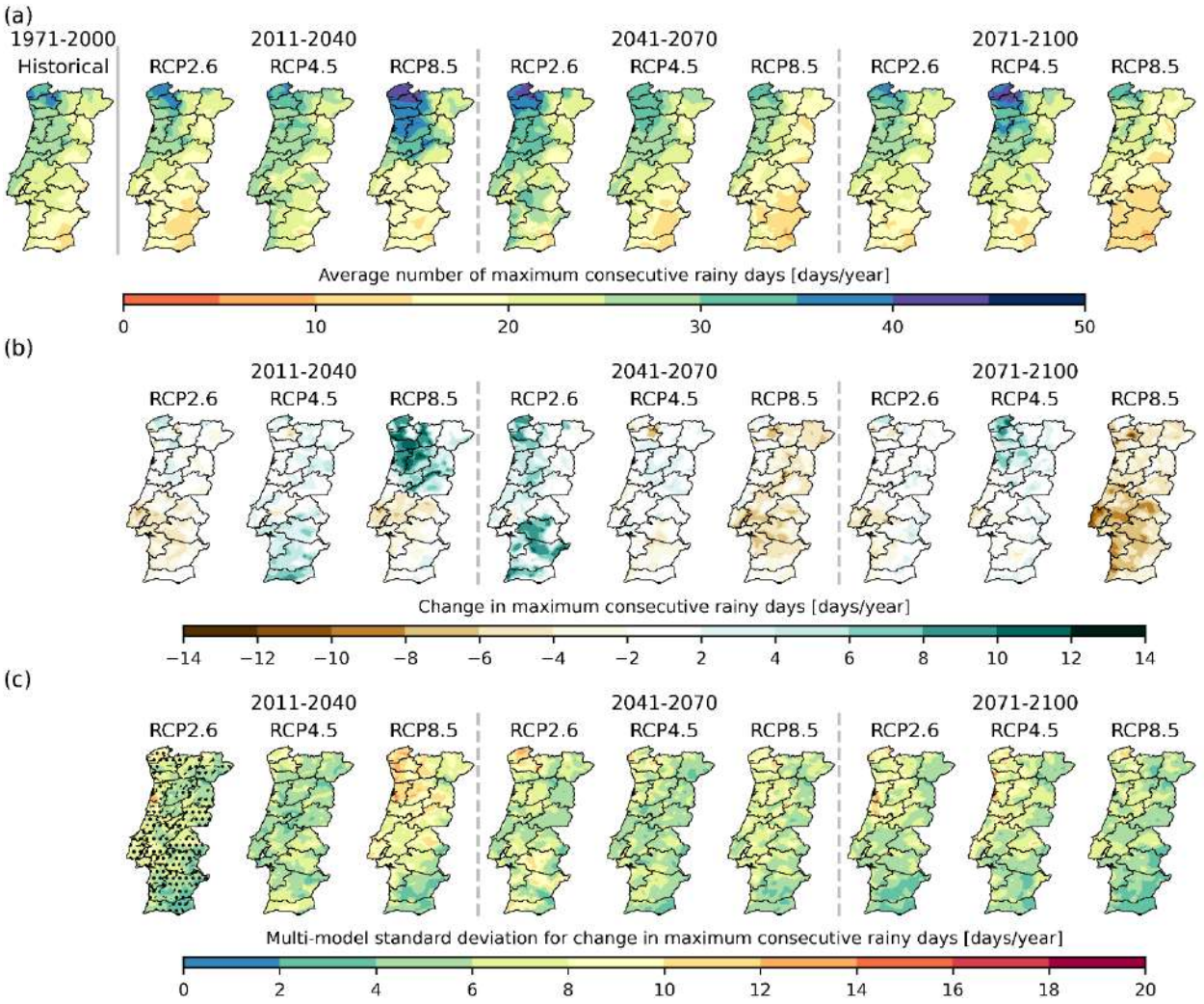

Figure 6.24 (a) Annual average number of maximum consecutive rainy days (precipitation exceeding 1 mm/day) for historical period (1971-2000) and for the future periods considering different GHG emission scenarios. (b) Future projected changes in average number of maximum consecutive rainy days over mainland Portugal, considering the 1971-2000 period as reference. (c) Multi-model spread in future projected changes in average number of maximum consecutive rainy days over mainland Portugal, considering the 1971-2000 period as reference. The spread is quantified by the standard deviation of the anomalies between different models. Grid-points where the change signal does not agree in at least 66% of the models is identified by dotted hatching.

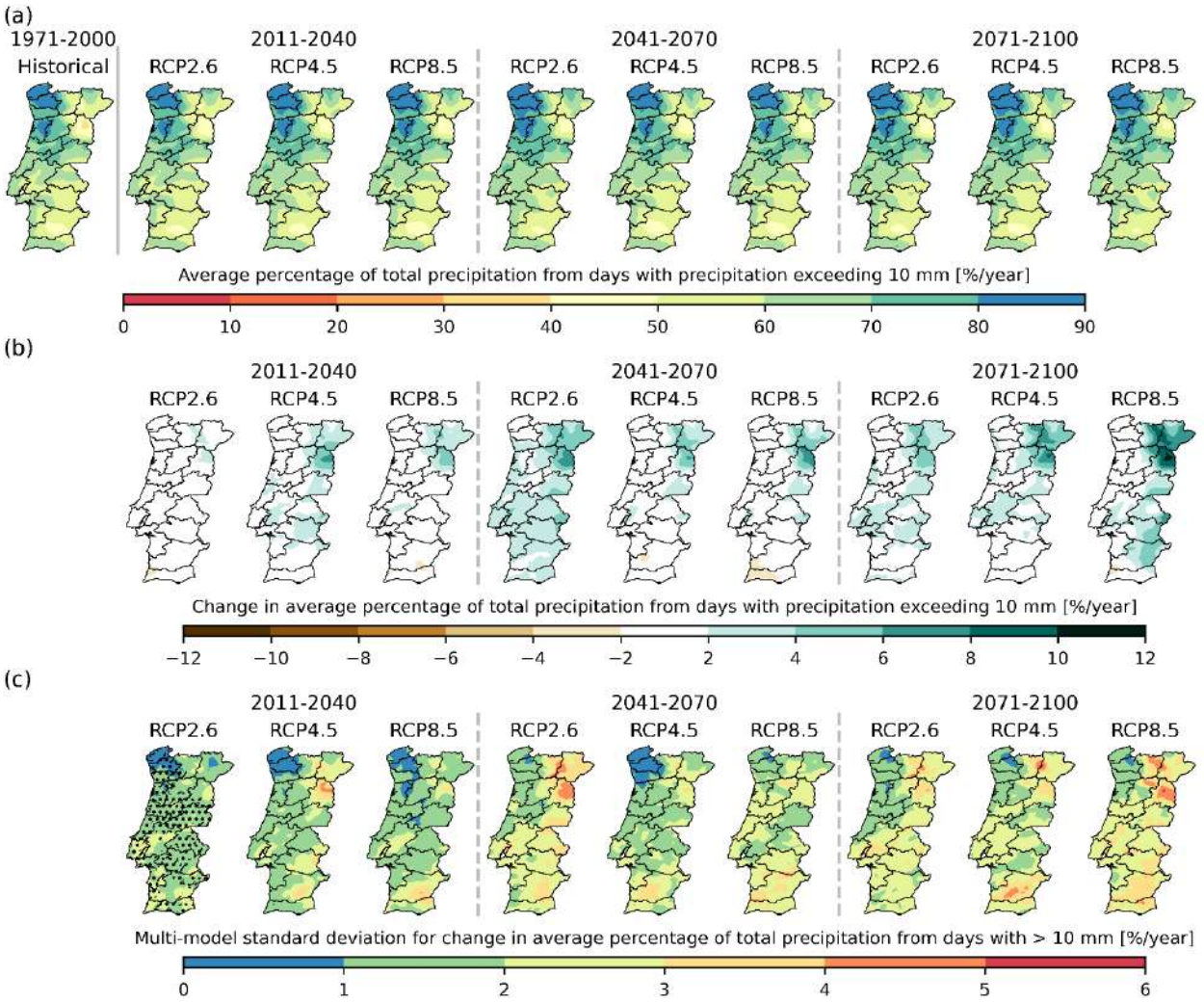

Figure 6.25 (a) Annual average percentage of total precipitation from days with precipitation exceeding 10 mm for historical period (1971-2000) and for the future periods considering different GHG emission scenarios. (b) Future projected changes in average percentage of total precipitation from days with precipitation exceeding 10 mm over mainland Portugal, considering the 1971-2000 period as reference. (c) Multi-model spread in future projected changes in average percentage of total precipitation from days with precipitation exceeding 10 mm over mainland Portugal, considering the 1971-2000 period as reference. The spread is quantified by the standard deviation of the anomalies between different models. Grid-points where the change signal does not agree in at least 66% of the models is identified by dotted hatching.

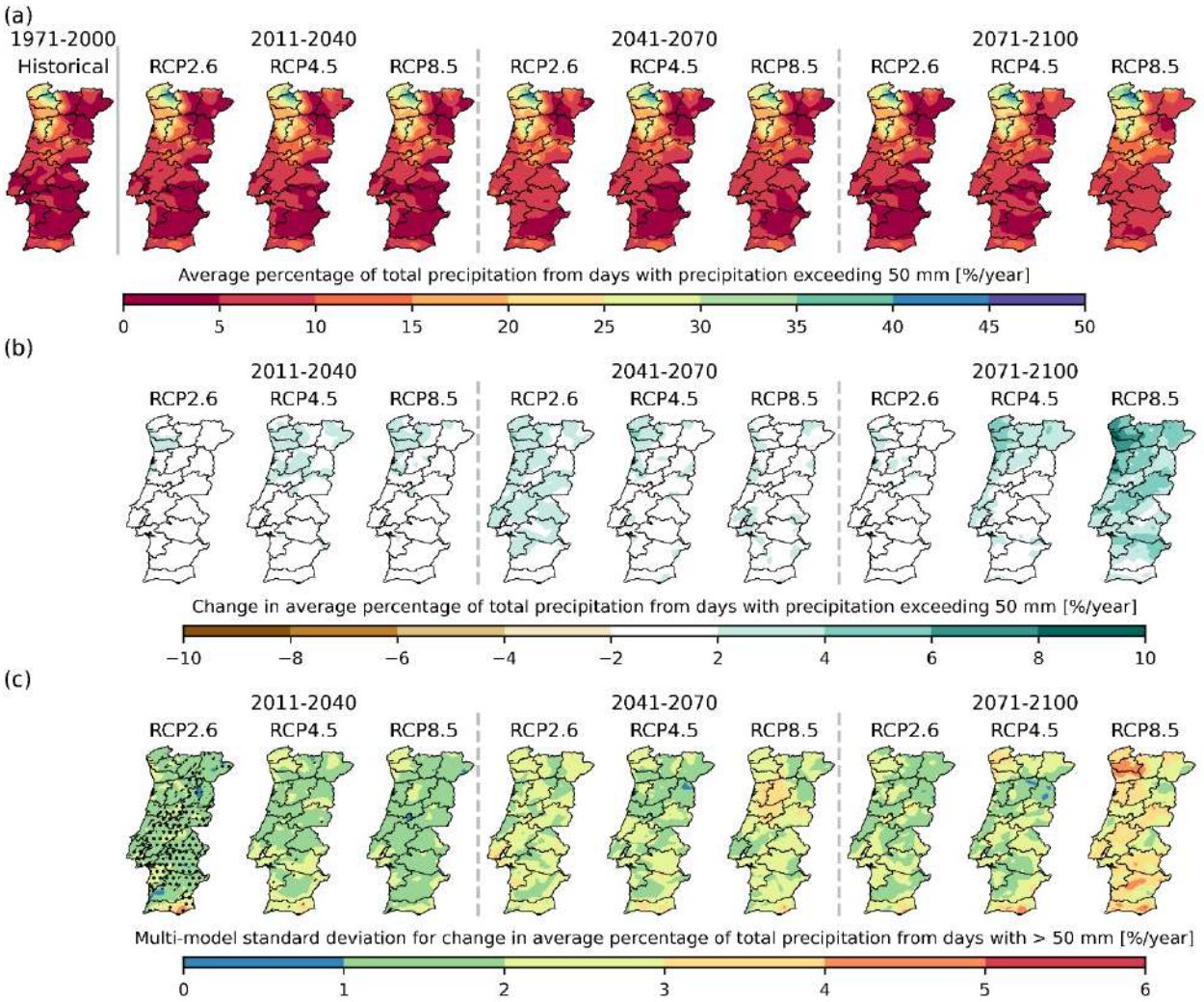

Figure 6.26 (a) Annual average percentage of total precipitation from days with precipitation exceeding 50 mm for historical period (1971-2000) and for the future periods considering different GHG emission scenarios. (b) Future projected changes in average percentage of total precipitation from days with precipitation exceeding 50 mm over mainland Portugal, considering the 1971-2000 period as reference. (c) Multi-model spread in future projected changes in average percentage of total precipitation from days with precipitation exceeding 50 mm over mainland Portugal, considering the 1971-2000 period as reference. The spread is quantified by the standard deviation of the anomalies between different models. Grid-points where the change signal does not agree in at least 66% of the models is identified by dotted hatching.

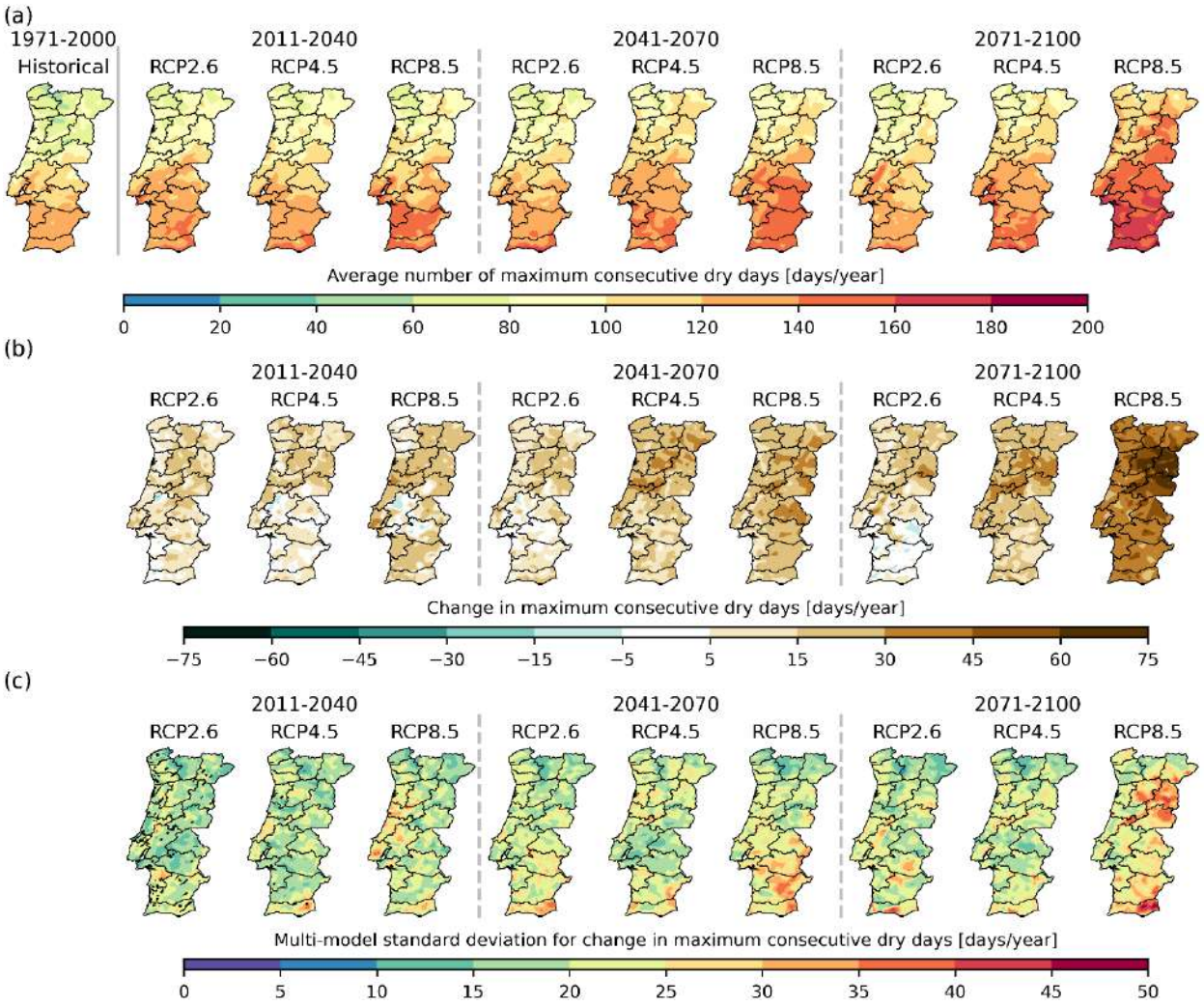

Figure 6.27 (a) Annual average number of maximum consecutive dry days (precipitation below 1 mm/day) for historical period (1971-2000) and for the future periods considering different GHG emission scenarios. (b) Future projected changes in average number of maximum consecutive dry days over mainland Portugal, considering the 1971-2000 period as reference. (c) Multi-model spread in future projected changes in average number of maximum consecutive dry days over mainland Portugal, considering the 1971-2000 period as reference. The spread is quantified by the standard deviation of the anomalies between different models. Grid-points where the change signal does not agree in at least 66% of the models is identified by dotted hatching.

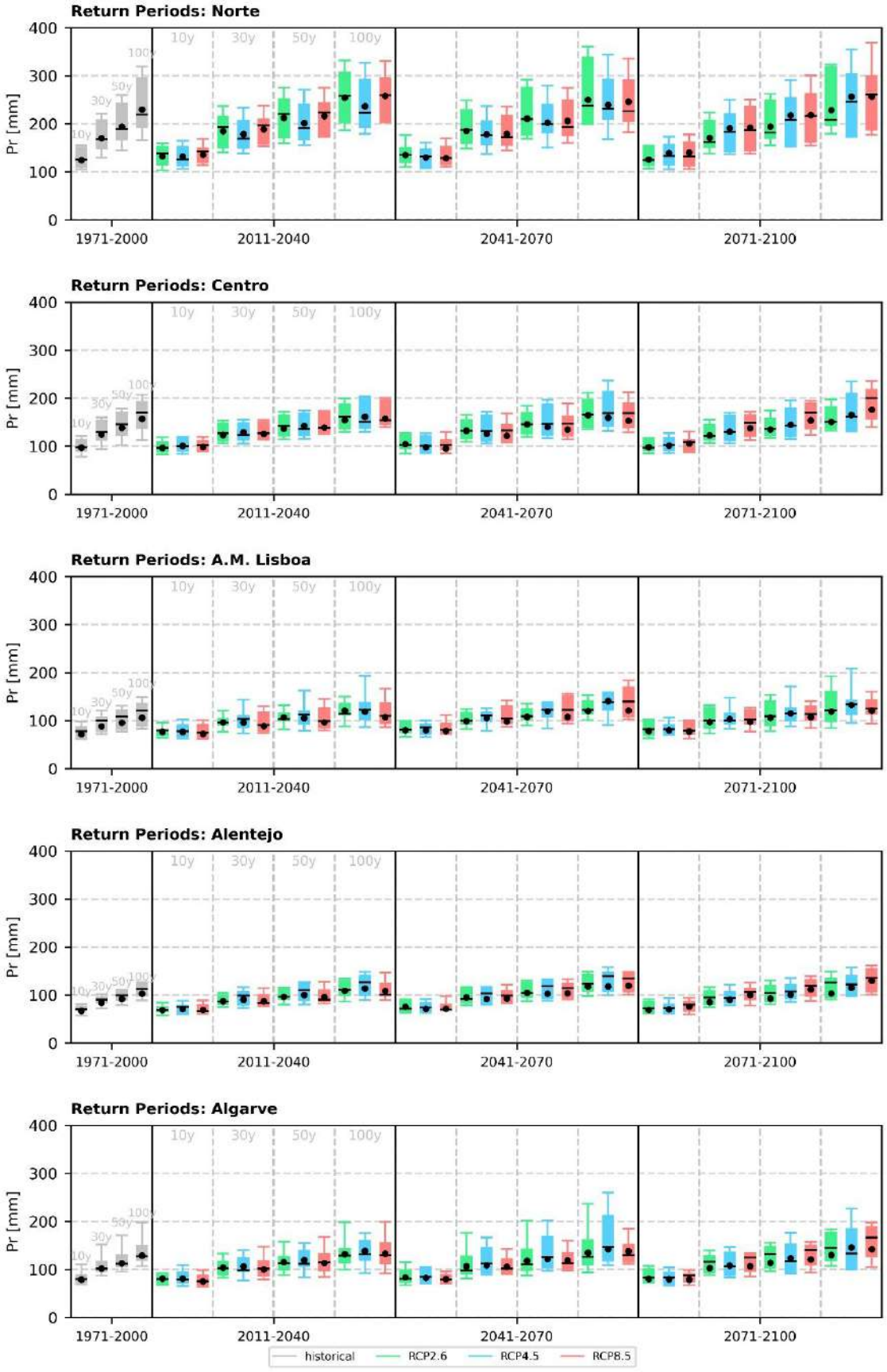
Return Periods: Norte
Return Periods: Centro
Return Periods: A.M. Lisboa
Return Periods: Alentejo
Return Periods: Algarve
Pr [mm]
0
100
200
300
400
10y
30y
50y
100y
1971-2000
2011-2040
2041-2070
2071-2100
historical
RCP2.6
RCP4.5
RCP8.5

Figure 6.28 Return levels associated with 10-, 30-, 50-, and 100-years events for daily precipitation for NUTS II regions: Norte, Centro, A.M. Lisboa, Alentejo and Algarve, from top to bottom. Three future periods are shown: 2011-2040, 2041-2070, and 2071-2100, under all emission scenarios – RCP2.6 (green), RCP4.5 (blue) and RCP8.5 (red), with historical period (grey) for 1971-2000 period. The black point represents the multi-model ensemble mean.

6.3. Wind Extremes

Maximum daily mean 10-m wind speed is presented in Figure 6.29. The annual climatology for historical period shows differences between the coastal regions, where the 10-m wind speed can reach its maximum around 15 m/s, and the interior regions where the maximum wind speed at 10 m is below 10 m/s (Figure 6.29a). For future scenarios and periods, this pattern is similar to historical period, however there are small changes for all periods and scenarios (Figure 6.29b), with small associated uncertainties (Figure 6.29c). The anomalies referent to the historical period clearly shows a decrease of the maximum daily mean wind speed in the Alentejo and centre regions for all periods and scenarios, which can reach -2 m/s. In the northwestern region, an increase in maximum daily mean 10-m wind speed is projected, but its positive anomalies depend on the RCP: the RCP8.5 shows an increase that can reach +2 m/s at the end of the century; for RCP4.5 the positive anomalies are higher at mid-century of about +1 m/s. At least 66% of the models agree in the change signal for all grid-points and scenarios for mid- and end-century. For the beginning of the century, in all RCPs, some grid-points do not agree in the climate change signal.

Maximum of daily maximum wind gust is displayed in Figure 6.30. Winter storms are the most important cause for the occurrence of wind gusts in mainland Portugal. For historical period, the maximum values are found in the northwestern regions, exceeding 32 m/s (Figure 6.30a). Along the west and south coastal regions the maximum of wind gust can reach 34 m/s. In the interior regions, the maximum of wind gust does not exceed 30 m/s. For future scenarios and periods, this pattern is similar to historical period, however there are small changes for all periods and scenarios (Figure 6.30b). For the beginning of the century, all RCPs agree in the increase of maximum wind gust in the Lisbon metropolitan area higher than +2 m/s. For mid- and end-of-century, the RCP2.6 project a rising in maximum wind gust in most of the country. In RCP4.5 and RCP8.5, for mid-of-century, a reduction in maximum wind gust is expected in most of the country. In the northwestern regions an increase is projected higher than 1 m/s. For the end-of-century, in the RCP4.5, a rising in maximum wind gust is found in northwestern and southern regions. In what concerns the RCP8.5, a reduction in maximum wind gust is expected south of Tagus River and an increase is projected in some areas north of Tagus River. The multi-model spread is almost as large as the climate change signal (Figure 6.30c).

Return levels associated with 10-, 30-, 50-, and 100-years events for daily maximum wind gusts are displayed in Figure 6.31 for the five regions of NUTS II. As for precipitation, the Norte is the region where the return levels of maximum wind gust are higher, followed by the A.M. Lisboa, where a maximum value of 31 m/s and 30 m/s (35.5 m/s and 34 m/s) in a day occurs every 10 (100) years during the historical period. The future projections point to a general slight reduction in the return level for each return period considered. For 2071-2100 and for all the return periods, the RCP8.5 scenario displays slightly lower return levels when compared to the other two future scenarios, noticeable especially in the South area. The projections from RCP2.6 and RCP4.5 emission scenarios are relatively similar, with projected increases (decreases) mainly in the A.M. Lisboa and Centro (remaining) regions.

Number of days with daily mean 10-m wind speed exceeding 5.5 m/s, in Figure 6.32, show that over continental Portugal, in the historical period between 0-60 days per year, the daily mean 10-m wind speed exceeds 5.5 m/s (Figure 6.32a). However, in the Lisbon metropolitan area the number of days is greater than 100. For the end of the century and assuming the worst-case scenario, a reduction in the number of days is projected for the entire country, where the northern regions show less 12 days per year with daily mean 10-m wind speed exceeding 5.5 m/s (Figure 6.32b). These regions also show the higher standard deviation values (Figure 6.32c). At least 66% of the models agree in the change signal for all grid-points, scenarios, and periods, except for RCP2.6 in the beginning of the century in some grid-points where there are small changes.

Number of days with daily mean 10-m wind speed exceeding 10.8 m/s is displayed in Figure 6.33. This index has values close to 0 over continental Portugal, except in the Lisbon metropolitan area and in an area in the northern border (Figure 6.33a). Here, the number of days with daily mean 10-m wind speed exceeding 10.8 m/s is around 4 days. For future scenarios, the pattern remains similar, with a small decrease in the number of days in these two areas, which can reach -1 day/year (Figure 6.33b). Although the anomalies referent to historical period are very small, overall, at least 66% of the models agree in the climate change signal.

Calm days (number of days with daily mean 10-m wind speed below 2 m/s) are presented in Figure 6.34. The historical period shows a north cluster of calm days in continental Portugal, ranging between 80 – 160 days, whereas the remaining territory (centre and south regions) is mainly defined by 0 – 80 calm days per year (Figure 6.34a). For future scenarios, there is a gradual increase in the number of calm days over the northwestern region of continental Portugal (Figure 6.34b). For the end of the century and for the worst-case scenario, the northwestern region presents an increase in the number of calm days that can reach +16 days per year. The largest standard deviations are found in this region of continental Portugal (7 to 10 days), coinciding with the larger positive anomalies (Figure 6.34c). At least 66% of the models agree in the change

signal for all grid-points, scenarios, and periods, except for RCP2.6 in the beginning of the century in some grid-points where there are small changes.

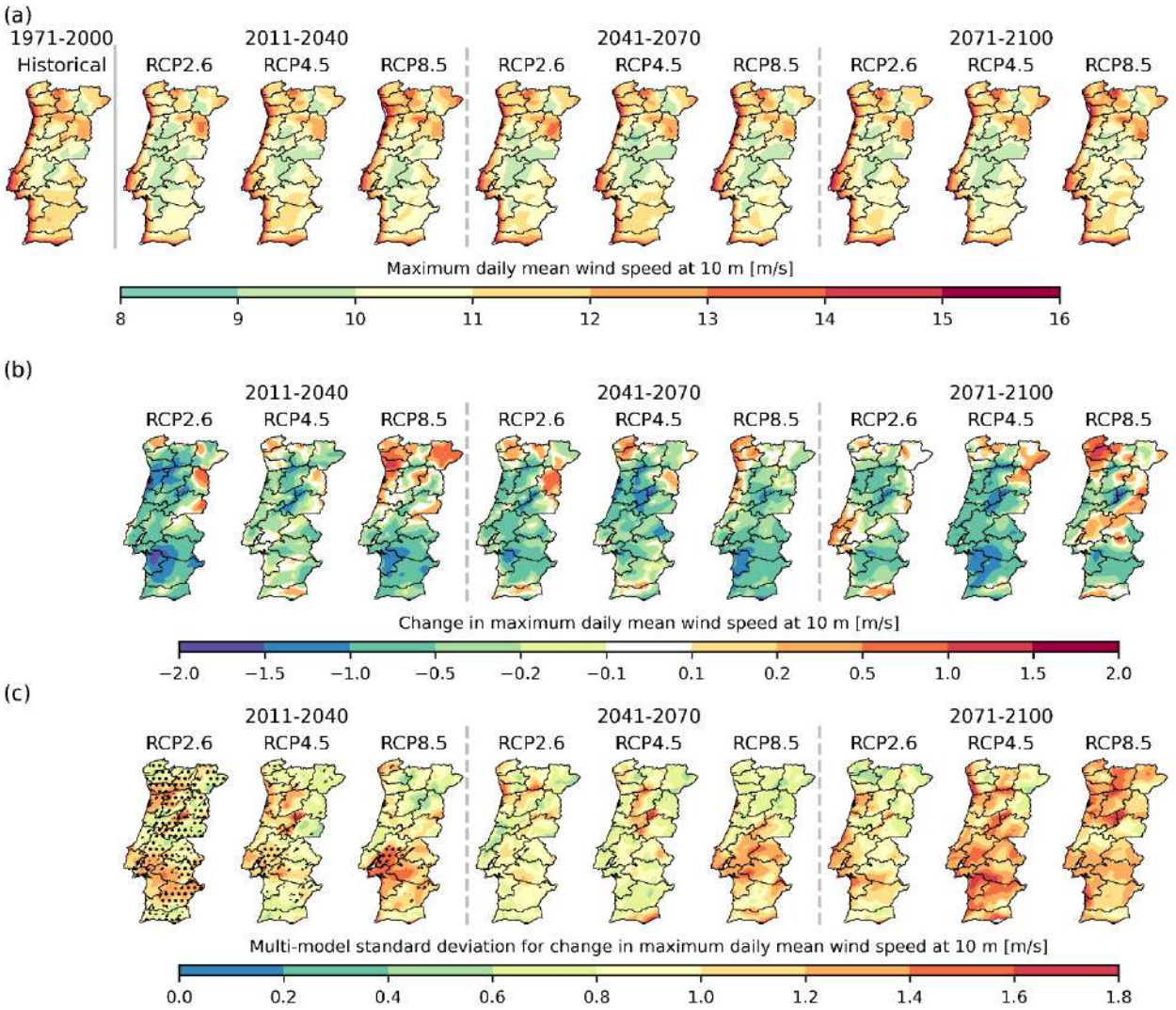

Figure 6.29 (a) Maximum daily mean wind speed at 10 m for historical period (1971-2000) and for the future periods considering different GHG emission scenarios. (b) Future projected changes in maximum daily mean wind speed at 10 m over mainland Portugal, considering the 1971-2000 period as reference. (c) Multi-model spread in future projected changes in maximum daily mean wind speed at 10 m over mainland Portugal, considering the 1971-2000 period as reference. The spread is quantified by the standard deviation of the anomalies between different models. Grid-points where the change signal does not agree in at least 66% of the models is identified by dotted hatching.

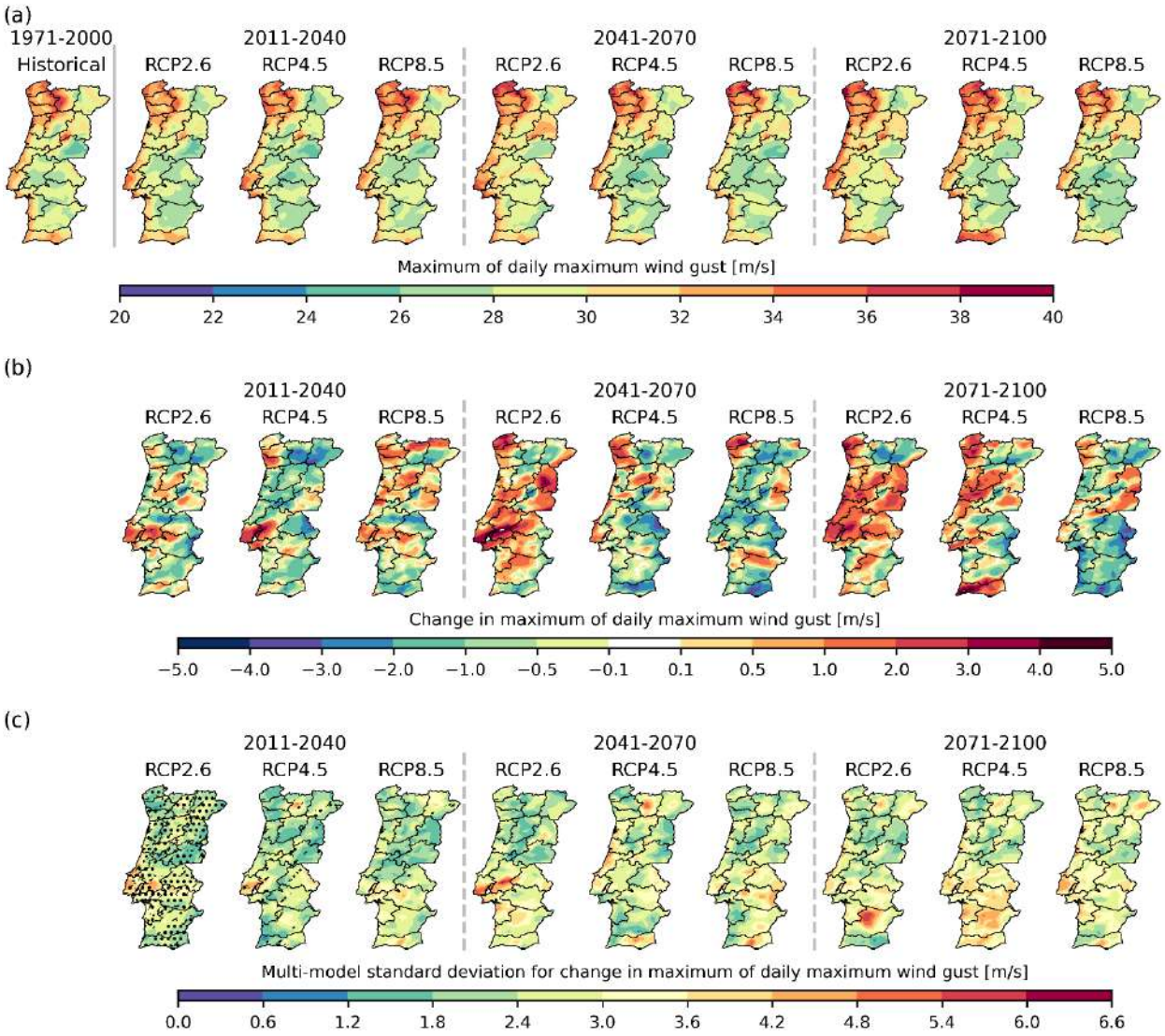

Figure 6.30 (a) Maximum of daily maximum wind gust for historical period (1971-2000) and for the future periods considering different GHG emission scenarios. (b) Future projected changes in maximum of daily maximum wind gust over mainland Portugal, considering the 1971-2000 period as reference. (c) Multi-model spread in future projected changes in maximum of daily maximum wind gust over mainland Portugal, considering the 1971-2000 period as reference. The spread is quantified by the standard deviation of the anomalies between different models. Grid-points where the change signal does not agree in at least 66% of the models is identified by dotted hatching.

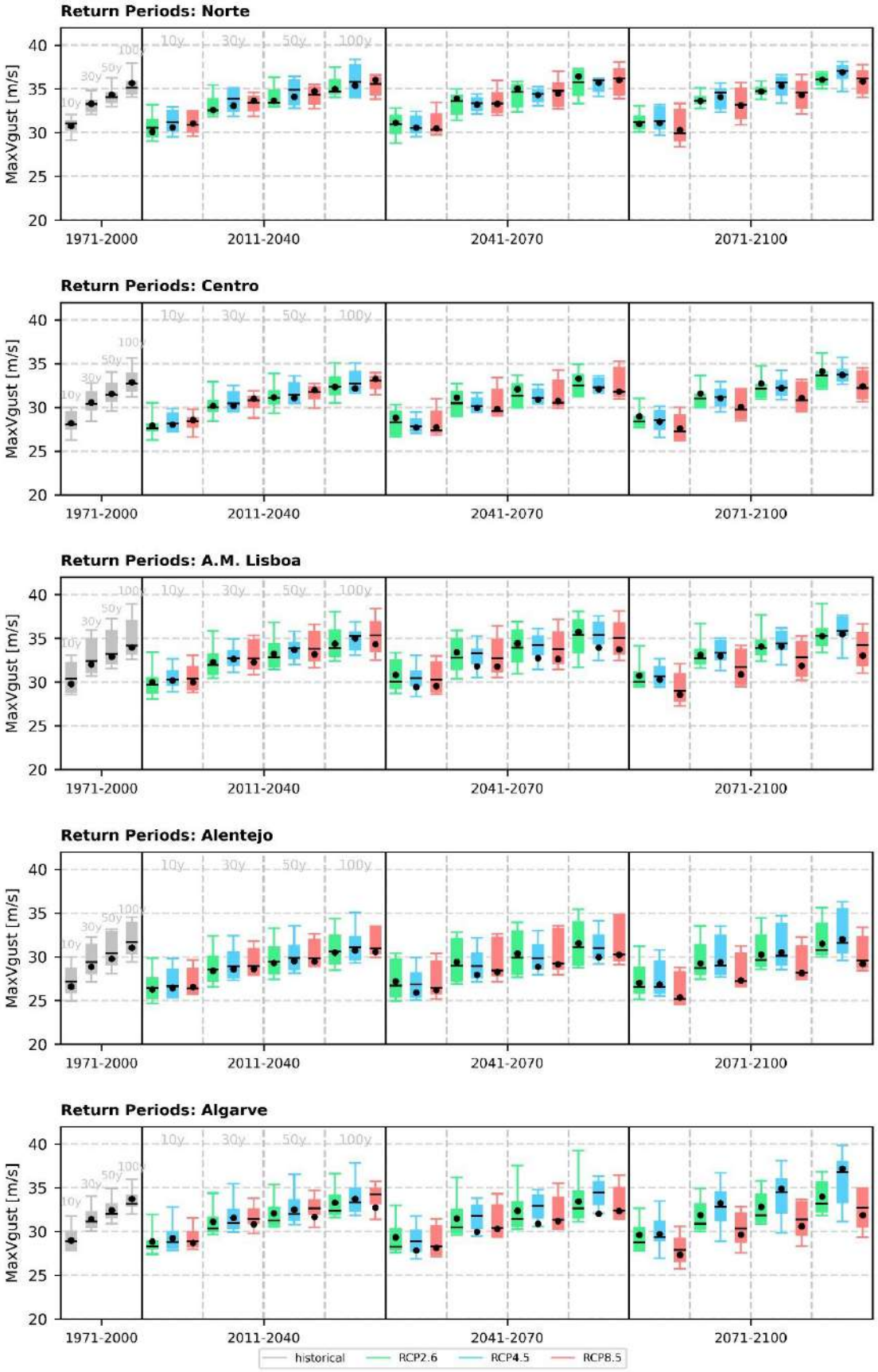
Return Periods: Norte
Return Periods: Centro
Return Periods: A.M. Lisboa
Return Periods: Alentejo
Return Periods: Algarve
MaxVgust [m/s]
10y
30y
50y
100y
1971-2000
2011-2040
2041-2070
2071-2100
historical
RCP2.6
RCP4.5
RCP8.5

Figure 6.31 Return levels associated with 10-, 30-, 50-, and 100-years events for maximum of daily maximum wind gusts for NUTS II regions: Norte, Centro, A.M. Lisboa, Alentejo and Algarve, from top to bottom. Three future periods are shown: 2011-2040, 2041-2070, and 2071-2100, under all emission scenarios – RCP2.6 (green), RCP4.5 (blue) and RCP8.5 (red), with historical period (grey) for 1971-2000 period. The black point represents the multi-model ensemble mean. Individual boxes span from the 25th to the 75th percentile, with the median represented by a straight line, and the whiskers span from 10th to the 90th percentile.

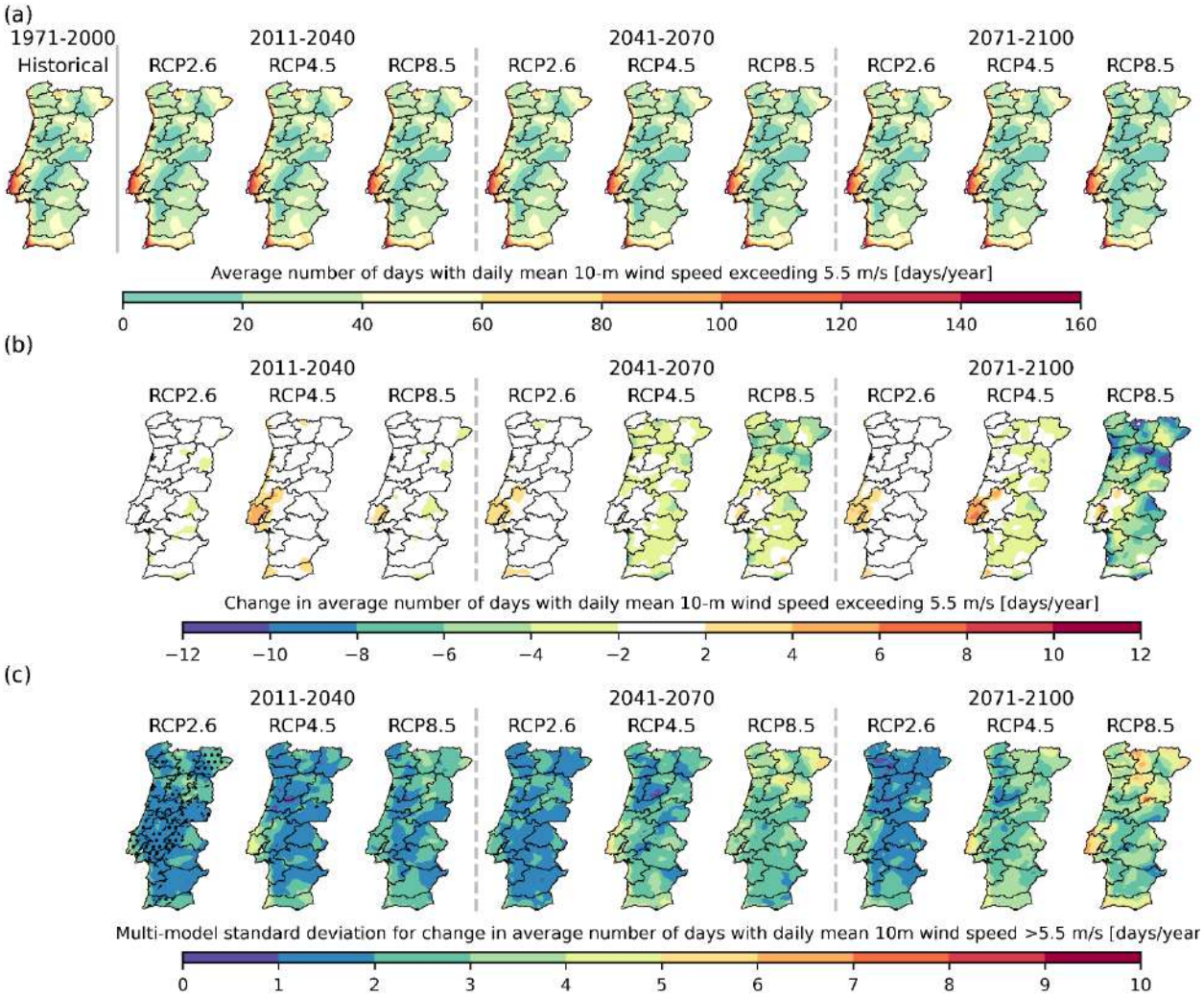

Figure 6.32 (a) Annual average number of days per year where daily mean 10-m wind speed exceeds 5.5 m/s over mainland Portugal, for historical period (1971-2000) and for the future periods considering different GHG emission scenarios. (b) Future projected changes in the average number of days per year where daily mean 10-m wind speed exceeds 5.5 m/s, considering the 1971-2000 period as reference. (c) Multi-model spread in future projected changes in average number of days per year where daily mean 10-m wind speed exceeds 5.5 m/s, considering the 1971-2000 period as reference. The spread is quantified by the standard deviation of the anomalies between different models. Grid-points where the change signal does not agree in at least 66% of the models is identified by dotted hatching.

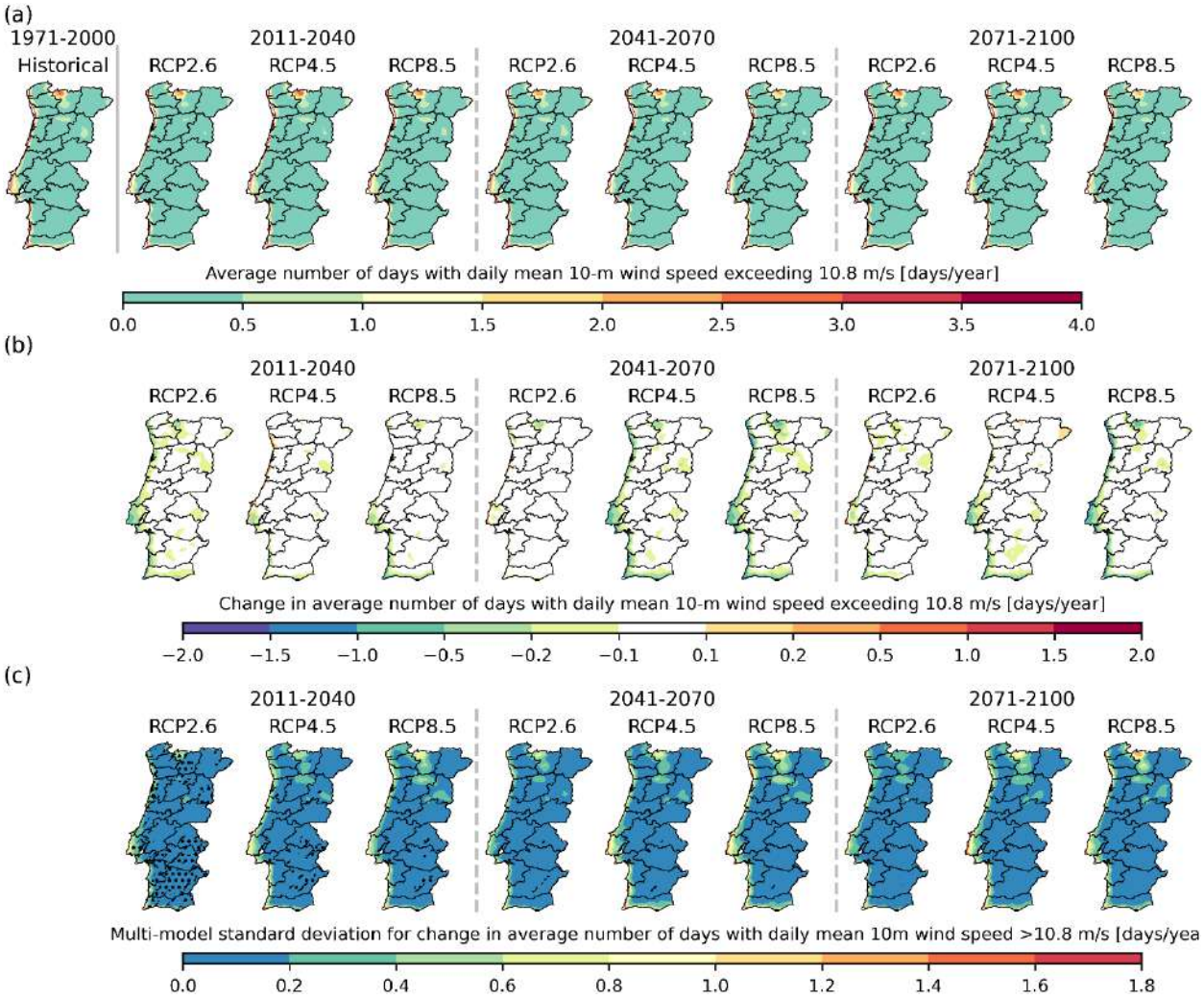

Figure 6.33 (a) Annual average number of days per year where daily mean 10-m wind speed exceeds 10.8 m/s over mainland Portugal, for historical period (1971-2000) and for the future periods considering different GHG emission scenarios. (b) Future projected changes in the average number of days per year where daily mean 10-m wind speed exceeds 10.8 m/s, considering the 1971-2000 period as reference. (c) Multi-model spread in future projected changes in average number of days per year where daily mean 10-m wind speed exceeds 10.8 m/s, considering the 1971-2000 period as reference. The spread is quantified by the standard deviation of the anomalies between different models. Grid-points where the change signal does not agree in at least 66% of the models is identified by dotted hatching.

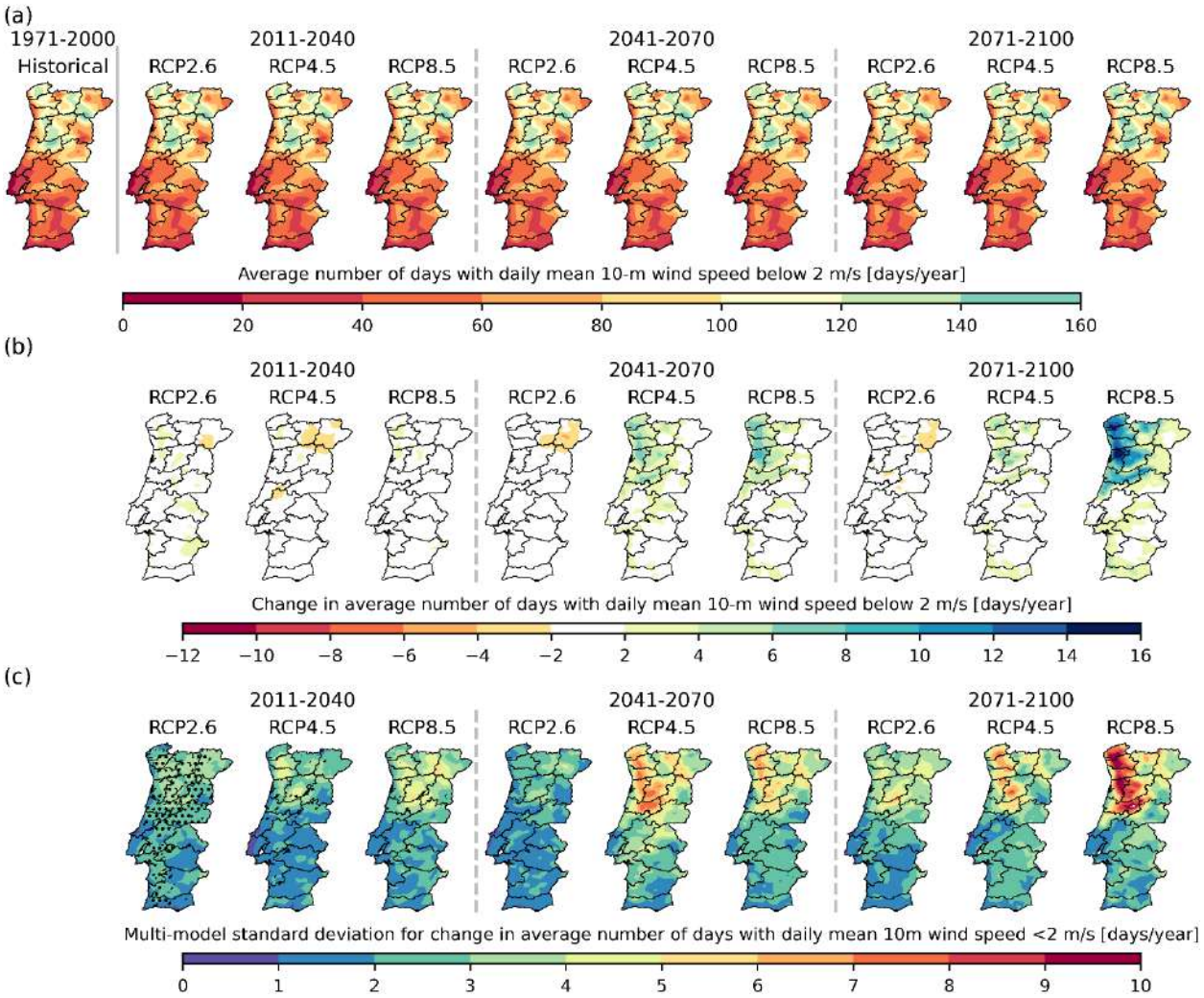

Figure 6.34 (a) Annual average number of days per year where daily mean 10-m wind speed is below 2 m/s (calm days) over mainland Portugal, for historical period (1971-2000) and for the future periods considering different GHG emission scenarios. (b) Future projected changes in the average number of calm days, considering the 1971-2000 period as reference. (c) Multi-model spread in future projected changes in average number of calm days, considering the 1971-2000 period as reference. The spread is quantified by the standard deviation of the anomalies between different models. Grid-points where the change signal does not agree in at least 66% of the models is identified by dotted hatching.

7. Climate Indices and other variables

7.1. Wind Energy

In section 5.3, the future projections for the mean wind speed at 10 m was presented. Here, the multi-model ensemble future projections for mean wind speed at 30 and 60 m is presented to analyse the potential of wind energy over Portugal. These results were computed using the daily mean wind speed at 10 m following equation 19, as explained in sub-section 2.4.3.

The present climate wind speed at 30 m at the annual and seasonal scales, given by the EURO-CORDEX multi-model ensemble is displayed in Figure 7.1. Overall, the values of wind speed at 30 m range between 2 and 7 m/s in all seasons, where the higher values are found in the Lisbon metropolitan area. Also, over Alentejo and Algarve regions the mean 30-m wind speed is above 4 m/s in most of the area. Looking to the wind speed at 60 m, the pattern is rather similar with to the 30 m, with values ranging from 3 to 8 m/s (Figure 7.7). In coastal regions of Lisbon metropolitan area and southwestern area, the mean wind speed at 60 m can reach 8 m/s. The maximum of daily mean wind speed at 30 and 60 m (Figure 7.2 and Figure 7.8, respectively) shows that the maximum values are found during winter (above 12 m/s) and the minimum during summer (below 10 m/s). Both spring and autumn seasons display values around 12 m/s over the entire territory.

The EURO-CORDEX multi-model ensemble future projections for mean wind speed at 30 and 60 m are displayed in Figure 7.3 and Figure 7.9, respectively. As expected, due to the logarithm extrapolation, the anomalies referent to the historical period are rather similar between them and with the 10-m wind speed projections. For the end-of-century and assuming the worst-case scenario, the largest changes are found during winter and autumn with a reduction in wind speed that can reach -0.6 m/s. During summer, and increase is found over the Lisbon metropolitan area for the begin-of-century, rising in intensity for end-of-century under both RCP4.5 and RCP8.5 scenarios. Also, over Alentejo and southwestern area an increase in wind speed is also observed under RCP8.5 for mid- and end-of-century, and under RCP4.5 for end-of-century. For the RCP2.6 scenario, the projections show values closer to zero, except during autumn where a small reduction is found over entire territory for the mid- and end-of-century (-0.2 m/s). The inter-model spread for these results are also very similar and is small is all cases (Figure 7.4 and Figure 7.10, respectively).

The future projections for the maximum wind speed at 30 and 60 m show largest changes in some areas and seasons (Figure 7.5 and Figure 7.11, respectively). At the annual scale, an increase in maximum wind speed is expected in the north area of Portugal below +1.5 m/s, whilst a reduction is found over the Alentejo region, for all the future scenarios and periods. Assuming the worst-case scenario, a reduction that can reach

-3 m/s in maximum wind speed is found in north region in all periods during spring. During summer, an increase is found over all the territory below +1 m/s. The inter-model spread for these results presents higher uncertainties in the grid-points where the anomalies are higher Figure 7.6 and Figure 7.12, respectively). However, at least 66% of the models agree in the change signal for all grid-points and scenarios for mid- and end-century. In the beginning of the century, in all RCPs, some grid-points does not agree the climate change signal.

Notice that these results are in agreement with (Nogueira et al. 2019) results reporting the largest reduction on wind energy production over continental Portugal to occurring during winter and autumn over northern Portugal, and a small increase during summer over A.M. Lisboa and Alentejo regions. In fact, it is important to point out, that despite the wind speed changes at 30 and 60 m are small in some cases, the impact on wind turbine energy production is significantly enhanced due to the logarithm wind profile combined with the cubic dependence of wind energy production on wind speed, and the high and low cut-off thresholds of wind turbines for energy production.

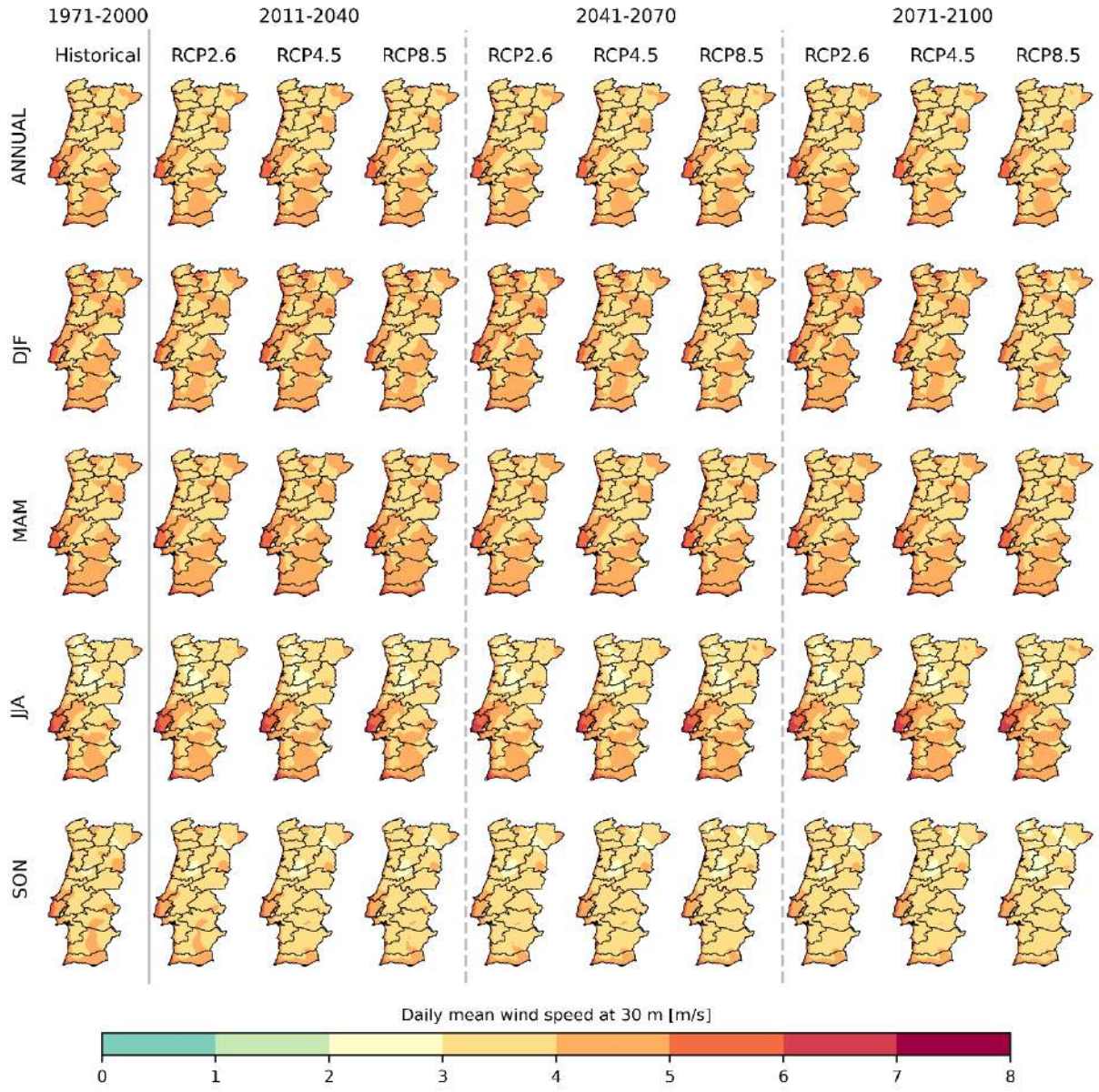

Figure 7.1 Annual and seasonal average of daily mean wind speed at 30 m over mainland Portugal, for historical period (1971-2000) and for the future periods considering different GHG emission scenarios. The different rows from top to bottom represent averaged taken over all months, DJF, MAM, JJA and SON respectively. The different columns represent the historical and the future periods considering different GHG emission scenarios.

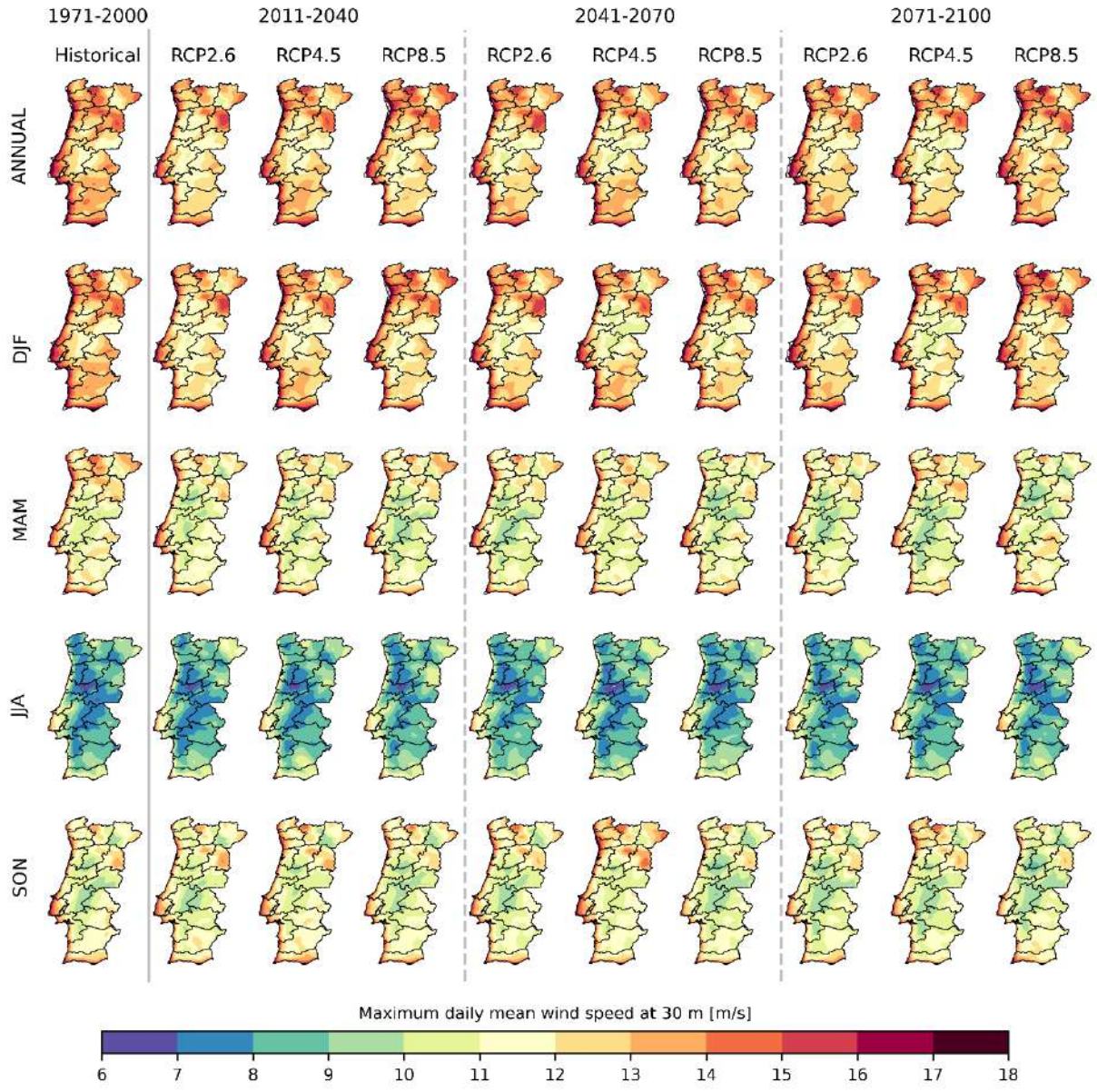

Figure 7.2 Annual and seasonal maximum of daily mean wind speed at 30 m over mainland Portugal, for historical period (1971-2000) and for the future periods considering different GHG emission scenarios. The different rows from top to bottom represent averaged taken over all months, DJF, MAM, JJA and SON respectively. The different columns represent the historical and the future periods considering different GHG emission scenarios.

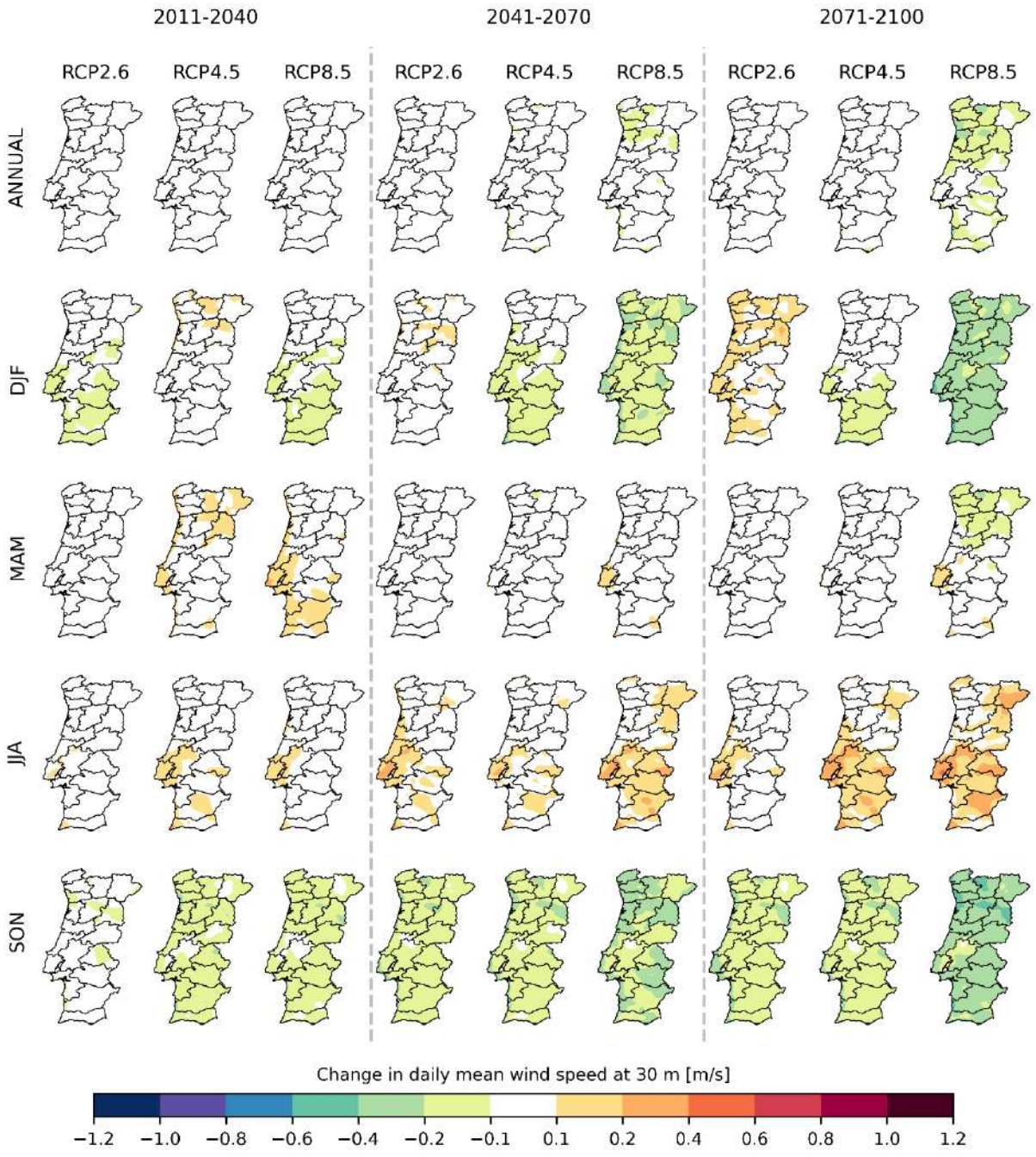

Figure 7.3 Future projected changes in daily mean wind speed at 30m over mainland Portugal, considering the 1971-2000 period as reference. The different rows from top to bottom represent averaged taken over all months, DJF, MAM, JJA and SON respectively. The different columns represent the future periods considering different GHG emission scenarios.

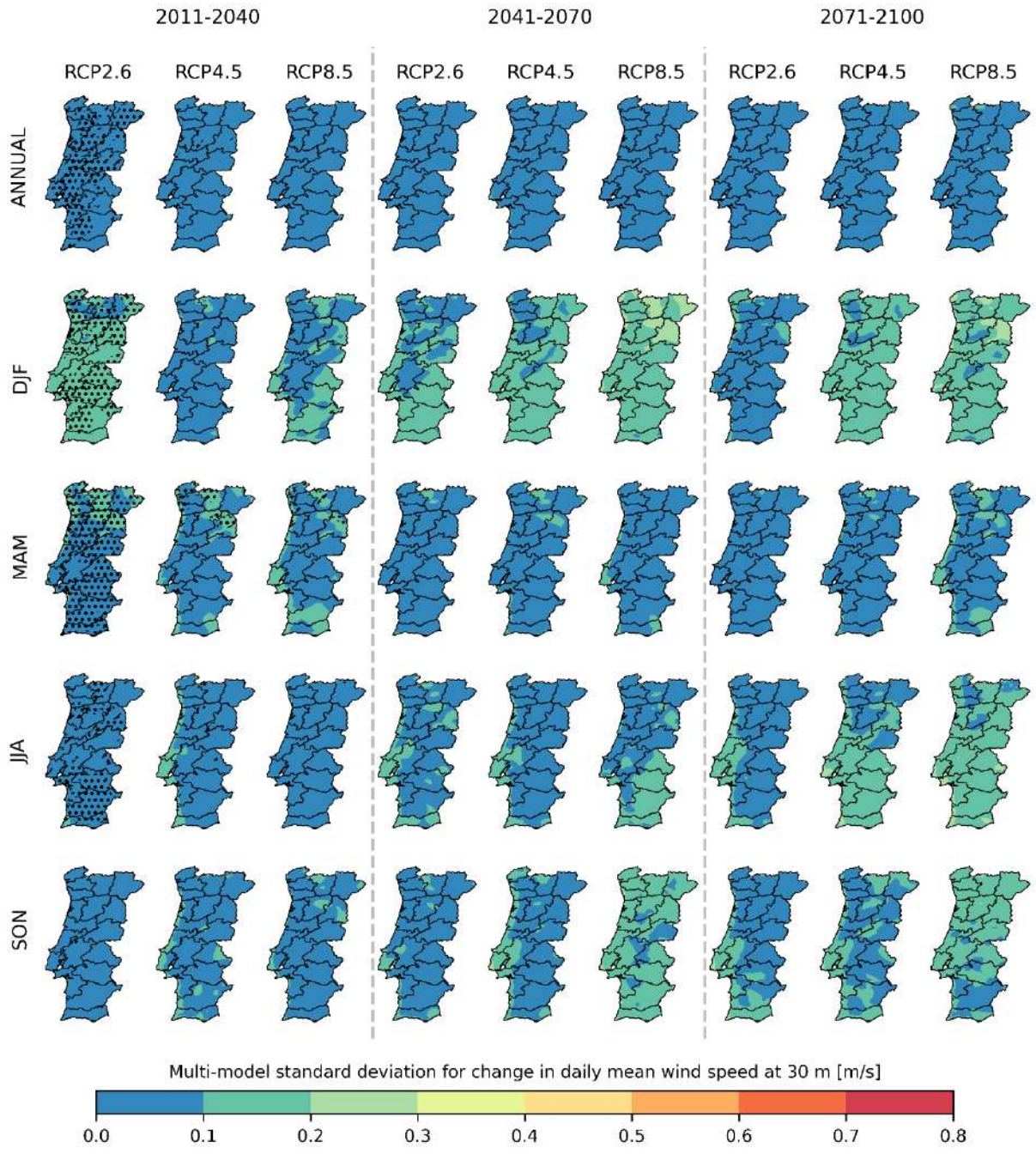

Figure 7.4 Multi-model spread in future projected changes in daily mean wind speed at 30 m over mainland Portugal, considering the 1971-2000 period as reference. The spread is quantified by the standard deviation of the anomalies between different models. The different rows from top to bottom represent averaged taken over all months, DJF, MAM, JJA and SON respectively. The different columns represent the future periods considering different GHG emission scenarios. Grid-points where the wind speed change signal does not agree in at least 66% of the models is identified by dotted hatching.

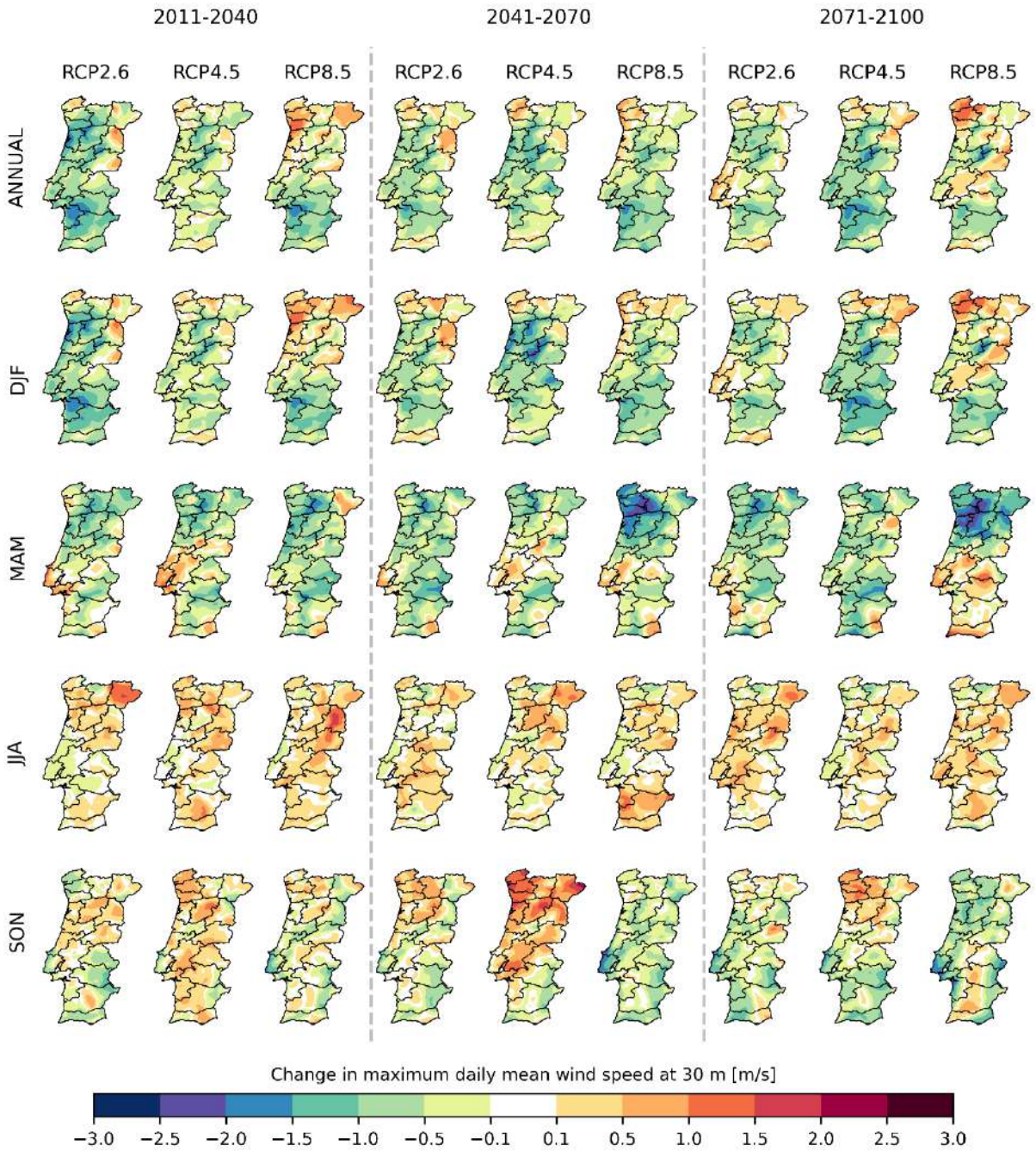

Figure 7.5 Future projected changes in maximum daily mean wind speed at 30m over mainland Portugal, considering the 1971-2000 period as reference. The different rows from top to bottom represent averaged taken over all months, DJF, MAM, JJA and SON respectively. The different columns represent the future periods considering different GHG emission scenarios.

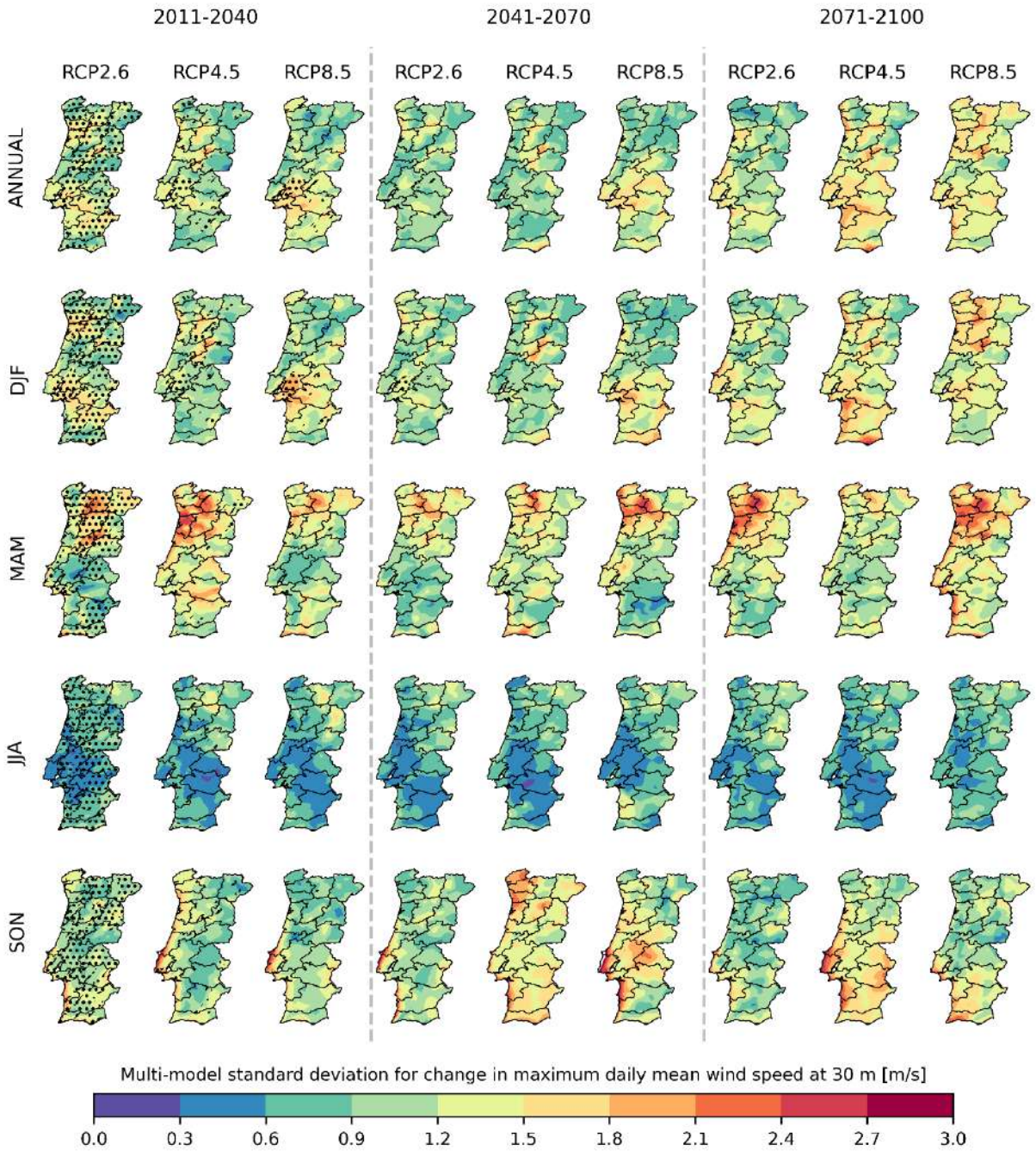

Figure 7.6 Multi-model spread in future projected changes in maximum daily mean wind speed at 30 m over mainland Portugal, considering the 1971-2000 period as reference. The spread is quantified by the standard deviation of the anomalies between different models. The different rows from top to bottom represent averaged taken over all months, DJF, MAM, JJA and SON respectively. The different columns represent the future periods considering different GHG emission scenarios. Grid-points where the wind speed change signal does not agree in at least 66% of the models is identified by dotted hatching.

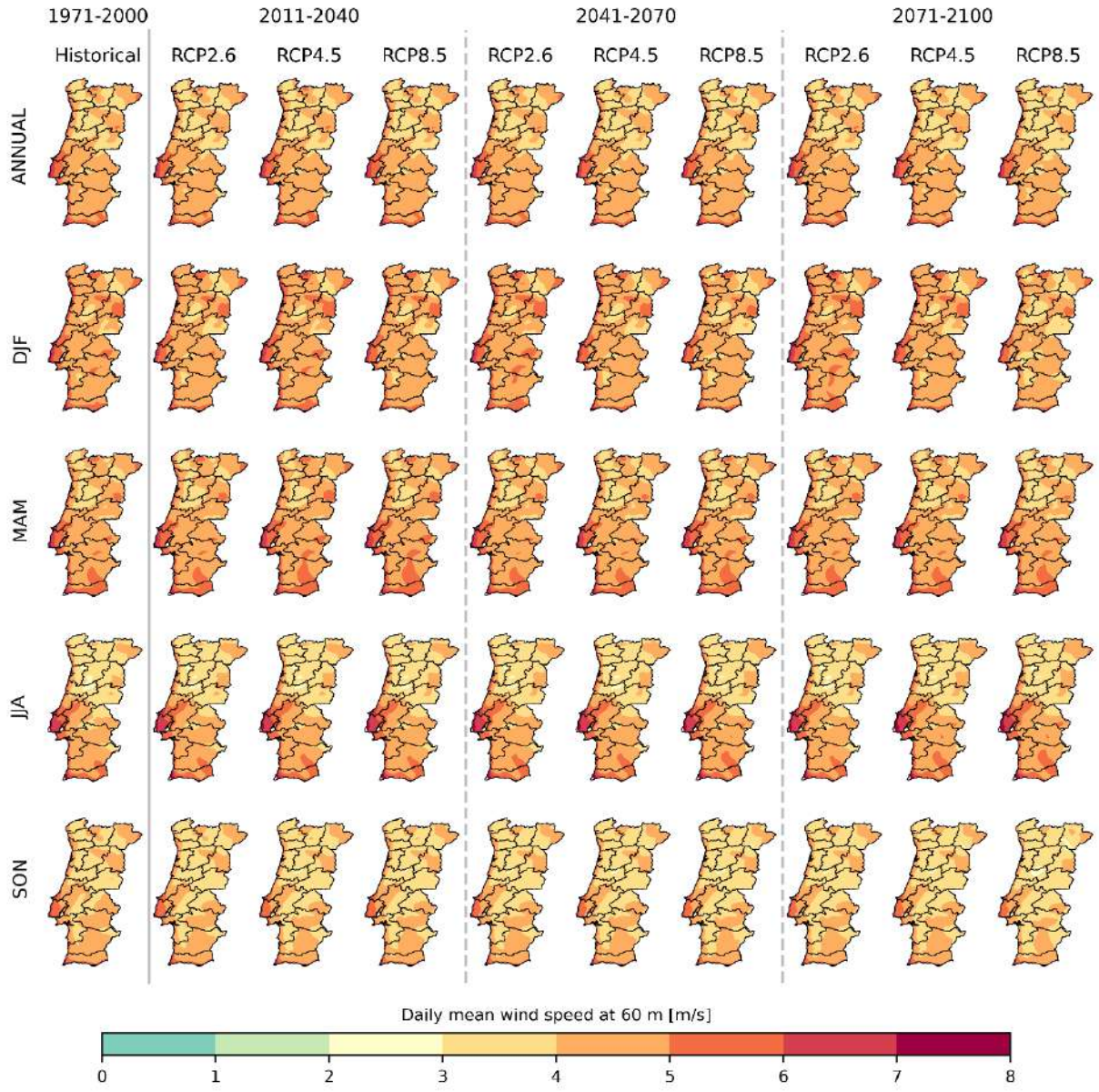

Figure 7.7 Annual and seasonal average of daily mean wind speed at 60 m over mainland Portugal, for historical period (1971-2000) and for the future periods considering different GHG emission scenarios. The different rows from top to bottom represent averaged taken over all months, DJF, MAM, JJA and SON respectively. The different columns represent the historical and the future periods considering different GHG emission scenarios.

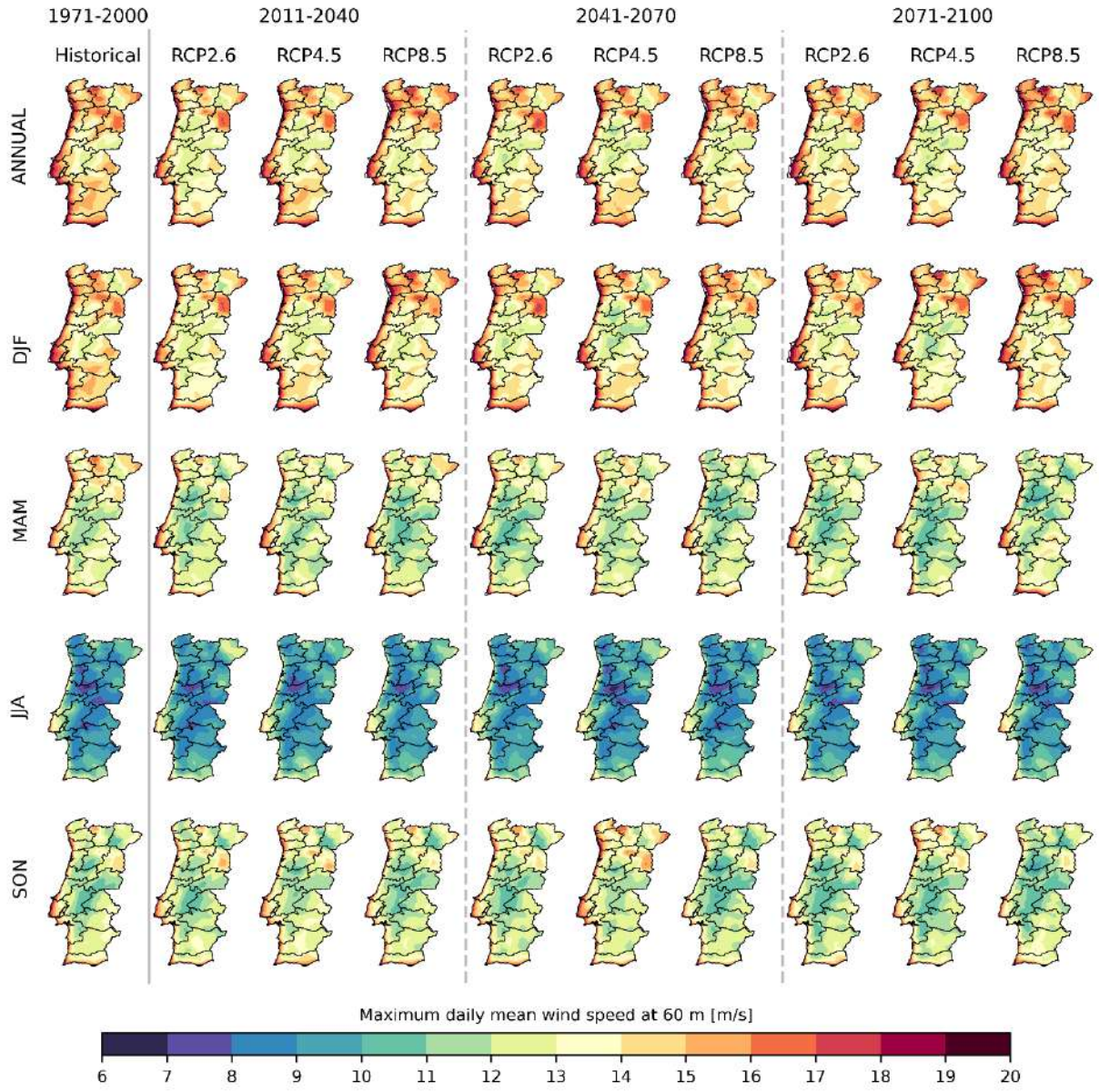

Figure 7.8 Annual and seasonal maximum of daily mean wind speed at 60 m over mainland Portugal, for historical period (1971-2000) and for the future periods considering different GHG emission scenarios. The different rows from top to bottom represent averaged taken over all months, DJF, MAM, JJA and SON respectively. The different columns represent the historical and the future periods considering different GHG emission scenarios.

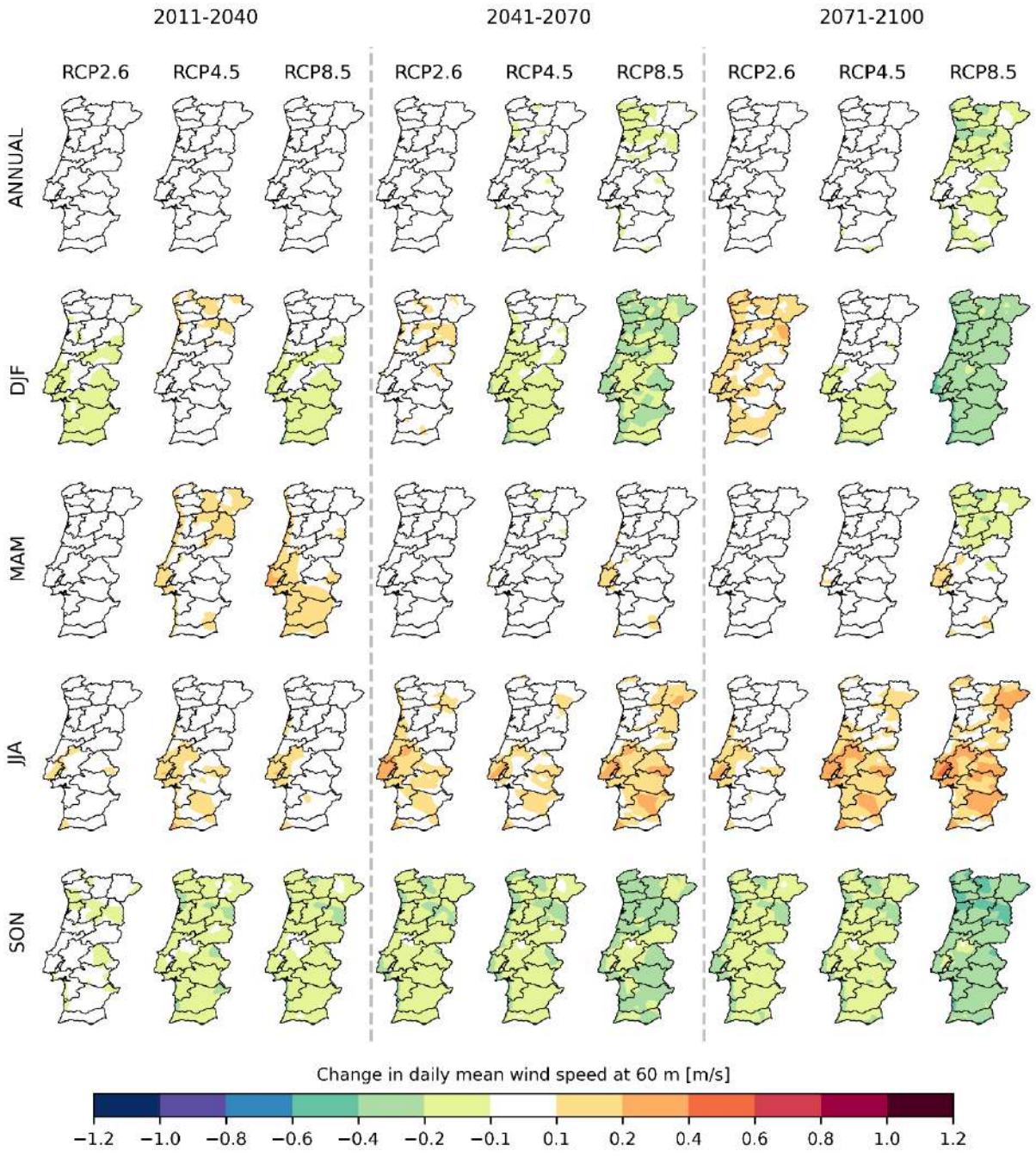

Figure 7.9 Future projected changes in daily mean wind speed at 60 m over mainland Portugal, considering the 1971-2000 period as reference. The different rows from top to bottom represent averaged taken over all months, DJF, MAM, JJA and SON respectively. The different columns represent the future periods considering different GHG emission scenarios.

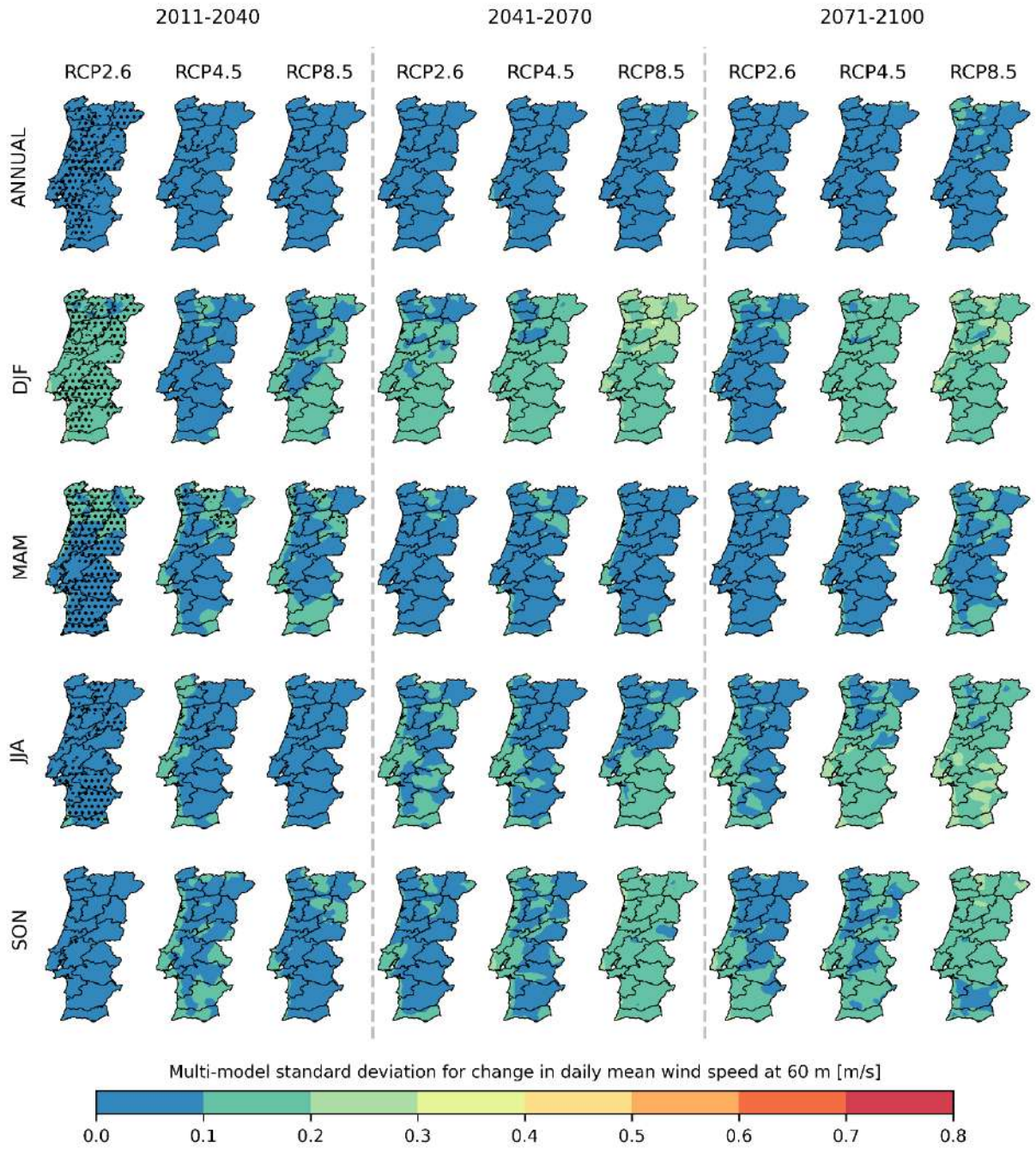

Figure 7.10 Multi-model spread in future projected changes in daily mean wind speed at 60 m over mainland Portugal, considering the 1971-2000 period as reference. The spread is quantified by the standard deviation of the anomalies between different models. The different rows from top to bottom represent averaged taken over all months, DJF, MAM, JJA and SON respectively. The different columns represent the future periods considering different GHG emission scenarios. Grid-points where the wind speed change signal does not agree in at least 66% of the models is identified by dotted hatching.

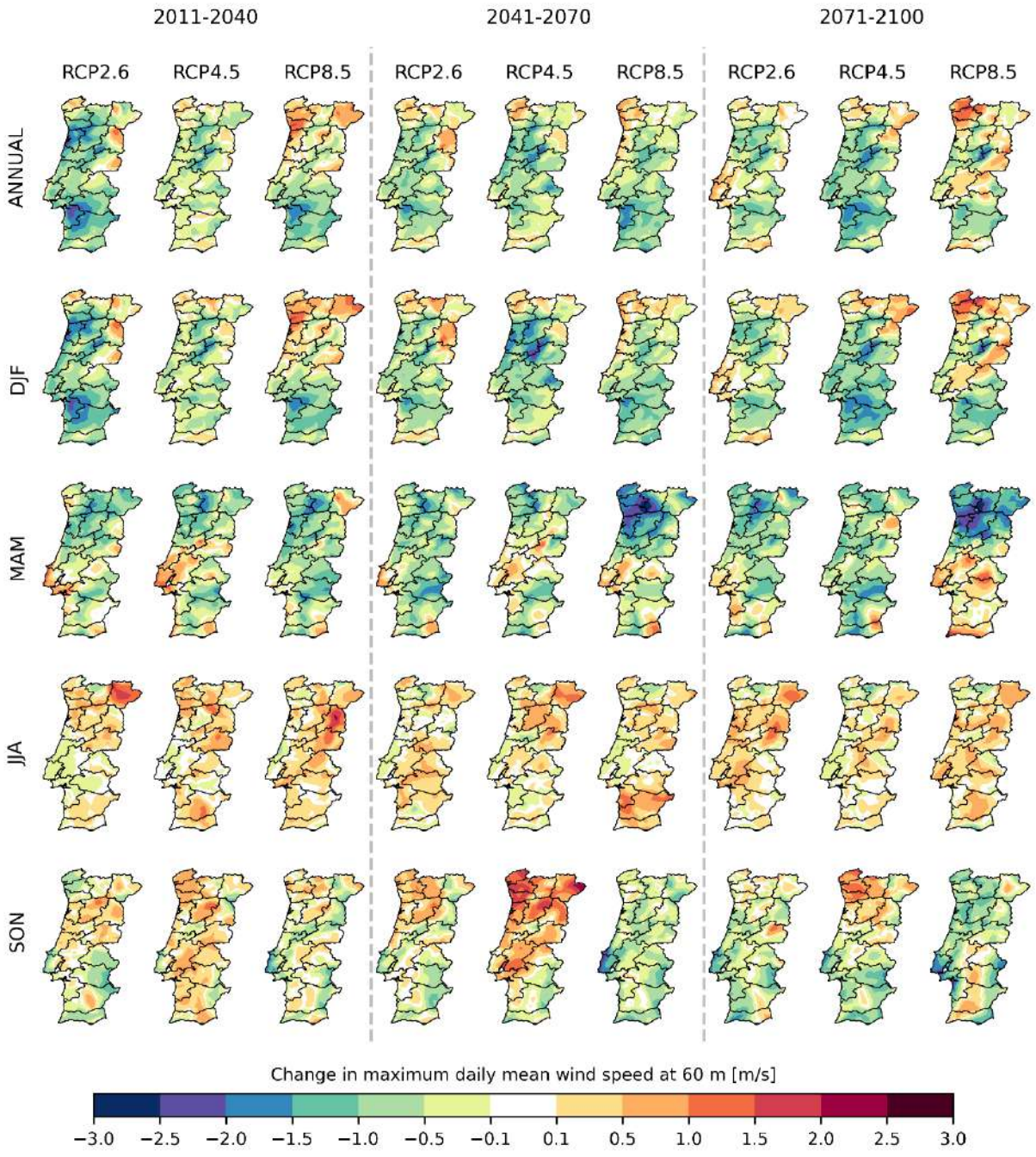

Figure 7.11 Future projected changes in maximum daily mean wind speed at 60 m over mainland Portugal, considering the 1971-2000 period as reference. The different rows from top to bottom represent averaged taken over all months, DJF, MAM, JJA and SON respectively. The different columns represent the future periods considering different GHG emission scenarios.

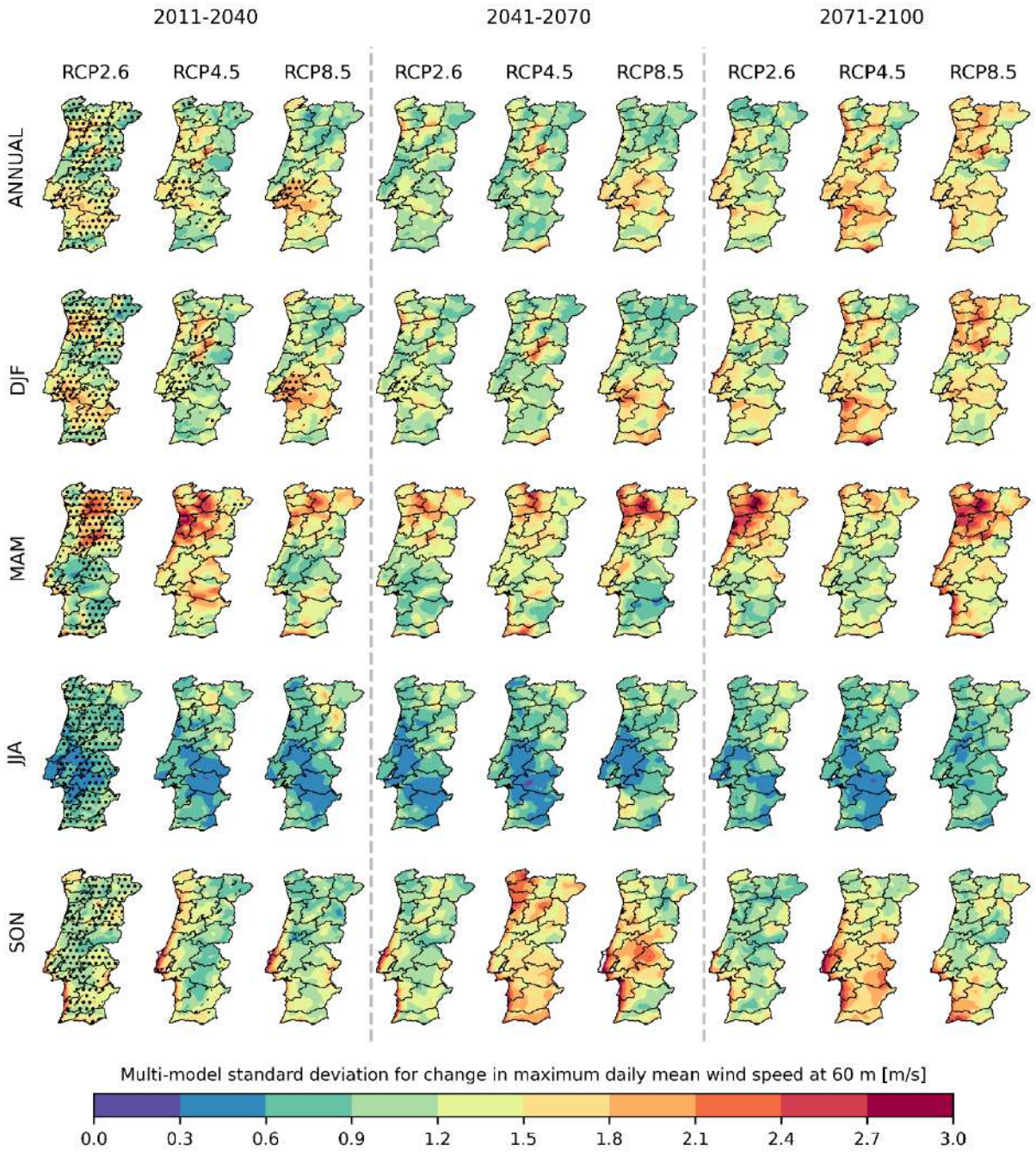

Figure 7.12 Multi-model spread in future projected changes in maximum daily mean wind speed at 60 m over mainland Portugal, considering the 1971-2000 period as reference. The spread is quantified by the standard deviation of the anomalies between different models. The different rows from top to bottom represent averaged taken over all months, DJF, MAM, JJA and SON respectively. The different columns represent the future periods considering different GHG emission scenarios. Grid-points where the wind speed change signal does not agree in at least 66% of the models is identified by dotted hatching.

7.2. Humidity and Potential Evapotranspiration

With increasing surface temperature, the amount of water vapour in the atmosphere increases whenever the air is not saturated. Saturated vapour pressure increases exponentially with temperature as expected from the Clausius–Clapeyron relation and in some regions the amount of water vapour in the atmosphere has been increasing in excess of 7% per kelvin (Willett et al. 2010). However, increasing global temperatures are not translated into increasing relative humidity over land, the opposite or a plateauing of RH has been observed (Simmons et al. 2010). In large regions of the globe, the majority of moisture over land has origins over the oceans. Since oceans are warming at a lower rate than the land surface, the rate of evaporation over their surfaces is lower than over land. Thus, the amount of moisture advected from the oceans into the land areas is not enough to keep the ratio between the air's vapour pressure and the saturated vapour pressure constant and a decrease in RH is observed. In some areas like Portugal, changes to general circulation also imply a reduction in moister transport from the oceans, further reducing the moisture availability, escalating surface warming and increasing the saturated vapour pressure. In RCP 2.6 relative humidity (Figure 7.13) decreases by less than 2%, while in RCP 4.5 reductions of 2% are only projected for areas near the coast and reductions up to 4% are expected near the Spanish border. In RCP 8.5, a reduction between 2 and 4% is projected by mid-century and a further reduction between 4 and 6% for the areas near the border with Spain by the end of the century. In winter the advection of moist air accompanying the winter storms, with their expected increase in intensity (*i.e.*, including more moisture), is enough to imply an increase in RH for mainland Portugal for RCP2.6 and for the regions above the Tagus River in RCP 4.5. In RCP 8.5 not only a decrease of precipitation is projected but also a significant increase in temperature thus the projected decline of RH. The reduction in RCP 8.5 is particularly severe in the north-eastern regions during summer, where relative humidity is projected to decrease between 6 and 8%, exacerbated by the extreme rise in surface temperatures. The uncertainty of the RH projections is high with the multi-model spread up to 75% of ensemble value for RCP2.6 and RCP 4.5. In RCP 8.5, there is lower spread, about 50% (Figure 7.14).

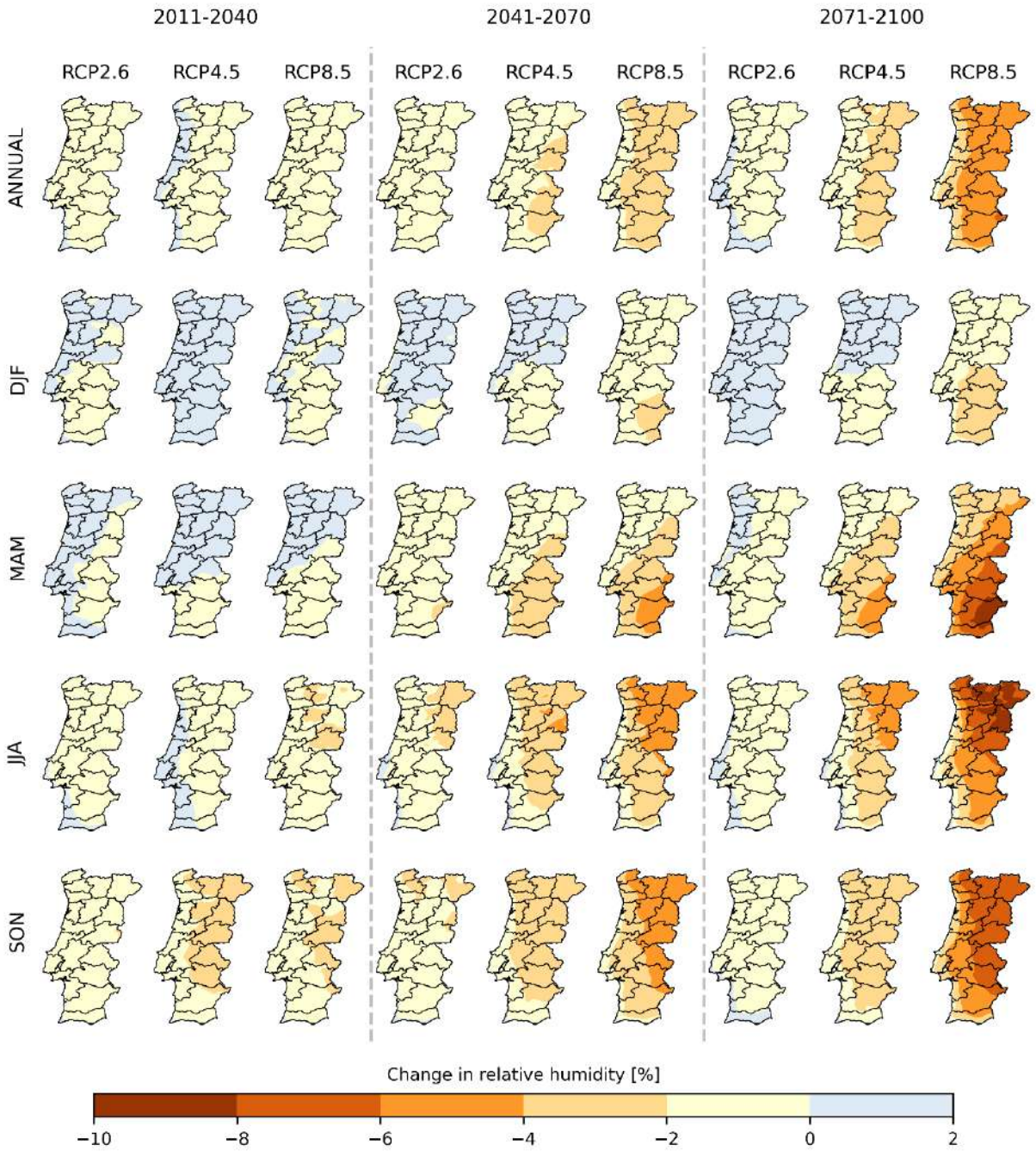

Figure 7.13 Future projected changes in relative humidity over mainland Portugal, considering the 1971-2000 period as reference. The different rows from top to bottom represent averaged taken over all months, DJF, MAM, JJA and SON respectively. The different columns represent the future periods considering different GHG emission scenarios.

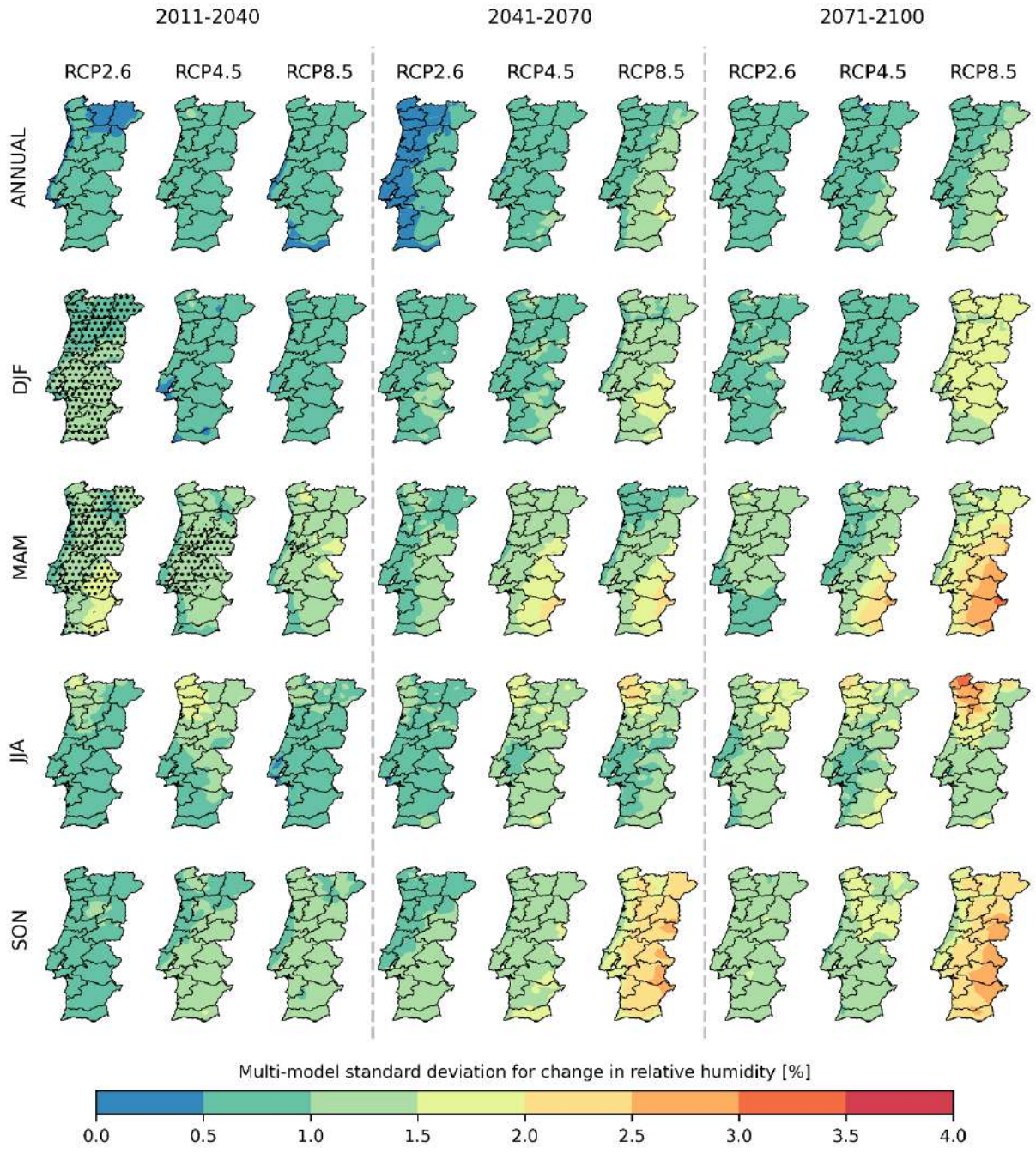

Figure 7.14 Multi-model spread in future projected changes in relative humidity over mainland Portugal, considering the 1971-2000 period as reference. The spread is quantified by the standard deviation of the anomalies between different models. The different rows from top to bottom represent averaged taken over all months, DJF, MAM, JJA and SON respectively. The different columns represent the future periods considering different GHG emission scenarios. Grid-points where the temperature change signal does not agree in at least 66% of the models is identified by dotted hatching.

Potential evapotranspiration increases in all scenarios up to mid-21st century (Figure 7.15Figure 7.33). The projected increase in PET primarily occurs due to similar processes that lead to the reduction in RH which leads to an increase in vapor pressure deficit over land and the nonlinear increase of saturation vapor pressure as a function of temperature associated to the Clausius–Clayperon relationship (Sherwood and Fu 2014; Scheff and Frierson 2014). Since under the RCP2.6 scenario, temperature stabilises by mid-century (Figure 5.1) no further increase in PET is projected until the end of the century. Overall, a rise lower than 10% is projected. In scenario RCP4.5, temperature rises at a smaller rate from mid-century onwards, thus in most regions PET stabilises and an increase between 10 and 15% is projected at the end of the century. In RCP8.5, the sharp rise in temperature leads to an enhancement up to 30% in PET in the north by the end of the century. The highest rise in PET occurs in the northeast during Autumn at the end of the century in RCP8.5. Once again, the multi-model spread is almost as large as the climate change signal, indicating a large uncertainty associated to the PET computation (Figure 7.16).

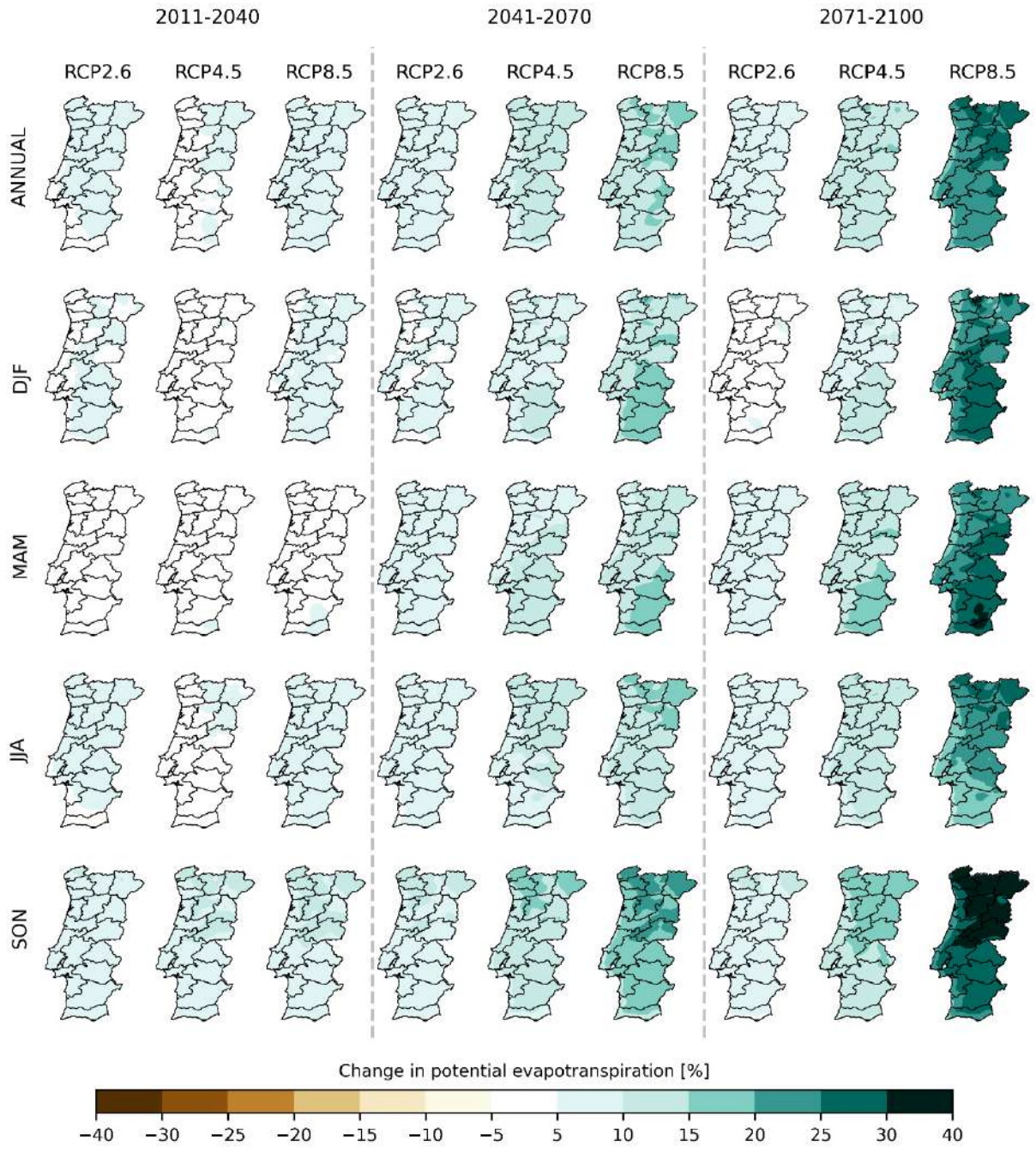

Figure 7.15 Future projected changes in potential evapotranspiration (in percentage) over mainland Portugal, considering the 1971-2000 period as reference. The different rows from top to bottom represent averaged taken over all months, DJF, MAM, JJA and SON respectively. The different columns represent the future periods considering different GHG emission scenarios.

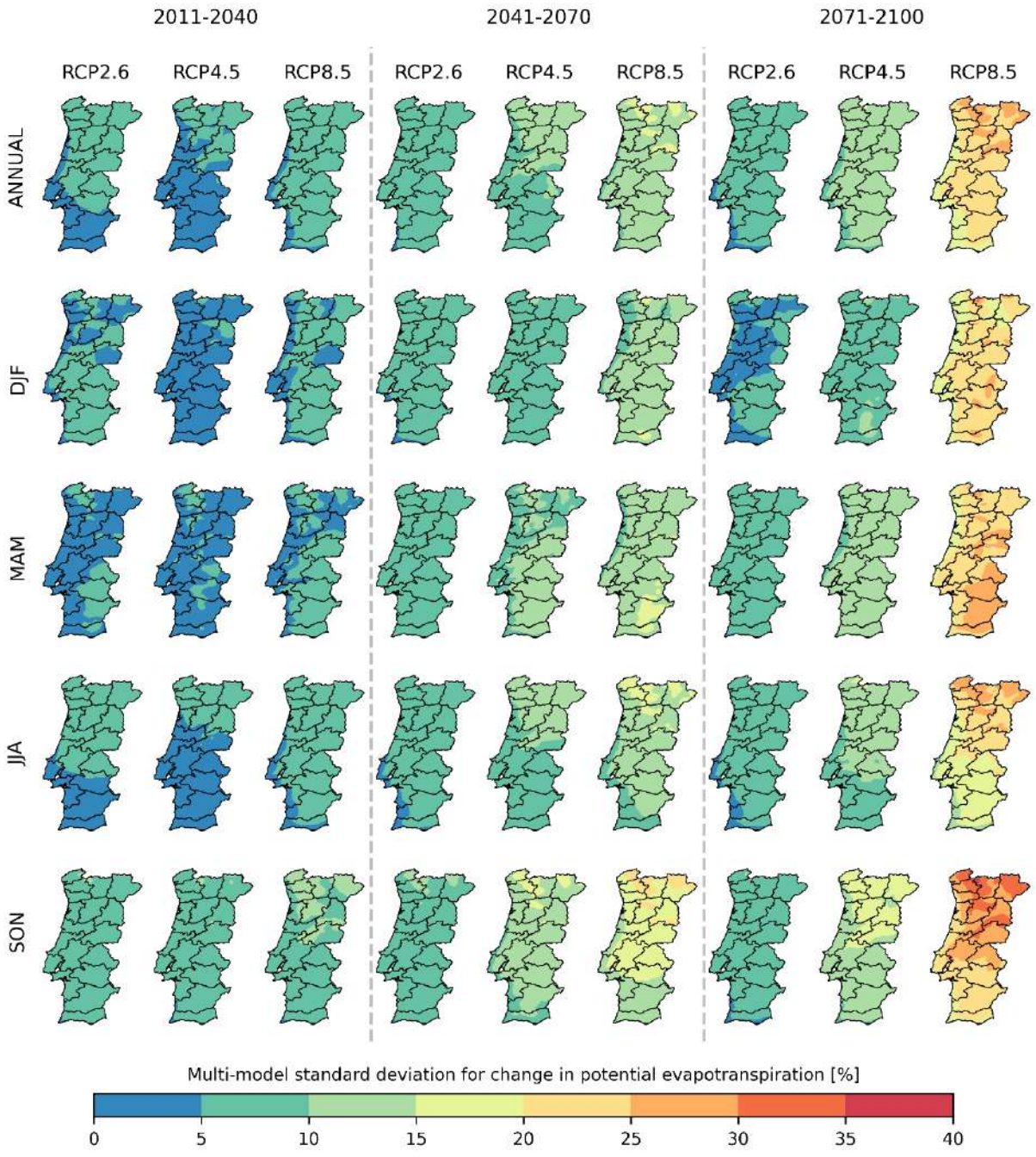

Figure 7.16 Multi-model spread in future projected changes in potential evapotranspiration over mainland Portugal, considering the 1971-2000 period as reference. The spread is quantified by the standard deviation of the anomalies between different models. The different rows from top to bottom represent averaged taken over all months, DJF, MAM, JJA and SON respectively. The different columns represent the future periods considering different GHG emission scenarios. Grid-points where the temperature change signal does not agree in at least 66% of the models is identified by dotted hatching.

7.3. Soil Moisture and Evaporation

The annual cycle of total soil moisture in Portugal (Figure 7.17a), given by the models, corresponds to a typical Mediterranean climate cycle, where maximum values of soil moisture occur in late winter (for Portugal in February) and minimum values in late summer (September). This annual cycle is rather pronounced and reveals a soil moisture annual amplitude of around 200 mm, or one quarter of maximum winter values.

Looking to the future projections of soil moisture (Figure 7.17), for the three time periods and three RCP scenarios, overall, as expected, a clear and monotonous decrease with time and RCP of the full annual cycle is identified, with much larger magnitudes when going from the RCP2.6 to RCP8.5. In fact, for the RCP2.6 a rather small decrease of soil moisture if projected for almost all months and time periods, under 3% in relative values and peaking in November. In fact, for this emission scenario a small recovery (little increase and less decrease) is seen when comparing the mid-century and the end-of-century in spring. For the RCP4.5, the reductions are gradually enhanced throughout the 21st century, especially between the beginning and mid-century and reaching -7% in November for 2071-2100. In spring and summer, from mid-century to end-of-century, a small recovery or stabilization of soil moisture is projected. For the RCP8.5, the soil moisture reductions are much more severe, and always increasing throughout the century, jumping from maximum reductions, in November, of around – 3% in 2011-2041, to -9% and -14% in mid- and end-of-century, respectively.

Overall, some changes in the annual cycle may be identified besides the omnipresent decreases of water availability in the soil. For Portugal mainland, the annual soil moisture amplitude is projected to augment slightly for the RCP2.6, the one showing a rather small diminishing of soil moisture, as well as for the RCP4.5 but in a mitigated manner. For the RCP8.5, the severe reductions of soil moisture throughout the year are accompanied by a decrease of the annual soil moisture amplitude in absolute values.

A spatial view of the projected soil moisture changes at the annual and seasonal scales, for the three time periods and the three emission scenarios, is displayed in Figure 7.18 focusing absolute. The future projections display a clear reduction of soil moisture, especially for the RCP4.5 and RCP8.5, pointing to a dramatic aggravation of water scarcity throughout the 21st century in Portugal, if emissions are not reduced. For the first future period, all scenarios have associated projections of a small reduction of annual soil moisture (smaller than 40 mm) but that intensifies greatly with time and scenario. For the mid-century, the projected reductions for the RCP4.5 are between -40 and -80 mm for all the southern of Portugal, and for the RCP8.5 almost those reach values in the range of -80 and -120 mm for the south and, -40 and -80 mm for the north. For the end of the century, the soil moisture decrease is enhanced for the RCP8.5, attaining

values between -120 and -160 mm for large extensions of the southern regions. This change dynamics also applies in a great measure for all the seasons, with some exceptions. For spring, the projections according to the RCP2.6 reveals some increases of soil moisture for the end of the century in some mountainous and big river valleys, such as the Tagus; and, for autumn the decreases of soil moisture associated with the RCP8.5 are more homogeneous spatially. As with the other moisture related variables, the ensemble spread is very large, almost as large as the climate change signal (Figure 7.19).

In Figure 7.20, the PDFs of soil moisture anomalies normalized by the respective standard deviations are displayed, for the historical and future periods and in agreement with the three RCP scenarios, for Portugal mainland (Figure 7.20a) and for the NUTS II regions (Figure 7.20b). Strikingly the soil moisture PDFs time evolution, in response to the emissions scenarios, reminds immediately the temperature classical shift and flattened PDFs, where a great increase of extreme temperature occurrence is identified both due to the lateral shift and the flattening of the temperature PDFs. In fact, the soil moisture PDFs reveal distinct shifts and flattening, in an increasingly manner with time and scenario, which corresponds to multiplying for various orders of magnitude the occurrence of soil moisture deficits, w.r.t. the historical climate.

For Portugal and the period 2011-2040 a very slight shift for lower soil moisture values and flattening of the PDFs is seen, for all RCPs. For the RCP2.6 the PDFs remain rather unchanged for all future time periods but for the RCP4.5 and RCP8.5 those PDF changes are enhanced in 2041-2070 and further in 2071-2100. In the historical period, soil moisture deficits rarely reach values 3x over the standard deviation, but projections reveal that for the RCP4.5 (RCP8.5) for the mid-century deficits up to 5x (6x) are projected to occur, and for the end-of-century even 7x for the RCP8.5.

The shift for lower values and the flattening of the soil moisture PDFs is projected for all Portuguese NUTS II regions, from north to south. However, the PDF's projected modifications are more severe for the two southern regions, Alentejo and Algarve. These regions are already presently the ones suffering recurrently of water scarcity problems, with impacts even on public water supply for human consummation. For these regions, in the case of RCP8.5, a dramatic decrease of the occurrences when soil moisture anomalies will be positive is projected, and for example, deficits of 3x the standard deviation (historical) are projected to increase from 0.06% in the historical period to 3% at mid-of-century and 4% at end-of-century, so as impressive as 67x. Noteworthy, if mitigation is pursued and RCP2.6 achieved the PDFs for those regions almost do not change when compared with the historical period.

The reduced soil moisture contributes to the overall reduction of evaporation at the surface (Figure 7.21) particularly in summer and autumn. As before, the multi-model spread is large and in summer and autumn it is as large as the climate change signal in RCP8.5 (Figure 7.22).

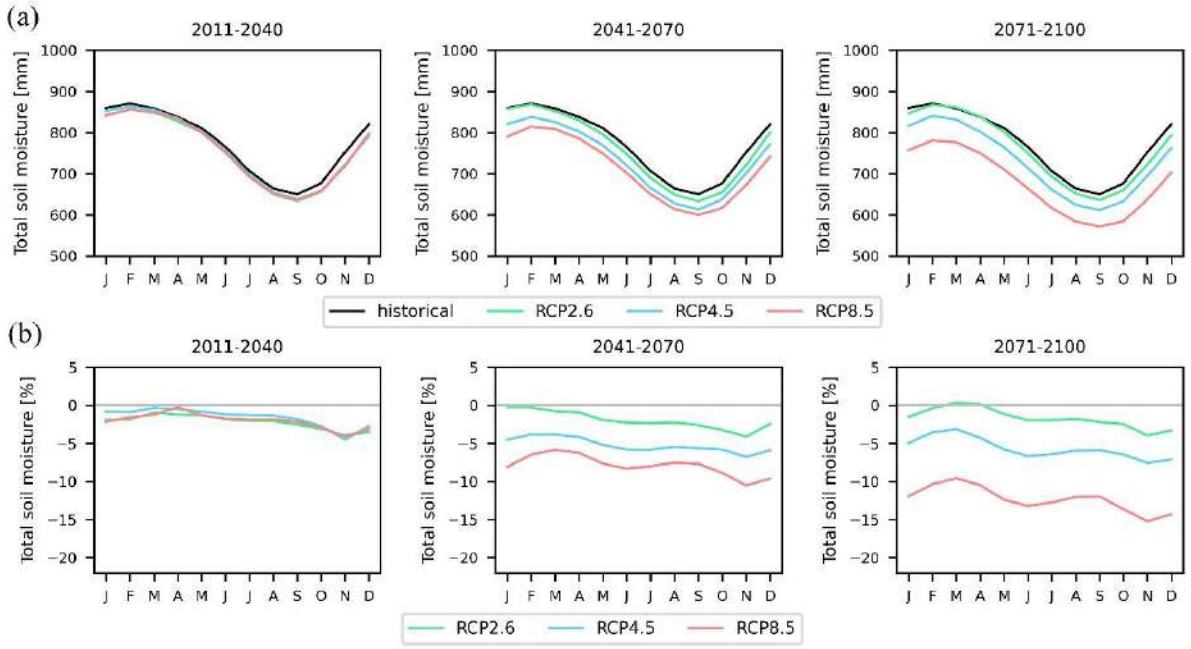

Figure 7.17 (a) Annual cycle at the monthly scale of soil moisture for the historical and futures periods, (b) Annual cycle at the monthly scale of soil moisture differences for future climates (w.r.t. to the historical climate) in percentage (%) values, considering the three RCP emission scenarios - RCP2.6 (green), RCP4.5 (blue) and RCP8.5 (red).

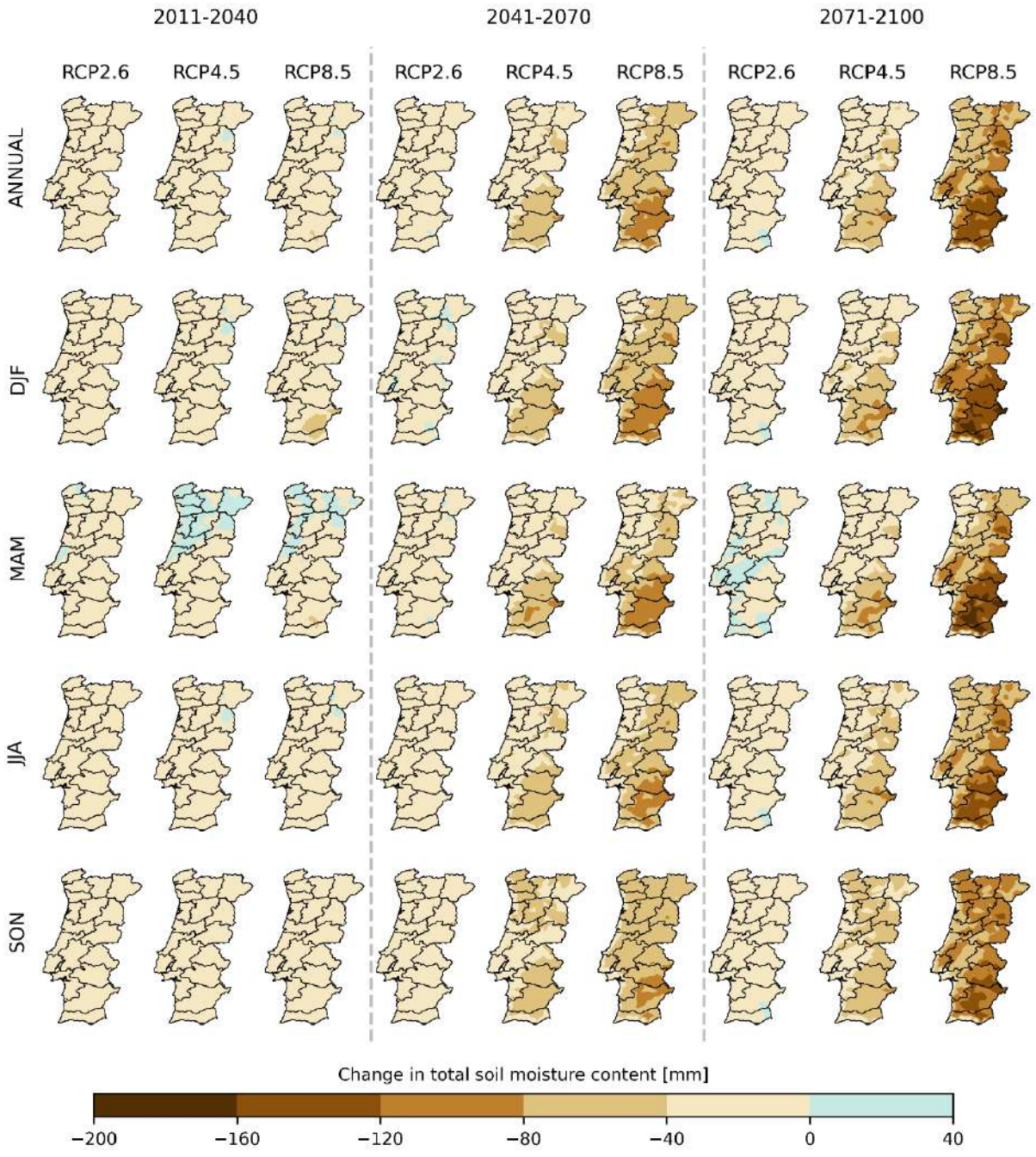

Figure 7.18 Future projected changes in total soil moisture content over mainland Portugal, considering the 1971-2000 period as reference. The different rows from top to bottom represent averaged taken over all months, DJF, MAM, JJA and SON respectively. The different columns represent the future periods considering different GHG emission scenarios.

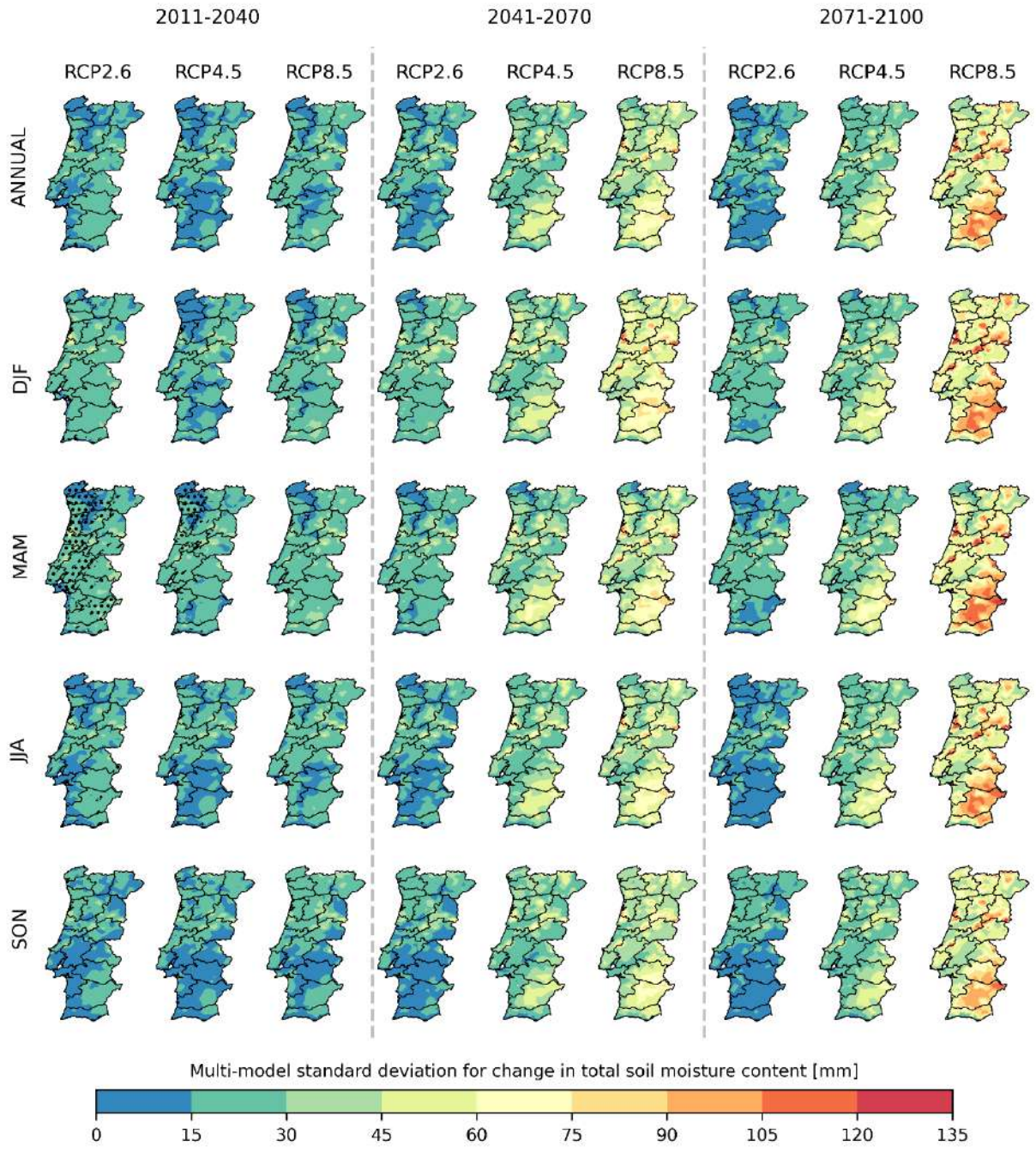

Figure 7.19 Multi-model spread in future projected changes in total soil moisture content over mainland Portugal, considering the 1971-2000 period as reference. The spread is quantified by the standard deviation of the anomalies between different models. The different rows from top to bottom represent averaged taken over all months, DJF, MAM, JJA and SON respectively. The different columns represent the future periods considering different GHG emission scenarios. Grid-points where the temperature change signal does not agree in at least 66% of the models is identified by dotted hatching.

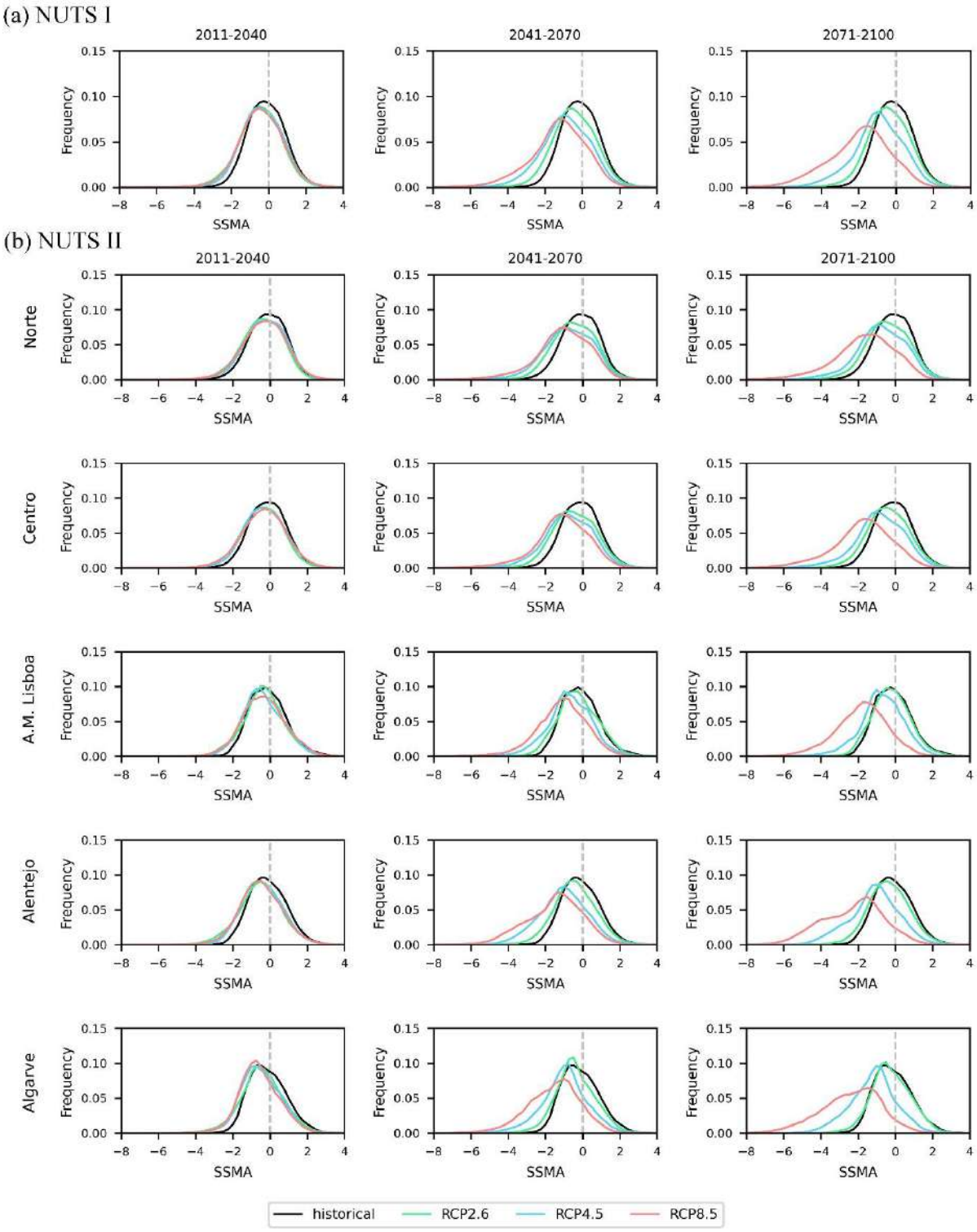

Figure 7.20 PDFs of Standardised Soil Moisture Anomaly (SSMA) at the daily scale for mainland Portugal NUTS I and II, historical (black) and future periods considering the three RCP emission scenarios – RCP2.6 (green), RCP4.5 (blue) and RCP8.5 (red).

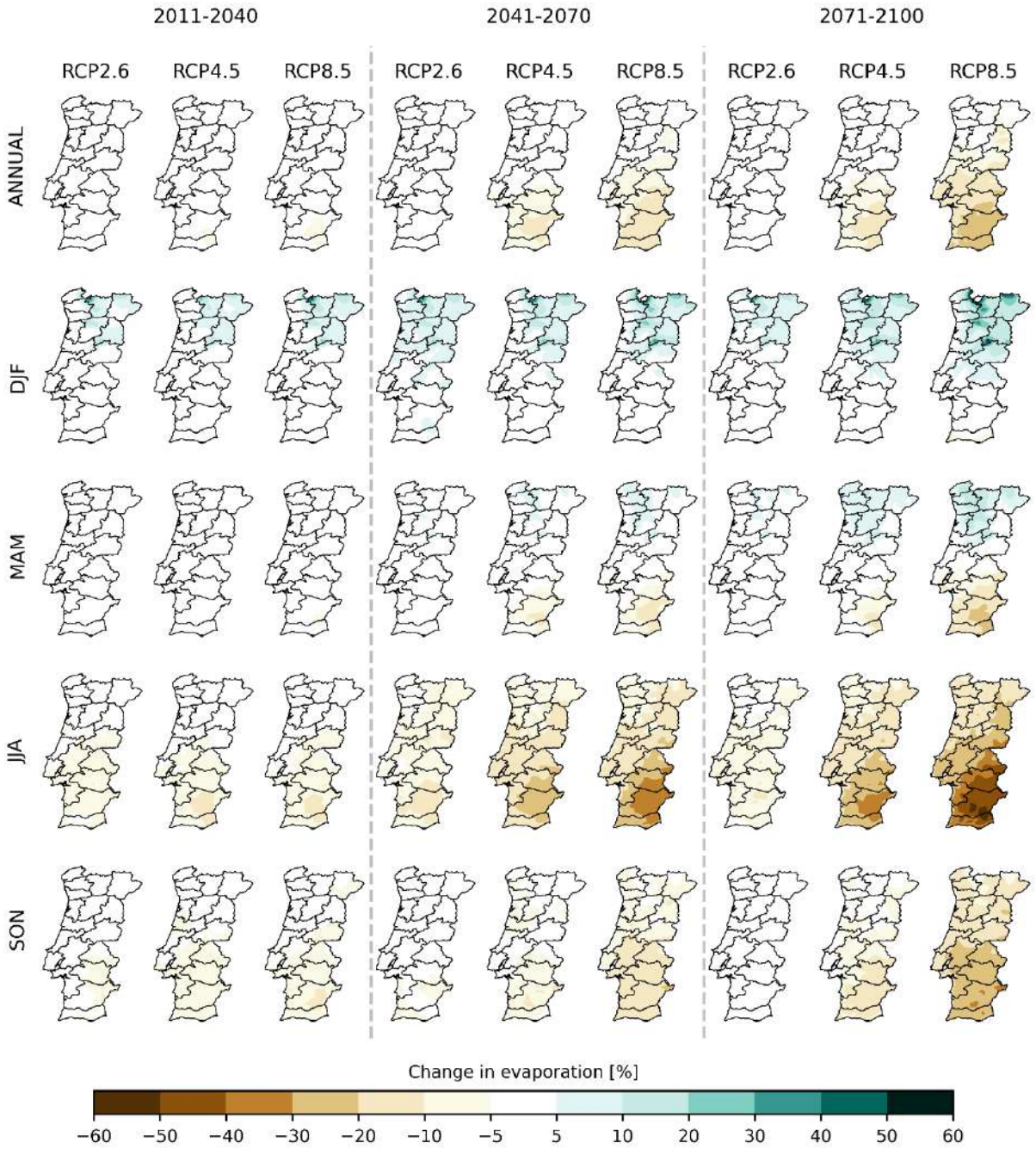

Figure 7.21 Future projected changes in evaporation (in percentage) over mainland Portugal, considering the 1971-2000 period as reference. The different rows from top to bottom represent averaged taken over all months, DJF, MAM, JJA and SON respectively. The different columns represent the future periods considering different GHG emission scenarios.

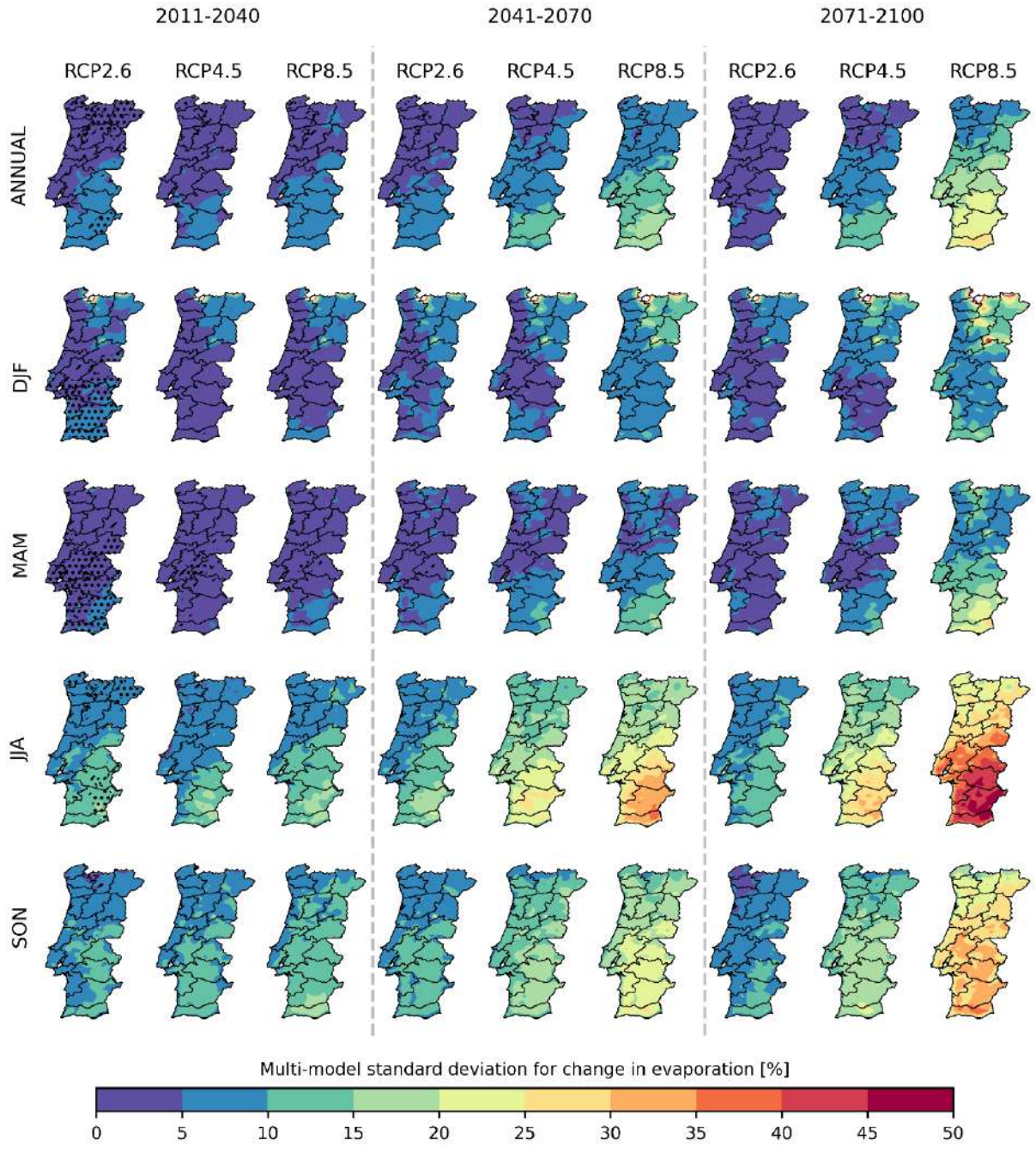

Figure 7.22 Multi-model spread in future projected changes in evaporation over mainland Portugal, considering the 1971-2000 period as reference. The spread is quantified by the standard deviation of the anomalies between different models. The different rows from top to bottom represent averaged taken over all months, DJF, MAM, JJA and SON respectively. The different columns represent the future periods considering different GHG emission scenarios. Grid-points where the temperature change signal does not agree in at least 66% of the models is identified by dotted hatching.

7.4. Radiation

The reduction in atmospheric humidity, evaporation, and soil moisture favours the shrinkage of cloud cover, thus an increase in solar radiation which reaches the surface (Figure 7.23). This occurs not only at the annual level but also for summer and autumn for the entire century and in spring from mid-century onwards. The rise in evaporation during winter leads to an increase in cloud cover and thus to a reduction in radiation that reaches the surface.

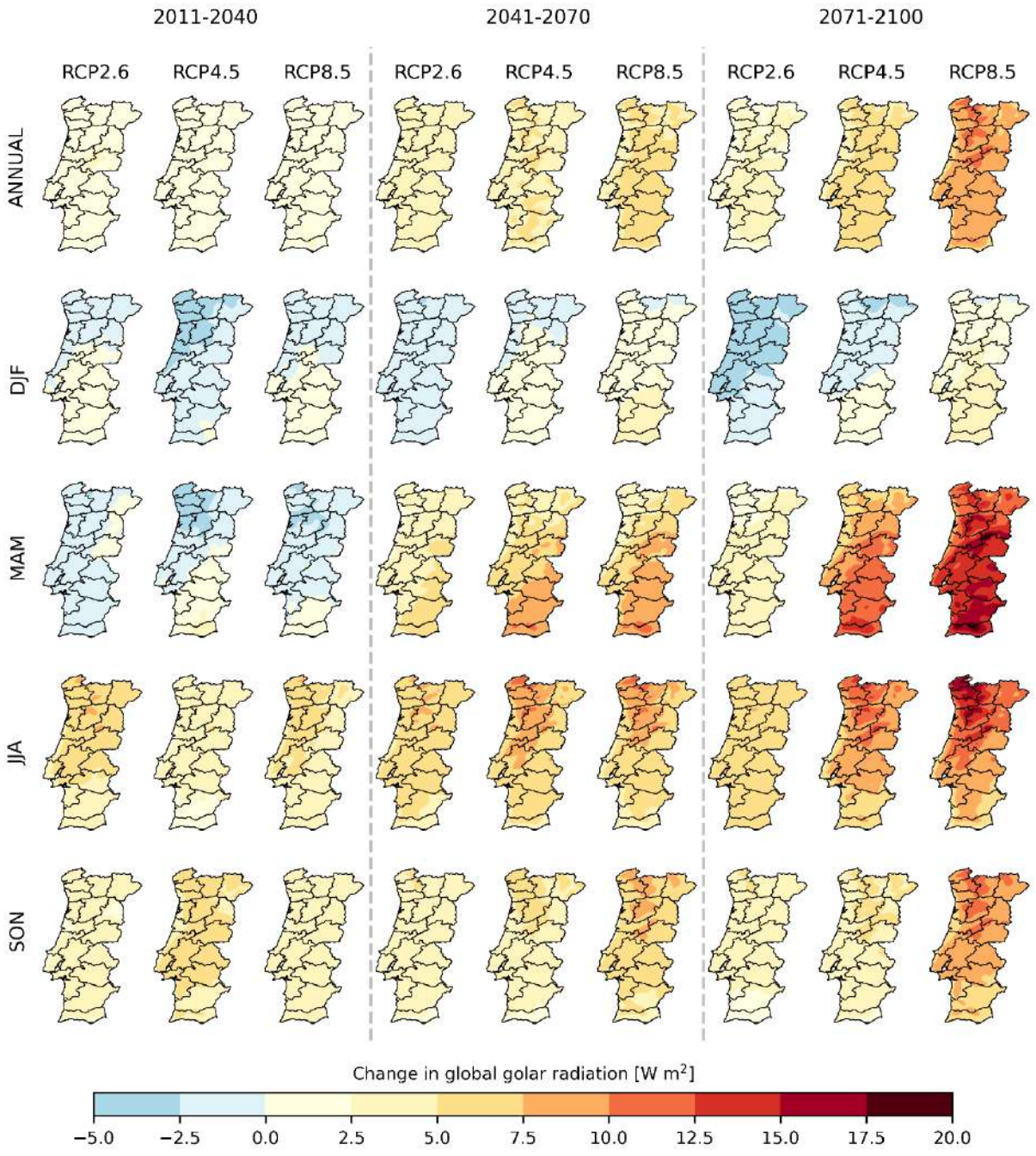

Figure 7.23 Future projected changes in global solar radiation over mainland Portugal, considering the 1971-2000 period as reference. The different rows from top to bottom represent averaged taken over all months, DJF, MAM, JJA and SON respectively. The different columns represent the future periods considering different GHG emission scenarios.

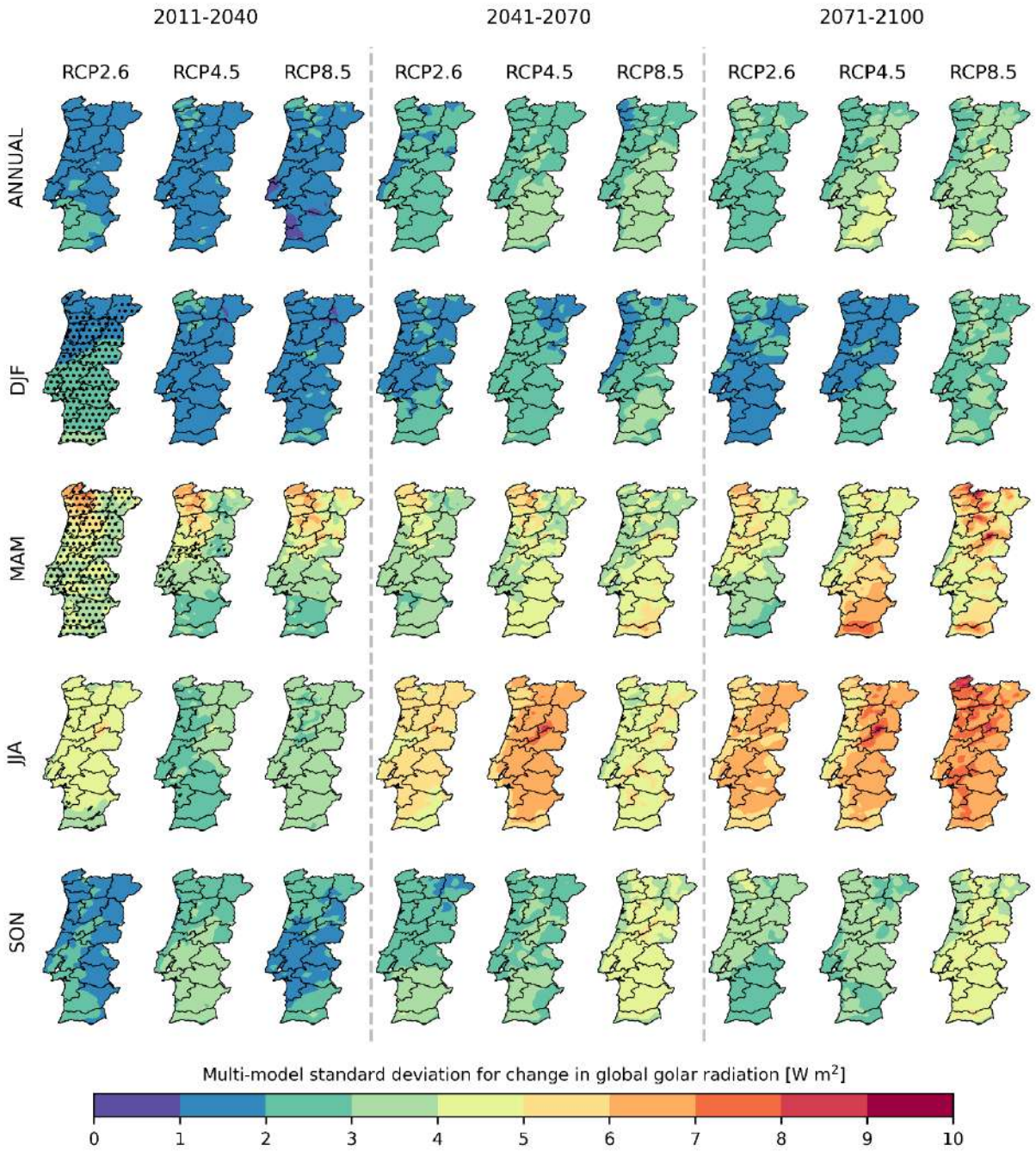

Figure 7.24 Multi-model spread in future projected changes in global solar radiation over mainland Portugal, considering the 1971-2000 period as reference. The spread is quantified by the standard deviation of the anomalies between different models. The different rows from top to bottom represent averaged taken over all months, DJF, MAM, JJA and SON respectively. The different columns represent the future periods considering different GHG emission scenarios. Grid-points where the temperature change signal does not agree in at least 66% of the models is identified by dotted hatching.

7.5. Thermal comfort indices

On the annual scale, the map of universal thermal climate index (UTCI) for mainland Portugal shows that most of the country has no heat stress in the historical period, except in the north-eastern region of Portugal that has a slightly cold stress Figure 7.25. The future projections show a change to no heat stress across all the country, reducing the areas with a slightly cold thermal condition. As expected, the thermal conditions between seasons are different. The thermal comfort during winter is characterised by a slightly cold thermal condition over mainland Portugal, except in the north-eastern region that a moderately cold stress is presented. The evolution of the thermal comfort during the 21st century in winter shows a reduction in the land area with a moderately cold stress to a slightly cold stress, in all future periods and scenarios. In the RCP8.5 for the end-of-century, an area along the Alentejo coast shifts its thermal comfort condition to no heat stress. In spring, part of the north and centre regions, and the Lisbon area have a slightly cold condition, and the remaining country has no heat stress in the historical period. Throughout the 21st century, in all scenarios, the land area with a slightly cold condition changes to no heat stress. For summer season, the thermal comfort over all country is characterised by no heat stress. By mid-of-century, in RCP4.5 and RCP8.5, an area in Alentejo changes its thermal comfort condition to moderately hot stress, which expands to most of south and centre regions for the end-of-century in RCP8.5. During autumn season, the evolution of the thermal conditions is similar with the annual patterns, with a less land area with a slightly cold thermal condition.

To analyse the effect of heat stress during the occurrence of heatwaves, the analysis of daily UTCI was constrained to the days under a temperature driven heatwave (Figure 7.26). In the historical period, 50% of heatwaves have a UTCI of less than 21, indicating that on average they do not pose much heat stress and alleviate cold spring and autumn temperatures (Figure 7.26a). Only 24% induce a classification of moderately hot and only 1% are on average hot. However, from the maximum severity (Figure 7.26b), 75% of these events have within them days with UTCI larger than 26 (moderately hot), and 15% can have hot conditions (UTCI larger than 32). Even with the reduction in GHGs at the end of the 21st century, in RCP2.6, an increase of in 7% of events with average moderately hot conditions, a 27% rise in heatwaves with moderately hot days within the event is projected and 56% of the heatwaves will have hot days within them. For the most severe scenario and by the end of the 21st century, 39% of heatwaves will be moderately hot on average and 10% will have an average of hot conditions. Within all heatwaves, only 1% will not have a moderately hot day, 89% will have at least a day with maximum UTCI above 32 (hot days) and most significantly will be the 32% with very hot conditions.

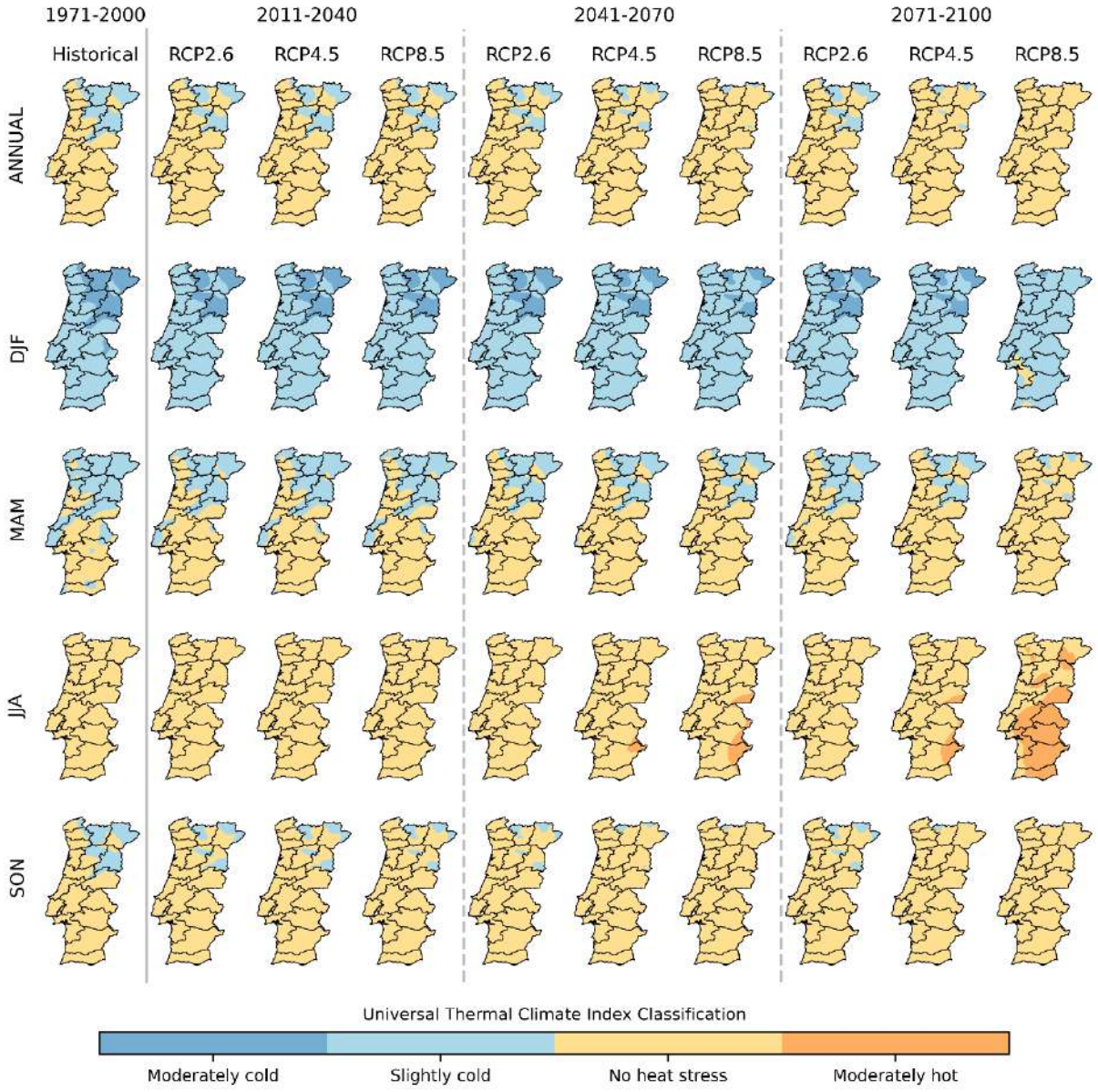

Figure 7.25 Annual and seasonal Universal Thermal Climate Index Classification over mainland Portugal for historical climatological period (1971-2000) and for the future periods considering different GHG emission scenarios. The different rows from top to bottom represent averaged taken over all months, DJF, MAM, JJA and SON respectively. The different columns represent the future periods considering different GHG emission scenarios.

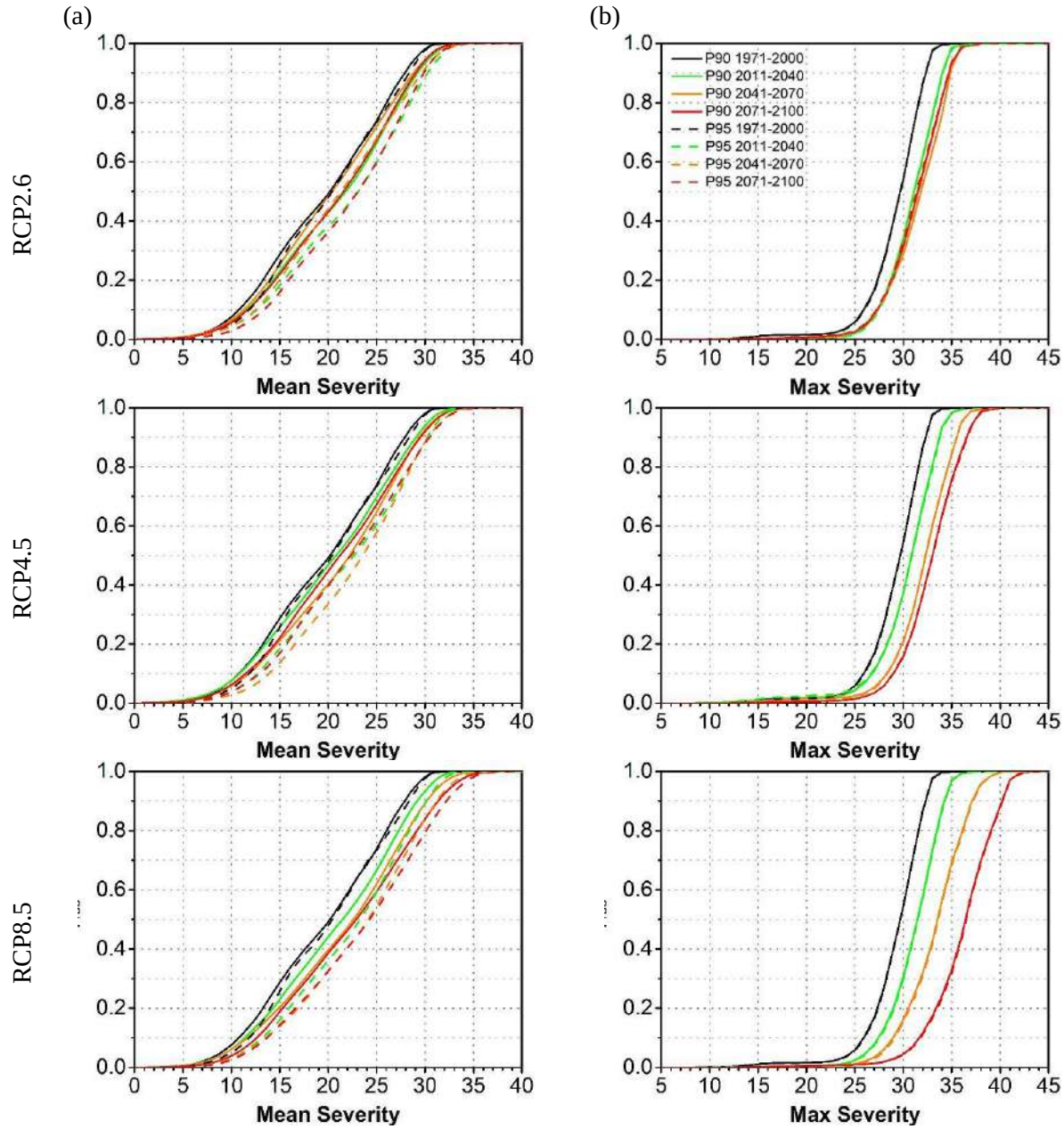

Figure 7.26 Multi-model ensemble empirical cumulative distribution functions of Universal Thermal Climate Index Classification heatwave a) mean intensity and b) maximum intensity for the historical period (1971-2000) and for the future periods considering different GHG emission scenarios.

Since the perception of extreme heat by the human body is not limited to the influence of temperature alone, here and following Di Napoli et al. (2019) we use the 95th percentile as a threshold for extreme heat and apply a similar methodology as in section 3.1. Hence, in this context, extreme heat stress occurs when UTCI's daily P_{95} is exceeded for 5 or more consecutive days. As with heatwaves, and in the historical period, the extreme heat stress events per year fluctuates between 1 and 2 over continental Portugal (Figure 7.27). At the beginning of the century, the number of cases increases to 2 to 3 in all scenarios and areas,

indicating that while the coastal areas are not subject to an increase in the number of events with consecutive very extreme temperatures, the events with maximum temperature above P_{90} (Figure 6.8) will also induce heat stress. Additionally, at least one of the events with maximum temperature above P_{90} (Figure 6.8) farther from the coast will not generate heat stress. In RCP2.6 the number of events, at the end of the century, does not change relative to the beginning of the century. For both RCP4.5 and 8.5, the number of extreme heat cases, increases throughout the 21st century and in the latter scenario, more than 7 occurrences of extreme heat stress will arise. As before, this value is in between the number of events for $T_{max} > P_{90}$ and $T_{max} > P_{95}$. The length of these extreme heat stress events is less than 7 days and in some coastal and northern areas is less than 6 days (Figure 7.27b). In those areas, the days with heat stress is lower than the days under heatwave (Figure 6.9). In RCP2.6, and at the end of the century, the north will experience on average 7 to 8 days of consecutive heat stress, while in central and southern continental Portugal these events will last 6 to 7 days. In the most severe scenario, the length of these cases will be 9 to 10 days in the south and 10 to 12 near the Spanish border.

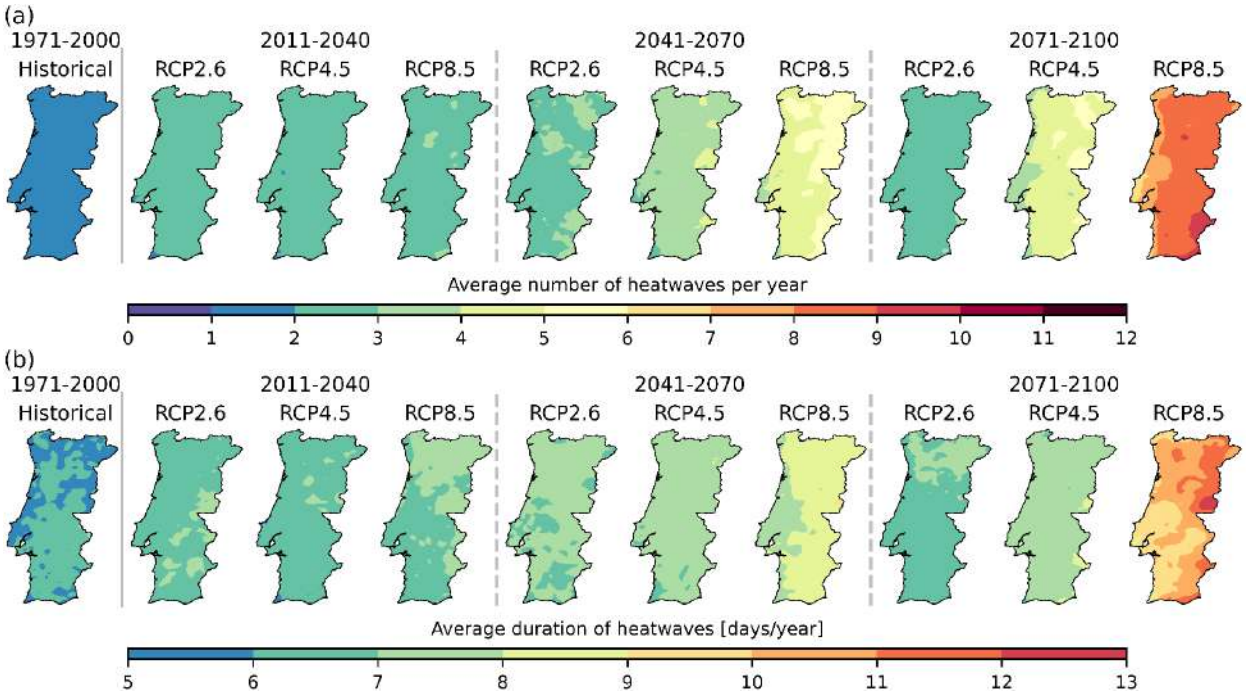

Figure 7.27 Annual average number of heatwaves per year over mainland Portugal (a) and annual average length of heatwaves per year (b) for the historical period (1971-2000) and for the future periods considering different GHG emission scenarios.

Figure 7.28 shows the empirical cumulative distribution functions of the extreme heat stress and heatwaves. As expected, the length of the extreme heat stress events is larger than the extreme heatwaves for all scenarios and time periods. This is more prominent in RCP8.5. Here, the severity of the events is measured in a similar way as for heatwaves, *i.e.*, it is a normalised distance from the UTCI P_{25}. For all scenarios the

severity above 1 in heat stress occurs for fewer percentage of events than for extreme heatwaves and less than 5% have severities above 2. While in the historical period, the heat stress events cover less land than extreme heatwaves, in the projections for the 21st century all of these occurrences have a similar areal extension in RCP2.6 and 4.5. Yet, in RCP8.5 from mid-century onwards, the extent of these extreme heat stress events is considerably larger than the extreme heat waves. By the end of the century, 50% of the events will cover more than 40% of the country.

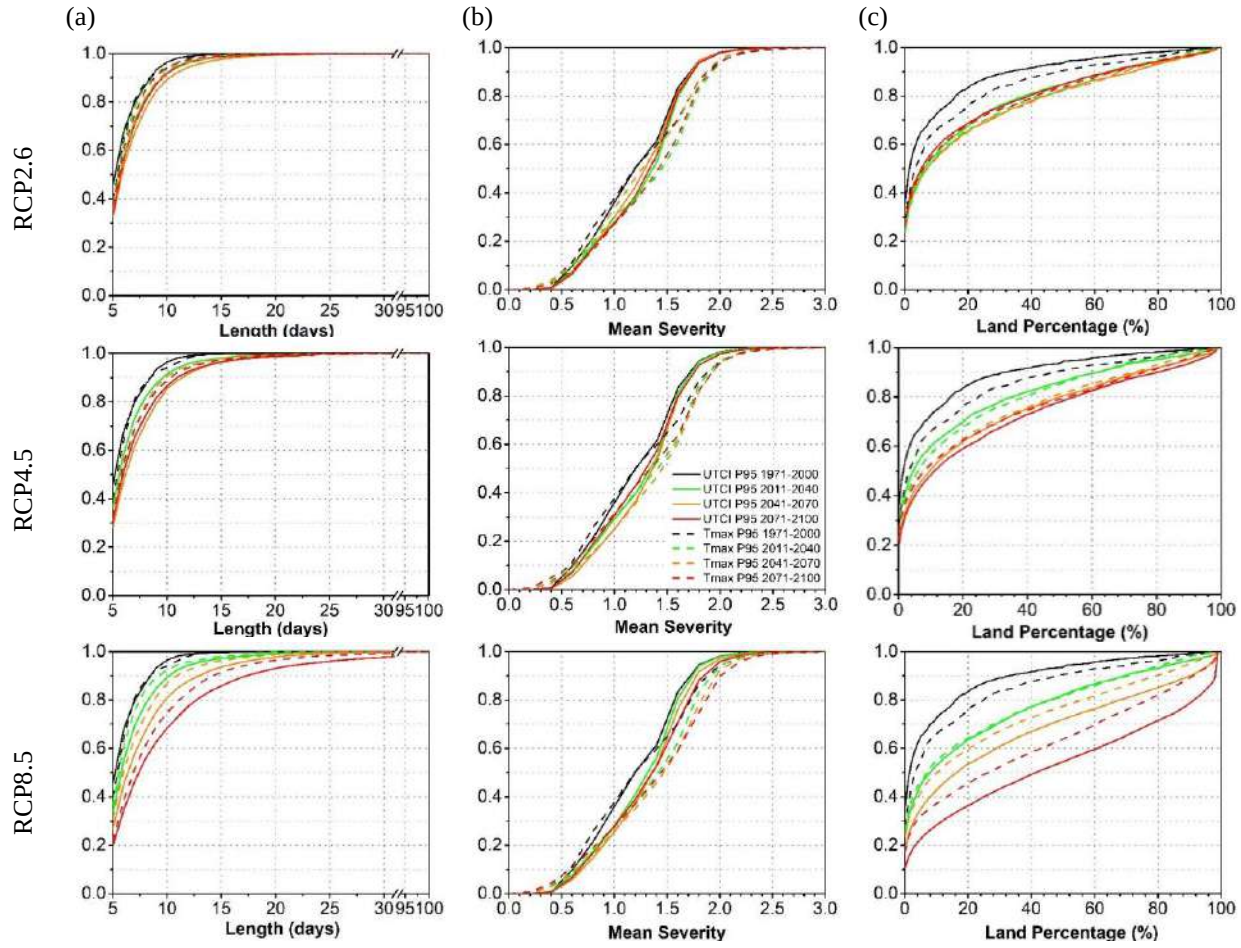

Figure 7.28 Multi-model ensemble empirical cumulative distribution functions of UTCI (solid line) and Maximum temperature (hashed line) driven heatwaves (a) length (days), (b) severity and (c) areal extension (%) for the historical period (1971-2000) and for the future periods considering different GHG emission scenarios.

7.6. Droughts

In this sub-section, a brief analysis of the drought results is presented based on calculation of two indices: the SPI and SPEI at 12-months of accumulation period. We also want to emphasize that an exhaustive analysis based on a new daily-SPI and daily-SPEI indices, with accumulation periods of 7-, 15-, 90-, 180-, and 360-days, will be delivered in a report regarding the WP4.

Figure 7.29 and Figure 7.30 display the future projected changes in average number of moderate droughts per decade and the average duration of moderate drought events computed for index SPI and SPEI at 12-months accumulation period, respectively.

Observing the Figure 7.29a, the future climate projections point to a small increase in the frequency of occurrence of moderate droughts, representing an increase of 2 events per decade in the south region and 1 event per decade in the north region, in RCP8.5 for the mid- and end-of century. However, a noteworthy increase in the average duration of each event is projected (Figure 7.29b). This increase is slightly higher in the southern than in the northern region and can reach increases on average duration of 12 months (1-year). In the beginning of the century, all the RCPs project a slightly decrease in the number of moderate droughts over most of north region, and a slightly increase in the south region. The same occurs in the mid-of-century for RCP2.6 and RCP4.5. These results are linked to the future projections in annual precipitation since the SPI is only based on precipitation. In regions where the projections point to a significant reduction in annual precipitation, the frequency of occurrence of moderate droughts increases, whilst in the regions where there is a reduction in the number of moderate droughts per decade, it is expected changes in annual precipitation close to zero.

Using SPEI, the future projections for moderate droughts show some differences to the ones based on SPI. The SPEI includes a simplified water balance between precipitation and potential evapotranspiration, which means that it is dependent of the precipitation and temperature future projections. Regarding moderate droughts based on SPEI, the future projections show a significant increase in the frequency of these events, with more 4 drought events per decade in the south region, and 2 – 3 in north region, in RCP8.5 for the mid- and end-of century. The duration of moderate droughts points to an increase between 20 to 28 months in south region and between 8 to 16 months in north region. These changes are in line with the increase of mean temperature and the reduction of annual precipitation.

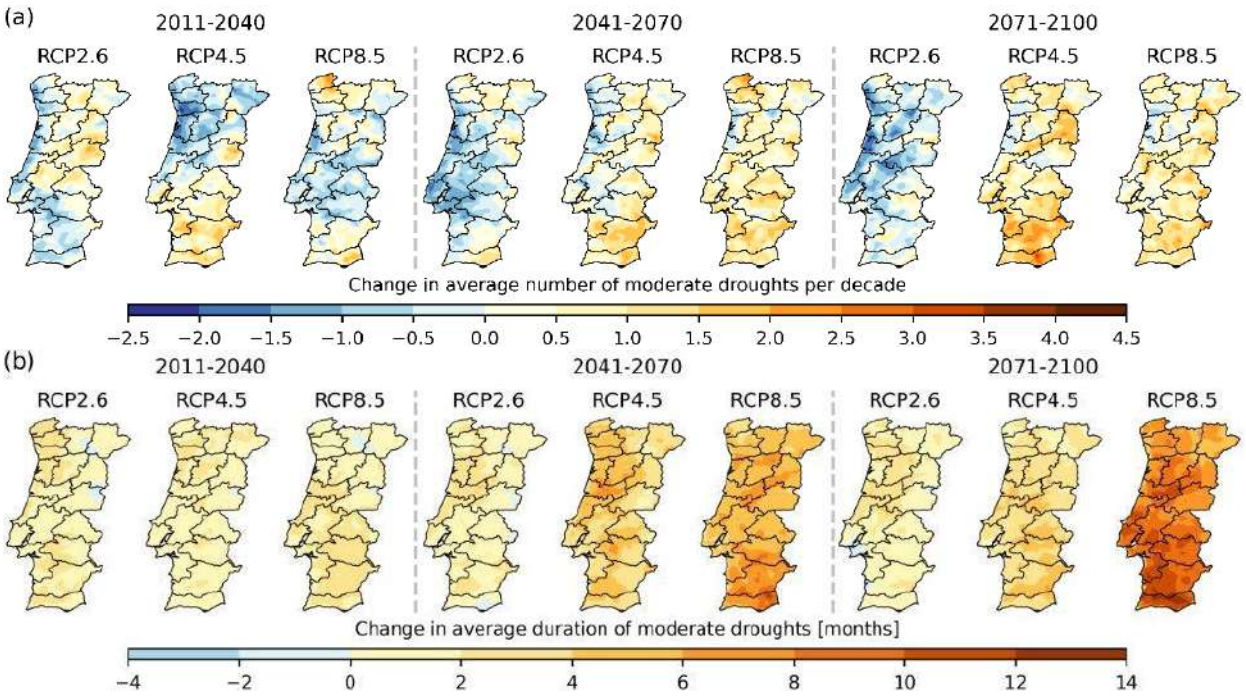

Figure 7.29 Future projected changes in (a) average number of moderate droughts per decade, and (b) average duration of moderate drought events over mainland Portugal computed for index SPI at 12 months accumulation period, considering the 1971-2000 period as reference. The different columns represent the future periods considering different GHG emission scenarios.

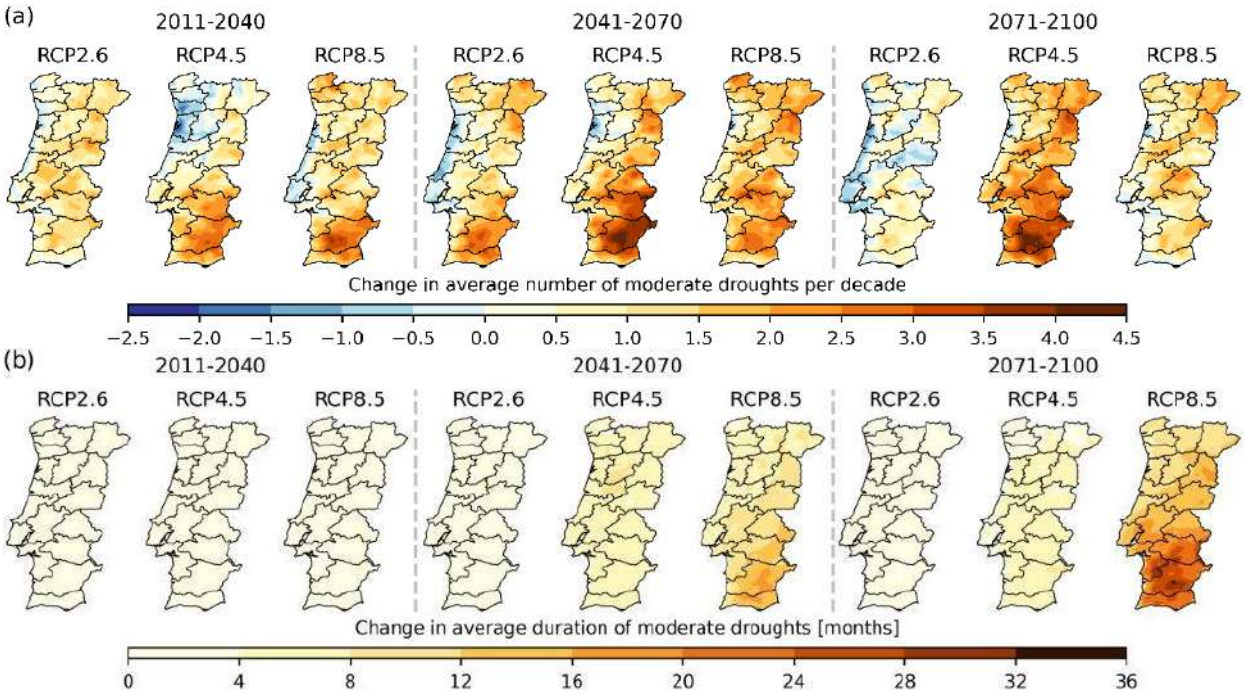

Figure 7.30 Future projected changes in (a) average number of moderate droughts per decade, and (b) average duration of moderate drought events over mainland Portugal computed for index SPEI at 12 months accumulation period, considering the 1971-2000 period as reference. The different columns represent the future periods considering different GHG emission scenarios.

7.7. Köppen-Geiger system

The map of Köppen-Geiger climate classification for Portugal mainland shows that only one (C) of the main climate types are presented in historical period (Figure 7.31). The dominant climate type over Portugal is the temperate. The north region and a small band near the coast north of Lisbon area are characterised by a temperate climate with a dry and warm summer (Csb), whilst the remaining regions are described by a temperate climate with dry and hot summer (Csa). For the future projections, a reduction of the land area with a Csb classification is expected for the RCP2.6 and in the beginning of the century for the other two future scenarios. The area classified as Csb almost disappears in RCP4.5 and RCP8.5 for the mid- and end-of-century due to the expansion of the Csa type. For the middle of the century, a new climate type designated as arid (B), characterised as an arid climate steppe and hot (Bsh), appears over south-eastern region of Portugal, which is more visible in the RCP8.5. This area expands for the end-of-century to Alentejo region. These results are associated to the decrease of the precipitation and the increase of the mean temperature.

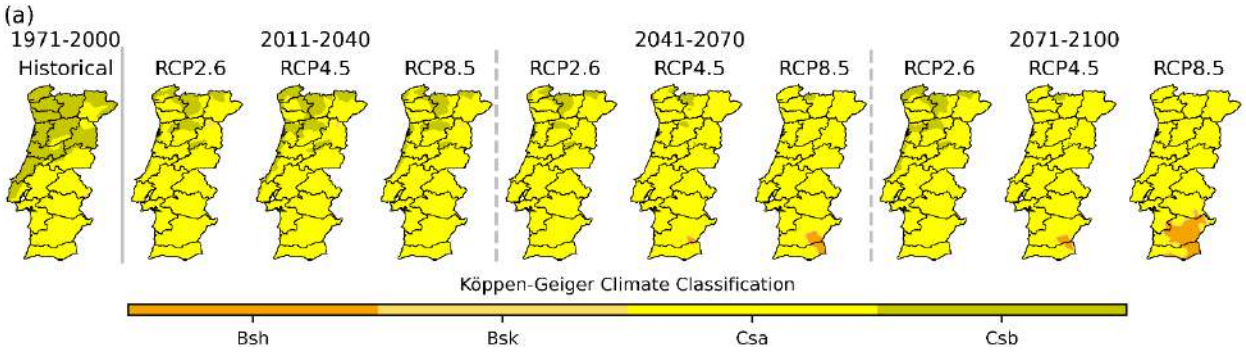

Figure 7.31 (a) Köppen-Geiger Climate Classification over mainland Portugal for historical climatological period (1971-2000) and for the future periods considering different GHG emission scenarios.

7.8. Agriculture Indices

The growing season (Figure 7.32) defined the period during which temperatures are consistently above 5 ^{o}C occurs practically all year round (on average for more than 345 days) south of serra da Estrela and on a band near the coast. Except for two small zones near the Spanish border, the remaining land area has more than 295 days suitable for plant development. In the near future (2011-2040), growing season will have, on average, more than 305 days in all scenarios for mainland Portugal, with an expansion eastward and northward of the area with GSL > 355 days. For this period there is no significant distinction between scenarios. The GSL for the RCP2.6 scenario does not change during the 21st century, while in RCP4.5 and RCP8.5 the number of days increases throughout the century, and by 2100 the entire Portuguese mainland registers more than 325 days in the first and 345 days in the second.

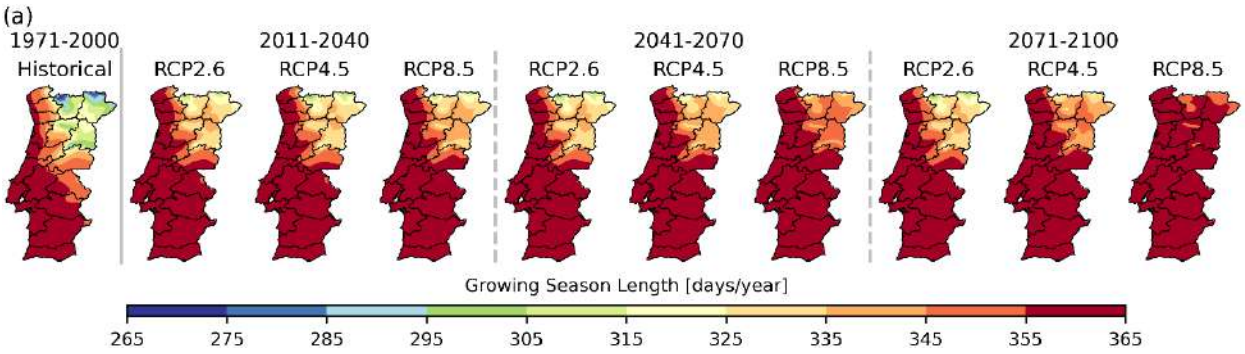

Figure 7.32 (a) Growing Season Length over mainland Portugal for historical climatological period (1971-2000) and for the future periods considering different GHG emission scenarios.

The Aridity index (Figure 7.33) shows that, historically, only in the southeast does the demand for water from the atmosphere, evapotranspiration, is more than double that is provided by precipitation. This region is considered semi-arid with $AI < 0.5$. Except for an area in Norte Alentejo and a small band near the coast, the remainder of mainland Portugal has a humid climate ($AI > 0.65$). In the future projections, the Aridity index does not change considerably for RCP2.6 and in the near future for the other scenarios (Figure 7.33). By mid-century the expansion of the semi-arid regions is visible in the south and most of the Tagus River basin becomes dry subhumid in RCP4.5 and RCP 8.5. By the end of the century and in RCP8.5, areas in the Tagus basin and near the Spanish border become semi-arid.

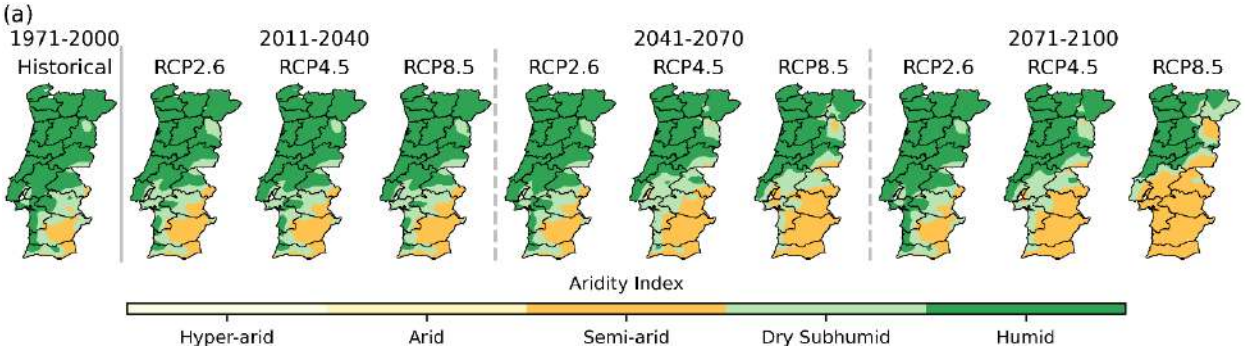

Figure 7.33 (a) Aridity Index over mainland Portugal for historical climatological period (1971-2000) and for the future periods considering different GHG emission scenarios.

Growing season precipitation (Figure 7.34) in the historical period has a north-south gradient wherein the northwest spring and summer precipitations are near the top threshold of 600 mm. Only the higher altitude regions of Gerês have a precipitation regime which is excessively wet. South of the Tagus River, the precipitation regime is below 200 mm, *i.e.*, extremely dry. As expected, the overall reduction of precipitation throughout the 21st century leads to a northward expansion of the extremely dry areas in

RCP4.5 and RCP8.5 and in the latter, only the northwestern region of mainland Portugal has sufficient precipitation during spring and summer to sustain viticulture. In RCP2.6 the historical precipitation distribution remains throughout the 21st century.

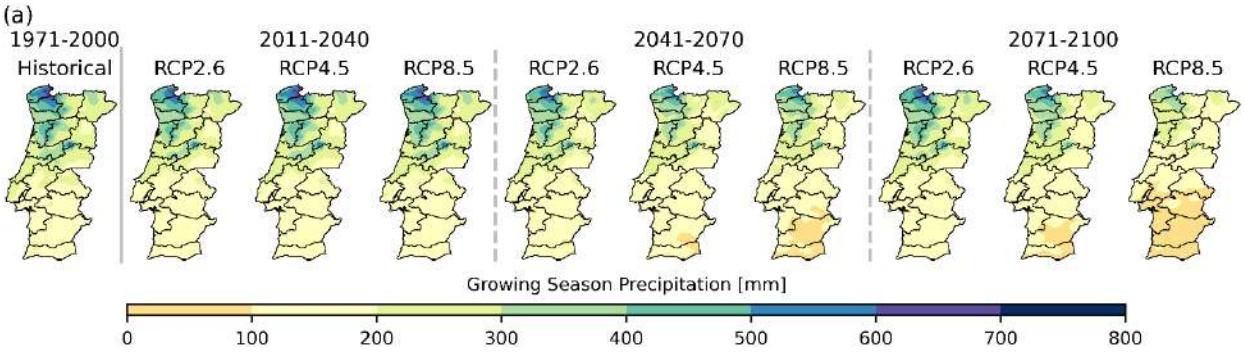

Figure 7.34 (a) Growing season precipitation over mainland Portugal for historical climatological period (1971-2000) and for the future periods considering different GHG emission scenarios.

According to the Selianinov Index, the historical growing season precipitation in most of the areas south of the river Tagus is insufficient to support the development of vineyards. For the 2011 to 2040 scenarios, this area has expanded to all the region south of the Tagus River. While there is no significant enlargement for RCP2.6 throughout the 21st century, by the end of the century, only a small region in the northwest has normal precipitation in RCP8.5 and in RCP4.5 all the Tagus basin and the south has insufficient precipitation during the growing season in addition to an area which encompasses the part of the Douro's demarcated region, very important for the production of Port.

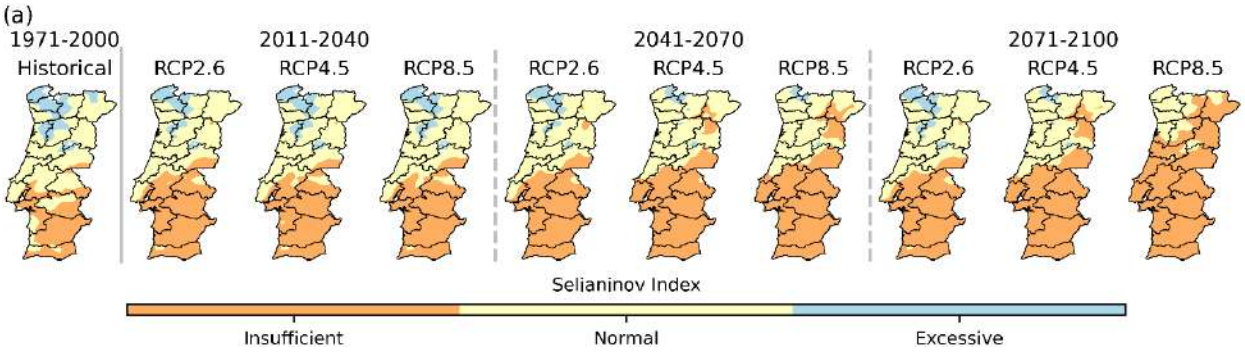

Figure 7.35 (a) Selianinov Index over mainland Portugal for historical climatological period (1971-2000) and for the future periods considering different GHG emission scenarios.

Asides from precipitation, temperature also plays an important role in the development of downy mildew. The high risk of the emergence of downy mildew is limited to the northwestern regions in the historical period (Figure 7.36). In RCP8.5 this risk almost disappears by the end of the century, with only a small high-altitude area in Gerês and the area with low risk expands up to the river Tagus along with a band near the Spanish border. In RCP2.6, the high-risk area remains unchanged throughout the century and a small

increment in the regions with low risk is projected for south of Portugal. The changes in the high-risk area occur mainly from mid-century onwards in both RCP4.5 and RCP8.5. In RCP4.5 the expansion of the low-risk region is somewhat similar to RCP8.5, but with a smaller amplitude along the Spanish border.

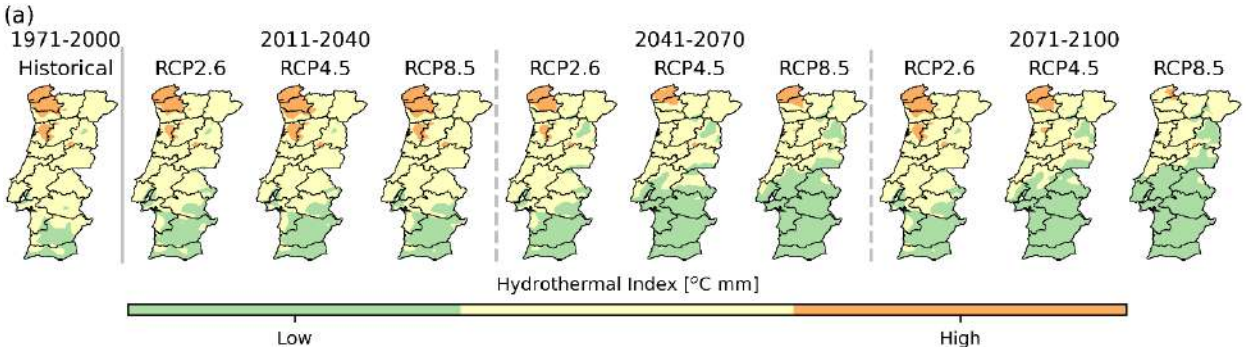

Figure 7.36 (a) Hydrothermal Index over mainland Portugal for historical climatological period (1971-2000) and for the future periods considering different GHG emission scenarios.

While vineyards in the northeast are subject to very cool nights in September during the historical period, on average, these nights disappear throughout the 21st century for all scenarios except for a very small region in Gerês at the beginning of the century which lingers for the entire 21st century in RCP2.6 (Figure 7.37). Cool nights occur north of the Tagus River near the coast and replace the very cool nights at the beginning of the century for all for all scenarios. During this period, the region with cool nights is displaced by temperate nights. With the progression of the century, cool nights occur mostly in RCP2.6, vanish in RCP8.5 and a small region lingers in Gerês in RCP4.5. The south of mainland Portugal has mostly temperate nights which, by mid-century, start to be replaced by warm nights in RCP4.5 and RCP8.5. By the end of the century, and for RCP8.5, warm nights become the norm in most of the territory except in some regions in the northeast.

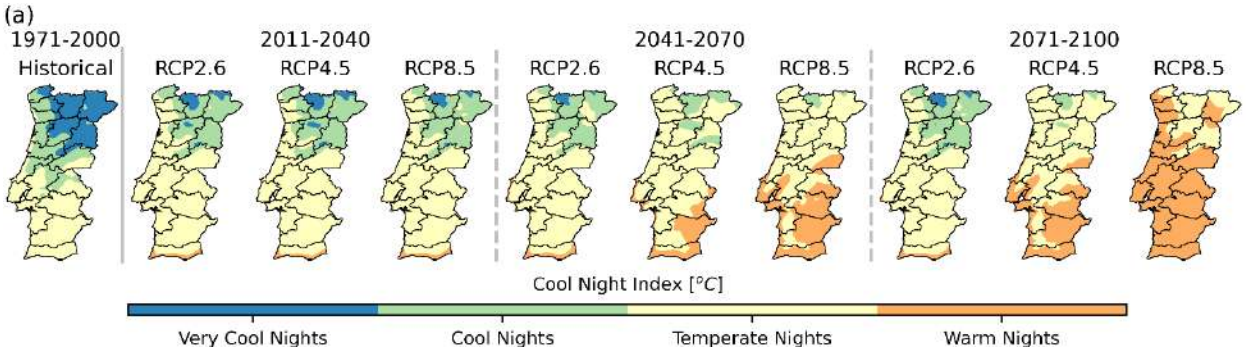

Figure 7.37 (a) Cool Night Index over mainland Portugal for historical climatological period (1971-2000) and for the future periods considering different GHG emission scenarios.

In the historical climate all of mainland Portugal has suitable conditions for the development of gravepine for more than 80% of the days between April and September (Figure 7.38). South of the Tagus River and

along the northern coast the suitability is higher than 95%. In a small band along the southern coasr and the Algarve the number of days with temperature below 10° C is, on average, less than two per year. The growing season suitability increases for all scenarios and by end of the 21st century and in RCP8.5, all of Portugal will have suitable conditions for viticulture 95% of the time.

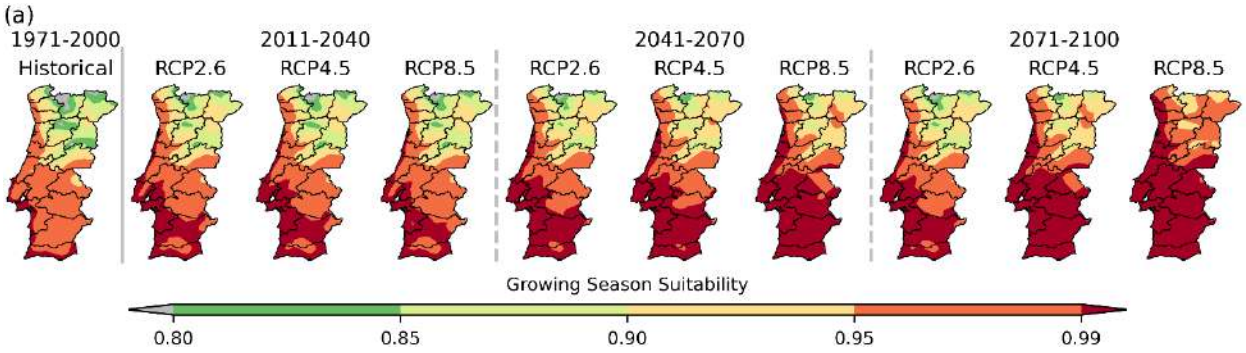

Figure 7.38 (a) Growing Season Suitability (fraction of days in April−September with daily mean air temperature equal or above 10°C) over mainland Portugal for historical climatological period (1971-2000) and for the future periods considering different GHG emission scenarios.

In the historical period, and according to the Huglin Heliothermal Index (Figure 7.39), the higher altitudes of Gerês are only suitable for grapevines with early maturation. In this period, the other higher altitude regions are suitable for a wide variety of grapes. In the remaining territory, temperatures between April and September imply the usage of varieties which mature later in the season and south of the Tagus River the heliothermal potential exceeds the grapevine needs to ripen. For early 21st century and all scenarios, the very cool regions almost disappear, lingering only in a small region in Gerês and the warm category envelops all the area south of the Tagus River. The heliothermal characteristics in RCP2.6 remain constant throughout the century, while in RCP8.5 and for the 2071-2100 period, all the territory has warm (above the Tagus River) and very warm conditions.

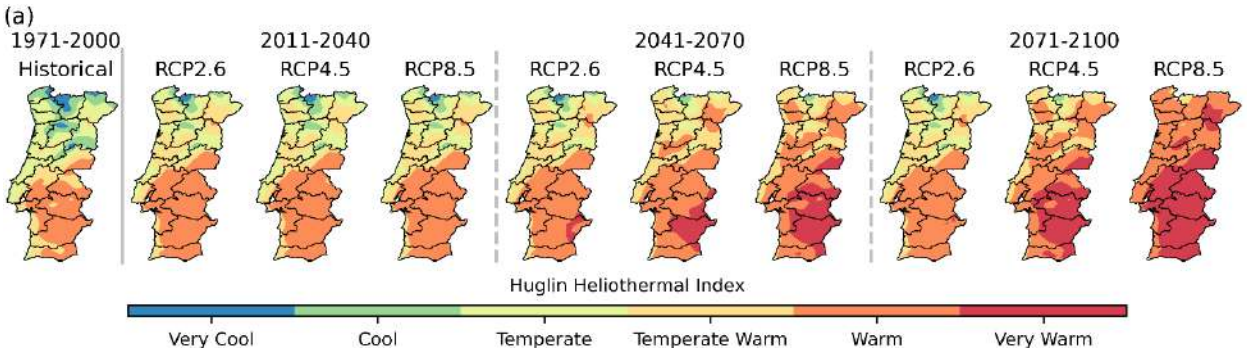

Figure 7.39 (a) Huglin Heliothermal Index over mainland Portugal for historical climatological period (1971-2000) and for the future periods considering different GHG emission scenarios.

The growing degree day has very limited change in RCP2.6 and in the beginning of the century in all scenarios (Figure 7.40). In RCP4.5 and in northeast, it increases by ~50% by the end of the century, while this increase starts in mid-century in RCP8.5 and by the end of the century some regions double the growing degree day index. South of the Tagus River the index indicates that high production which is able to achieve acceptable table wine quality is feasible in the historical period and only a small region in the Guadiana Basin has an acumultaion of temperatures detrimental for the production of good quality wines or is suitable for wines that are consumed early in the season. By mid-century this later category extends to all of the region south of the Tagus River and in both RCP4.5 and 8.5, the latter region becomes too warm for wine production. In RCP8.5 the excessive temperature category extends further into Baixo Alentejo. At the end of the century, the excessive temperatures south of the Tagus River in RCP8.5 will preclude the production of wine in this region and in the remaining territory only varieties which tolerate early season harvesting will be feasible. In RCP4.5 and north of the Tagus River, the accumulation of temperatures still allows the production of good quality wine in some regions.

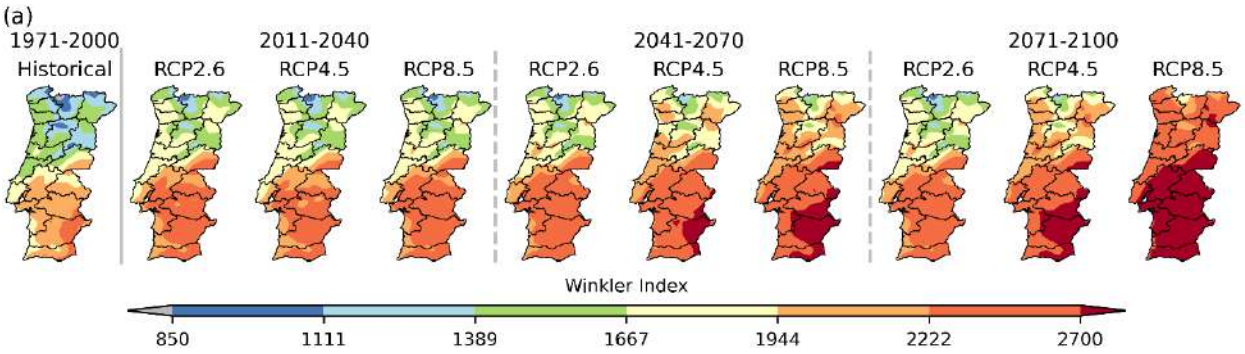

Figure 7.40 (a) Winkler Index over mainland Portugal for historical climatological period (1971-2000) and for the future periods considering different GHG emission scenarios.

In the historical period, lower Growing Degree Hours are associated to the high elevation areas of the north and northeast of mainland Portugal (Figure 7.41). Values of GDH greater than 55000 are widespread south of the Tagus River basin and in the northern coast. In the early 21st century scenarios, the warming temperatures lead to a decrease in the very low north-eastern GDH. Yet, the warming is not strong enough to induce relevant changes in other areas of the country. As expected, form the temperature evolution in RCP2.6 throughout the 21st century, the distribution of GDH is very similar in the mid and late century periods. By mid-century, the increased temperatures in both RCP4.5 and 8.5, leads to a further northward enlargement of the areas with GDH greater than 55000 and an emergence of a strip with GDH greater than 70000 along the coast. The overall distribution of GDH in RCP4.5 does not change until the end of the century, however the limiting condition of 36 ºC, above which GDH stops accumulating leads to a decrease in GDH in a strip along the Spanish border in RCP8.5 by the end of the century. While a good resemblance between GDH and the Winkler index is obtained in the historical period and for early 21st century, the temperature critical threshold and the sub-daily temperatures ranges preclude the large increases of the growing conditions south of the river Tagus projected in both RCPs (4.5 and 8.5) for mid and late century.

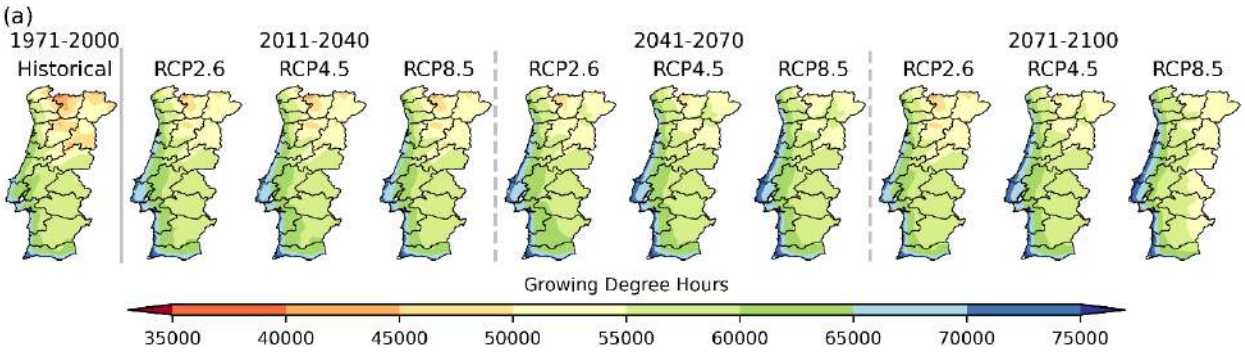

Figure 7.41 (a) Growing Degree Hours over mainland Portugal for historical climatological period (1971-2000) and for the future periods considering different GHG emission scenarios.

Chilling portions between 75 and 100 are indicative of the temperate winter temperatures observed in mainland Portugal (Figure 7.42). Only the higher altitudes have CP greater than 100 in the historical period. As the 21st century progresses, the lower CPs which emerge in the south at the beginning of the century, advance northwards. By the end of the century, in RCP8.5 only the north-eastern elevated areas have chilling portions between 75 and 100.

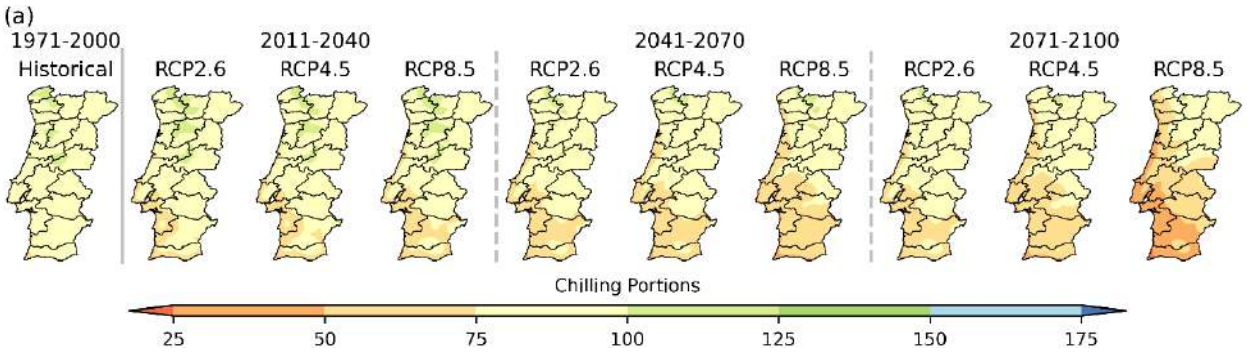

Figure 7.42 (a) Chilling Portions over mainland Portugal for historical climatological period (1971-2000) and for the future periods considering different GHG emission scenarios.

8. Conclusions

This report is the result of a joint effort by Instituto Dom Luiz and APA through the National Roadmap for Adaptation XXI (RNAXXI) project. It provides the most accurate, up-to-date, and coherent climate information available to support the assessment of climate change impacts and decisions regarding adaptation and mitigation in Portugal. The results presented in this report will be a central piece for an overview reflection on the impacts of climate change, and its translation into the storylines, exploiting predominantly climate indices for different sectors.

The Mediterranean basin, in which Portugal is included, is in the transition zone between the arid to semiarid subtropical, and the humid climates of northern Europe, being these regions very vulnerable to climate change. Mediterranean climates are prone to large spatio-temporal precipitation and temperature gradients. According to the Fifth Assessment Report of the Intergovernmental Panel on Climate Change, the observed and projected rates of climate change exceed the global trends for most variables over the Mediterranean. Moist mild winters and dry warm/hot summers are a common feature that characterises the Mediterranean climate, including Portuguese climate. Several studies reported a general warming and drying trends across the Mediterranean basin that will continue throughout the 21st century.

In this report, the EURO-CORDEX high resolution regional climate simulations (0.11º resolution) are used to investigate and obtained climate projections for the main climate variables, and a set of climate indices relevant for stakeholders and policymakers. Three different future time periods were considered (2011-2040, 2041-2070 and 2071-2100) according to RCP2.6, RCP4.5 and RCP8.5 greenhouse gas emission scenarios. All simulations for the historical period (1971-2000) were evaluated against the Iberia-01 dataset. This dataset was used to evaluate the quality of precipitation, maximum and minimum temperature of the 45 RCM simulations. Moreover, these results were used to build a multi-model ensemble to depict the climate change signal on a set of climate variables and indices over Portugal. The evaluation results for precipitation showed that most of the models were able to simulate the precipitation patterns during the present climate. However, the models tended to overestimated precipitation, with only 22% (10) of the models showing an underestimation. Regarding the maximum temperature, 93% (42) of the simulations showed a cold bias, which in some cases could be linked to the forcing GCM. This was not the case of the minimum temperature, where one-third of the models depicted warm bias. Nevertheless, the simulations were able to represent the maximum and minimum temperature patterns in the present climate. The ranking of the models for precipitation and each temperature (maximum and minimum), relying on skill scores, allowed the construction of multi-model ensembles. Four different multi-model ensembles were analysed considering five different groups of RCMs dependent of the RCP availability. The first was an ensemble produced for each variable based on its overall model performance weights; the second and third were

constructed based on the individual weights of the three evaluated variables; and in the fourth the weights are equal for all models. An analysis of the different multi-model ensemble groups was pursued but only the multi-model ensembles including the 13 RCMs that have all RCPs were considered. The ensemble 1 presented the better performance in each variable, which is expected since it only considers the quality of each individual variable. For the ensemble including multi-variables, the ensemble 3 had the best performance for precipitation and maximum temperature. For the minimum temperature the best performing ensemble was ensemble 2, however both ensembles (2 and 3) had results close to each one. Based on this evaluation, the EURO-CORDEX multi-model ensemble with 13 RCMs was built following the ensemble 3 formulation and was adopted to characterise and assess the future climate change projections and their uncertainty. All the climate variables and indices presented in this report were computed following the ensemble 3 formulation.

The projected temperature changes over Portugal are rather severe and significant. Temperature is projected to increase in all seasons and regions in Portugal during the 21st century, with a stronger warming in summer than in winter. Also, the strongest anomalies are found over north-eastern Portugal. The strength of the warming at the end-of-century (2071-2100) relative to the historical period (1971-2000) is highly dependent on the greenhouse gas emission scenario considered. The positive anomalies are stronger for higher emission scenarios, and amplifying throughout the 21st century, except for RCP2.6 where they stabilise from mid-century onwards. For the mitigation scenario RCP2.6, an increase of 1 – 2ºC is projected during summer for daily mean temperature compared to an increase of 4 – 7ºC for the scenario without mitigation RCP8.5. In general, future projections for maximum temperature show a slightly larger warming than those for minimum temperature. Considering the worst-case scenario (RCP8.5), the daily maximum temperature rise is largest in summer, with maximum increases larger than +6ºC, whereas in winter ranges between +3 and +4ºC. For daily minimum temperature, the positive anomalies reach magnitudes larger than +5ºC in summer and autumn, while an increase of about +3 to +4ºC is projected to occur during winter and spring under RCP8.5 scenario. Although the maximum temperature warming is slightly larger than in minimum temperature, the strong similarities in the climate change signal leads to a weak change in the diurnal temperature range, reaching magnitudes not larger than +1ºC in all seasons and most regions under RCP8.5 scenario for the end-of-century. For temperature (mean, maximum, and minimum) the signal of climate change was coherent amongst all models in all seasons, periods, and emission scenarios, which means that the temperatures in Portugal will very likely rise over the course of the 21st century.

The goal of the Paris Agreement is to limit the global temperature increase to 1.5ºC relative to pre-industrial levels, while pursuing efforts to avoid the +2ºC warming threshold. Observing the results presented here Portugal will likely experience a further annual mean warming of +1 to +2ºC relative to the historical period

for the strong mitigation scenario RCP2.6. For the scenario without mitigation RCP8.5 warming will increase by more +5ºC than in RCP2.6 until the end of the 21st century.

Precipitation changes depend on the season, region, and the future emission scenario. Overall, the future projections point to a decrease in precipitation throughout the 21st century, which indicates an intensification of the drying conditions in mainland Portugal. Under the RCP8.5 scenario, the climate change signal points to an yearly decrease greater than 10% in the northwest and above 30% in the southern areas for the end-of-century. This reduction is also presented in the mid-of-century but less pronounced and in the beginning of the century in southern areas between -10 and -5% of precipitation. For the mid- and end-of-century, the decline of precipitation occurs mostly in spring, summer, and autumn with projected reductions over 20% and 30%, respectively. Although summer precipitation does not have a significant contribution for the annual total due to its lower values, relative changes above 40% are expected during 2071-2100. For RCP4.5, the negative relative anomalies are similar to the ones for RCP8.5 but less significant, although it tends to stabilise towards the end-of-century. In fact, in winter a slightly increase of 10% in precipitation is expected in northern areas. For the mitigation scenario RCP2.6 a wetted winter is projected in most of mainland Portugal with an increase above 10% for mid- and end-of-century. Like temperature, most ensemble members (> 66%) agree on the signal of the precipitation projections throughout all time periods, seasons, and emission scenarios. Exceptions are found for the beginning of century in winter and spring for the RCP2.6 scenario that may be linked to the lower expected changes ranging from -5 to +5%. For the scenario without mitigation RCP8.5 the precipitation over Portugal will likely decrease during all seasons.

Warming and drying conditions will cause a decline in the relative humidity, and consequently an increase in potential evapotranspiration. These changes are highly dependent on the emission scenario. For the mitigation scenario RCP2.6 the lower changes in relative humidity range from -2 to +2% throughout the 21st century and an increase in potential evapotranspiration lower than 10% is projected. In RCP4.5 the reduction in relative humidity increases over the course of the 21st century in all seasons up to -6% over the north-eastern region, except during winter when it stabilises by mid-of-century. The projections of potential evapotranspiration point to an increase between 10 and 15% until the end of the century. For the scenario without mitigation RCP8.5 the reduction in relative humidity is amplified throughout the 21st century, particularly in the north-eastern region during summer where a decrease between 6 and 8% is expected. Regarding potential evapotranspiration an enhancement up to 40% is projected to occur in autumn at the end-of-century and above 20% in the remaining seasons. However, the multi-model spread for these two climate variables is almost as large as the climate change signal, which points to a large uncertainty

associated to the computation of the relative humidity and potential evapotranspiration. Consequently, these results need to be analysed carefully.

In line with the projected reduction in precipitation, a decline in soil moisture is also expected. The future projections in soil moisture are similar in all scenarios but amplified throughout the 21st century. Although the projections show a slight increase in winter precipitation in most of the scenarios and periods, the winter warming enhances the evaporation rate at the surface and an increase in soil moisture content does not arise. Over the southern regions the reduction in soil moisture and precipitation, and the increase in air temperature contributes to the decline of evaporation at the surface. As in relative humidity and potential evapotranspiration, the multi-model spread is large conducting to a large uncertainty of climate change projections in soil moisture and evaporation.

As a result of warming, the frequency and intensity of extreme climate events will also change. Along with warming maximum temperature, summer days and hot days will be more frequent. Additionally, heatwaves and very hot days will be more frequent, more intense, and longer lasting. Under RCP8.5 scenario mainland Portugal shows more than 100 summer days in the north and close to 200 in the south for the end-of-century. The number of hot days will also increase over the entire country with more than 60 hot days per year and close to 160 in south-eastern region. As with hot days, the increase in the number of very hot days is more noticeable in south-eastern region. At the end-of-century the positive anomalies depict more 20 to 70 days from the north-western coastal regions to south-eastern regions. Along with the increase of very hot days an increase in the consecutive number of very hot days is also projected. For the end-of-century and under RCP8.5 scenario the maximum number of consecutive very hot days can reach 3 months (90 days) near the Spanish border. For the RCP2.6 the climate change signal is the same but the increases are less pronounced. In the case of the RCP4.5 scenario the positive anomalies are milder. The rise in the number of heatwaves is evident and larger near the Spanish border than near the coast. Considering the scenario without mitigation RCP8.5 for the end-of-century the number of heatwaves can reach 13 events per year contrasting with 2 to 4 events per year in the historical period. The average duration of a heatwave also increases to an average of 16 days per event near the Spanish border and 12 days in the areas closer to the coast. In addition, the maximum duration of a heatwave can reach 3 months. For RCP2.6 and RCP4.5 in mid-of-century the average number of heatwaves per year increases of 4 – 7 and of 5 – 8, respectively. In the case of average duration of these events an increase of 1 to 4 days is expected. Although in these two RCPs the increase is smaller, the projections show a maximum duration that can reach two months. Aligned with the rising of minimum temperature tropical nights will be more common and the number of frost days and cold days will decrease. A rise in number of tropical nights is expected throughout the 21st century with a significant increase from mid- to end-of-century for RCP4.5 and RCP8.5. The positive anomalies of tropical nights

show an increase that go from 10 – 20 nights in the RCP2.6 (2011-2040 and 2041-2070) to an increase that exceeds 80 nights in the end-of-century for RCP8.5. In mainland Portugal, there is a north-eastern cluster where the number of frost days and cold days are maximum. The future projections show that there is a gradual shrinking of this cluster, with less frost days and cold days throughout the 21st century. The results of maximum number of consecutive cold days are aligned with the projections of cold days. For all the emission scenarios and time periods the reduction in number of coldwaves is expected to occur over all country. However cold winter periods will continue to occur even if less frequent and less lasting. Regarding heat and cold extremes, most of the models agree in the climate change signal for most regions, time periods and emission scenarios, which gives us very high confidence in the results presented.

Along with warming mean temperatures, there will be a part of the country in moderately hot stress in summer season in mid- and end-of century for the RCP4.5 and RCP8.5. In addition, in winter the slightly cold stress condition will be dominant over mainland Portugal until the end of the 21st century.

In addition to changes in temperature extremes, changes in precipitation extremes are also expected. The precipitation projections show a significant increase in the maximum consecutive dry days throughout the 21st century in all emission scenarios. The number of wet days is expected to decrease until the end of the century. Indeed, a reduction above 24 wet days is projected in RCP8.5 at the end-of-century. Under RCP4.5 scenario, the reduction is around 12 days per year and in RCP2.6 the decrease is very lower. The projections for the maximum consecutive wet days show differences between emission scenarios and time periods. Under RCP8.5 scenario, at the beginning of the century an increase in expected in northern region and a slightly increase occurs over Tagus basin, whilst in at the mid- and end-of-century a decrease is projected more noticeable in centre and southern regions. For RCP2.6 the maximum changes are found at the middle of the century with a rise in maximum consecutive rainy days over almost all country. There is a considerable reduction in the number of days with daily rainfall below 20 mm. In the case of number of days with daily rainfall exceeding 50 mm, the future climate projections remain similar to the ones in historical climate. However, the average percentage of annual precipitation from rainy days above 10 mm and 50 mm rises more than 10% per year throughout the 21st century more and it is more noticeable in the interior north and south regions. This means that even the number of wet days will decrease, the amount of precipitation during wet periods will increase leading to an intensification of heavy rainfall.

The magnitude of the projected daily mean 10-m wind speed changes throughout the 21st century is strongest for the RCP8.5 scenario, with a significant sub-regional variability of wind speed anomalies under a warming climate, both at annual and seasonal averaging timescales. The largest reductions are found in winter and autumn seasons over elevated terrain in northern and central-eastern regions, and over the southwestern coastal regions for the end-of-century. In contrast, an increase in 10-m wind speed is projected

to occur in summer over the entire country. For maximum daily mean 10-m wind speed, a decrease is expected over the Alentejo and central regions for all time periods and emission scenarios. Positive anomalies are projected over the northwestern region, but its magnitude depends on the emission scenario considered with the highest changes observed in the RCP8.5. In what concerns the maximum of daily maximum wind gust, the future projections differ between RCPs. Since winter storms are the most important cause for the occurrence of wind gusts, the expected changes may be related with the future changes on these phenomena. A reduction in the number of days with daily mean 10-m wind speed exceeding 5.5 m/s is expected over mainland Portugal except in the Lisbon metropolitan area where an increase is projected. These negative anomalies are more noticeable for the end-of-century in the RCP8.5 scenario, whilst the positive anomalies are more pronounced in RCP4.5. For the number of days with daily mean 10-m wind speed exceeding 10.8 m/s, a slightly decline in found over the Lisbon metropolitan area. Regarding calm days, there is a gradual rise over the northwestern region of Portugal further marked for the end of the century and for the scenario without mitigation RCP8.5.

The future projections for daily mean wind speed at 30 and 60 m are in line with those of 10-m wind speed. A reduction is expected in winter and autumn, gradually intensify throughout the 21st century and from the scenario with high mitigations for the non-mitigation scenario. Additionally, a similar evolution is found in summer where an increase is found over the Lisbon metropolitan area. Regarding the maximum daily mean wind speed at 30 and 60 m, a rising on the intensity is projected in summer over mainland Portugal. A north-south dipole is found in spring, where a reduction is expected in north and an increase in south. The opposite arises in winter. In what concerns the future projections of daily mean wind speed at two different levels, the results need to be analysed carefully. It is important to point out that despite the small magnitude changes of the wind speed at 30 and 60 m, the impact on wind turbine energy production is significantly enhanced due to the cubic dependence of wind energy production on wind speed, and the high and low cut-off thresholds of wind turbines for energy production.

Changes in the core variables are obviously echoed in the bioclimatic indices relevant for agriculture. The overall warming in all scenarios induces an increase in the growing season length hence, its large number of days (> 300 days). The changes are more significant in the northeast high elevation areas, where, at the end of the century, temperatures above 5 ^{o}C are projected to occur almost all year round in RCP8.5 and for 11 months in RCP4.5. When the temperature daily variability is accounted for as well as thresholds for excessive temperatures which imped development are considered, a decrease in the suitability for plant growth is the regions near the Spanish border is projected in RCP8.5 for the end of the century. The latter restriction also limits the expansion of the GDH in the centre of the country from mid-century onwards. The areas that benefit from the temperature increase are near the coast. The rise of the daily mean

temperatures will have a significant impact on the viticulture sector, particularly on the quality of the wine and on the suitability of certain regions for wine production. At the end of the century, the excessive temperatures south of the Tagus River in RCP8.5 will preclude the production of wine south of the Tagus River basin and in the remaining territory only varieties which tolerate early season harvesting will be feasible. In RCP4.5 and north of the Tagus River, the accumulation of temperatures still allows the production of good quality wine in some regions. The impact of higher minimum temperatures will lead to a considerable reduction of the very cool nights in the northeast in RCP2.6 and a shift to temperate nights in the other scenarios by the end of the 21st century. In the latter two scenarios, the emergence of warm nights south of the river Tagus and in a coastal band in the northwest for RCP8.5 will have a significant impact on the quality of wine, since these are essential in the ripening process. Additionally, the projected reduction in chilling portions in the same areas will not only impact on all the vineyards winter development, but also temperate trees. Depending on the species, this will reduce the ability of plants to accumulate cold and break their dormancy, inducing budburst. Thus, the productivity of some tree species will be reduced. Heightening the impact of the rise in temperatures will be the reduction of precipitation with the emergence of semi-arid climate and the insufficient precipitation regimes for the regions south of the Tagus River in all scenarios and in almost all the country in RCP8.5.

The compound effect of precipitation and temperature will however have a positive impact on the development of downy mildew since its risk of incidence will be reduced.

9. References

Abramowitz G, Bishop CH (2015) Climate Model Dependence and the Ensemble Dependence Transformation of CMIP Projections. J Clim 28:2332–2348. https://doi.org/10.1175/JCLI-D-14-00364.1

Allen RG, Jensen ME, Wright JL, Burman RD (1989) Operational Estimates of Reference Evapotranspiration. Agron J 81:650–662. https://doi.org/10.2134/AGRONJ1989.00021962008100040019X

APREN (2022) Produção Energias Renováveis. https://www.apren.pt/pt/energias-renovaveis/producao. Accessed 10 May 2022

Barcikowska MJ, Weaver SJ, Feser F, et al (2018) Euro-Atlantic winter storminess and precipitation extremes under 1.5°C vs. 2°C warming scenarios. Earth Syst Dyn 9:679–699. https://doi.org/10.5194/ESD-9-679-2018

Beck HE, Zimmermann NE, McVicar TR, et al (2018) Present and future köppen-geiger climate classification maps at 1-km resolution. Sci Data 5:1–12. https://doi.org/10.1038/sdata.2018.214

Bengtsson L, Hodges KI, Keenlyside N (2009) Will Extratropical Storms Intensify in a Warmer Climate? J Clim 22:2276–2301. https://doi.org/10.1175/2008JCLI2678.1

Bengtsson L, Hodges KI, Roeckner E (2006) Storm Tracks and Climate Change. J Clim 19:3518–3543. https://doi.org/10.1175/JCLI3815.1

Bishop CH, Abramowitz G (2013) Climate model dependence and the replicate Earth paradigm. Clim Dyn 41:885–900. https://doi.org/10.1007/s00382-012-1610-y

Blanco-Ward D, Queijeiro JMG, Jones G V. (2007) Spatial climate variability and viticulture in the Miño River Valley of Spain. VITIS - J Grapevine Res 46:63–63. https://doi.org/10.5073/VITIS.2007.46.63-70

Boberg F, Berg P, Thejll P, et al (2009) Improved confidence in climate change projections of precipitation evaluated using daily statistics from the PRUDENCE ensemble. Clim Dyn 32:1097–1106. https://doi.org/10.1007/s00382-008-0446-y

Bock L, Lauer A, Schlund M, et al (2020) Quantifying Progress Across Different CMIP Phases With the ESMValTool. J Geophys Res Atmos 125:. https://doi.org/10.1029/2019JD032321/FORMAT/PDF

Branas J, Bernon G, Levadoux L (1946) Éléments de viticulture générale - Jean Branas, G. Bernon, Louis Levadoux - Google Livros. Imp. Dehan, Montpellier

Bröde P, Fiala D, Błażejczyk K, et al (2012) Deriving the operational procedure for the Universal Thermal Climate Index (UTCI). Int J Biometeorol 56:481–494. https://doi.org/10.1007/S00484-011-0454-1

Cardoso RM, Soares PMM, Lima DCA, Miranda PMA (2019) Mean and extreme temperatures in a warming climate: EURO CORDEX and WRF regional climate high-resolution projections for Portugal. Clim Dyn 52:129–157. https://doi.org/10.1007/s00382-018-4124-4

Cardoso RM, Soares PMM, Lima DCA, Semedo A (2016) The impact of climate change on the Iberian low-level wind jet: EURO-CORDEX regional climate simulation. Tellus, Ser A Dyn Meteorol Oceanogr 68:1–15. https://doi.org/10.3402/tellusa.v68.29005

Casanueva A, Kotlarski S, Herrera S, et al (2016) Daily precipitation statistics in a EURO-CORDEX RCM ensemble: added value of raw and bias-corrected high-resolution simulations. Clim Dyn 47:719–737. https://doi.org/10.1007/S00382-015-2865-X/FIGURES/10

Charlton-Perez AJ, Aldridge RW, Grams CM, Lee R (2019) Winter pressures on the UK health system dominated by the Greenland Blocking weather regime. Weather Clim Extrem 25:100218. https://doi.org/10.1016/J.WACE.2019.100218

Christensen JH, Kjellström E, Giorgi F, et al (2010) Weight assignment in regional climate models. Clim Res 44:179–194. https://doi.org/10.3354/cr00916

Collins JK, Perkins-Veazie P, Roberts W (2006) Lycopene: From Plants to Humans. HortScience 41:1135–1144. https://doi.org/10.21273/HORTSCI.41.5.1135

Cos J, Doblas-Reyes F, Jury M, et al (2022) The Mediterranean climate change hotspot in the CMIP5 and CMIP6 projections. Earth Syst Dynam 13:321–340. https://doi.org/10.5194/esd-13-321-2022

Cramer W, Guiot J, Fader M, et al (2018) Climate change and interconnected risks to sustainable development in the Mediterranean. Nat Clim Chang 8:972–980. https://doi.org/10.1038/S41558-018-0299-2

Deser C, Phillips A, Bourdette V, Teng H (2012) Uncertainty in climate change projections: The role of internal variability. Clim Dyn 38:527–546. https://doi.org/10.1007/S00382-010-0977-X/FIGURES/17

ECA&D (2013) European Climate Assessment & Dataset, Algorithm Theoretical Basis Document (ATBD)

Edwards DC, McKee TB (1997) Characteristics of 20th century drought in the United States at multiple time scales. Climatology Report No. 97-2. Colorado State University. Libraries

Eyring V, Cox PM, Flato GM, et al (2019) Taking climate model evaluation to the next level. Nat Clim

Chang 9:102–110. https://doi.org/10.1038/s41558-018-0355-y

Ferro CAT, Hannachi A, Stephenson DB (2005) Simple nonparametric techniques for exploring changing probability distributions of weather. J Clim 18:4344–4354. https://doi.org/10.1175/JCLI3518.1

Fiala D, Havenith G, Bröde P, et al (2012) UTCI-Fiala multi-node model of human heat transfer and temperature regulation. Int J Biometeorol 56:429–441. https://doi.org/10.1007/S00484-011-0424-7/TABLES/4

Fischer EM, Schär C (2010) Consistent geographical patterns of changes in high-impact European heatwaves. Nat Geosci 3:398–403. https://doi.org/10.1038/ngeo866

Flato G, Marotzke J, Abiodun B, et al (2013) Evaluation of climate models. In Climate Change 2013: The Physical Science Basis. Contribution of Working Group I to the Fifth Assessment Report of the Intergovernmental Panel on Climate Change. 741–866. https://doi.org/10.1017/CBO9781107415324.020

Frei C, Isotta FA (2019) Ensemble Spatial Precipitation Analysis From Rain Gauge Data: Methodology and Application in the European Alps. J Geophys Res Atmos 124:5757–5778. https://doi.org/10.1029/2018JD030004

Frich P, Alexander L V., Della-Marta P, et al (2002) Observed coherent changes in climatic extremes during the second half of the twentieth century. Clim Res 19:193–212. https://doi.org/10.3354/cr019193

Giorgi F (2006) Climate change hot-spots. Geophys Res Lett 33:8707. https://doi.org/10.1029/2006GL025734

Giorgi F, Bi X (2009) Time of emergence (TOE) of GHG-forced precipitation change hot-spots. Geophys Res Lett 36:. https://doi.org/10.1029/2009GL037593

Giorgi F, Jones C, Asrar GR (2009) Addressing climate information needs at the regional level: The CORDEX framework. WMO Bull 58:175–183

Giorgi F, Lionello P (2008) Climate change projections for the Mediterranean region. Glob Planet Change 63:90–104. https://doi.org/10.1016/J.GLOPLACHA.2007.09.005

Hardy B (1998) ITS-90 FORMULATIONS FOR VAPOR PRESSURE, FROSTPOINT TEMPERATURE, DEWPOINT TEMPERATURE, AND ENHANCEMENT FACTORS IN THE RANGE –100 TO +100 C Bob Hardy. Proc Third Int Symp Humidity Moisture 1–8

Harvey BJ, Shaffrey LC, Woollings TJ (2014) Equator-to-pole temperature differences and the extra-tropical storm track responses of the CMIP5 climate models. Clim Dyn 43:1171–1182.

https://doi.org/10.1007/S00382-013-1883-9/FIGURES/9

Hawkins E, Sutton R (2009) The Potential to Narrow Uncertainty in Regional Climate Predictions. Bull Am Meteorol Soc 90:1095–1108. https://doi.org/10.1175/2009BAMS2607.1

Held IM, Soden BJ (2006) Robust Responses of the Hydrological Cycle to Global Warming. J Clim 19:5686–5699. https://doi.org/10.1175/JCLI3990.1

Herrera S, Margarida Cardoso R, Matos Soares P, et al (2019) Iberia01: A new gridded dataset of daily precipitation and temperatures over Iberia. Earth Syst Sci Data 11:1947–1956. https://doi.org/10.5194/essd-11-1947-2019

Hewitt CD, Griggs DJ (2004) Ensembles-based predictions of climate changes and their impacts. Eos (Washington DC) 85:566. https://doi.org/10.1029/2004EO520005/FORMAT/PDF

Hidalgo L (2002) Tratado De Viticultura General - Livro - WOOK

Huglin MP (1978) Nouveau mode d'évaluation des possibilités héliothermiques d'un milieu viticole. Comptes Rendus l'Académie d'Agriculture Fr 64:1117–1126

IPCC (2013) Climate Change 2013: The Physical Science Basis. Contribution of Working Group I to the Fifth Assessment Report of the Intergovernmental Panel on Climate Change. Cambridge University Press

IPCC (2021) Climate Change 2021: The Physical Science Basis. Contribution of Working Group I to the Sixth Assessment Report of the Intergovernmental Panel on Climate Change. Cambridge University Press, Cambridge, United Kingdom and New York, NY, USA, In press

Jacob D, Petersen J, Eggert B, et al (2014) EURO-CORDEX: New high-resolution climate change projections for European impact research. Reg Environ Chang 14:563–578. https://doi.org/10.1007/s10113-013-0499-2

Jacob D, Teichmann C, Sobolowski S, et al (2020) Regional climate downscaling over Europe: perspectives from the EURO-CORDEX community. Reg Environ Chang 20:. https://doi.org/10.1007/s10113-020-01606-9

Kang SM, Lu J (2012) Expansion of the Hadley Cell under Global Warming: Winter versus Summer. J Clim 25:8387–8393. https://doi.org/10.1175/JCLI-D-12-00323.1

Karyono K, Abdullah BM, Cotgrave AJ, Bras A (2020) The adaptive thermal comfort review from the 1920s, the present, and the future. Dev Built Environ 4:. https://doi.org/10.1016/J.DIBE.2020.100032

Kim J, Waliser DE, Mattmann CA, et al (2014) Evaluation of the CORDEX-Africa multi-RCM hindcast:

Systematic model errors. Clim Dyn 42:1189–1202. https://doi.org/10.1007/s00382-013-1751-7

Kliewer WM (1977) Effect of High Temperatures during the Bloom-Set Period on Fruit-Set, Ovule Fertility, and Berry Growth of Several Grape Cultivars. Am J Enol Vitic 28:215–222

Knist S, Goergen K, Buonomo E, et al (2017) Land-atmosphere coupling in EURO-CORDEX evaluation experiments. J Geophys Res Atmos 122:79–103. https://doi.org/10.1002/2016JD025476

Knutti R, Sedláček J, Sanderson BM, et al (2017) A climate model projection weighting scheme accounting for performance and interdependence. Geophys Res Lett 44:1909–1918. https://doi.org/10.1002/2016GL072012

Köppen W (1936) Das geographisca System der Klimate, in: Handbuch der Klimatologie, edited by: K ̈oppen, W. and Geiger, G., 1. C. Gebr, Borntraeger

Kotlarski S, Lüthi D, Schär C (2015) The elevation dependency of 21st century European climate change: an RCM ensemble perspective. Int J Climatol 35:3902–3920. https://doi.org/10.1002/JOC.4254

Kovats RS, Hajat S (2008) Heat Stress and Public Health: A Critical Review. http://dx.doi.org/101146/annurev.publhealth29020907090843 29:41–55. https://doi.org/10.1146/ANNUREV.PUBLHEALTH.29.020907.090843

Lima DCA, Soares PMM, Cardoso RM, et al (2021) The present and future offshore wind resource in the Southwestern African region. Clim Dyn 56:1371–1388. https://doi.org/10.1007/s00382-020-05536-4

Lionello P, Scarascia L (2018) The relation between climate change in the Mediterranean region and global warming. Reg Environ Chang 2018 185 18:1481–1493. https://doi.org/10.1007/S10113-018-1290-1

Magalhães N (2008) Tratado de Viticultura - A Videira, A Vinha e o "Terroir"

Mariotti A (2010) Recent Changes in the Mediterranean Water Cycle: A Pathway toward Long-Term Regional Hydroclimatic Change? J Clim 23:1513–1525. https://doi.org/10.1175/2009JCLI3251.1

Mckee TB, Doesken NJ, Kleist J (1993) The Relationship of Drought Frequency and Duration to Time Scales. Eighth Conf Appl Climatol 17–22

Mearns LO, Gutowski W, Jones R, et al (2009) A regional climate change assessment program for North America. Eos (Washington DC) 90:311. https://doi.org/10.1029/2009EO360002/FORMAT/PDF

Meehl GA, Boer GJ, Covey C, et al (2000) The Coupled Model Intercomparison Project (CMIP). Bull Am Meteorol Soc 81:313–318. https://doi.org/10.1175/1520-0477(2000)081

Meehl GA, Tebaldi C (2004) More intense, more frequent, and longer lasting heat waves in the 21st century. Science (80-) 305:994–997.

https://doi.org/10.1126/SCIENCE.1098704/SUPPL_FILE/MEEHL.SOM.PDF

Miyasaka T, Nakamura H (2005) Structure and Formation Mechanisms of the Northern Hemisphere Summertime Subtropical Highs. J Clim 18:5046–5066. https://doi.org/10.1175/JCLI3599.1

Moemken J, Reyers M, Feldmann H, Pinto JG (2018) Future Changes of Wind Speed and Wind Energy Potentials in EURO-CORDEX Ensemble Simulations. J Geophys Res Atmos 123:6373–6389. https://doi.org/10.1029/2018JD028473

Nogueira M, Lima DCA, Soares PMM (2020) An integrated approach to project the future urban climate response: Changes to Lisbon's urban heat island and temperature extremes. Urban Clim 34:100683. https://doi.org/10.1016/j.uclim.2020.100683

Nogueira M, Soares PMM (2019) A surface modelling approach for attribution and disentanglement of the effects of global warming from urbanization in temperature extremes: application to Lisbon. Environ Res Lett 14:114023. https://doi.org/10.1088/1748-9326/ab465f

Nogueira M, Soares PMM, Tomé R, Cardoso RM (2019) High-resolution multi-model projections of onshore wind resources over Portugal under a changing climate. Theor Appl Climatol 136:347–362. https://doi.org/10.1007/s00704-018-2495-4

Orlowsky B, Seneviratne SI (2013) Elusive drought: Uncertainty in observed trends and short-and long-term CMIP5 projections. Hydrol Earth Syst Sci 17:1765–1781. https://doi.org/10.5194/HESS-17-1765-2013

Palmer T, Stevens B (2019) The scientific challenge of understanding and estimating climate change. Proc Natl Acad Sci U S A 116:24390–24395. https://doi.org/10.1073/pnas.1906691116

Peel MC, Finlayson BL, Mcmahon TA (2007) Hydrology and Earth System Sciences Updated world map of the Köppen-Geiger climate classification. Hydrol Earth Syst Sci 11:1633–1644

Perkins SE, Pitman AJ, Holbrook NJ, McAneney J (2007) Evaluation of the AR4 Climate Models' Simulated Daily Maximum Temperature, Minimum Temperature, and Precipitation over Australia Using Probability Density Functions. J Clim 20:4356–4376. https://doi.org/10.1175/JCLI4253.1

Peterson EW, Hennessey Jr. JP (1978) On the Use of Power Laws for Estimates of Wind Power Potential. J Appl Meteorol 17:390–394

Prein AF, Gobiet A, Truhetz H, et al (2016) Precipitation in the EURO-CORDEX 0.11∘ and 0.44∘ simulations: high resolution, high benefits? Clim Dyn 46:383–412. https://doi.org/10.1007/s00382-015-2589-y

Pryor SC, Barthelmie RJ (2011) Assessing climate change impacts on the near-term stability of the wind energy resource over the United States. Proc Natl Acad Sci 108:8167–8171. https://doi.org/10.1073/pnas.1019388108

Russo S, Sillmann J, Fischer EM (2015) Top ten European heatwaves since 1950 and their occurrence in the coming decades. Environ Res Lett 10:124003. https://doi.org/10.1088/1748-9326/10/12/124003

Sanderson BM, Knutti R, Caldwell P (2015) A Representative Democracy to Reduce Interdependency in a Multimodel Ensemble. J Clim 28:5171–5194. https://doi.org/10.1175/JCLI-D-14-00362.1

Sanderson BM, Wehner M, Knutti R (2017) Skill and independence weighting for multi-model assessments. Geosci Model Dev 10:2379–2395. https://doi.org/10.5194/GMD-10-2379-2017

Santos JA, Malheiro AC, Pinto JG, Jones G V. (2012) Macroclimate and viticultural zoning in Europe: Observed trends and atmospheric forcing. Clim Res 51:89–103. https://doi.org/10.3354/CR01056

Scheff J, Frierson DMW (2014) Scaling Potential Evapotranspiration with Greenhouse Warming. J Clim 27:1539–1558. https://doi.org/10.1175/JCLI-D-13-00233.1

Schleussner CF, Lissner TK, Fischer EM, et al (2016) Differential climate impacts for policy-relevant limits to global warming: The case of 1.5 °c and 2 °c. Earth Syst Dyn 7:327–351. https://doi.org/10.5194/ESD-7-327-2016

Schoetter R, Cattiaux J, Douville H (2015) Changes of western European heat wave characteristics projected by the CMIP5 ensemble. Clim Dyn 45:1601–1616. https://doi.org/10.1007/S00382-014-2434-8/TABLES/4

Sherwood S, Fu Q (2014) A drier future? Science (80-) 343:737–739. https://doi.org/10.1126/SCIENCE.1247620/SUPPL_FILE/SHERWOOD.SM.PDF

Sillmann J, Kharin V V., Zwiers FW, et al (2013) Climate extremes indices in the CMIP5 multimodel ensemble: Part 2. Future climate projections. J Geophys Res Atmos 118:2473–2493. https://doi.org/10.1002/JGRD.50188

Simmons AJ, Willett KM, Jones PD, et al (2010) Low-frequency variations in surface atmospheric humidity, temperature, and precipitation: Inferences from reanalyses and monthly gridded observational data sets. J Geophys Res Atmos 115:1110. https://doi.org/10.1029/2009JD012442

Soares PMM, Cardoso RM, Lima DCA, Miranda PMA (2017a) Future precipitation in Portugal: high-resolution projections using WRF model and EURO-CORDEX multi-model ensembles. Clim Dyn 49:2503–2530. https://doi.org/10.1007/s00382-016-3455-2

Soares PMM, Lima DCA, Cardoso RM, et al (2017b) Western Iberian offshore wind resources: More or less in a global warming climate? Appl Energy 203:72–90. https://doi.org/10.1016/j.apenergy.2017.06.004

Soares PMM, Lima DCA, Cardoso RM, Semedo A (2017c) High resolution projections for the western Iberian coastal low level jet in a changing climate. Clim Dyn 49:1547–1566. https://doi.org/10.1007/s00382-016-3397-8

Soares PMM, Lima DCA, Nogueira M (2020) Global offshore wind energy resources using the new ERA-5 reanalysis. Environ Res Lett 15:1040a2. https://doi.org/10.1088/1748-9326/abb10d

Soares PMM, Lima DCA, Semedo A, et al (2019) Assessing the climate change impact on the North African offshore surface wind and coastal low-level jet using coupled and uncoupled regional climate simulations. Clim Dyn 52:7111–7132. https://doi.org/10.1007/s00382-018-4565-9

Spellman G (1999) Wine, weather and climate. Weather 54:230–239. https://doi.org/10.1002/j.1477-8696.1999.tb07256.x

Suklitsch M, Gobiet A, Leuprecht A, Frei C (2008) High Resolution Sensitivity Studies with the Regional Climate Model CCLM in the Alpine Region. Meteorol Zeitschrift 467–476. https://doi.org/10.1127/0941-2948/2008/0308

Tobin I, Vautard R, Balog I, et al (2015) Assessing climate change impacts on European wind energy from ENSEMBLES high-resolution climate projections. Clim Change 128:99–112. https://doi.org/10.1007/s10584-014-1291-0

Tonietto J, Carbonneau A (2004) A multicriteria climatic classification system for grape-growing regions worldwide. Agric For Meteorol 124:81–97. https://doi.org/10.1016/J.AGRFORMET.2003.06.001

Trenberth KE (2011) Changes in precipitation with climate change. Clim Res 47:123–138. https://doi.org/10.3354/cr00953

Tuel A, Eltahir EAB (2020) Why Is the Mediterranean a Climate Change Hot Spot? J Clim 33:5829–5843. https://doi.org/10.1175/JCLI-D-19-0910.1

Turco M, Rosa-Cánovas JJ, Bedia J, et al (2018) Exacerbated fires in Mediterranean Europe due to anthropogenic warming projected with non-stationary climate-fire models. Nat Commun 2018 91 9:1–9. https://doi.org/10.1038/s41467-018-06358-z

Ulbrich U, Pinto JG, Kupfer H, et al (2008) Changing Northern Hemisphere Storm Tracks in an Ensemble of IPCC Climate Change Simulations. J Clim 21:1669–1679. https://doi.org/10.1175/2007JCLI1992.1

Van Oldenborgh GJ, Mitchell-Larson E, Vecchi GA, et al (2019) Cold waves are getting milder in the northern midlatitudes. Environ Res Lett 14:114004. https://doi.org/10.1088/1748-9326/AB4867

van Vuuren DP, Edmonds J, Kainuma M, et al (2011) The representative concentration pathways: an overview. Clim Change 109:5–31. https://doi.org/10.1007/s10584-011-0148-z

Vautard R, Kadygrov N, Iles C, et al (2021) Evaluation of the Large EURO-CORDEX Regional Climate Model Ensemble. J Geophys Res Atmos 126:e2019JD032344. https://doi.org/10.1029/2019JD032344

Vicente-Serrano SM, Beguería S, López-Moreno JI (2010) A Multiscalar Drought Index Sensitive to Global Warming: The Standardized Precipitation Evapotranspiration Index. J Clim 23:1696–1718. https://doi.org/10.1175/2009JCLI2909.1

Vicente-Serrano SM, Lopez-Moreno J-I, Beguería S, et al (2014) Evidence of increasing drought severity caused by temperature rise in southern Europe. Environ Res Lett 9:044001. https://doi.org/10.1088/1748-9326/9/4/044001

Vicente-Serrano SM, Quiring SM, Peña-Gallardo M, et al (2020) A review of environmental droughts: Increased risk under global warming? Earth-Science Rev 201:102953. https://doi.org/10.1016/J.EARSCIREV.2019.102953

Wenzel S, Eyring V, Gerber EP, Karpechko AY (2016) Constraining Future Summer Austral Jet Stream Positions in the CMIP5 Ensemble by Process-Oriented Multiple Diagnostic Regression. J Clim 29:673–687. https://doi.org/10.1175/JCLI-D-15-0412.1

Wilks DS (2006) Statistical Methods in the Atmospheric Sciences. Academic Press

Willett KM, Jones PD, Thorne PW, Gillett NP (2010) A comparison of large scale changes in surface humidity over land in observations and CMIP3 general circulation models. Environ Res Lett 5:025210. https://doi.org/10.1088/1748-9326/5/2/025210

Willmott CJ, Robeson SM, Matsuura K (2012) A refined index of model performance. Int J Climatol 32:2088–2094. https://doi.org/10.1002/joc.2419

Winkler AJ, Cook JA, Kliewer WM, Lider LA (1974) General viticulture. University of California Press, Berkeley, CA

WMO (2012) Standardized Precipitation Index User Guide | World Meteorological Organization

Zhang X, Hegerl G, Zwiers FW, Kenyon J (2005) Avoiding Inhomogeneity in Percentile-Based Indices of Temperature Extremes. J Clim 18:1641–1651. https://doi.org/10.1175/JCLI3366.1